Nanostructuring of binary liquids and water by confinement in periodic mesoporous organosilicates

Aicha Jani

ANNÉE 2021

UNIVERSITÉ DE RENNES 1

UNIVERSITE BRETAGNE LOIRE

THÈSE / UNIVERSITÉ DE RENNES 1
sous le sceau de l'Université Bretagne Loire

pour le grade de

DOCTEUR DE L'UNIVERSITÉ DE RENNES 1

Mention : Physique

Ecole doctorale (3M)

Présentée par

Aîcha Jani

Préparée à l'unité de recherche UMR 6251, IPR
Institut de Physique de Rennes
UFR Sciences et Propriétés de la Matière

Nanostructuring of binary liquids and water by confinement in periodic mesoporous organosilicates

Soutenance prévue à Rennes

le 06 Décembre 2021

devant le jury composé de :

Diane REBISCOUL
Chercheuse CEA, ICSM / *rapporteur*
Sophie LE CAER
Directrice de Recherche CNRS, CEA Saclay/ *rapporteur*
Jean LE BIDEAU
Professeur, IMN - Université de Nantes / *examinateur*
Marie-Vanessa COULET
Chargée de Recherche CNRS, MADIREL - Aix Marseille Université / *examinateur*
Anthony SZYMCZYK
Professeur, ISCR - Université de Rennes 1/ *examinateur*
Denis MORINEAU
Directeur de Recherche CNRS, IPR - Université de Rennes 1 / *directeur de thèse*

DEDICACES

A ma très chère mère

Affable, honorable, aimable : Tu représentes pour moi le symbole de la bonté par excellence, la source de tendresse et l'exemple du dévouement qui n'a pas cessé de m'encourager et de prier pour moi. Ta prière et ta bénédiction m'ont été d'un grand secours pour mener à bien mes études. Aucune dédicace ne saurait être assez éloquente pour exprimer ce que tu mérites pour tous les sacrifices que tu n'as cessé de me donner depuis ma naissance, durant mon enfance et même à l'âge adulte. Tu as fait plus qu'une mère puisse faire pour que ses enfants suivent le bon chemin dans leur vie et leurs études. Je te dédie ce travail en témoignage de mon profond amour. Puisse Dieu, le tout puissant, te préserver et t'accorder santé, longue vie et bonheur.

A la mémoire de mon très cher père

Je dédie cet événement marquant de ma vie à la mémoire de mon père disparu trop tôt. J'espère que, du monde qui est sien maintenant, il apprécie cet humble geste comme preuve de reconnaissance de la part d'une fille qui a toujours prié pour le salut de son âme. Puisse Dieu, le tout puissant, l'avoir en sa sainte miséricorde !

A mon cher Hamza, ma très chère sœur, mon cher frère et A ma famille et à tous mes amis

A mon cher 'Boss' Denis

A tous mes amis de l'équipe de l'Institut de Physique de Rennes

A tous mes enseignants tout au long mon cursus académique

A tous ceux qui me sont chers,

Je vous dédie en signe de reconnaissance et de dévouement cet humble travail qui n'aura pas vu jour sans vos soutiens et vos collaborations.

ACKNOWLEDGEMENTS

Denis Morineau has been an ideal teacher, mentor, and thesis supervisor, offering advice and encouragement with a perfect blend of insight and humor. I'm proud of, and grateful for, my time working with you Denis. You have inspired me in so many ways both at the personal and scientific levels and for that I'll be forever beholden.

I would also like to express my gratitude towards all the jury members (Diane Rebiscoul, Sophie Le Caer, Jean Le Bideau, Marie-Vanessa Coulet and Anthony Szymczyk) for accepting to be a part of this long process.

Much gratitude goes to the management of the IPR (Jean-Christophe Sangleboeuf) for welcoming me in IPR and to all the IPR staff (permanents and non-permanents) and all the administrative service for making me feel like home over the last three years. A particular thanks goes to all my friends in IPR and equip partner Benjamin Malfait for their collaboration, nice discussions and support.

Thanks to the management of the ILL and LLB for welcoming me in their institutes and giving me several opportunities to perform neutron scattering experiments. My appreciation extends to the beamline scientists at ILL (D16 – Viviana Cristiglio, IN6-SHARP – Jean-Marc Zanotti and Quentin Berrod, IN16B - Bernhard Frick and Markus Appel, IN5B – Jacques Ollivier) and at LLB (PAXY – Laurence Noirez).

Thanks to ANR/DFG funding and to all NanoLiquids project collaborators from Technische Universität Hamburg (Patrick Huber and Mark Busch) and Hamburg Universität (Michael Fröba and JB Mietner). Thank you for the invitation to Hamburg and the nice discussions

making possible to carry out several scientific productions. In your own ways, you have each added to this project and helped shape me both as a student and a researcher.

Special thanks to my CSI members (Fabienne Gauffre and Thierry Tassaing) for the sincere efforts and valuable time given. Their valuable guidance and feedback has helped me in completing this project.

Much gratitude goes to all for the organizers of all the seminars that I was able to attend and for the trainers (SFN school trainers, USTV trainers and Emmanuel Schaub). Thanks to you I was able to acquire several skills and make several acquaintances and friends.

Last but not least, I want to thank all the teachers and PhD students with whom I have taught and supervised exams. Thank you for your trust, your help and kindness.

TABLE OF CONTENTS

CHAPTER I

INTRODUCTION

ABSTRACT

To initiate the following manuscript, I propose to start with this introductory chapter which will:

- *give the reader a scientific background and review theoretical knowledge, assumed necessary to a better understanding of my thesis subject.*
- *provide a general description of the current understanding of the two main effects of confinement on liquids properties (pore size reduction and surface interactions) with a primary focus on phase transitions, structure and dynamics at molecular scale properties.*
- *focus on surface interaction effect to discuss the possibility to use confinement as a tool to manipulate the properties of liquids by modulating the liquid-surface interaction and review literature studies that treated this issue. a tool to manipulate liquid properties*
- *provide the scientific justifications, the objectives and the organization of my thesis.*

The properties of materials confined in porous media are important in multiple scientific and technological aspects. The confinement of liquids at the nanoscale significantly influences their physical properties, leading to radical modification of their static and dynamical properties compared to the bulk counterparts. The study of the different properties at the nanoscale, has promoted an intensive research activity giving rise to an entire field renowned as *nanosciences*.

Several mechanisms contribute to the confinement effects, could be reviewed mainly into two, that dominate on a few molecular diameters scale. The first is the so-called finite size effect engendered by the reduction of the volume accessible to molecular fluids via confinement. It emphasizes that restricted geometries imply "cut-off" effects on the growth of any correlation or cooperativity lengths which is bounded by the pore size. The second is based on the surface effect through the introduction of a wall interface leading to a competition between liquid-wall and liquid-liquid forces. Hence, in this chapter, I initially address the two main effects of confinement (pore size reduction and the surface interaction), on liquid properties with a primary focus on the following: phase transitions, dynamics and structure.

In this first part of this chapter, I first provide a general description of the confinement effects on phase transition properties of vapor/liquid phase (capillary condensation), liquid/solid phase (melting behavior) and supercooled liquid/solid phase (glass transition), by linking this change in properties to the two main effects of confinement. Since the phase transition behavior is strongly linked to structural and dynamical properties, these two aspects are addressed subsequently. I address the structure behavior of the solid phase (crystal structure of water) and liquid phase at macroscopic scale (average and radial density) which shows a major pore size dependence and at molecular scale (molecular self-association), which is more influenced by surface interaction. Then I address the dynamic behavior in different systems with various pore geometry (with interconnected porosity such as Vycor glass and with well-defined geometry such as mesostructured porous silica) and various chemical compositions (hydrophilic nanopores such as mesostructured porous silica and hydrophobic nanopores such as carbon nanotubes and hydrophobically modified MCM-41). In this description of the confinement effects on physical properties I address a selection of examples on confinement studies (in particular water and H-bonding liquids) to achieve a better understanding of my thesis subject.

In the second part of this chapter, I focus on surface interaction effect and the possibility to use it as a tool to manipulate the properties of liquids and I review literature studies that treated this issue. This idea comes after understanding that the key parameter that determines the molecules behavior in pores is the liquid-surface interaction. Therefore, manipulating liquids properties under confinement can be established by controlling liquid-surface interactions at the molecular scale. In the first paragraph, I discuss modulating the liquid-surface interaction by using binary liquids comprising a H-bonded component and an aprotic component that induce different interaction with pore wall that induces new molecular behavior. In the second, I consider another way to manipulate liquids properties by using hybrid pores in order to modulate the types of interactions.

After providing the scientific justifications, in the end of chapter I give the reader the aim of my thesis project and the organization of the following manuscript.

I. EFFECT OF PORE SIZE REDUCTION AND SURFACE INTERACTIONS ON CONFINED LIQUID PROPERTIES

The purpose of this part is to provide a general description of the current understanding of the two main effects of confinement on liquids properties. This will allow the reader to have a preliminary idea of the interest of the physical phenomena associated to pore size reduction and surface interaction effects and to gradually introduce the scientific justifications and the objectives of my thesis.

The evaluation of the pore size effect has been studied owing to the arrival of new system with a tunable diameter and a well-defined geometry (straight and parallel nanochannels) such as mesostructured porous silica and the discovery of the M41S family in 1992[1] and later the family of Santa Barbara Amorphous (SBA) materials in 1998[2].

The evaluation of the surface effect has been studied thanks to chemical modifications of the surface modifying the nature of the interaction such as its hydrophilicity.

Depending on the interest of different fields, the effect of confinement with the pore size reduction and the surface interaction on liquid properties has been the subject of several reviews.[3-9] In the following, we primary focus on phase transitions, dynamics and structure.

1. Phase Transitions Properties

1-1- Vapor/liquid phase transition: focus on the capillary condensation process

1-1-1-Pore size reduction effect on the capillary condensation process

A theoretical understanding of the reduction of pore size effect on capillary condensation requires a preliminary understanding of vapor behavior in equilibrium with its liquid.

Laplace-Young's law relates the vapor pressure P_v to the liquid pressure P_l according to:

$$P_v - P_l = \frac{2\gamma}{R_c} \qquad (I\text{-}1)$$

Where γ is the liquid surface tension at temperature T and R_c is the average curvature radius of the vapor/liquid interface.

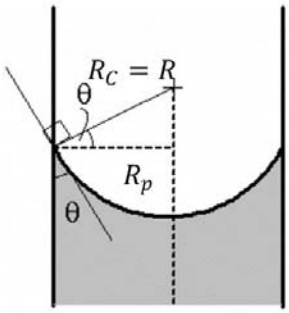

Figure I-1: Laplace-Young's law parameters in a particular case where the system has a tubular form of circular cross-section of a radius R_p and the interface forms a meniscus that is a portion of the surface of a sphere R equivalent to the curvature radius R_C with a wetting angle θ less than 90°.

In the case where the system has a tubular form of circular cross-section with radius R_p (same as the case of confinement in cylindrical pore of a size R_p) and the interface forms a meniscus that is a portion of the surface of a sphere, then the curvature radius R_c becomes equivalent to the sphere radius R (as shown in Figure I-1) and the equation (I-2) can be rewritten as:

$$P_v - P_l = \frac{2\,\gamma\,cos(\theta)}{R_p} \qquad (I\text{-}2)$$

Since the equilibrium of the two phases is established, there is, consequently, a chemical potential equivalence $d\mu_v = d\mu_l$. At constant temperature this equivalence may be written as a function of molar volume of vapor and liquid, respectively V_v^m and V_l^m and becomes $V_v^m\,dP_v = V_l^m\,dP_l$. Therefore, the derivative of the Laplace-Young's equation for an ideal gas can be rewritten as:

$$\frac{RT}{V_v^m}\frac{d\,P_v}{P_v} = d\left(\frac{2\,\gamma}{R_c}\right) \qquad (I\text{-}3)$$

According to the Kelvin's model (presented in Figure I-2-A), when the vapor/liquid interface is flat, the pressure at the interface is, then, equal to the saturated vapor pressure P_{Sat} allowing to integrate the equation (I-3):

$$\int_{P_{Sat}}^{P_v}\frac{RT}{V_v^m}\frac{d\,P_v}{P_v} = \int_{\infty}^{R_c} d\left(\frac{2\,\gamma}{R_c}\right) \qquad (I\text{-}4)$$

To obtain the Kelvin's equation:

$$\frac{RT}{V_v^m}\,ln\left(\frac{P_v}{P_{Sat}}\right) = \frac{2\,\gamma}{R_c} \qquad (I\text{-}5)$$

Equivalent to:

$$\frac{RT}{V_v^m}\, ln(\frac{P_v}{P_{Sat}}) = \frac{2\,\gamma\, cos(\theta)}{R_p} \qquad (I\text{-}6)$$

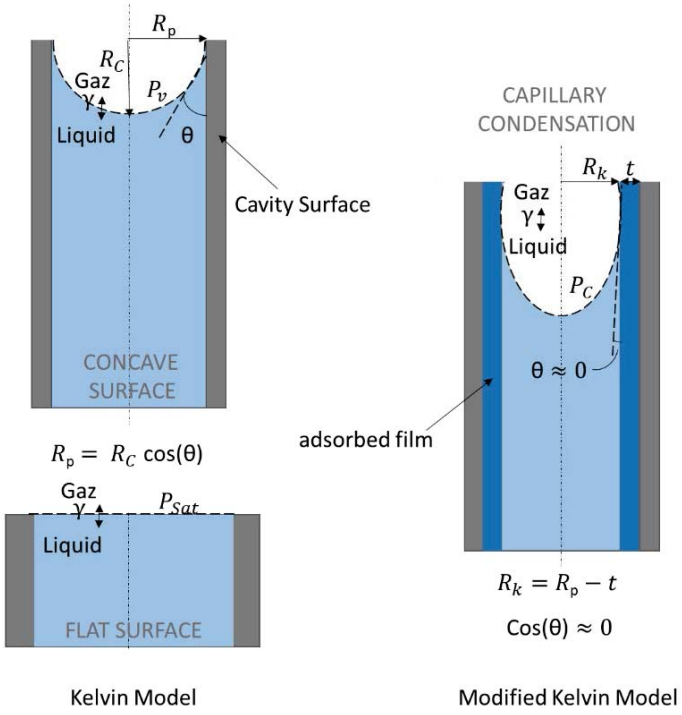

Figure I-2: Presentation of A) the Kelvin's equation parameters: the pore radius R_p can be described as a function of contact angle θ between pore surface and condensed water and the curvature radius R_c. The below supplementary figure shows the vapor pressure over a flat surface P_{Sat}. B) the modified kelvin's equation parameters at capillary condensation ($P_v = P_c$): an adsorbed film of a thickness t is taken into account then the pore radius R_p is reduced by the layer thickness t to give the Kelvin's radius $R_K = R_p - t$.

At capillary condensation (i.e. $P_v = P_c$), we can assume a meniscus break allowing to neglect $\cos(\theta)$ term (since $\theta \approx 0$ as described in Figure I-2-B). In this condition, we can write the equation (I-6) as following:

$$\frac{RT}{V_v^m}\, ln(\frac{P_c}{P_{Sat}}) = \frac{2\,\gamma}{R_p} \qquad (I\text{-}7)$$

Figure I-3, handled by Claudia Marcolli (2014)[10] and which presents the relative humidity of capillary condensation for different pore sizes, shows the ability of the Kelvin's equation to reproduce condensation branch of the adsorption isotherms by taking the relative humidity RH_w /100 as the relative vapor pressure $\frac{P_c}{P_{Sat}}$ of the Kelvin's equation (I-7).

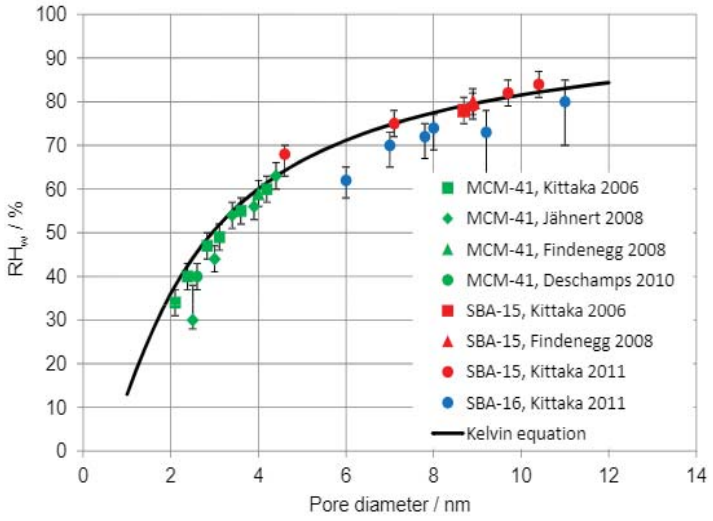

Figure I-3: Relative humidity of capillary condensation of water in pores of different mesoporous silica materials as a function of pore diameter. Data is from Kittaka et al. (2006) (measured gravimetrically at 25◦C), Jähnert et al. (2008) (DVS (dynamic vapor sorption) at 20◦C), Findenegg et al. (2008) (measurements at 20◦C), Deschamps et al. (2010) (DVS), and Kittaka et al. (2011) (measured gravimetrically). The black solid line indicates Relative humidity of capillary condensation predicted by the Kelvin equation (for T=298 K). Data is collected by Claudia Marcolli.[10]

1-1-2-Surface effect on the capillary condensation process

To take into account the surface effect, a corrected Kelvin of the equation (I-7), has been proposed by R.A. Zsigmondy (1911) assuming the presence of an adsorbed film of a thickness t which reduces the porous radius $\mathrm{R_p}$ by the length t giving rise to the Kelvin's radius $R_K = \mathrm{R_p} - t$, as presented in Figure I-2-B. This method was being applied by several works[11-13] to reproduce the sorption isotherm.

$$RT\ ln\left(\frac{P_v}{P_{Sat}}\right) = -2\,\gamma\,\left(\frac{V_M}{R_p - t}\right) = -2\,\gamma\,\left(\frac{V_M}{R_K}\right) \qquad (I\text{-}8)$$

1-2- Liquid/solid phase transition: focus on the melting behavior

1-2-1-Pore size reduction effect on the melting behavior

An important decrease of the melting temperatures has been noticed for confined water,[14-16] aqueous solutions[17] and a broad range of organic compounds.[18] NMR analysis and differential scanning calorimetry (DSC) can provide detailed information on thermal events inside the samples. The Gibbs-Thomson equation is the simplest model used to interpret the

depression of the melting/freezing temperature under confinement in cylindrical pores of radius R_p:

$$T_0 - T_P\left(R_p\right) = \frac{C_{GT}}{R_p} \qquad (I\text{-}9)$$

Where T_0 and T_P denotes the melting temperature in bulk and in the pore, respectively, and $C_{GT} = \frac{2\,T_0\,(\gamma_{WS}-\gamma_{WL})\,V}{\Delta H} = \frac{2\,T_0\,\gamma_{SL}\,V\,Cos(\Phi)}{\Delta H}$ is the Gibbs–Thomson constant with the quantities γ_{WS}, γ_{WL} and γ_{SL} represent the surface free energies per unit of area of the wall/solid, wall/liquid and solid/liquid interfaces, respectively. Φ is the contact angle between the liquid and its own crystal, ΔH is the melting/freezing enthalpy in bulk and V is the molar volume.

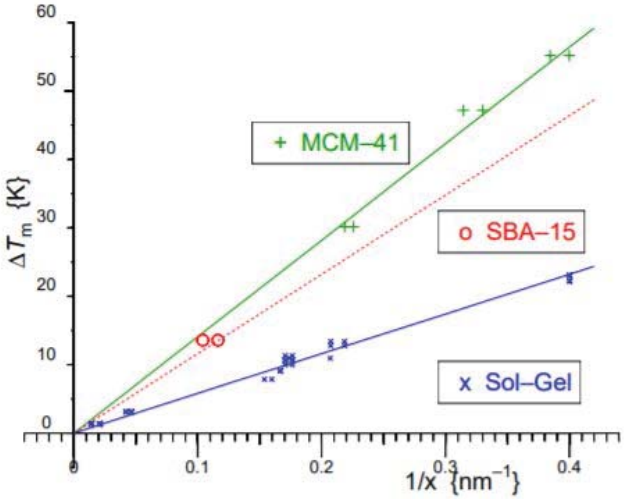

Figure I-4: Melting point depression as a function of reciprocal pore diameter $x=2R_p$ for water in sol gel (blue symbol), SBA-15 (red symbol) and MCM-41 (Green symbol). Lines present the fit with the classic Gibbs-Thomson equation (I-8). Data is collected by JBW Webber.[19]

This equation succeeds to fit the melting point decrease due to confinement for water and organic liquids in several works.[18, 19] Figure I-4, shows a fit of the melting point depression $\Delta T_m = T_0 - T_P\left(\mathrm{R_p}\right)$ for water in pores of different types (Sol-Gel, SBA-15 and MCM-41) and different sizes ($\mathrm{R_p}$ or x/2 in reference[19]) with the classical Gibbs-Thomson equation.

Depending on the wettability of the liquid on pore surface, Φ can varies significantly; for water on super-hydrophilic surface Φ is very small and could be completely neglected when an adsorbed layer is formed, contrariwise in hydrophobic surface it takes a notable values. We explain, clearly, the difference through Figure I-5.

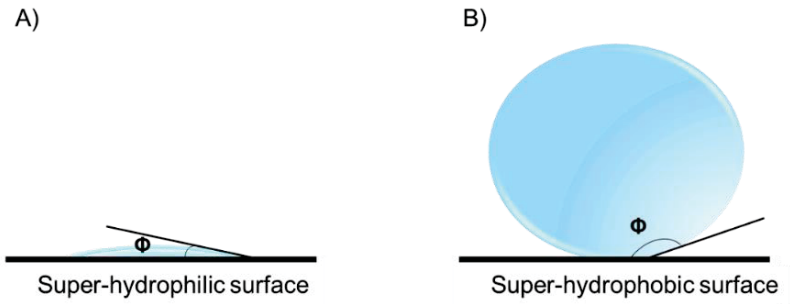

Figure I-5: Two different behaviors of drop of water in contact with two surfaces a) super-hydrophilic where the contact angle Φ is less than 40° [20] and B) super-hydrophobic where the contact angle Φ exceeds 150°.[20]

1-2-2-Surface effect on the melting behavior

By taking into account the existence of an unfrozen water molecules layer in the pore surface of a thickness t, which decreases the radius R_p, the melting process of ice in pores can be also described allowing to rewrite equation (I-9) as:

$$T_0 - T_P\left(R_p\right) = \frac{C_{GT}}{R_p - t} \qquad (I\text{-}9)$$

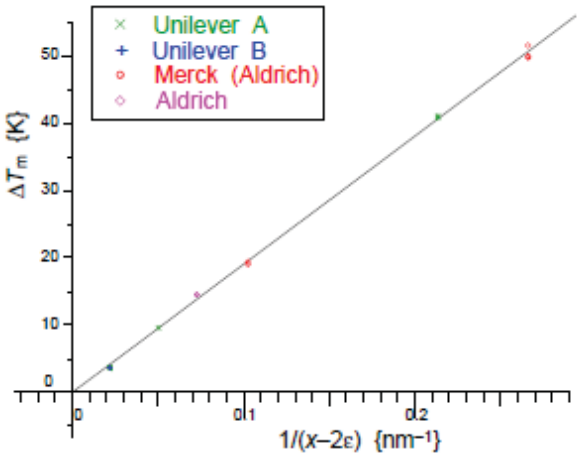

Figure I-6: Melting point depression as a function of reciprocal $x - 2\varepsilon$ with x is the pore radius (corresponds to R_p) in the equation (I-10) and ε is the surface layer for cyclohexane (corresponds to t in equation (I-10) in various sol gel silicas of diameter 25 Å to 500 Å (symbols). Measurement was made by NMR echo experiment, with a measurement time of 20 ms. Straight line presents the fit with the modified Kelvin equation (I-10) by assuming a surface layer of $t = 0{,}121\ nm$ and gives $C_{GT} = 190{,}1\ K\ nm$. Graph reproduced by J. B. W. Webber.[19]

The Figure I-6, shows a fit of the melting point depression $\Delta T_m = T_0 - T_P(\mathrm{R_p})$ for cyclohexane in different sol gel silicas pores of different sizes that varies from 25 Å to 500 Å with the modified Gibbs-Thomson equation (I-10).

1-3- Supercooled liquid/solid phase transition: glass transition

1-3-1-Pore size and surface effect on the glass transition

When cooling below the melting temperature does not lead to crystallization, the system enters a metastable state named supercooled liquid. Upon further cooling, the supercooled state will, eventually, disappear to be replaced by a new state called glassy state at a particular temperature of glass transition T_g.

Figure I-7-A describes the two different paths; the one in blue leading to crystallization and the second leading to vitrification. In parallel, two different schematic aspects of the Gibbs free energy are presented in Figure I-7-B to show the energetic behavior of a metastable state of a supercooled liquid at a temperature T_1 and the unstable state of glass at a temperature T_2.

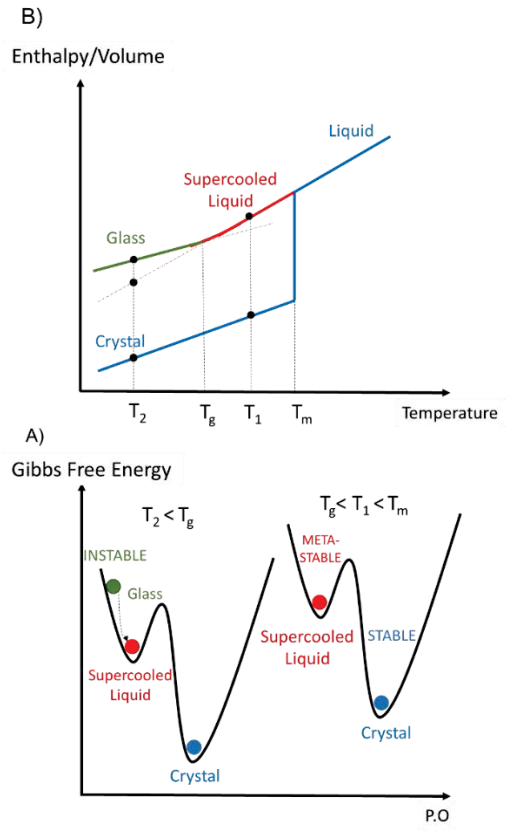

Figure I-7: A qualitative phase diagram (A) and a schematics of the free energy landscape (B) as a function of the configurational space coordinate at two different temperatures T_1 and T_2.

In bulk samples, crystallization usually limits the possible formation of supercooled and glassy states, especially for simple and symmetric small molecules. However, these states are very frequently attained, even using normal cooling conditions, for polymers and more complex organic molecules. Under confinement, the molecule-molecule interactions become, strongly, in competition with molecule-surface interactions leading to their progressive decrease with the pore size and surface affinity which disfavor the crystallization. This important effect of confinement on supercooled and glassy state has made the subject of many studies[21-24] and has given access to study the glass transition of systems which was not accessible in bulk state such as water.[25, 26]

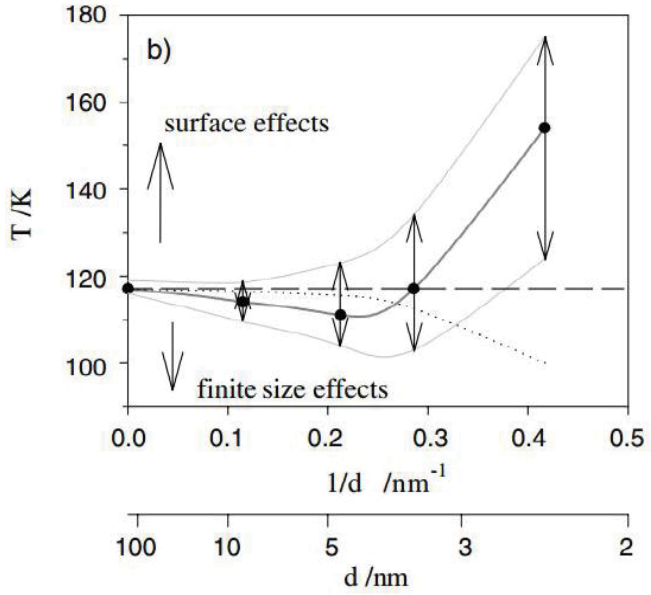

Figure I-8: The Glass transition versus the pore diameter for toluene confined in MCM-41 and SBA-15 nanopores. Dashes illustrate the Tg of bulk toluene, the points represent the average bulk Tg at the same density in the pore and the arrows represent the Tg region.[24]

Despite all these different studies, a general behavior of T_g under confinement is still unavailable. This has been related to the coexistence of multiple effects, including the competition between size and surface interaction effects as shown in Figure I-8 for toluene confined in MCM-41 and SBA-15 nanopores. To resolve this problem, some studies have been able to separate the two parameters in order to follow the effect of one without the perturbation of the other[24]. Indeed, the decrease of confinement size without surface induced retardation effect, decrease the glass transition temperature. Contrariwise, when the surface interaction is more important the glass transition temperature increases. Hence, in small pores of diameter equal to a few molecules, most of confined molecules can interact with the surface, which reduce their mobility that favors the increase of T_g. Otherwise, in large pores the average effect of surface on the sum of confined molecules is very low compared to the geometric confinement effect thus T_g decreases. This phenomenon has raised many

questions regarding the relaxation processes in confined geometries, for this reason, the 3rd part is dedicated to the effect of confinement on the liquid dynamics.

2. Structural Properties of Solid/Liquid Phase

The effect of confinement on the phase transition behavior has raised many questions about the structural properties of liquids/solids in mesoporous systems. Indeed, these properties are strongly linked since any change in physical state necessarily generates a change in the arrangement of molecules in their space. For this reason, we devote this part to a better understanding of the effect of confinement structure.

Several studies have been interested on water structure to be able to identify different crystals formed into pores; their structure, their locations into pores and their dependency on temperature and on the size/nature of the pores. I devote, in more details, the first paragraph of this part to talk about different crystal structures identified on one model system (water).

Investigating the molecular structure can be done through the study of density that means that any change of the average density of confined liquids gives a direct evidence to the change in structural properties. In the second paragraph of this part, I mention the effect of confinement on structure through the average density change and by presenting the density variation along the radial pore axis.

Since in my thesis I am interested in H-bonding liquids which have an interested structure in bulk state with their tendency to self-association, it seems to be relevant to show the effect of confinement on the stability of this molecules organization. And this will be the subject of the third paragraph of this part.

2-1- Solid phase structure: focus on the crystal structure of water

Under ambient conditions, only two crystalline forms of water can exist[27-29] out of 18 possible forms in other different conditions.[30] The hexagonal form of Ice Ih is the most prevalent and stable phase of ice.

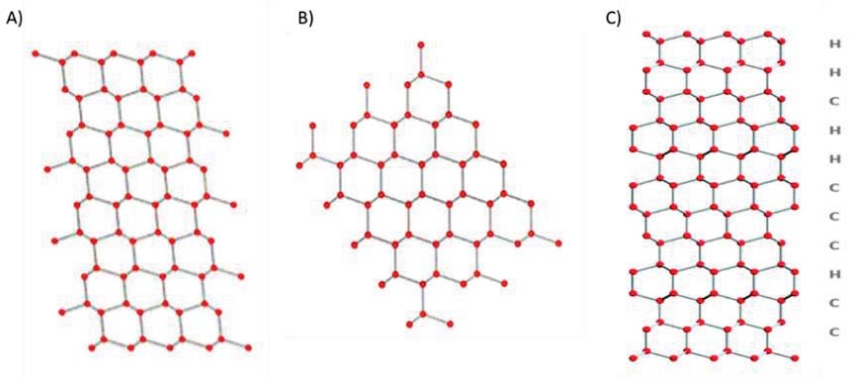

Figure I-9: Different crystal structures of H: (A) hexagonal[31], (B) cubic[31] and (C) an arbitrary example of stacking disorder ice[32] The oxygen atom is shown in red spheres and the bonds in grey lines.

It is formed by cooling water under common environmental conditions and persists thermodynamically stable over a wide range of temperatures. On the other hand, the cubic form of Ice Ic is a metastable phase of ice and needs specific conditions such as nano-confinement for its formation.[33-35] Both crystalline structures are composed by different layers each one consists of six-membered rings of hydrogen bonded water molecules, but differ from each other by the stacking mode of the layers (Figure I-9-(A,B)). The structure of nano-confined ice is not only different from the hexagonal structure (Ih)[36-41] but also different from pure cubic structure (Ic)[42-44]. It is becoming progressively clear that the formed ice phase is typically made up of a combination of both cubic and hexagonal stacking sequences which together do not possess cubic nor hexagonal symmetry. In order to insist on the fact that the formed metastable ice is neither hexagonal nor cubic, and not, as well, a simple mixture of the two forms, this combined phase of stacking disordered ice is called Isd[45]. Figure I-9-C shows a possible structure of stacking disordered ice Isd.

Although in this part we have, only, cited one model system (water), we have been able to emphasize the power of confinement process on the manipulation of the solid structure such as favoring structures being metastable in bulk (cubic form). This phenomenon, leads us to retreat several physical phenomena which seemed, at the bulk scale, as acquired.

2-2- Liquid phase structure at macroscopic scale (density) and molecular scale (molecular self-association): focus on organic liquids

2-2-1-Liquid phase structure at macroscopic scale (average and radial density) showing the pore size effect

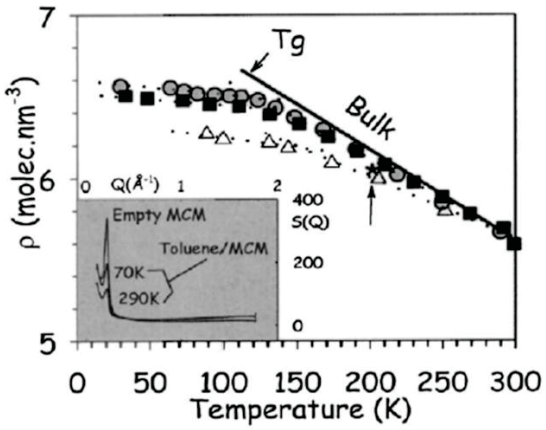

Figure I-10: Temperature dependence of the density of bulk and confined toluene. Pore diameter: Δ: 2.4 nm, ■: 3.5 nm, ●: 4.7nm.[24]

As confinement causes a change in the structure of the solid phase, large variations affect the structure of the liquid phase. Indeed, we can go back to structural information by studying the density of confined liquid. An experimental study has been proposed to document the variation of the average density of toluene confined in MCM-41 and SBA-15 silicates with different pore sizes by neutron diffraction experiments.[24, 46] They evaluated the liquid density by the analysis of the Bragg peak intensities of the hexagonally ordered mesoporous materials based on the use of contrast matching methods. Figure I-10, summarizes these results and show the dependence of the density on temperature (horizontal axis), pore size (different symbols comparison) and on confinement (bulk / confined comparison).

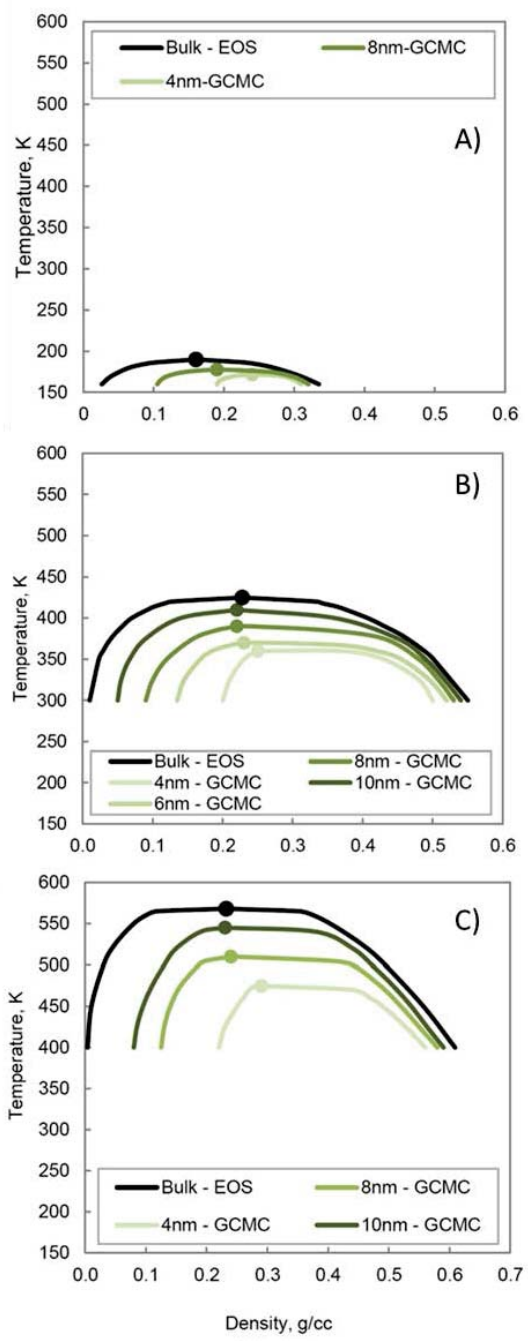

Figure I-11:: Phase diagrams of (A) methane, (B) n-butane and (C) n-octane in graphite slit pores of 4-8nm, 4-6-8-10nm and 4-8-10nm, respectively. Data obtained from GCMC simulations performed by B. R. Didar et al. and compared to bulk (black curves). The dots indicate critical temperature.

A study by GCMC methods,[47] investigated the influence of confinement and pore size on the density of both, vapor and liquid phases. They were able to show that in very small pore sizes, the density of its two phases decreases and becomes closer to each other. This appears in Figure I-11, which presents the density variation of three fluids (methane, n-butane and n-octane) in slit-pore graphite of the order of nanometer. Different studies have also indicated a non-uniform radial density variation of pure fluids across the pore width by molecular simulation.[48, 49] They showed that the density is high close to the pore-wall and it decreases as we move away to the center. The decline shape from pore-wall to pore-center depends on pore size, temperature and pressure.

A phenomenon of radial density oscillation has been exhibited by a study of nanoconfined methanol with MD simulation.[50] This phenomenon of layering is demonstrated in Figure I-12, which shows the oscillation of the radial density of methanol's carbon atoms around the typical liquid density (ρ= 0.014 nm^{-3}) across the pore. The evolution of these layers in the pore reflects the propagation of a translational order from the pore surface towards the center breaking the bulk's translational uniformity.

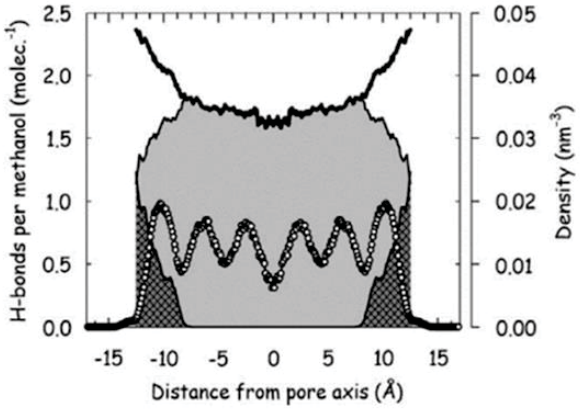

Figure I-12: Radial ρ profile of methanol in silica nanopores. Open circles: local ρ of methanol. Dark shaded area: average number of H-bonds, bounding a methanol and a silanol. Light shaded area: average number of H-bonds linking two methanol molecules. Solid line: average number of H-bonds per methanol molecule.[50]

2-2-2-Liquid phase structure at molecular scale (molecular self-association) showing the pore surface effect

Confinement can influence the self-association of liquid molecules. In fact, specific liquid-surface interactions, as observed for H-bonding sites, compete with liquid-liquid

interactions, which can result in different molecular association. Confinement in mesoporous silicates like MCM-41 and SBA-15 offers the possibility of H-bonding between liquid molecule and interfacial silanols, allowing the formation of new surface-induced self-assemblies. A typical example is the structural study of tert-butanol (TBA) in MCM-41 that launch the project on the associating liquids under confinement.

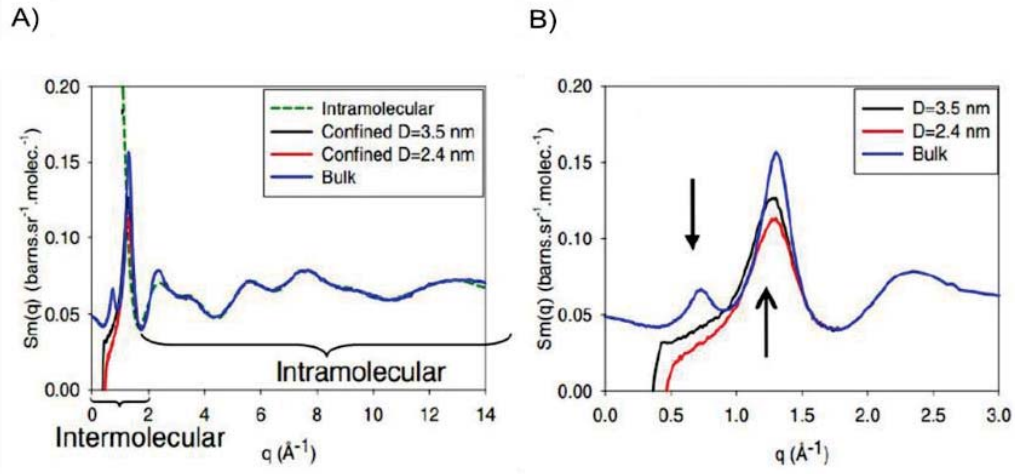

Figure I-13: Neutron structure factor of liquid TBA in bulk and confined in MCM-41. (A): Bulk liquid (blue line), liquid in MCM-41 with D = 3.5 nm (black line), liquid in MCM-41 with D = 2.4 nm (red line), and intramolecular form factor (dashed line); (B): magnified view of the low-q region. [51]

The Figure I-13 obtained from this study, shows the neutron structure factor S(q) of TBA revealing significant changes in the low q region suggesting that the local order of the liquid phase is greatly disturbed by nanoconfinement. The major change induced by confinement is the disappearance of the pre-peak associated to supermolecular assemblies (q= 0.8 $Å^{-1}$) indicating that density correlations related to the super-molecular clustering of TBA could be obscured by additional TBA-surface correlations, and excluded volume effects.[51]

3. Dynamics at Molecular Scale: pore size and surface effect

As we have seen in last paragraphs, confined liquids may take a very different state compared to bulk. Under these new conditions, the molecular behavior, including dynamics, varies significantly.[52, 53] The pioneering studies performed in the mid-90's to study the dynamics of liquid water in spatially confined geometry used Vycor glass by experimental methods[54] (incoherent quasielastic and inelastic neutron scattering). Later, P. Gallo and al. performed a computer simulation method to study the same system. Both studies were able to distinguish two water dynamics one of molecules close to surface and second of in-pore molecules. However, the interconnected porosity of Vycor glass, as clear in SEM images in Figure I-14, is considered as an obstacle in the study of liquid dynamics.

An alternative system with well-defined geometry such as mesostructured porous silica can solve this problem. The discovery of the family of M41S in 1992[1] and later the family of Santa Barbara Amorphous (SBA) materials in 1998,[2] has allowed studying liquids

dynamics with a unique control of the pore geometry since it is characterized by straight and parallel nanochannels with tunable diameter.

Hence, MCM-41 and SBA-15 have been extensively used as model systems to study the dynamics of different liquids with great interest to water. MD simulation[55-57] and various experimental methods that cover a large time scale such as differential scanning calorimetry (DSC), nuclear magnetic resonance (NMR),[58-60] dielectric spectroscopy (DS)[61-64] and quasielastic neutron scattering (QENS),[54, 65-73] have been performed.

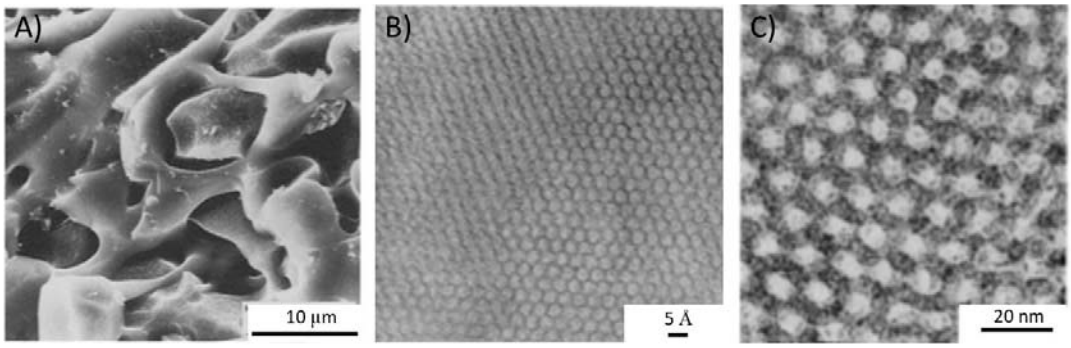

Figure I-14: Different microscopy images of three different materials: (A) representive scanning electron micrograph of vycor.[74] (B) and (C) transmission electron micrograph of SBA-15 (60 Å)[2] and MCM-41 (45 Å),[75] respectively.

Although, MCM-41 and SBA-15 brought a tunable control of the pore size, it appeared that the unchanged chemical composition of hydrophilic silicas could be, indeed, a predominant parameter affecting the characteristics of the water dynamics. This issue was addressed with hydrophobic nanopores formed by Carbon nanotubes[76] and hydrophobically modified MCM-41,[77] which elucidated the respective roles of surface interaction and purely geometric effects. The other limiting case of ultra-strong interaction was illustrated by the ability of Zr−OH and Al−OH terminated MCM-41 surfaces to immobilize water molecules.[70] A recent study focused on the surface dynamics of water measured at very low coverage fraction of SBA-15 revealed that the non-diffusing fraction of water molecules was involved in slow jump processes between sites that could be spatially separated by up to 0.4nm.[78]

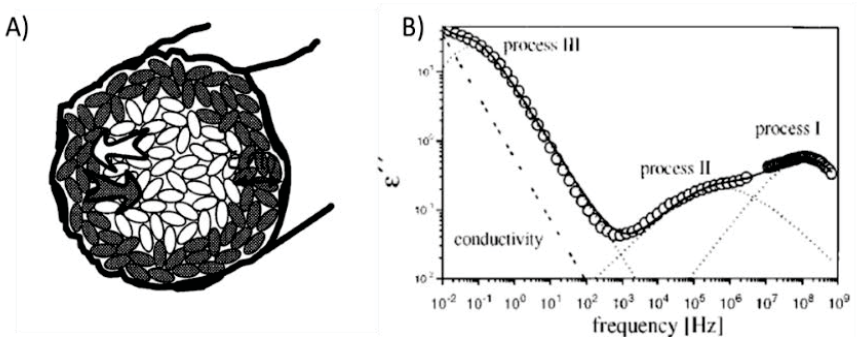

Figure I-15: A) Sketch of filled pore according to the model proposed by M. Arndt et al. which shows the surface layer (dark gray) and the pore center (white). B) Spectrum obtained by dielectric spectroscopy which shows the presence of 3 processes I, II and III. The two first processes are related to the presence of the two regions presented in (A).[79]

In general, these studies have revealed that water in pores shows two different dynamics related to the fact that there are two populations; one is in the surface layer and second in the pore center. The Figure I-15-A presents a model proposed by M. Arndt et al.[79] to interpret their dynamics study of three liquids (salol, pentylene glycol and glycerol) in sol-gel glasses with three different pore sizes (2.5, 5.0, and 7.5 nm) by broadband dielectric spectroscopy. They were able to highlight the existence of two process dynamics (I and II of Figure I-15-B), Hence, their model shows two distinguished environments; pore walls are covered by a surface bound layer of molecules and the remaining volume is filled with bulk-like molecules.

Other studies have revealed that water in pores presents more than two different dynamics[80] with two or three molecular layers at the interface with reduced mobility with the first one is considerably slower because of the important interaction with the pore interface. This studies have been performed by measuring molecular correlation times by means of NMR relaxometry,[81] NMR spectroscopy[59] and computer simulation by molecular dynamics and grand canonical Monte Carlo.[55, 82-90]

M. I. Velasco and co-workers,[80] combined NMR experiments and multiscale molecular dynamics simulation to study water in TiO_2 nanoporous materials. Figure I-16-A, presented in their work, shows the three different water populations with two monolayers and bulk-like core in the center. It reveals an excellent agreement with NMR results which shows three different behaviors (different colors in Figure I-16-B). They attributed the two curves with constant amount (blue and red curves of Figure I-16-B) of water to the first two layers as they still present even at very low filling degrees.

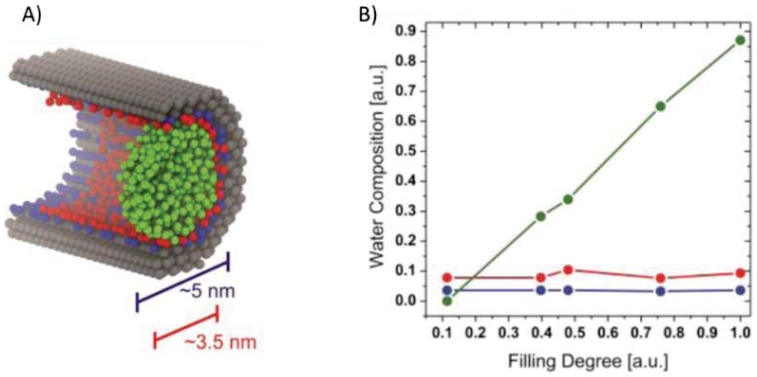

Figure I-16: (A) Filling mechanisms of water in TiO_2 nanoporous materials obtained by molecular dynamics simulations that shows the presence of 3 different water population. (B) An experimental insight on the water dynamics inside the titania pore space by nuclear magnetic resonance (NMR) which supports simulation results.[80]

II. FOCUS ON SURFACE INTERACTION EFFECT : A TOOL TO MANIPULATE LIQUID PROPERTIES

After having reviewed the confinement effects on the liquid physical properties, this section aims at considering the possibility to use confinement as a tool to manipulate the properties of liquids in a controlled manner. This objective comes after understanding that a key parameter that determines the molecules behavior in pores is the liquid-surface interaction. In hydrophilic pores, a preferential interaction with the hydrophilic molecules is created, whereas in the contrary case where the surface is hydrophobic, an interaction with the hydrophobic molecules will preferably be created. The quantification of these different interactions has been shown by adsorption experiments for binary systems. Dutta et al.[91] were able to quantify the affinity of pore walls to different components of the mixture (tert-butanol and toluene) by a thermodynamic model. Interaction of the polar silica with tert-butanol is 100 times greater than that with toluene. However, in the case of hydrophobic walls a greater affinity of toluene is identified.

Manipulating liquids properties under confinement can be established, therefore, by controlling liquid-surface interactions at the molecular scale. In the first paragraph, I will discuss modulating the liquid-surface interaction by using binary liquids comprising a H-bonded component and an aprotic component that induce different interaction with pore wall to create new molecular structures and dynamics. In the second, I will consider another way to manipulate liquids dynamics by using hybrid pores composed by hydrophilic and hydrophobic units in order to modulate the types of interactions.

1. Modulating surface interaction by confining Binary Mixture in a Uniform Pore system with a Hydrophilic Surface

1-1- Effect on structural properties

The introduction of binary mixtures with distinct interactions paves the way to new structures that do not initially exist fully miscible systems in the bulk. Indeed, studies of a typical mixture of tert-butanol and toluene confined in MCM-41[92, 93] and SBA-15[94] have shown the existing of a micro-phase separation with the segregation of alcohol to the pore surface that forms a layer in the “shell” and a rich toluene mixture incarcerated in the “core” as shown in Figure I-17.

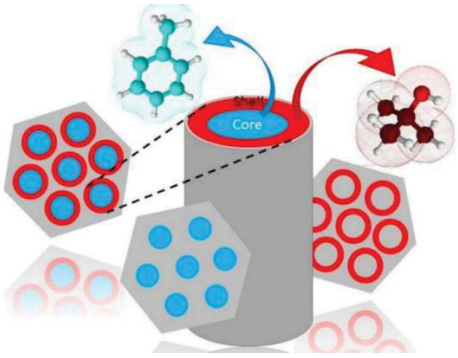

Figure I-17: Schematic representation of core-shell model in a silica matrix (grey); shell composed of tert-butanol (red) and core composed of rich toluene mixture (cyan).[94]

This study has been performed with neutron diffraction experiments based on isotopic contrast effects. The experimental Bragg intensities arising from the mesostructured porous matrix for different contrast matching mixtures are consistent with the predictions from two models presented by red and pink lines. Both models suggest that TBA is on the silica surface and toluene is in the center.

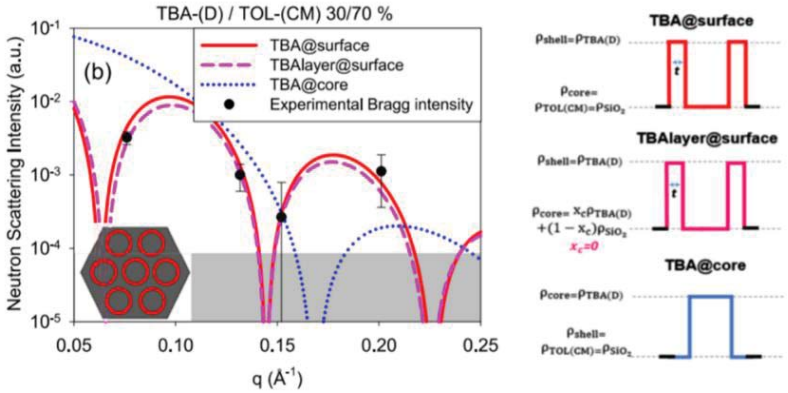

Figure I-18: Experimental value of the integrated intensity of the four Bragg peaks of SBA-15 filled with binary liquids of deuterated TBA mixed with contrast matching TOL. The solid lines are the predicted results for three different models: microphase separated core-shell structures with TBA at the surface (TBA@surface), with one molecular TBA layer at the surface (TBA-layer@surface), and with TOL at the surface (TBA@core). Right panel: sketch of the scattering length density profile.[94]

The difference between the two models is that one assumes that TBA forms only a monolayer on the surface (tbalayer@surface) while the second assumes that all the TBA is on the surface. As Figure I-18 shows, both models correspond to very similar structures for the pore size and the compositions studied, and are in equally good quantitative agreement with experiments. On the contrary, the alternative core-shell model assuming a toluene layer on the surface (blue line) can be obviously eliminated. This behavior was further supported

by the study of the thermal behavior showing that the molecules forming the two regions never crystallize but indeed exhibit two distinct glass transitions.[93]

The observation of confinement induced micro-phase separation of fully miscible tert-Butanol/Toluene (TBA/TOL) binary mixtures confined in different types of straight, mono-disperse, rigid channels of mesoporous MCM-41 and SBA-15 silicates (D = 3.5, 8.3 nm) comes as a further step of the investigation of the microstructure and the self-association of H-bonding either under confinement[51] or during dilution in aprotic solvents[95, 96] by combining neutron diffraction and MD simulations.[97, 98] This particular confinement-induced structure was related to specific interfacial interactions with alcohol that was quantified by Dynamical Vapor Sorption experiments.[91]

1-2- Effect on dynamics properties

The possibility of modifying the binary mixture dynamics by confinement has been demonstrated by the work of Mhanna et al. (2020). They studied the dynamics of TBA/TOL mixtures confined in the straight and monodispersed channels of ordered SBA-15 mesoporous materials by elastic fixed window scans and they compared to MD simulation results.[99] Selective isotopic labeling was used to highlight the dynamics of the hydrogenated component. According to these experiments (Figure I-19), the dynamics of confined TOL in different TOL(H)/TBA(D) mixtures, does not vary significantly with the addition of TBA. However, a significant reduction of the mean-squares-displacements (MSDs) of TBA, in different TBA(H)/TOL(D) mixtures, is noticed when adding TOL.

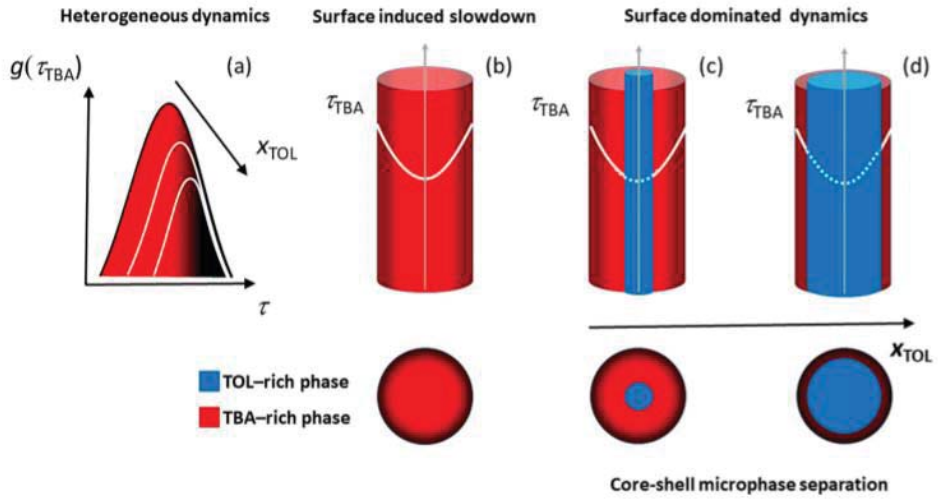

Figure I-19: Schematic illustrations of (a) variation of relaxation times distribution g(τ) and (b−d) dynamical heterogeneities formed by TBA-rich (red) and TOL-rich (blue) regions inside a cylindrical nanopore as a function of the volume fraction of TOL x_{TOL}. Slower (interfacial) regions are identified by a darker red color.[94]

TOL being a less viscous and non-H-bonded solvent, simple mixing rules, which apply for the bulk state, would have predicted an opposite plasticizing effect. This mixing effect on TOL and TBA dynamics is therefore apparently contradictory under confinement. On the other hand, this behavior was better understood when a comparison with the microscopic pictures provided by MD simulation was made, and when they link it to the recently discovered tendency of nanoconfined binary liquids to form core−shell microphase separated structures.[94]

These findings verify and confirm from a dynamic point of view the structure proposed by the modeling of small angle neutron scattering data.[94] This shows the possibility of making the link between structure and dynamics to confirm, experimentally, the confinement-induced microphase separation of liquids which is rather unique in the literature.

2. Modulating surface interaction by confining water in a hybrid pore system with a Hydrophilic/Hydrophobic Surface

2-1-1-Effect on dynamic properties

It was recently demonstrated in a pulsed field gradient (PFG) NMR study that the water transport in hybrid material with organic and silicates units such as PMOs (see next chapter), could be related either to their chemistry or to the architecture of their agglomerates.[100] This couldn't be settle because this method probes the molecule displacements in the µm-range so probably a displacement that also covers the inter-particle space. As a result, the difference observed for the diffusivities in the two hybrid pore systems members of the same family of PMOs (described with more details in next chapter) with similar pore sizes (≈ 3.5nm) first is A-PMO (Figure I-23-A) with silicates and aniline (C_6H_3-NH_2) bridging units and second is B-PMO (Figure I-23-B) with silicates and benzyl (C_6H_4) bridging units, can be related either to slowing down of the intra-particle diffusivities due to a strong hydrogen bonding in the A-PMO channels due to the presence of amino groups (-NH_2) or to a specific architecture of the agglomerates as revealed by the SEM study (Figure I-23).

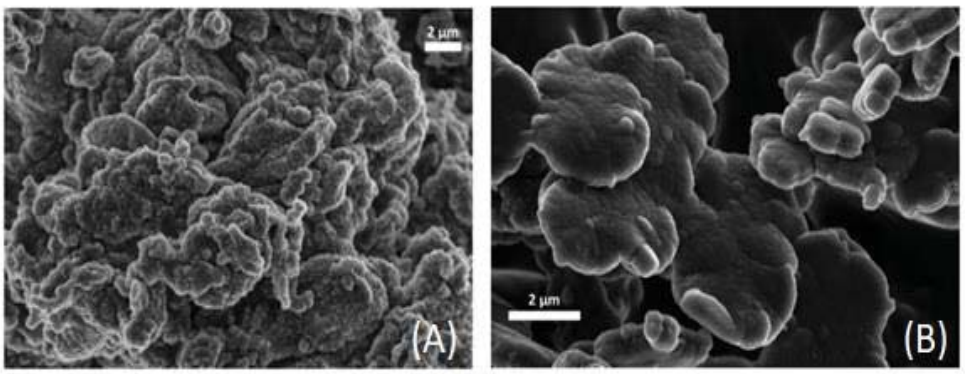

Figure I-20: Representative SEM images of A-PMO (A) and B-PMO (B) samples that show a specific architecture of the agglomerates of each sample.[100]

Although significant for technological applications, the determination of long-distance transport leaves unanswered questions about the dynamics of water within the pores. At this level, finding an alternative technique seems necessary to resolve the spatio–temporal correlations of water molecule on a timescale ranging from a few picoseconds to a few nanoseconds and at the nanometer length scale, i.e. a few times smaller than the characteristic distances defined by the PMOs pores diameter (in the range 3.5 nm–4.1 nm) and by the period of modulation of the surface interaction (about 1.2 nm).

Mietner et al. (2017)[101] have demonstrated that not only pore size but also surface interaction (polarity) contribute to the water structure. In comparison to MCM-41 silica, a different response of the confinement is observed for PMOs owing to the unique periodic structure of the pore walls. The spatial arrangement of water molecules inside the pores and their interaction at the interface depends on the hydrophobicity of organic units of PMO.

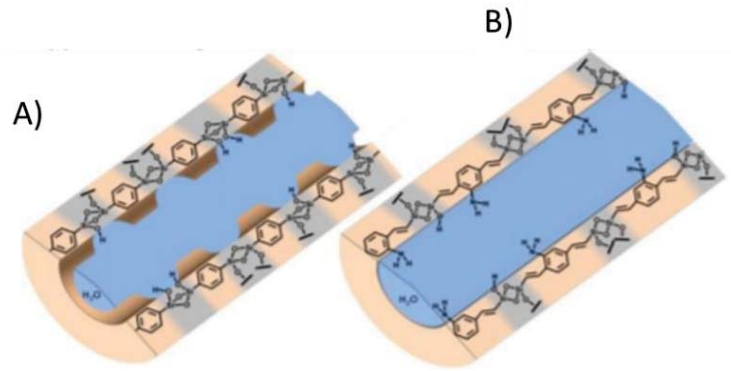

Figure I-21: Schematic representation of the pore filling modes. A) Modulated pore filling for alternating hydrophobic-hydrophilic pore surfaces as in BP- and B-PMO. B) Uniform pore filling for alternating hydrophilic-hydrophilic pore surfaces as in A-PMO.[101]

As shown in Figure I-21, the spatial arrangement of water molecules inside A-PMO pores (aniline-PMO), is compared to that of B-PMO (benzyl-PMO) revealing two different pore filling modes; modulated in the case of B-PMO with hydrophobic organic units and uniform in the case of A-PMO with an hydrophilic aniline group in the organic units. This finding was obtained with the multidimensional solid state NMR, a technique offering a direct probe on the spatial arrangement of water inside the pores at a molecular level.

As shown in Figure I-21, this technique provides detailed information about the spatial proximity between atomic by studying short or long range correlation of neighboring atomic species. Indeed, the water molecules interact strongly with the organic region in the case of A-PMO through hydrogen bonds between -NH_2 and water since ^{1}H and ^{13}C are highly the correlated (as shown in Figure I-22-d), however in the case of B-PMO with no correlation between ^{1}H and ^{13}C (Figure I-22-b), water molecules did not interact with the B-PMO organic region. Concerning silica units, for both PMOs, they have a strong interaction with water molecules (high correlation between ^{1}H and ^{29}Si as shown in Figure I-22-(a,c)). To conclude, the surface interaction (hydrophobicity) contribute in the spatial arrangement of water molecules inside the pores and their interaction at the interface leading to significant changes in dynamic properties which will makes the subject of the next paragraph.

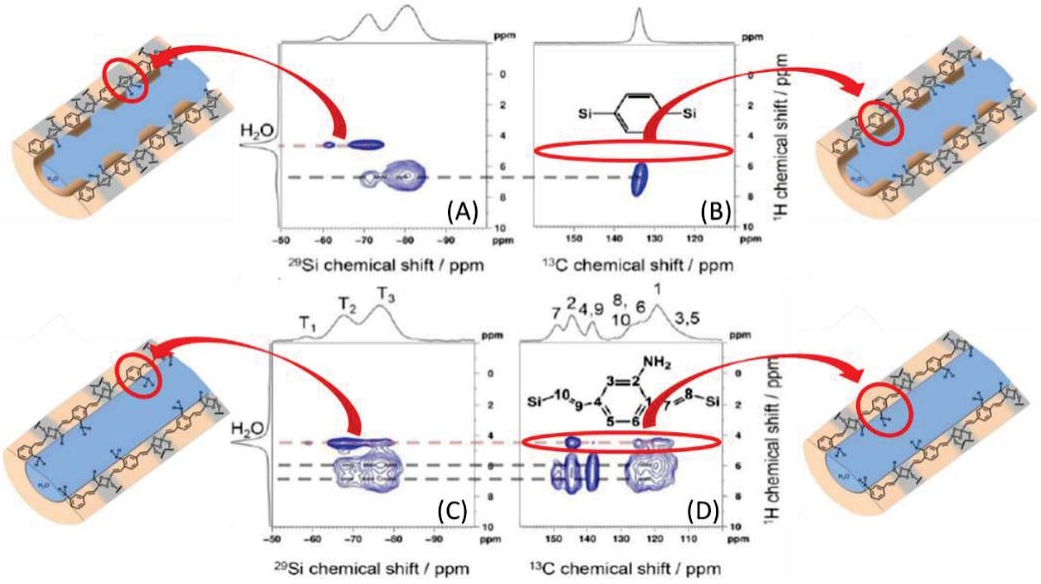

Figure I-22: Right panels: $^{2}D\ ^{1}H–^{29}Si$ HETCOR NMR spectra of the B-PMO (A) and A-PMO (C) with fully filled pores. Left panels: $^{2}D\ ^{1}H–^{13}C$ HETCOR NMR spectra of the B-PMO (B) and A-PMO (D) with fully filled pores. We show with the extra schema the corresponding pore filling mode to correlations between water and organic groups (left schema) and between water and silica groups (right schema).

III. AIM OF THE THESIS

The thesis project is based on the very numerous studies and observations of confinement effects on fluid physical properties, as described in the previous part. Inspired by all these studies, we aimed to get a better understanding on how could we modify/control physical properties (in particular dynamics and structure) through nanoscale control of surface interactions. This goal may be achieved thanks to the development of a hybrid surface with hydrophobic/hydrophilic modulated units with a regular arrangement of cylindrical mesopore and crystal-like organization of the organic bridges within the pore walls (PMOs) which opens the door to the modulation of surface interactions.

Furthermore, we have been more motivated by recent advanced works that demonstrated that not only pore size but also surface interaction (polarity) may modify the structure and dynamics of water (as discussed later) and other studies that confirm, experimentally and by MD simulation, the confinement-induced microphase separation of TBA/TOL binary mixture from a structural and dynamic point of view.[93, 94, 99]

We suggest to study the dynamics by quasielastic neutron scattering (QENS). This technique is the unique method that resolve the spatio–temporal correlations of water molecule on required timescale (from a few picoseconds to a few nanoseconds) and at the pore size scale (3.5 nm – 4.1 nm) and by the period of modulation of the surface interaction

(about 1.2 nm). QENS also allows studying the effect of the modulation of surface chemistry on the water and TBA/TOL binary mixture mobility.

We propose, also, to study the effect of modulating both liquid and surface properties on confinement-induced microphase separated liquids from a structural point of view. Neutron diffraction and sorption experiments were performed in our study of TBA/TOL mixture bulk and confined in DVB-PMO matrix in order to favor hydrophobic interaction to induce new kind of microphase separation (different of the core-shell).

To our knowledge, such a complete study from structural and dynamical point of view is rather unique in the literature.

IV.ORGANIZATION OF THE THESIS

The thesis consists of five chapters, the structure is as follows: after this introductory chapter, Chapter II is dedicated to give a description of PMOs family hybrid pore systems with a modulated surface chemistry. Chapter III is a comprehensive dynamical study of water into PMO to better understand the effect of surface-interaction modulation. We address the study of surface-interaction modulation effect on binary mixtures from structural (Chapter IV) and dynamical (Chapter V) point of view.

REFERENCES

1. *Beck JS, Vartuli JC, Roth WJ, et al. A NEW FAMILY OF MESOPOROUS MOLECULAR-SIEVES PREPARED WITH LIQUID-CRYSTAL TEMPLATES. Journal of the American Chemical Society 1992;114(27): 10834-43.*

2. *Zhao DY, Feng JL, Huo QS, et al. Triblock copolymer syntheses of mesoporous silica with periodic 50 to 300 angstrom pores. Science 1998;279(5350): 548-52.*

3. *Radhakrishnan R, Gubbins KE, Sliwinska-Bartkowiak M. Existence of a hexatic phase in porous media. Physical Review Letters 2002;89(7).*

4. *Schuller J, Melnichenko YB, Richert R, Fischer EW. DIELECTRIC STUDIES OF THE GLASS-TRANSITION IN POROUS-MEDIA. Physical Review Letters 1994;73(16): 2224-27.*

5. *Warnock J, Awschalom DD, Shafer MW. GEOMETRICAL SUPERCOOLING OF LIQUIDS IN POROUS-GLASS. Physical Review Letters 1986;57(14): 1753-56.*

6. *Sillescu H. Heterogeneity at the glass transition: a review. Journal of Non-Crystalline Solids 1999;243(2-3): 81-108.*

7. *Tracht U, Wilhelm M, Heuer A, Feng H, Schmidt-Rohr K, Spiess HW. Length scale of dynamic heterogeneities at the glass transition determined by multidimensional nuclear magnetic resonance. Physical Review Letters 1998;81(13): 2727-30.*

8. *Liu AJ, Durian DJ, Herbolzheimer E, Safran SA. WETTING TRANSITIONS IN A CYLINDRICAL PORE. Physical Review Letters 1990;65(15): 1897-900.*

9. *Zickler GA, Jaehnert S, Wagermaier W, Funari SS, Findenegg GH, Paris O. Physisorbed films in periodic mesoporous silica studied by in situ synchrotron small-angle diffraction. Physical Review B 2006;73(18).*

10. *Marcolli C. Deposition nucleation viewed as homogeneous or immersion freezing in pores and cavities. Atmospheric Chemistry and Physics 2014;14(4): 2071-104.*

11. *Gregg SS, KSW. Adsorption, Surface Area end Porosity.1967.*

12. *Coelingh FMB. Optical investigations of the fluid-vapour balance in capillary systems. Kolloid-Zeitschrift 1938;87(3): 251-76.*

13. *Cohan LH. Sorption hysteresis and the vapor pressure of concave surfaces. Journal of the American Chemical Society 1938;60: 433-35.*

14. *Schreiber A, Ketelsen I, Findenegg GH. Melting and freezing of water in ordered mesoporous silica materials. Physical Chemistry Chemical Physics 2001;3(7): 1185-95.*

15. *Findenegg GH, Jaehnert S, Akcakayiran D, Schreiber A. Freezing and Melting of Water Confined in Silica Nanopores. Chemphyschem 2008;9(18): 2651-59.*

16. *Denoyel R, Pellenq RJM. Simple phenomenological models for phase transitions in a confined geometry. 1: Melting and solidification in a cylindrical pore. Langmuir 2002;18(7): 2710-16.*

17. *Malfait B, Pouessel A, Jani A, Morineau D. Extension and Limits of Cryoscopy for Nanoconfined Solutions. Journal of Physical Chemistry Letters 2020;11(14): 5763-69.*

18. *Jackson CL, McKenna GB. THE MELTING BEHAVIOR OF ORGANIC MATERIALS CONFINED IN POROUS SOLIDS. Journal of Chemical Physics 1990;93(12): 9002-11.*

19. *Webber JBW. Studies of nano-structured liquids in confined geometries and at surfaces. Progress in Nuclear Magnetic Resonance Spectroscopy 2010;56(1): 78-93.*

20. *Bhushan B, Jung YC. Wetting, adhesion and friction of superhydrophobic and hydrophilic leaves and fabricated micro/nanopatterned surfaces. Journal of Physics-Condensed Matter 2008;20(22).*

21. *Mundra MK, Donthu SK, Dravid VP, Torkelson JM. Effect of spatial confinement on the glass-transition temperature of patterned polymer nanostructures. Nano Letters 2007;7(3): 713-18.*

22. *Wang H, Hor JL, Zhang Y, Liu T, Lee D, Fakhraai Z. Dramatic Increase in Polymer Glass Transition Temperature under Extreme Nanoconfinement in Weakly Interacting Nanoparticle Films. Acs Nano 2018;12(6): 5580-87.*

23. *Kim S, Roth CB, Torkelson JM. Effect of Nanoscale Confinement on the Glass Transition Temperature of Free-Standing Polymer Films: Novel, Self-Referencing Fluorescence Method. Journal of Polymer Science Part B-Polymer Physics 2008;46(24): 2754-64.*

24. *Morineau D, Xia YD, Alba-Simionesco C. Finite-size and surface effects on the glass transition of liquid toluene confined in cylindrical mesopores. Journal of Chemical Physics 2002;117(19): 8966-72.*

25. *Gallo P, Rovere M, Spohr E. Glass transition and layering effects in confined water: A computer simulation study. Journal of Chemical Physics 2000;113(24): 11324-35.*

26. *Oguni M, Kanke Y, Nagoe A, Namba S. Calorimetric Study of Water's Glass Transition in Nanoscale Confinement, Suggesting a Value of 210 K for Bulk Water. Journal of Physical Chemistry B 2011;115(48): 14023-29.*

27. *Lonsdale K. THE STRUCTURE OF ICE. Proceedings of the Royal Society of London Series a-Mathematical and Physical Sciences 1958;247(1251): 424-34.*

28. *Lobban C, Finney JL, Kuhs WF. The structure of a new phase of ice. Nature 1998;391(6664): 268-70.*

29. *Chou IM, Blank JG, Goncharov AF, Mao HK, Hemley RJ. In situ observations of a high-pressure phase of H2O ice. Science 1998;281(5378): 809-12.*

30. *del Rosso L, Celli M, Ulivi L. New porous water ice metastable at atmospheric pressure obtained by emptying a hydrogen-filled ice. Nature Communications 2016;7.*

31. *Thangswamy M, Maheshwari P, Dutta D, et al. Evolution of confined ice nano structures at different levels of pore filling: a synchrotron based X-ray diffraction study. Physical Chemistry Chemical Physics 2020;22(25): 14309-17.*

32. *Malkin TL, Murray BJ, Salzmann CG, Molinero V, Pickering SJ, Whale TF. Stacking disorder in ice I. Physical Chemistry Chemical Physics 2015;17(1): 60-76.*

33. *Morishige K, Yasunaga H, Uematsu H. Stability of Cubic Ice in Mesopores. Journal of Physical Chemistry C 2009;113(8): 3056-61.*

34. *Morishige K, Uematsu H. The proper structure of cubic ice confined in mesopores. Journal of Chemical Physics 2005;122(4).*

35. *Steytler DC, Dore JC, Wright CJ. NEUTRON-DIFFRACTION STUDY OF CUBIC ICE NUCLEATION IN A POROUS SILICA NETWORK. Journal of Physical Chemistry 1983;87(14): 2458-59.*

36. *Kuhs WF, Sippel C, Falenty A, Hansen TC. Extent and relevance of stacking disorder in "ice I-c". Proceedings of the National Academy of Sciences of the United States of America 2012;109(52): 21259-64.*

37. *Arnold GP, Finch ED, Rabideau SW, Wenzel RG. NEUTRON-DIFFRACTION STUDY OF ICE POLYMORPHS .3. ICE IC. Journal of Chemical Physics 1968;49(10): 4365-&.*

38. *Salzmann CG, Mayer E, Hallbrucker A. Thermal properties of metastable ices IV and XII: comparison, isotope effects and relative stabilities. Physical Chemistry Chemical Physics 2004;6(6): 1269-76.*

39. *Hansen TC, Koza MM, Kuhs WF. Formation and annealing of cubic ice: I. Modelling of stacking faults. Journal of Physics-Condensed Matter 2008;20(28).*

40. *Hansen TC, Koza MM, Lindner P, Kuhs WF. Formation and annealing of cubic ice: II. Kinetic study. Journal of Physics-Condensed Matter 2008;20(28).*

41. *Kuhs WF, Bliss DV, Finney JL. HIGH-RESOLUTION NEUTRON POWDER DIFFRACTION STUDY OF ICE-IC. Journal De Physique 1987;48(C-1): 631-36.*

42. *Mayer E, Hallbrucker A. CUBIC ICE FROM LIQUID WATER. Nature 1987;325(6105): 601-02.*

43. *Kohl I, Mayer E, Hallbrucker A. Thermal properties of metastable ice XII. Journal of Physical Chemistry B 2000;104(51): 12102-04.*

44. *Murray BJ, Bertram AK. Formation and stability of cubic ice in water droplets. Physical Chemistry Chemical Physics 2006;8(1): 186-92.*

45. *Malkin TL, Murray BJ, Brukhno AV, Anwar J, Salzmann CG. Structure of ice crystallized from supercooled water. Proceedings of the National Academy of Sciences of the United States of America 2012;109(4): 1041-45.*

46. *Morineau D, Guegan R, Xia YD, Alba-Simionesco C. Structure of liquid and glassy methanol confined in cylindrical pores. Journal of Chemical Physics 2004;121(3): 1466-73.*

47. *Behnaz RD, I YA. Confinement Effects on Hydrocarbon Mixture Phase Behavior in Organic Nanopore. Unconventional Resources Technology Conference. SAN ANTONIO, TEXAS, USA; 2015.*

48. *Mosher K, He J, Liu Y, Rupp E, Wilcox J. Molecular simulation of methane adsorption in micro- and mesoporous carbons with applications to coal and gas shale systems. International Journal of Coal Geology 2013;109: 36-44.*

49. *Firouzi M, Wilcox J. Molecular modeling of carbon dioxide transport and storage in porous carbon-based materials. Microporous and Mesoporous Materials 2012;158: 195-203.*

50. *Guegan R, Morineau D, Alba-Simionesco C. Interfacial structure of an H-bonding liquid confined into silica nanopore with surface silanols. Chemical Physics 2005;317(2-3): 236-44.*

51. *Morineau D, Alba-Simionesco C. Does Molecular Self-Association Survive in Nanochannels? Journal of Physical Chemistry Letters 2010;1(7): 1155-59.*

52. *Alba-Simionesco C, Dosseh G, Dumont E, et al. Confinement of molecular liquids: Consequences on thermodynamic, static and dynamical properties of benzene and toluene. European Physical Journal E 2003;12(1): 19-28.*

53. *Alcoutlabi M, McKenna GB. Effects of confinement on material behaviour at the nanometre size scale. Journal of Physics-Condensed Matter 2005;17(15): R461-R524.*

54. *Bellissentfunel MC, Chen SH, Zanotti JM. SINGLE-PARTICLE DYNAMICS OF WATER-MOLECULES IN CONFINED SPACE. Physical Review E 1995;51(5): 4558-69.*

55. *Milischuk AA, Ladanyi BM. Structure and dynamics of water confined in silica nanopores. Journal of Chemical Physics 2011;135(17).*

56. *Gallo P, Rovere M, Chen SH. Water confined in MCM-41: a mode coupling theory analysis. Journal of Physics-Condensed Matter 2012;24(6).*

57. *Kuon N, Milischuk AA, Ladanyi BM, Flenner E. Self-intermediate scattering function analysis of supercooled water confined in hydrophilic silica nanopores. Journal of Chemical Physics 2017;146(21).*

58. *Sattig M, Reutter S, Fujara F, Werner M, Buntkowsky G, Vogel M. NMR studies on the temperature-dependent dynamics of confined water. Physical Chemistry Chemical Physics 2014;16(36): 19229-40.*

59. *Grunberg B, Emmler T, Gedat E, et al. Hydrogen bonding of water confined in mesoporous silica MCM-41 and SBA-15 studied by H-1 solid-state NMR. Chemistry-a European Journal 2004;10(22): 5689-96.*

60. *Demuth D, Sattig M, Steinrucken E, Weigler M, Vogel M. H-2 NMR Studies on the Dynamics of Pure and Mixed Hydrogen-Bonded Liquids in Confinement. Zeitschrift Fur Physikalische Chemie-International Journal of Research in Physical Chemistry & Chemical Physics 2018;232(7-8): 1059-87.*

61. *Yao Y, Fella V, Huang W, et al. Crystallization and Dynamics of Water Confined in Model Mesoporous Silica Particles: Two Ice Nuclei and Two Fractions of Water. Langmuir 2019;35(17): 5890-901.*

62. *Lederle C, Sattig M, Vogel M. Effects of Partial Crystallization on the Dynamics of Water in Mesoporous Silica. Journal of Physical Chemistry C 2018;122(27): 15427-34.*

63. *Swenson J, Cerveny S. Dynamics of deeply supercooled interfacial water. Journal of Physics-Condensed Matter 2015;27(3).*

64. *Sjostrom J, Swenson J, Bergman R, Kittaka S. Investigating hydration dependence of dynamics of confined water: Monolayer, hydration water and Maxwell-Wagner processes. Journal of Chemical Physics 2008;128(15).*

65. *Teixeira J, Bellissentfunel MC, Chen SH, Dorner B. OBSERVATION OF NEW SHORT-WAVELENGTH COLLECTIVE EXCITATIONS IN HEAVY-WATER BY COHERENT INELASTIC NEUTRON-SCATTERING. Physical Review Letters 1985;54(25): 2681-83.*

66. *Soper AK, Ricci MA. Structures of high-density and low-density water. Physical Review Letters 2000;84(13): 2881-84.*

67. *Liu L, Chen SH, Faraone A, Yen CW, Mou CY. Pressure dependence of fragile-to-strong transition and a possible second critical point in supercooled confined water. Physical Review Letters 2005;95(11).*

68. *Zanotti JM, Bellissent-Funel MC, Chen SH. Relaxational dynamics of supercooled water in porous glass. Physical Review E 1999;59(3): 3084-93.*

69. *Faraone A, Liu L, Mou CY, Shih PC, Copley JRD, Chen SH. Translational and rotational dynamics of water in mesoporous silica materials: MCM-41-S and MCM-48-S. Journal of Chemical Physics 2003;119(7): 3963-71.*

70. *Briman IM, Rebiscoul D, Diat O, et al. Impact of Pore Size and Pore Surface Composition on the Dynamics of Confined Water in Highly Ordered Porous Silica. Journal of Physical Chemistry C 2012;116(12): 7021-28.*

71. *Aso M, Ito K, Sugino H, et al. Thermal behavior, structure, and dynamics of low-temperature water confined in mesoporous organosilica by differential scanning calorimetry, X-ray diffraction, and quasi-elastic neutron scattering. Pure and Applied Chemistry 2013;85(1): 289-305.*

72. *Baum M, Rieutord F, Jurany F, Rey C, Rebiscoul D. Dynamical and Structural Properties of Water in Silica Nanoconfinement: Impact of Pore Size, Ion Nature, and Electrolyte Concentration. Langmuir 2019;35(33): 10780-94.*

73. *Diallo SO, Vlcek L, Mamontov E, et al. Translational diffusion of water inside hydrophobic carbon micropores studied by neutron spectroscopy and molecular dynamics simulation. Physical Review E 2015;91(2).*

74. *Vogel W. Glass Chemistry1994.*

75. *Kresge CT, Leonowicz ME, Roth WJ, Vartuli JC, Beck JS. ORDERED MESOPOROUS MOLECULAR-SIEVES SYNTHESIZED BY A LIQUID-CRYSTAL TEMPLATE MECHANISM. Nature 1992;359(6397): 710-12.*

76. *Mamontov E, Burnham CJ, Chen SH, et al. Dynamics of water confined in single- and double-wall carbon nanotubes. Journal of Chemical Physics 2006;124(19).*

77. *Faraone A, Liu KH, Mou CY, Zhang Y, Chen SH. Single particle dynamics of water confined in a hydrophobically modified MCM-41-S nanoporous matrix. Journal of Chemical Physics 2009;130(13).*

78. *Kiwilsza A, Pajzderska A, Gonzalez MA, Mielcarek J, Wasicki J. QENS and NMR Study of Water Dynamics in SBA-15 with a Low Water Content. Journal of Physical Chemistry C 2015;119(29): 16578-86.*

79. *Arndt M, Stannarius R, Gorbatschow W, Kremer F. Dielectric investigations of the dynamic glass transition in nanopores. Physical Review E 1996;54(5): 5377-90.*

80. *Velasco MI, Franzoni MB, Franceschini EA, et al. Water Confined in Mesoporous TiO2 Aerosols: Insights from NMR Experiments and Molecular Dynamics Simulations. Journal of Physical Chemistry C 2017;121(13): 7533-41.*

81. *Steiner E, Bouguet-Bonnet S, Blin JL, Canet D. Water Behavior in Mesoporous Materials As Studied by NMR Relaxometry. Journal of Physical Chemistry A 2011;115(35): 9941-46.*

82. *Shirono K, Daiguji H. Molecular simulation of the phase behavior of water confined in silica nanopores. Journal of Physical Chemistry C 2007;111(22): 7938-46.*

83. *Yamashita K, Daiguji H. Molecular Dynamics Simulations of Water Uptake into a Silica Nanopore. Journal of Physical Chemistry C 2015;119(6): 3012-23.*

84. *Solveyra EG, de la Llave E, Molinero V, Soler-Illia G, Scherlis DA. Structure, Dynamics, and Phase Behavior of Water in TiO2 Nanopores. Journal of Physical Chemistry C 2013;117(7): 3330-42.*

85. *Factorovich MH, Solveyra EG, Molinero V, Scherlis DA. Sorption Isotherms of Water in Nanopores: Relationship Between Hydropohobicity, Adsorption Pressure, and Hysteresis. Journal of Physical Chemistry C 2014;118(29): 16290-300.*

86. *Bonnaud PA, Coasne B, Pellenq RJM. Molecular simulation of water confined in nanoporous silica. Journal of Physics-Condensed Matter 2010;22(28).*

87. *Bourg IC, Steefel CI. Molecular Dynamics Simulations of Water Structure and Diffusion in Silica Nanopores. Journal of Physical Chemistry C 2012;116(21): 11556-64.*

88. *Yamashita K, Daiguji H. Molecular Simulations of Water Adsorbed on Mesoporous Silica Thin Films. Journal of Physical Chemistry C 2013;117(5): 2084-95.*

89. *Renou R, Szymczyk A, Ghoufi A. Influence of the pore length on the properties of water confined in a silica nanopore. Molecular Physics 2014;112(17): 2275-81.*

90. *Milischuk AA, Krewald V, Ladanyi BM. Water dynamics in silica nanopores: The self-intermediate scattering functions. Journal of Chemical Physics 2012;136(22).*

91. *Dutta S, Lefort R, Morineau D, et al. Thermodynamics of binary gas adsorption in nanopores. Physical Chemistry Chemical Physics 2016;18(35): 24361-69.*

92. *Hamid ARA, Mhanna R, Lefort R, et al. Microphase Separation of Binary Liquids Confined in Cylindrical Pores. Journal of Physical Chemistry C 2016;120(17): 9245-52.*

93. *Hamid ARA, Mhanna R, Catrou P, Bulteau Y, Lefort R, Morineau D. Multiple Glass Transitions of Microphase Separated Binary Liquids Confined in MCM-41. Journal of Physical Chemistry C 2016;120(20): 11049-53.*

94. *Mhanna R, Hamid ARA, Dutta S, et al. More room for microphase separation: An extended study on binary liquids confined in SBA-15 cylindrical pores. Journal of Chemical Physics 2017;146(2).*

95. *Hamid ARA, Lefort R, Lechaux Y, et al. Solvation Effects on Self-Association and Segregation Processes in tert-Butanol-Aprotic Solvent Binary Mixtures. Journal of Physical Chemistry B 2013;117(35): 10221-30.*

96. *Mhanna R, Lefort R, Noirez L, Morineau D. Microstructure and concentration fluctuations in alcohol-Toluene and alcohol-Cyclohexane binary liquids: A small angle neutron scattering study. Journal of Molecular Liquids 2016;218: 198-207.*

97. *Ghoufi A, Hureau I, Lefort R, Morineau D. Hydrogen-Bond-Induced Supermolecular Assemblies in a Nanoconfined Tertiary Alcohol. Journal of Physical Chemistry C 2011;115(36): 17761-67.*

98. *Hennous L, Hamid ARA, Lefort R, Morineau D, Malfreyt P, Ghoufi A. Crossover in structure and dynamics of a primary alcohol induced by hydrogen-bonds dilution. Journal of Chemical Physics 2014;141(20).*

99. *Mhanna R, Catrou P, Dutta S, et al. Dynamic Heterogeneities in Liquid Mixtures Confined in Nanopores. Journal of Physical Chemistry B 2020;124(15): 3152-62.*

100. *Mietner BJ, Froba M, Valiullin R. Water Transport in Periodic Mesoporous Organosilica Materials. Journal of Physical Chemistry C 2018;122(24): 12673-80.*

101. *Mietner JB, Brieler FJ, Lee YJ, Froba M. Properties of Water Confined in Periodic Mesoporous Organosilicas: Nanoimprinting the Local Structure. Angewandte Chemie-International Edition 2017;56(40): 12348-51.*

CHAPTER II

PERIODIC MESOPOROUS ORGANOSILIACES (PMOs): STRUCTURE AND PROPERTIES

ABSTRACT

This chapter is dedicated to give a description of PMOs family a hybrid pore system with a modulated surface chemistry. We summarize in this chapter the most relevant information about PMOs:

- *synthesis and characterization*
- *structure*
- *surface chemistry*

I. INTRODUCTION

Periodic mesoporous organosilicas are hybrid materials with organic and silica units characterized by large specific surface areas and pore sizes between 2 and 15 nm. As well as having a regular arrangement of cylindrical mesopores, PMOs also show crystal-like organization of the organic bridges within the pore walls.

The first PMO was synthesized in 1999 by three research groups working independently.[1, 2] The synthesis of this organic–inorganic hybrid materials is based on hydrolysis and condensation reactions of bridged organosilica precursors of the type $(R'O)_3SiRSi(OR')_3$. The organic units were incorporated in the three-dimensional network structure of the silica matrix through two covalent bonds and thus distributed totally homogeneously in the pore walls. These materials can have large inner surface areas of up to 1800 $m^2 g^{-1}$ as well as high thermal stability.

The PMO powders I used in my thesis were prepared and fully characterized by nitrogen physisorption, X-ray diffraction, neutron diffraction and electron microscopy in the group of Prof. M. Froeba and our group, in the frame of a French-German collaboration between our group and the university of Hamburg. We summarize in this chapter the most relevant information acquired from these studies.

II. SYNTHESIS AND CHARACTERIZATION

1. Synthesis

PMO powders were synthesized according to the following procedure. NaOH and the alkyltrimethylammonium bromide surfactant were dissolved in deionized water.

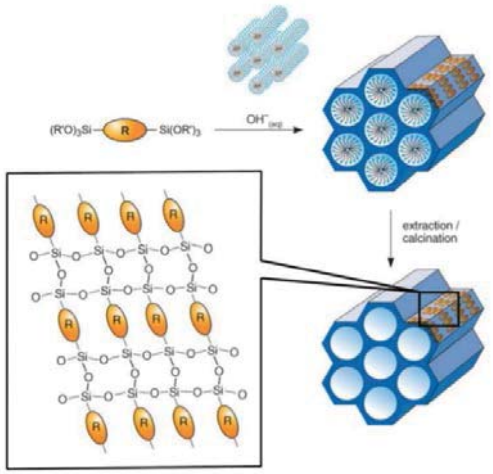

Figure II-1: Synthesis of PMOs with a crystal-like arrangement of the bridging organic units R in the pore walls. This representation is idealized: the bridges can be slightly tilted or twisted with respect to each other.[3]

The bis-silylated precursors of the form $(EtO)_3Si- R-Si(OEt)_3$ (R = organic bridging unit) were added at room temperature and the mixtures were stirred for 20 hours. The mixtures were transferred into a Teflon-lined steel autoclave and statically heated to 95 °C or 100 °C for 24 h. The resultant precipitate was collected by filtration and washed with 200 mL deionized water. After drying at 60 °C, the powder was extracted with a mixture of ethanol and hydrochloric acid (EtOH:HCl (37 %), 97:3, v/v) using a Soxhlet extractor.[4]

All precursors bear the same triethoxysilyl groups, however they differ through the organic bridges (-R-) between the silyl groups ($(EtO)_3Si-$). For example, BTEBP (4,4′-Bis(triethoxysilyl)-1,1′-biphenyl) carries a biphenyl, the BTEVB (2,5-[(E)-2-bis(triethoxysilyl)vinyl]benzol) has a benzene ring as an organic bridge connected via two vinyl groups to the silyl groups. BTEVA (2,5-[(E)-2-bis(triethoxysilyl)vinyl]anilin) has a similar structure, but the benzene ring has a primary amino group. The Figure II-2, shows the three precursors mentioned below.

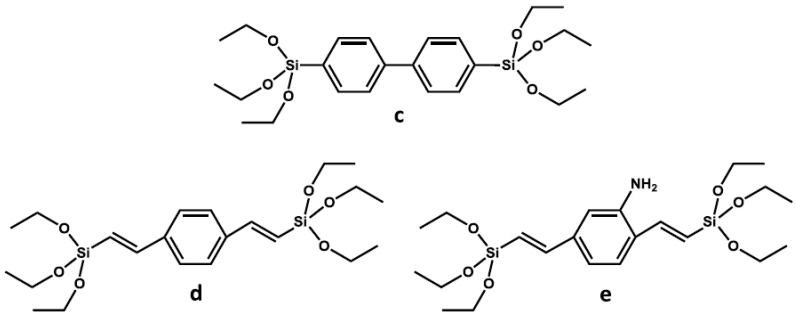

Figure II-2: Precursor molecules of BTEBP (a), BTEVB (b) and BTEVA (c).

2. Characterization

PMOs powders were characterized by nitrogen physisorption in the group of Prof. M. Froeba. Nitrogen physisorption isotherms at a temperature of 77K of three PMOs synthesized using different surfactants and precursors are presented in Figure II-3.

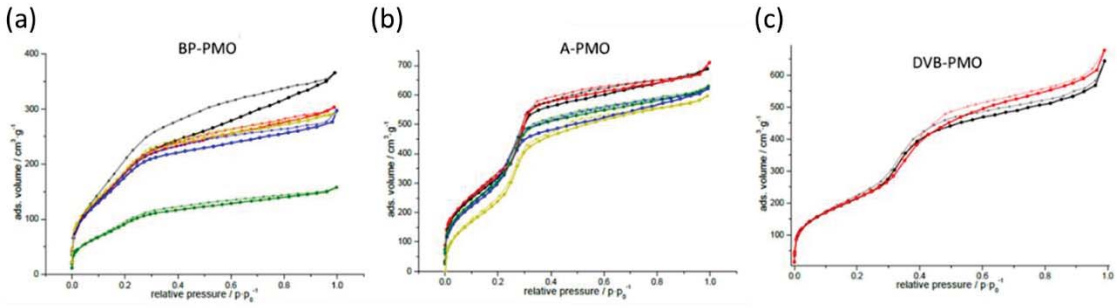

Figure II-3: Nitrogen physisorption isotherms (77 K) of BP-PMO, A-PMO and DVB-PMO obtained via different synthesis procedures (different colors).

Through these experiments, various information has been determined and the table below summarize, for the same three PMO samples characterized previously by nitrogen physisorption, the specific surface area (Spec Surf Area), pore size and pore volume.

Table II-1: PMOs' Sample information

PMOs / Sample	Used Surfactant	Used Precursor	Spec Surf Area [m2/g]	Pore Size (DFT) [nm]	Pore Volume [cc/g]
BP-PMO	C18TAB	BTEBP	786	3.3	0.445
A-PMO	C14TAB	BTEVA	1223	3.5	0.890
DVB-PMO	C18TAC	BTEVB	864	4.1	0.990

In order to have a better characterization, it's necessary to examine the synthetized materials more closely with regard to particle morphology and agglomeration. For this reason, Scanning Electron Micrography (SEM) was used.

The Figure II-4, shows the SEM images for 3 PMOs and for MCM-41 sample for comparison. We can notice that the MCM-41 sample shows small, slightly agglomerated particles with a diameter in the order of 500 nm. The particles of the DVA-PMO sample are significantly more agglomerated with an agglomerate size that could be estimated to 24 µm. The B-PMO and the BP-PMO samples have larger particles agglomerated into 20-30 µm agglomerates.

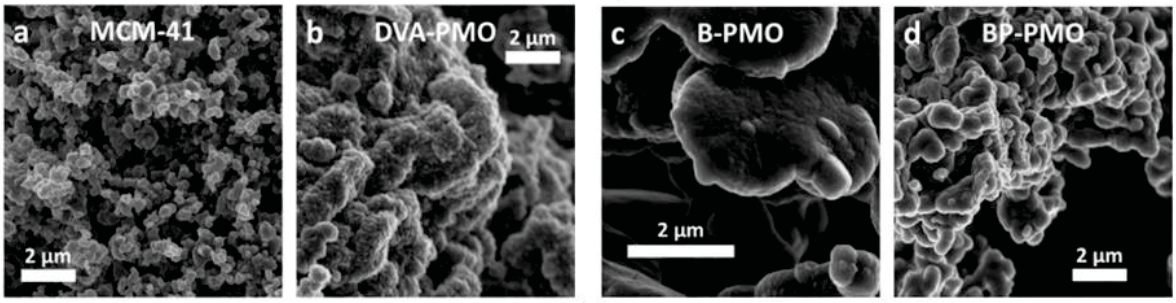

Figure II-4: SEM images of a: MCM-41, b: DVA-PMO, c: B-PMO and d: BP-PMO (after Mietner et al.[4]).

III. STRUCTURE

Figure II-5, shows 3 XRD patterns of BP-PMO, A-PMO and DVB-PMO obtained via different synthesis procedures. The diffractograms are presented in semi-logarithmic scale for an easier lecture. As we can see, the three materials show 3-5 Bragg peaks below 7°, which are caused by the mesoscopic, two-dimensional hexagonal order of the pores.

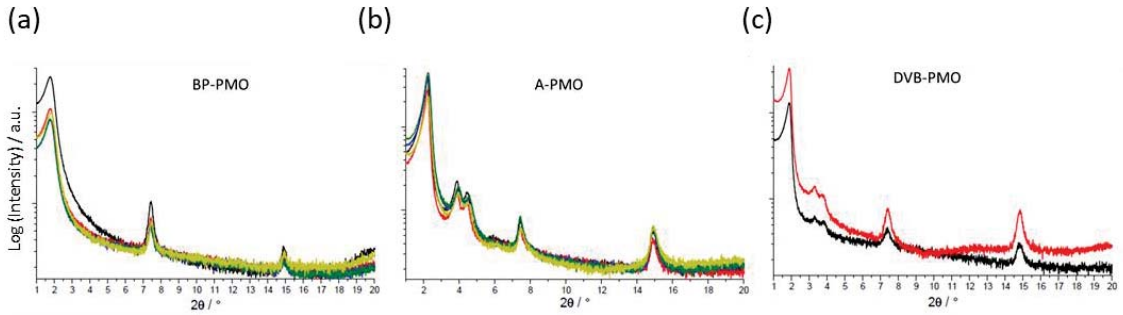

Figure II-5: XRD patterns of a:BP-PMO, b: A-PMO and c: DVB-PMO obtained via different synthesis procedures (different colors).

Miller indices (hkl) of Bragg peaks of BP-PMO, A-PMO and DVB-PMO materials shown in Figure II-5, as well as their positions, their correspondent d-spacing values according to Bragg's law (see equation) using a scattering wavelength λ = 0.1542 nm for XRD and λ = 0.451 nm for SANS and their relative intensities are summarized in the following table.

$$d = \frac{2\pi}{q} \text{ and } q = \frac{4\pi}{\lambda}\sin(\theta)$$

Table II-2: Miller indices (hkl), positions, d values and relative intensities of the Bragg peaks deduced from the diffractograms of the three PMOs materials presented in Figure II-5.

h	k	l	Pos. (q) /°2θ	d /Å	Rel. Int. /%
BP-PMO					
1	0	0	1.82	48.0	100
A-PMO					
1	0	0	1,93	45,7	100
1	1	0	3,34	26,5	6,16
2	0	0	3,86	22,9	3,38
2	1	0	5,10	17,3	0,63
3	0	0	5,77	15,3	0,28
DVB-PMO					
1	0	0	1,89	46,8	100
1	1	0	3,31	26,6	2,29
2	0	0	3,78	23,3	1,89

Only the BP-PMO shows a single peak in this area. This means that the pores have a certain mesoscopic regularity in terms of their size and spacing, but do not necessarily have to be two-dimensionally hexagonal arrangement over large areas. This difference could be

also attributed to the different hydrolysis and condensation behavior of the BP-PMO precursor in the synthesis.

Also, with the neutron diffraction method in the small Q range (< 0.35 $Å^{-1}$), the SANS pattern of DVB-PMO shows three Bragg peaks with Miller indexes (100), (110), and (200) as shown in Figure II-6.

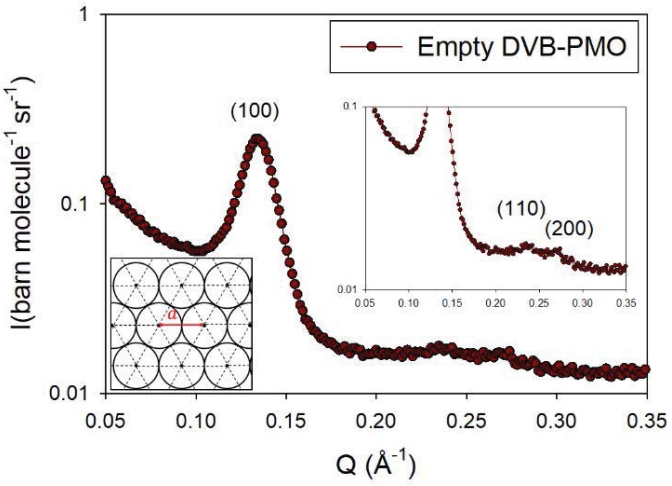

Figure II-6: The scattered intensity of empty DVB-PMO at low Q region which shows the 3 Bragg peaks corresponding to the hexagonal arrangement of the pores. Inset at lower left of the figure: interplanar distance a between two neighboring pores.

These peaks correspond to the organization of the pore channels in hexagonal lattice. Their Bragg peak positions Q_{hk} is obtained by

$$Q_{hk0} = \frac{4\pi}{\sqrt{3}\,a}\sqrt{h^2 + k^2 + hk}$$

With a is the unit cell distance which is related to the center-center distance of two neighboring pores and directly related to the most intense peak (100) as

$$a = \frac{4\pi}{\sqrt{3}\,Q_{100}} = 53.74Å \approx 5.4nm$$

The theoretical positions of the three Bragg peaks are compared to experimental ones in the table II-3.

Table II-3: Theoretical and experimental positions for the three Bragg peaks.

$Q_{hk0}(Å^{-1})$ (hk0)	(100)	(110)	(200)
Theoretical	0.135	0.234	0.270
Experimental	0.135	0.240	0.270

In addition to the characteristic hexagonal peaks, all PMOs show Bragg peak(s) at higher angles. With X-ray diffraction, BP-PMO, A-PMO and DVB-PMO show 2 extra-peaks (cf. Figure II-5). And with neutron diffraction, DVB-PMO reveals one extra-peak (cf. Figure II-7).

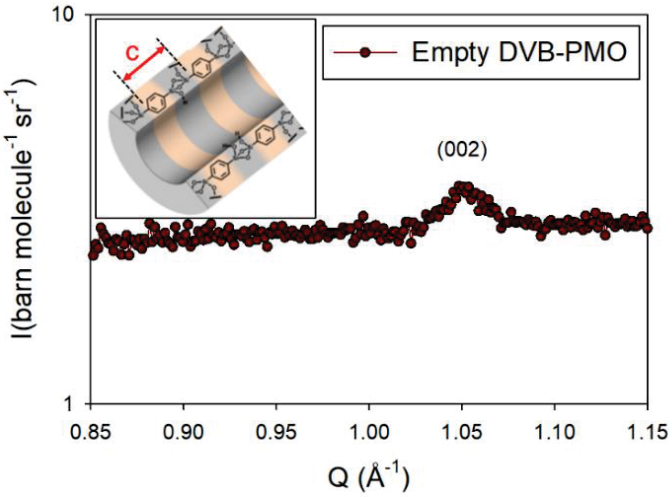

Figure II-7: The scattered intensity of empty DVB-PMO at high Q region which shows the (002) Bragg peaks corresponding to lateral arrangement of the pore. Inset at upper left of the figure: the repeating unit (composed by silica and DVB units) length c.

These higher angle peaks characterize the pseudo-crystalline order in the pore wall along the channel axis. These reflections can be labelled with (00l) Miller indexes. The following figure shows schematically how the individual pore walls are constructed with a periodic repetition of different inorganic and organic areas.

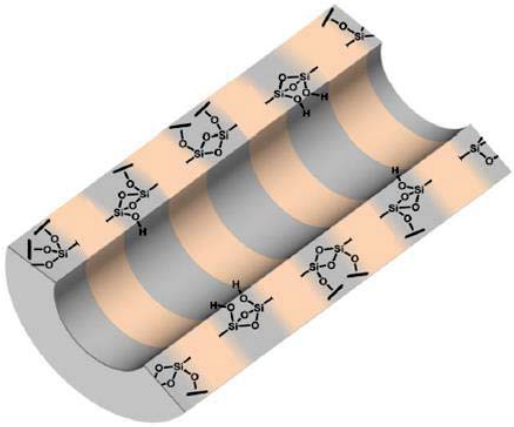

Figure II-8: Schematic structure of a PMO pore with pseudo-crystalline pore walls. Gray areas symbolize the inorganic, orange the organic areas of the pore wall.

The (002) Bragg peak offers a direct access to the molecular periodicities *c* of the unit cell that compose the pore wall as presented in Figure II-9 with arrow. From XRD measurements the length c is deduced for the 3 PMOs. And from SANS measurement we deduced it only for DVB-PMO. In the case of DVB-PMO, the same value of c (11.9 Å) is obtained from XRD and SANS measurements.

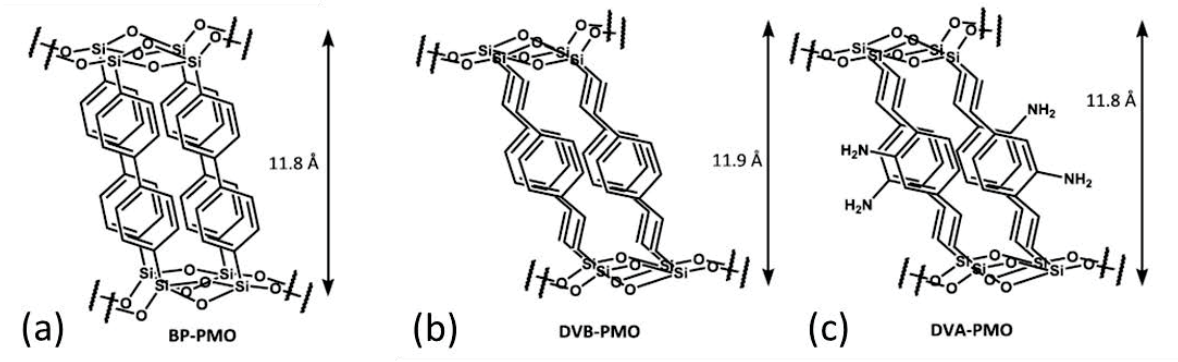

Figure II-9: Schematic representation of the pseudo-crystallinity in the pore walls of BP-PMO (a), A-PMO (b) and DVB-PMO (c). The arrows indicate the molecular periodicities c emerging from P-XRD measurements.

The one-dimensional pore channels of PMOs samples can be seen with the TEM images as shown in Figure II-10 for B-PMO sample. The pores show a high regularity in size and spacing.

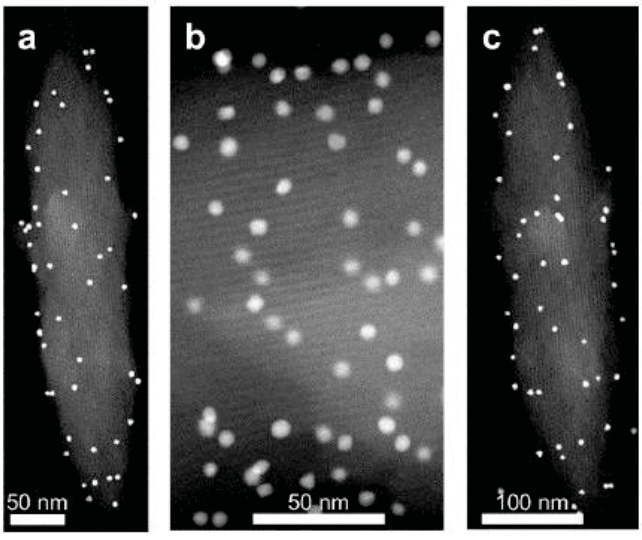

Figure II-10: TEM images of B-PMO sample. Bright spots on the images are gold particles added during preparation for the TEM image and do not belong to the PMO material. Images taken by Wu Wang using a microscope at the Karlsruhe Nano Micro Facility.[5]

IV. SURFACE CHEMISTRY

PMOs are characterized by the same pore geometries and the same mesostructure, however, their surface chemistry varies considerably with different organic bridges as shown in the Figure II-11.

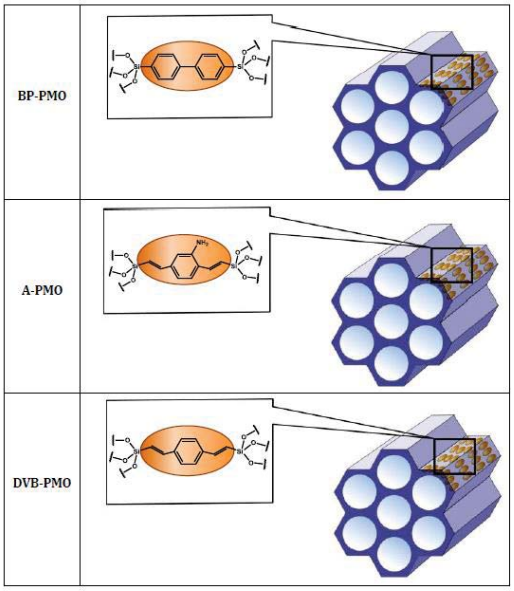

Figure II-11: Schematic representation of different structure of the three PMOs used in this work (after Mietner [5]).

This variation of surface chemistry influences the physico-chemical properties of PMOs such as their polarity and hydrophilicity. Comparison of one of this properties should be made between very similar materials, whereby only one parameter, such as pore size or surface polarity, should be varied to a defined extent. Therefore, polarity comparison can be realized by using PMOs with similar pore sizes. The 3 PMO materials used in this work, as well as MCM-41 silica materials as a reference, are listed schematically in Figure II-12, where the order of the materials according to surface hydrophilicity was chosen from hydrophobic to hydrophilic.

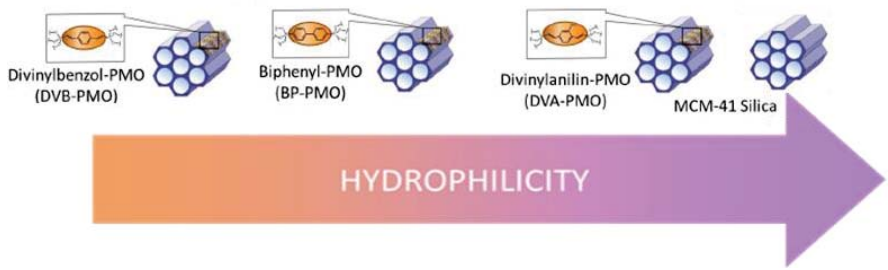

Figure II-12: Three PMOs materials with different organic bridging units in order of surface hydrophilicity.

This listing was based on the H_2O sorption measurements. In Figure II-13, sorption isotherms for 5 PMOs materials (including the 3 PMOs that we are interested on in this work) are presented simultaneously on the same graph for a better view

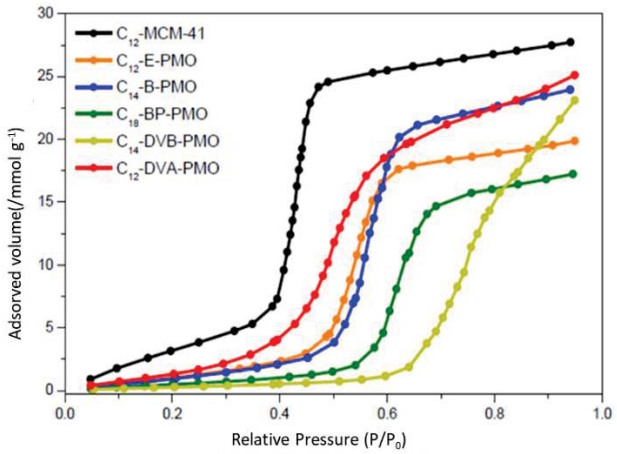

Figure II-13: H2O sorption isotherms (@ 25 °C) of MCM-41 and 5 PMOs materials with almost the same pore size (D ≈ 3.2 nm) (after Mietner[5]).

REFERENCES

1. *Inagaki S, Guan S, Fukushima Y, Ohsuna T, Terasaki O. Novel mesoporous materials with a uniform distribution of organic groups and inorganic oxide in their frameworks. Journal of the American Chemical Society 1999;121(41): 9611-14.*

2. *Asefa T, MacLachlan MJ, Coombs N, Ozin GA. Periodic mesoporous organosilicas with organic groups inside the channel walls. Nature 1999;402(6764): 867-71.*

3. *Hoffmann F, Cornelius M, Morell J, Froba M. Silica-based mesoporous organic-inorganic hybrid materials. Angewandte Chemie-International Edition 2006;45(20): 3216-51.*

4. *Mietner BJ, Froba M, Valiullin R. Water Transport in Periodic Mesoporous Organosilica Materials. Journal of Physical Chemistry C 2018;122(24): 12673-80.*

5. *Mietner JB. Visiting Nanopores : the great potential of PMOs for studying the properties of water in nanopores of different polarity, Doctoral dissertation, Universität Hamburg, 2018.*

CHAPTER III

EFFECT OF CONTROLLED SURFACE-MODULATION ON WATER DYNAMICS

ABSTRACT

In the present chapter we will focus on studying the dynamics of nanoconfined water in the presence of a spatial modulation of the surface/water interaction.

This confining condition is realized by using a series of periodic mesoporous silicas (MCM-41) and three organosilicas (PMOs) providing both: a variation of the surface chemistry and a variation in hydrophilic/hydrophobic character.

We performed a technique that allows the resolution of the spatio-temporal correlations of water molecule at the pore length scale and on a timescale ranging from a few picoseconds to a few nanoseconds. Quasi-elastic neutron scattering is the unique experimental technique covering both.

I. INTRODUCTION

In many situations, water is not present as a bulk liquid phase, but rather as a thin interfacial film or as a fluid embedded in a micro-/mesoporous medium. Interestingly, the specific properties of this nanoconfined situation determine the role played by water in many different fields, encompassing the biological activity of proteins[1], transport through membranes (including biological cells or membranes for proton exchange fuel cells or nanofluidics, nanofiltration /desalinization technology)[2] and environments of geological relevance.[3]

To study the dynamics of liquid water in spatially confined geometry synthetic pores were used as Vycor glass.[4] In first 90's and mesostructured porous silica such as MCM-41 and SBA-15 which provided a well-defined geometry in terms of straight and parallel nanochannels with tunable diameter.[5] [6] and an adjustable pore size.[5, 7] In the other hand, the evaluation of the effect of surface interaction on the water dynamics was limited due to the unchanged chemical composition of hydrophilic silicas.

To better address this issue, in the present chapter we will consider the interfacial mobility of nanoconfined water in the presence of a spatial modulation of the surface/water interaction. This confining condition is realized by using a series of periodic mesoporous silicas (MCM-41)[8, 9] and three organosilicas (PMOs)[10, 11] comprising different organic bridging units; biphenyl (BP-PMO), divinyl-benzene (DVB-PMO), and divinyl-aniline (A-PMO). These systems are well-suited to study the effect of tuning the water/surface interaction from hydrophilic to more hydrophobic by comparing results obtained for A-PMO and MCM-41 with respect to DVB-PMO and BP-PMO.

It was recently demonstrated in a pulsed field gradient (PFG) NMR study that the water transport in PMOs actually depends on their chemistry.[11] This method probes the molecule displacements in the μm-range. As a result, the diffusivities were found to be primarily determined by the macroscopic textural properties of the mesoporous particles that leaves unanswered questions about the dynamics of water within the pores.

In this chapter we investigate the effect of tuning the water/surface interaction on the water mobility within the pore by performing an alternative technique, allowing the resolution of the spatio-temporal correlations of water molecule on a timescale ranging from a few picoseconds to a few nanoseconds, and at the pore length scale.

II. METHODS

As mentioned above, we performed a technique that allows the resolution of the spatio-temporal correlations of water molecule at the pore length scale and on a timescale ranging from a few picoseconds to a few nanoseconds. Quasi-elastic neutron scattering is the unique technique rallied both. Experimental details are presented in first paragraph of this part and a detailed description of the QENS method is provided in Annex-I, we draw the reader's attention to it. To ensure the well filling of different matrixes, differential scanning calorimetry (DSC) experiments were performed and its experimental details are described in the next paragraph.

1. Samples

The four PMOs matrices were prepared according to the synthesis procedure described in the previous chapter. The synthesized product (a powder), was characterized by different methods in order to control its pore size and crystal network structure. The mesoporous materials MCM-41 silicates were prepared in our laboratory according to a procedure similar to that described elsewhere[9] with a mean pore diameter D = 3.65 nm. More details on the synthesis and characterization methods, the reader is invited to consult chapter II. Before experiments, all matrices powder was dried at 120°C under primary vacuum for 12H.

To check the filling status of the matrixes differential scanning calorimetry (DSC) experiments were performed with a Q-20 TA Instrument equipped with a liquid nitrogen cooling system and using Tzero hermetic aluminum pans. The melting transition of an indium sample was used for calibration of temperature and heat flux. Temperature scanning rates of 10 $K \cdot min^{-1}$ were applied during an initial cooling ramp and a subsequent heating ramp. The composition of the samples that were water filled at two different relative pressure (saturated samples RH = 75%, and overfilled samples RH = 100%) is described in Table III-1.

Table III-1 Composition of the water filled samples equilibrated at two different RH (saturated samples RH = 75%, and overfilled samples RH = 100%).

Porous Matrix	Pore Volume Vp [a] (cm3/g)	RH	Matrix mass m_p (mg)	Water mass m_w (mg)	Filling fraction x [b] (g/g)	Filling fraction ρ [c] (g/cm^3)
MCM-41	0.893	75%	4.28	2.52	0.659	0.589
		100%	3.81	2.52	0.661	0.740
A-PMO	0.890	75%	3.75	1.66	0.443	0.498
		100%	3.52	1.83	0.520	0.584
BP-PMO	0.445	75%	5.27	1.11	0.211	0.474
		100%	3.61	0.94	0.260	0.584
DVB-PMO	0.990	75%	1.13	0.47	0.420	0.424
		100%	1.64	1.31	0.807	0.99

[a]: evaluated from the nitrogen physisorption isotherms. [b]: defined as the amount of water per mass of matrix. [c]: defined as the amount of water per pore volume.

For all the four matrices, the porous materials filled at RH = 75% presented an exothermic peak, with on onset located in the range 227-237 K, which indicated the freezing of confined water. This onset of crystallization is also close to the temperature of the maximum position of the endothermic peak observed on heating that is due the melting of nanoconfined ice. The absence of thermal event around 273 K demonstrates unambiguously that these capillary filled samples do not contain bulk excess liquid outside the porosity.

On the contrary, samples filled at RH = 100% presented an additional thermal event around 273 K, due to excess water that is presumably located around the grains of the porous powder as well as in interstitial regions and behaves more like bulk water. This demonstrates that these samples were overfilled. For these samples, a quantification of the relative amount of confined and bulk liquid, based on the relative intensity of the two peaks is hardly possible because the melting enthalpy of ice is reduced by confinement. However, fruitful conclusions can be achieved based on their relative masses (see Figure III-2 and Table III-1 and earlier discussion). Except for DVB that obviously contained a larger amount of excess water, as seen by the prominent thermal event at 273 K, the difference of mass fraction between samples filled at RH = 75% and RH = 100% is small. In full agreement with the water adsorption isotherms, this demonstrates that the filling of the porosity with water had essentially reached its saturating limit at RH = 75%.

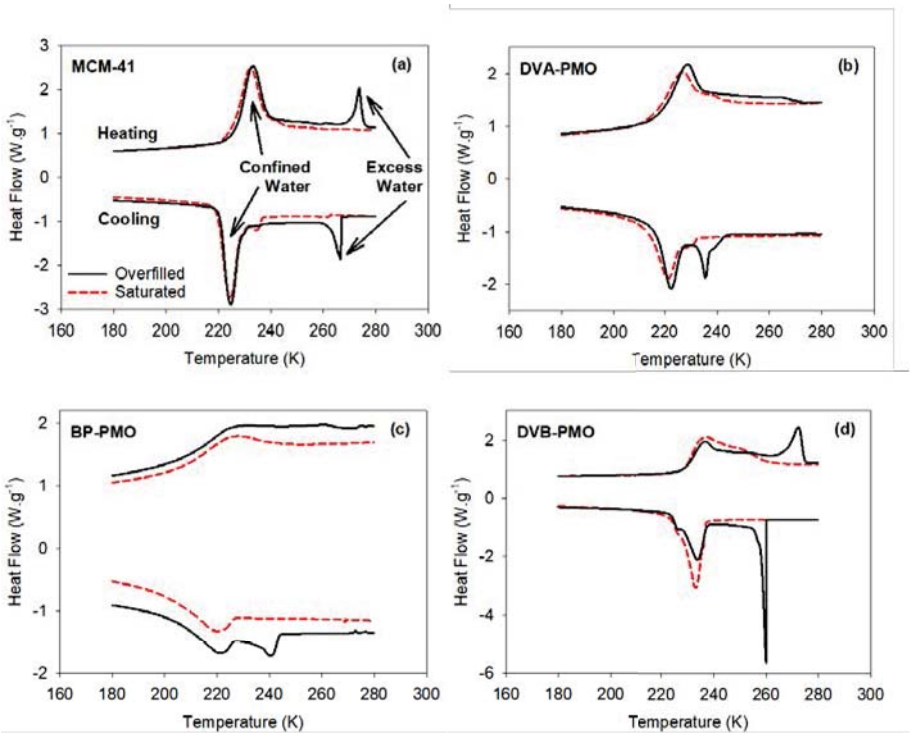

Figure III-1: DSC scans (endotherm up) of water-filled (a) MCM-41, (b) DVA-PMO, (c) BP-PMO, and (d) DVB-PMO. The thermograms of capillary filled (solid line) and overfilled samples (dashed line) were recorded on cooling (lower curves) and on heating (upper curves) with a temperature scanning rate of 10 K min^{-1}.

The filling fraction were calculated in two different ways: x is the amount of water m_w per mass of matrix m_p, ($x = m_w / m_p$) and ρ is the amount of water divided by the matrix pore volume ($\rho = x/V_p$), with V_p being determined by nitrogen adsorption isotherms. These results are also illustrated in Figure III-2.

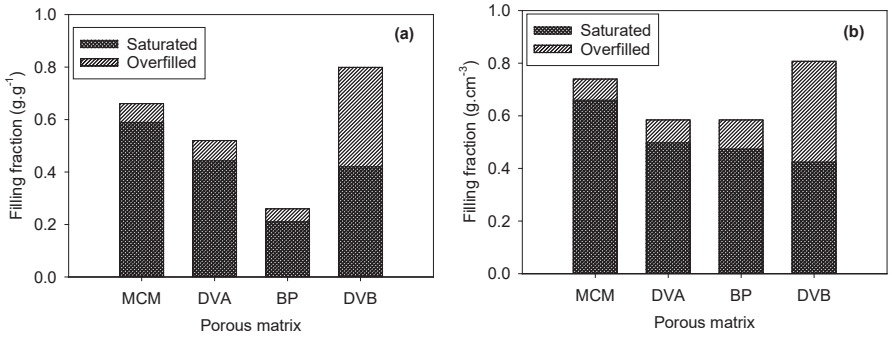

Figure III-2 (a) Water filling fraction x expressed in terms of mass of confined water per unit mass of porous matrix. (b) Water filling fraction ρ expressed in terms of mass of confined water per unit porous volume, as determined by nitrogen physisorption. Capillary filled and overfilled samples were obtained after equilibration in a chamber containing a saturated NaCl solution (RH = 75%), and pure water (RH = 100%), respectively.

2. QENS experiments

Quasielastic neutron scattering experiments were carried out using two spectrometers with different energy resolutions at the Institut Laue Langevin (ILL, Grenoble, France).[12, 13] The disc chopper time-of-flight spectrometer IN5B was used with an incident wavelength of 8 Å. In this configuration, the resulting energy resolution ΔE around the elastic peak is about 22 μeV (FWHM), corresponding to a timescale ($t=\Delta E/\hbar$) of about 30 ps. The quasielastic signal retained for the data evaluation covered an energy range ($E=\hbar\omega$) between -5.0 and 0.7 meV and a Q range between 0.2 and 1.3 $Å^{-1}$.

The high-resolution IN16B spectrometer was chosen with unpolished Si (111) monochromator and analyzers in backscattering geometry, which corresponds to an incident wavelength of 6.271 Å and results in an energy resolution of 0.75 μeV and a corresponding timescale of about 1 ns. The energy range was ±30 μeV with a Q range between 0.19 and 1.83 $Å^{-1}$. The background chopper of the instrument was run in its high signal-to-noise mode.[14] A cryofurnace and an ILL orange cryostat, were used on IN16B and IN5B spectrometers in order to regulate the sample temperature.

All matrices were dried at 120 °C under a primary vacuum. To prepare hydrated matrices, a constant amount of mesoporous materials was charged in a flat alumina rectangular cell (1 mm of thickness) and placed in a desiccator in the presence of a beaker containing a saturated aqueous solution of NaCl. The resulting relative humidity (RH) of 75% at 25 °C was above the partial pressure of the capillary condensation[15] and allowed the complete filling of the pore system which is validated by calorimetry measurements (as mentioned in Samples paragraph). The sample was kept in the atmosphere of constant humidity for 24H to ensure that an equilibrium condition is reached.

The cells were sealed with an indium wire to avoid water loss and ensure a constant hydration level during neutron scattering experiments. The measurements were performed after thermal equilibration at regularly spaced temperatures, which were reached sequentially on cooling (300, 278, 258 and 243 K on IN5B, and 278, 258 and 243 K on IN16B). The four different matrices were studied on IN5B (MCM-41, DVB-PMO, BP-PMO and A-PMO), and three of them on IN16B (MCM-41, DVB-PMO, and A-PMO).

Standard data corrections were applied using the packages MANTID[16] and LAMP[17] provided at the ILL. The experimental intensity was corrected for detector efficiency, for the background contribution arising from the empty cell and spectrometer, and transformed into the Q and energy dependent scattering function $S(Q,\omega)$. The fitting of scattering functions $S(Q,\omega)$ in the frequency domain was carried out using the QENSH program provided by the Laboratoire Léon Brillouin (LLB, Saclay, France).

III. RESULTS and DISCUSSSION

1. Obtained data

The QENS spectra of water filled MCM-41, DVA-PMO, DVB-PMO and BP-PMO are shown in Figure III-3 and Figure III-4. The temperature dependence of the scattering intensity is illustrated in Figure III-3 for the selected value of the transfer of momentum Q = 0.8-0.85 $Å^{-1}$. We observed a quasielastic broadening that covered a typical energy range from about 0.1 to 1 meV on IN5B and 30 μeV on IN16B.

Given the dominant contribution from the incoherent scattering cross section of hydrogen atoms, this quasielastic signal is attributed to the self-part of the dynamic structure factor $S(Q,\omega)$. Thus, it provides information on the single particle dynamics of water molecules. A continuous sharpening of the quasielastic peak was observed on decreasing the temperature from 300 K to 243 K. On a qualitative level, the width of the quasielastic scattering is inversely proportional to the typical timescale of motion of particles.

Therefore, this sharpening indicates that the water dynamics slows down gradually on cooling. The absence of a sharp increase of the elastic signal confirms that water remained liquid on the entire studied temperature range. It allows excluding the hypothetical presence of water outside the pores and the crystallization of in-pore water, which is in agreement with the DSC results.

The Q-dependence of the scattering intensity is illustrated in Figure III-4 for IN5B at the temperature T = 278 K. On increasing Q, we observed a significant reduction of the intensity contained in the elastic resolution (about a factor of ten) combined with a broadening of the quasielastic line. This Q-dependence probably arises from the combination of different effects, which are classically observed in QENS studies of liquids. It includes the effect of dispersive modes (e.g. translational diffusion) and the modulation of the elastic intensity due to vibrations (Debye Waller factor) or local quasielastic relaxations (e.g. rotation, libration), which comprise an elastic incoherent structure factor (EISF).

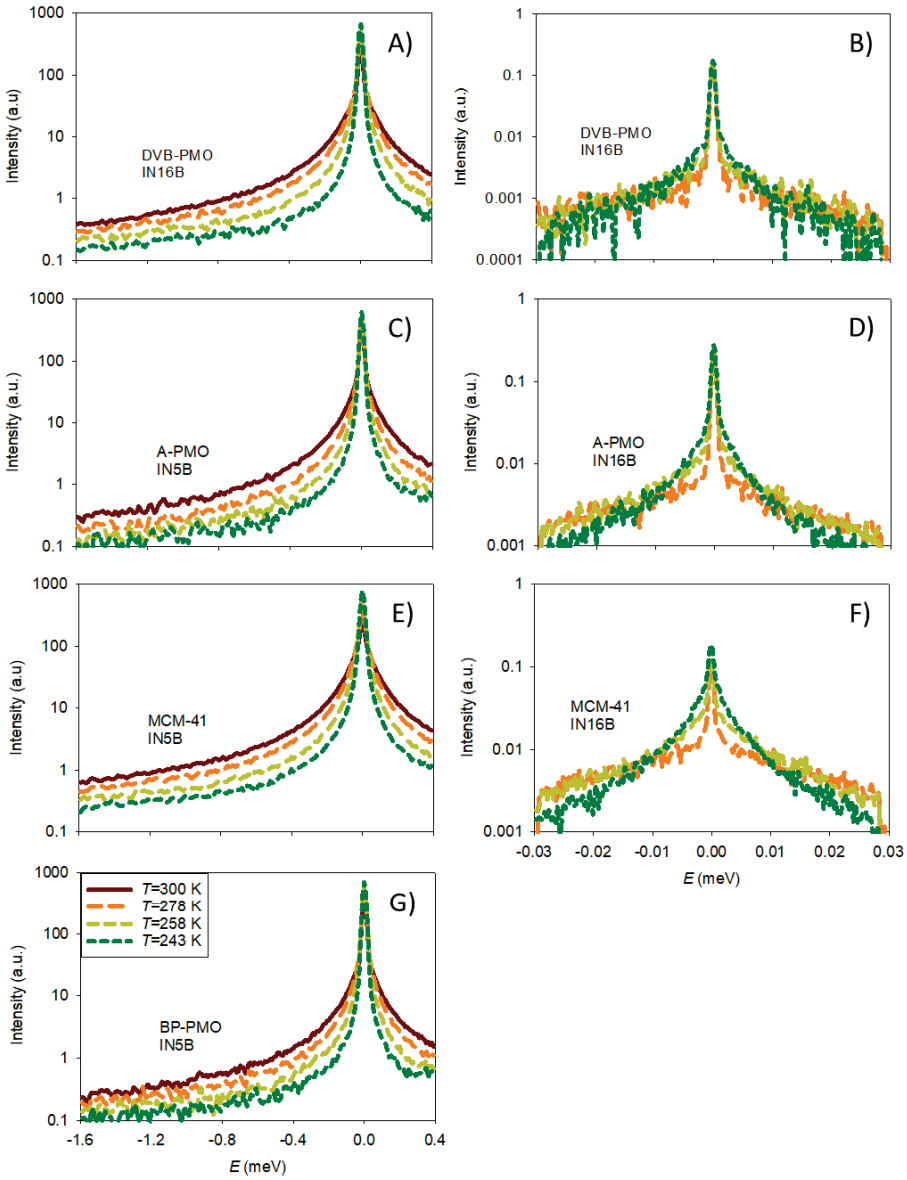

Figure III-3: Temperature dependence of the scattering intensity of water filled MCM-41 (A, B), water filled DVA-PMO (C, D), water filled DVB-PMO (E, F) and water filled BP-PMO (G). QENS spectra measured on IN5B at Q = 0.8 Å^{-1} (left panels A, C, E, G) and on IN16B at Q = 0.85 Å^{-1} (right panels B, D, F).

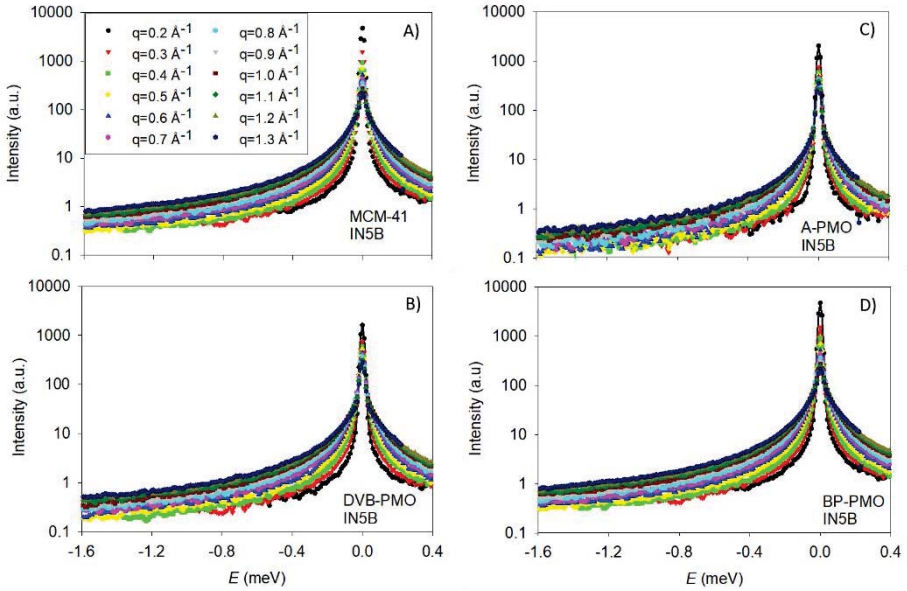

Figure III-4: Q-dependence of the scattering intensity measured on IN5B at the temperature T=278 K of water filled MCM-41 (a), water filled A-PMO (b), water filled DVB-PMO (c) and water filled BP-PMO (d).

2. Fitting procedure

All spectra were fitted individually at each Q with a model comprising one elastic component, i.e. a Dirac function $\delta(\omega)$, and a quasielastic contribution, which was approximated by one (IN16B) or a sum of two (IN5B) Lorentzian functions. Importantly, we did not assume any specific Q-dependence of the parameters, and therefore no implicit reference to a theoretical model was made. This reduced the possible introduction of bias in the data analysis, as demonstrated in the recent QENS study of bulk water.[18] The essentially elastic contribution arising from the pore wall atoms was accounted for by adding the scattered experimental intensity of the empty matrices to the theoretical functions, which were fitted to the experimental spectra of the water filled matrices. This means that the fitted Dirac function can be actually ascribed to an elastic contribution of water molecules.

For the two spectrometers, the scattering intensity of the empty matrices essentially presented an elastic peak and a small background. A tiny dependence on the temperature was observed on IN5B, with the elastic intensity varying by about 4-8% on the temperature range covered by this study (243-300K). This variation is likely due to a Debye Waller factor effect. This is in agreement with the absence of measurable quasielastic intensity and suggests that the dynamics of the framework of the porous matrices is dominated by vibrational modes. Beside the elastic contribution due to the empty matrices, an additional elastic term $A_0(Q)$ was used to fit scattering intensity of the capillary filled samples. The latter can be ascribed to the elastic contribution of water molecules.

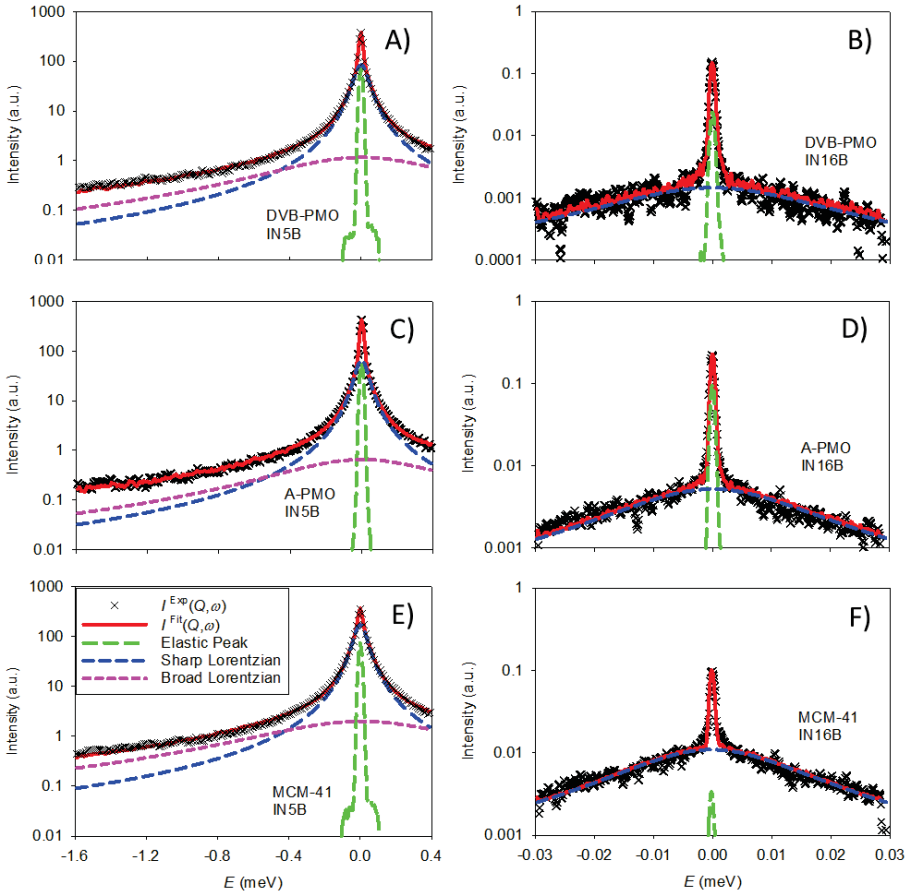

Figure III-5: QENS spectra (cross symbols) and fitted functions (lines) at the temperature T = 278 K of water filled DVB-PMO (A, B), A-PMO (C,E and D) and MCM-41 (E, F). QENS spectra measured on IN5B at Q = 0.8 Å^{-1} (left panels A, C and E) and on IN16B at Q = 0.85 Å^{-1} (right panels B, D and F).

On IN5B, two Lorentzian functions were needed to reproduce the quasielastic line shape attributed to water. On IN16B, one Lorentzian function was sufficient. No additional background, such as a constant term, was used in the fitting procedure. The modelled functions were convoluted by the instrument resolution $R(Q,\omega)$ obtained by measuring a vanadium sample according to:

$$I^{IN5B}(Q,\omega) = [A_0(Q)\delta(\omega) + A_1(Q)L_1(Q,\omega,\Gamma_1) + A_2(Q)L_2(Q,\omega,\Gamma_2)] \otimes R(Q,\omega) \quad \text{(III-1)}$$

$$I^{IN16B}(Q,\omega) = [A_0(Q)\delta(\omega) + A_1(Q)L_1(Q,\omega,\Gamma_1)] \otimes R(Q,\omega) \quad \text{(III-2)}$$

where $A_i(Q)$ is the intensity of the i^{th} component and L_i is a Lorentzian function with a linewidth HWHM Γ_i. The comparison between the fitted functions and the experimental QENS spectra acquired on both spectrometers is illustrated in Figure III-5 for water filled the four matrices. It confirms the very good agreement between the fitted function (red solid line) and the experimental data points (symbol), which match within experimental uncertainties. The additional curves shown in Figure III-5 illustrate the decomposition of the total intensity into one elastic and one (IN16B) or two (IN5B) quasielastic Lorentzian functions.

The continuous nature of the rotational motion of water molecules has been questioned by experiments and simulations,[19, 20] and it was also argued that the assumptions underlying this QENS model might not be strictly verified.[18] To limit any interpretational bias, we first performed a model-free fit of the data. Both the intensity and the width of the two Lorentzians were determined independently at each Q. On IN5B, the first fit revealed that the linewidth of the second (broadest) Lorentzian Γ_2 was barely varying with Q. Contrariwise, the sharpest Lorentzian Γ_1 was dispersive for both spectrometers (Figure III-6). In order to get a more robust fit, Γ_2 was fixed to its averaged value at each temperature, and the values of all the other parameters were refined again. We assumed that the two Lorentzian functions observed on IN5B reflected the presence of two independent dynamics. In the pioneering QENS studies of bulk water, two motions were identified and attributed to continuous rotational diffusion and jump-like translation.[21, 22] QENS studies on bulk[23, 24] and confined water have later adopted this model.[4, 25] In some studies, this model was also invoked, but because a simplified version of the fitted functional form was considered, the reference to rotational diffusion was actually lost.[26, 27]

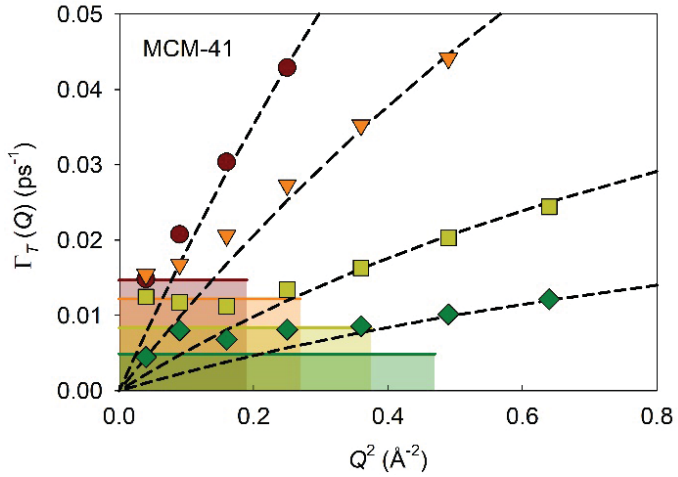

Figure III-6: Enlarged view of the half width at half-maximum Γ_1 in the region of small Qs from IN5B for water filled MCM-41 at four temperatures, 300, 278, 258, and 243K, from top to bottom (filled symbols). Fit using the jump diffusion model (thin dashed lines). The level of the low Q limits predicted by the model of diffusion inside a sphere are illustrated by shaded areas.[28]

Following the assignment made in recent studies of bulk water, we related the broad and sharp quasielastic components to two distinct dynamics: local motion (L) and translational diffusion (T), respectively.[18, 29] It is likely that only the slowest one, attributed to translation, was actually detected on IN16B. In fact, the broad quasielastic contribution arising from local dynamics likely appeared as a vanishing flat background, due to the reduced energy range covered by the high-resolution instrument. Therefore, the incoherent dynamic structure factor of water writes as:

$$S(Q,\omega) = K\,[A_T(Q)\delta(\omega) + (1 - A_T(Q))L_T(Q,\omega,\Gamma_T)]\otimes[A_L(Q)\delta(\omega) + (1 - A_L(Q))\,L_L(Q,\omega,\Gamma_L)] \qquad (\text{III-3})$$

where K is a scaling factor comprising the attenuation of the scattering intensity due to inelastic vibrational modes (Debye-Waller factor). The functions $A_T(Q)$ and $A_L(Q)$ are the

elastic incoherent structure factors (EISFs) of the translational and local motions.30 Their respective linewidth Γ_T and Γ_L were effectively separable since they differ by a factor of 7-10. These quantities were evaluated from the fitted parameters introduced in (III-1) and (III-2) after straightforward calculations, and considering that $\Gamma_T \ll \Gamma_L$.

3. Local water dynamics:

The experimental EISFs $A_L(Q)$ obtained from the fitting with (III-3))are illustrated in Figure III-7. They present an important elastic contribution, which is above 60% at 300 K and 95% at 243 K on the studied *Q*-range. It demonstrates the non-diffusive (i.e. localized) character of this motion. In the classical approach of Teixeira *et al*.[22] this dynamics was described as an isotropic rotation of hydrogens around the oxygen atom. The corresponding EISF writes as $A_R(Q) = [j_0(QR_R)]^2$, where j_0 is the zeroth-order spherical Bessel function and R_R = 0.98 Å for the O-H bong length.[30] A comparison of the prediction from the classical approach with the EISFs $A_L(Q)$ determined experimentally for water in MCM-41 is illustrated Figure III-7-a.

Only at 300 K, the standard model agreed well with the experiments. However, this model was unable to describe the increase of intensity observed at lower temperature. Satisfactory fits could still be obtained with the same functional form $A_R(Q)$, provided that R_R was allowed to vary with the temperature. When considered as a free fit parameter, the value of R_R decreased with decreasing temperature. It reached values as small as 0.5 Å, which cannot be related to the O-H bond length anymore. In that sense, the model lost its physical meaning. Another approach that maintains the classical interpretation of $A_L(Q)$ consists in adding a supplement *Q*-independent elastic term to the isotropic rotation function $A_R(Q)$ (i.e. $A_L(Q) = p\delta(\omega) + (1-p)\,A_R(Q)$).

From this viewpoint, it would imply that a fraction p of the water molecules does not perform rotation on the instrumental timescale due to confinement and interfacial restrictions. At 300 K, such an additional elastic peak was not required to best fit the data, meaning that all the molecules were dynamically active. However, this alternative model led to a large elastic component at sub-ambient temperature, reaching up to 80% at the lowest temperature. It is unlikely that the rotational diffusion would be frozen for such a large fraction of molecules, while it would be active and very fast (i.e. about 1-3 ps) for the unfrozen ones. It is also inconsistent with the analysis of the translational diffusion detailed in the next section, where much smaller fractions of dynamically frozen molecules were obtained. Our results rather suggest that this broad quasielastic line does not strictly correspond to isotropic rotational diffusion.

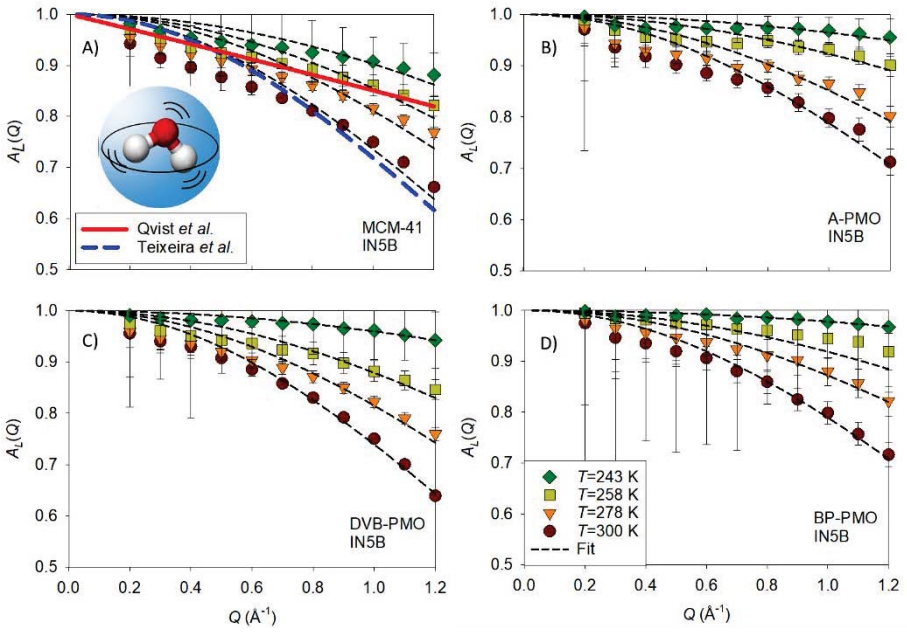

Figure III-7 Elastic incoherent structure factor of the local quasielastic relaxation (symbols) deduced from IN5B measurements at four different temperatures of water confined in different matrices (A) MCM-41, (B) A-PMO, (C) DVB-PMO, and (D) BP-PMO. Two different approaches describing the broadest quasielastic relaxation of bulk water are presented for comparison in the panel (A): (solid line) model-free EISF of the local relaxation averaged over 6 temperatures in the range 253-293 K, after Qvist et al.[18] and (long dashed line) the EISF of the continuous molecule rotation supposed independent on the temperature for the same temperature range after Teixeira et al.[22] Inset of panel (a): sketch of the local motion of water.

This conclusion appears in line with an alternative view proposed by Qvist *et al.* for bulk water.[18] This motion was attributed to a local dynamical "intra-basin" relaxation, also observed in the water molecules trajectories of Molecular Dynamics (MD) simulations. A comparison is made in Figure III-7-a with the polynomial fit of the bulk water data.[18] It is similar to the EISFs that we measured at 258 K. A univocal determination of the geometry of this local relaxation is elusive, as also discussed for bulk water by Arbe *et al*.[29] However, based on a Debye-Waller factor type of analysis, we can conclude on the gradual shrinkage of the mean-squared-amplitude of the local motion on decreasing the temperature for confined water.

On the entire temperature range studied, the relaxation time τ_L attributed to the local motion of water varied from 1 to 3 ps. These values are within the range of relaxation times reported for bulk water (1 to 3.5 ps) on a slightly reduced temperature range.[18] The effect of the matrix can be estimated from a comparison of the EISFs measured for water confined in MCM-41 (cf. Figure III-7-A) and the three PMOs (cf. Figure III-7-(B-C-D)). If present, the difference between the EISFs is very small and hardly resolved within experimental uncertainties. The temperature dependence of the relaxation time of water confined in the four different matrices was also very similar, with an averaged value of the activation energy of 10 ± 4 KJ mol^{-1}. The previous QENS studies of confined water were often limited to translational diffusion and results about the fast local dynamics are scarcer in the literature. To the best of our knowledge, there exists only one available QENS measurement of water confined in a benzene-bridged PMO by Aso et al.[25] In this study, the authors concluded on a significant slowdown (by a factor of three) of the local dynamics of water confined in

MCM-41, with respect to those of water confined in the PMO and bulk water. We note that the comparison with this PMO's result was based on an older QENS measurement of water confined in MCM-41,[5] which was moreover performed at two different temperatures. On the contrary, our conclusions are based on a single study, with measurements performed systematically under the same experimental conditions. Under these conditions, our results rather point towards a comparable fast local dynamics of water when confined in PMOs or in MCM-41. It is also worth mentioning that this conclusion is in line with the pioneering study of water in Vycor, which concluded that the fast QENS relaxation denoted as 'hydrogen-bond lifetime' was very close to the bulk one, both for fully and partly hydrated systems.[4]

4. Translational water dynamics – neutron time-of-flight study:

The sharpest quasielastic component detected on IN5B was attributed to the translational diffusion of the molecules' center of mass. However, we noticed that this intensity also contained a purely elastic component, as illustrated in Figure III-8. The existence of an EISF associated to this component, of which the intensity was dependent on both the temperature and the momentum transfer Q, is inconsistent with long range translation diffusion. The EISFs were fitted with a model that incorporate a fraction p of non-mobile molecules (*i.e.* dynamically frozen on the timescale of the instrument) and a fraction (1-p) of molecules performing restricted translational diffusion in a sphere.[28, 30] The corresponding expression of $A_T(Q)$ is

$$A_T(Q) = p\delta(\omega) + (1-p)\left[\frac{3\, j_1(QR_T)}{QR_T}\right]^2 \qquad \text{(III-4)}$$

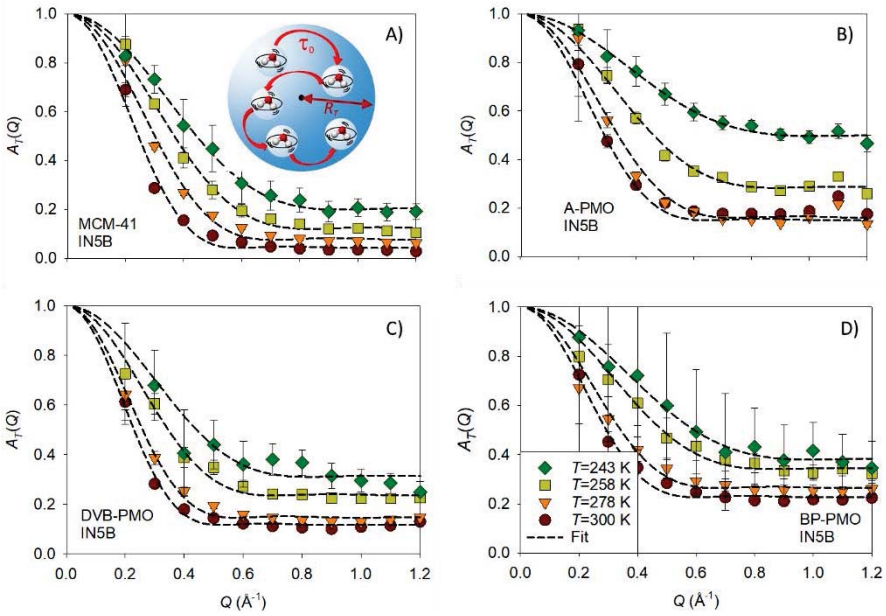

Figure III-8 Elastic incoherent structure factor of the first quasielastic relaxation (symbols) deduced from IN5B measurements at four different temperatures of water confined in different matrices (A) MCM-41, (B) A-PMO, (C) DVB-PMO, and (D) BP-PMO. Fits with a model of translation diffusion confined in a sphere (lines). Inset of panel (A): sketch of the confined jump diffusion motion of water.

where R_T is the radius of the confining sphere, p the fraction of non-mobile molecules, and j_1 is the first-order spherical Bessel function. This model could reproduce the experimental EISFs quantitatively, as illustrated by dashed lines in Figure III-8. However, the parameters obtained at the lowest temperatures (T = 243 K) presented large uncertainties, which was due to difficulties in separating the sharpest quasielastic component from a pure elastic one within the energy resolution of IN5B. The two fitted parameters p and R_T showed a systematic temperature dependence as can be inferred from Figure III-9.

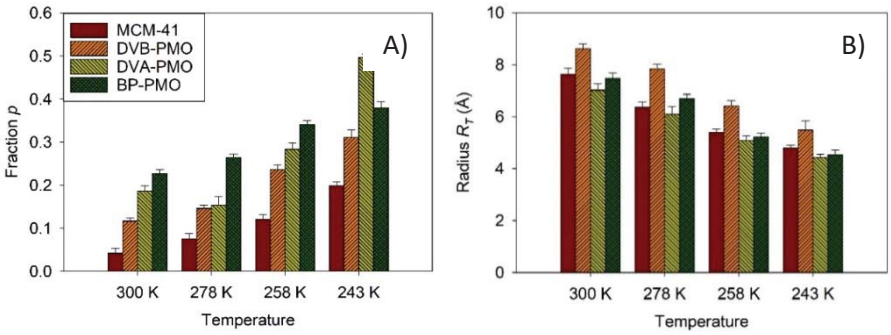

Figure III-9 Variation with the temperature and the confining matrix of the parameters obtained from the fit of the EISF of the translational diffusion (from IN5B measurements). (A) Fraction p of dynamically frozen water molecules. (B) Radius RT of the sphere confining the translational diffusion.

A systematic increase of p with decreasing temperature reflects the larger number of dynamically frozen molecules on cooling. It is about 10-20% at 300 K, and reaches values as large as 40-50% at 243 K. We also noticed a dependence of p on the confining matrix (cf. Figure III-9-A). The smallest value of p was obtained for the purely siliceous matrix MCM-41. It corresponds to half the value obtained for BP-PMO (Figure III-9-D)) that comprises hydrophobic bridging. At first sight, this feature appears counterintuitive. Indeed, MCM-41 has a larger surface density of silanol groups that may act as adsorbing sites, thus reducing the translational motion of water. On the other hand, the barrier of activation related to the molecule jump from one surface site to an adjacent site can be reduced when the surface presents a homogeneous distribution of equivalent silica units such as for MCM-41. For PMOs instead, the alternation of hydrophobic and hydrophilic sites might interrupt the surface diffusion of water. This reasoning should be moderated for hydrophilic A-PMO, considering that the amino groups also act as H-bonding sites, as shown by NMR.[15] The distance between NH_2 and silanols that is estimated to be a bit less than half of the repetition distance (i.e. 5 Å) is still too large to allow a direct interaction of a water molecule with both sites. We believe that this issue needs additional support from other methods, such as molecular simulation.

The radius R_T of the sphere confining the translational diffusion of the fraction $(1 - p)$ of mobile molecules decreases from 9 to 5 Å, during cooling from 300 to 243 K (cf. Figure III-9-B). The spatial restriction of the translational displacements on cooling is similar to the observation made for the local dynamics in the previous part in that it is decreasing. The values of R_T spanned from one quarter to one half of the pore radius. Hence, this confining sphere cannot be strictly identified as the pore itself. However, a correlation between R_T and R_{pore} is suggested by the systematically larger values of R_T for DVB-PMO, which pore size

is 15% larger than for the three other matrices (cf. Table III-1). This indicates a possible link between R_T and geometrical aspects of confinement.

Moreover, the role of surface effects can be invoked. Indeed, the fraction p of non-mobile molecules could be also taken into account as a secondary source of confinement. For simplicity, it can be assumed that these molecules are forming a homogeneous layer located at the interface with the pore wall. In this case, the radius R_{core} of the core region of the pore, where the mobile water molecules are located, is $R_{core} = R_{pore}\sqrt{(1-p)}$. Using the experimental values of p and R_{pore} from Table III-1, we obtained that R_{core} varies from 19 to 12.5 Å as a function of the matrix and the temperature, which is about twice the value of R_T. Interestingly, the thickness of the non-mobile layer (*i.e.* $e_{non-mob} = R_{pore} - R_{core}$) is in the range 1-5 Å, and is maximum at the lowest studied temperature 243 K, before crystallization occurs. It compares reasonably with the thickness of the non-crystalizing layer (t = 6 Å) evaluated by cryoporometry for water confined in MCM-41 and SBA-15 porous silicates,[31, 32] as well as with the thickness of the immobile, sticky layer inferred from capillary rise experiments for water in hydrophilic silica pores (Vycor).[33]

After the discussion of the EISFs, we address now the corresponding quasielastic part, which contains dynamical information about the fraction $(1 - p)$ of mobile molecules. The linewidth of the sharper Lorentzian quasielastic line Γ_T found on IN5B is illustrated in Figure III-10, as a function of the squared momentum transfer. The different panels correspond to the four different matrices, and the different curves illustrate different temperatures. The experimental results for bulk water are also illustrated for comparison. Only two curves from Qvist et al.[18] are presented in Figure III-10-A, because, unlike for the study by Teixeira *et al.*[22], the selection of temperatures was different from the one used the present work.

At intermediate Qs, Γ_T increases linearly with Q^2, which conforms the normal Fick's law of translational diffusion. However, deviations occur both at small and large Qs. When Q tends to zero, Γ_T does not really vanish but rather saturates towards a finite value, as illustrated in Figure III-6 for MCM-41. This feature can be explained as resulting from the confined character of the translational diffusion, which was demonstrated above from the analysis of the EISFs. In the frame of the model of confined diffusion in a sphere, it was predicted by Volino *et al.*[28] that Γ_T should deviate from the Fick law at $Q \approx \frac{3.3}{R_T}$ towards a plateau value $\mathrm{G}_T = \frac{4.33\, D_T}{{R_T}^2}$. The measured linewidths are in fair agreement with this prediction, as illustrated in Figure III-6 by the shaded areas.

At large Qs, Γ_T bends and tends asymptotically towards a constant value denoted $1/\tau_0$ (Figure III-10). In fact, the Fickian diffusion model assumes a continuous motion process. Deviation from this assumption is observed when considering small displacements (*i.e.* for Q larger than the inverse particle distance), where a discontinuous mechanism is related to the finite molecular size and the local order in the liquid. The linewidth was modelled by the well-known jump-diffusion model, which assumes that the translation motion proceeds by successive elementary jumps (thin dashed lines in Figure III-6).[30, 34] Between two jumps, the particle remains localized for a typical residence time τ_0 on a molecular site, with a spatial extension limited to the amplitude of vibrational modes. Applying the usual assumptions that the jump can be regarded as instantaneous with respect to the residence time τ_0 spent by the particle on a site, and that the jump length l is much larger than the spatial extension of each site, the linewidth of the Lorentzian was fitted with

$$G_T(Q) = \frac{D_T Q^2}{1+\tau_0 D_T Q^2} \qquad \text{(III-5)}$$

where D_T is the diffusion coefficient and τ_0 the mean residence time.

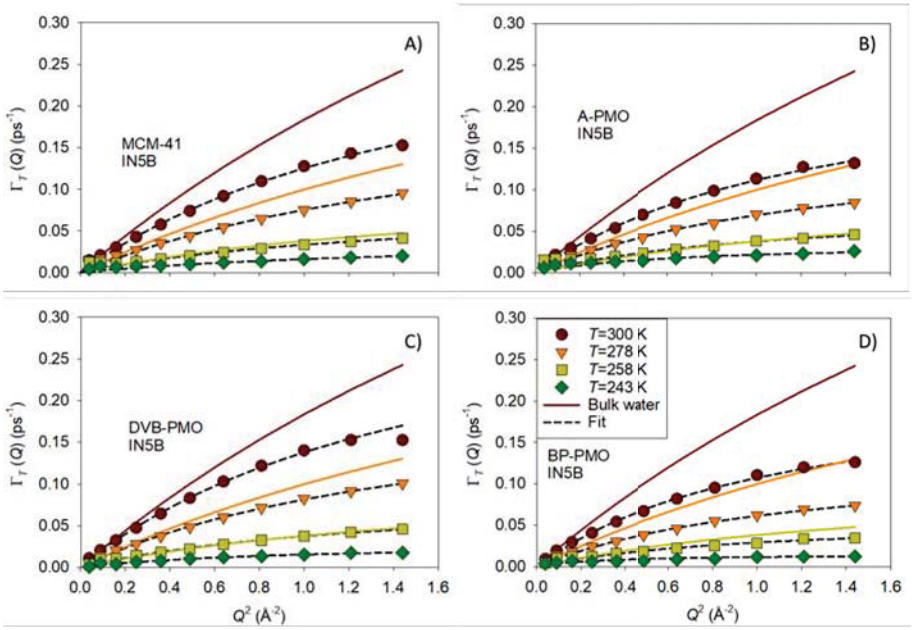

Figure III-10: Evolutions of the half width at half-maximum Γ_T of the sharp Lorentzian as a function of Q^2 obtained from the fitting of QENS spectra measured on IN5B for water confined in the four matrices (A) MCM-41, (B) A-PMO, (C) DVB-PMO, and (D) BP-PMO at four temperatures (filled symbols). Fit using the jump diffusion model (thin dashed lines). Bulk water experimental results at three temperatures, from top to bottom 300 K, 278 K, and 258 K (solid lines) from Teixeira et al.[22] In panel (A), bulk water experimental results at 293.4 K, and 257.8 K (dashed dotted line) from Qvist et al.[18]

These two parameters obtained for the four different matrices are illustrated in Figure III-11-A as a function of the temperature in Arrhenius coordinates. The bulk values of D_T and τ_0 determined from QENS measurements,[4, 22] and the diffusion coefficient measured by NMR[35] are also added for comparison. The values of the diffusion coefficient for the four confined materials are, within about 10%, in good accordance with those of the bulk water. Deviations observed at high and low temperature could indicate that the activation energy is reduced in confinement, although the difference remained in the limit of the data accuracy, especially at 243 K as Γ_T approaches the instrumental resolution limit of IN5B.

Significant differences between the confined and bulk water were obtained for the residence time τ_0. It is systematically larger in confinement than in the bulk as illustrated in Figure III-11-B. At 300 K, the residence time is three to four times longer in the porous matrices. Moreover, the activation energy is smaller in confinement, so that the residence times of the different systems apparently approach the bulk system at lower temperature (243 K). It is worth noting that both D_T and τ_0 exhibit a curvature, which indicates a super-Arrhenius character as usually observed in supercooled glass-forming liquids.[36, 37] This is illustrated in Figure III-11-B by the fit of the residence time with a Vogel-Fulcher-Tammann equation (dashed line). A mean jump length l could be estimated by combining the diffusion coefficient and the residence time noting that $D_T = \frac{\langle l^2 \rangle}{6\tau_0}$. The obtained values of l were in the

typical range from 0.65 to 1.2 Å for all the matrices with a systematic reduction when the temperature decreased from 300 to 243 K. A comparison with other QENS data obtained from the literature is given in Table III-2.

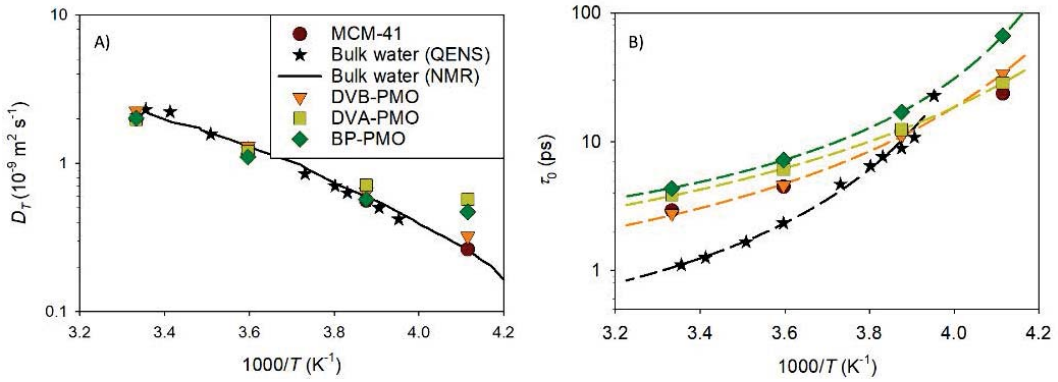

Figure III-11 (A) Translational diffusion coefficient DT and (B) residence time τ_0 of water evaluated from the fit of IN5B spectra with a jump-diffusion model for water confined in MCM-41 and three PMOs as a function of the inverse temperature. In panel A, the QENS data of bulk water are from Teixeira et al.[22] (stars) and the NMR diffusion coefficient from Price et al.[35] (solid line). VTF fits of the residence time (dashed line in panel b).

These experiments have been analyzed differently, and often the EISFs related to the fast local dynamics, the confined translation diffusion and the fraction of non-mobile molecules were not available simultaneously. Also, the temperature range was sometimes limited, which prevented a thorough comparison with our results.

Table III-2 Translation diffusion coefficient D_T and the residence time τ_0 of the mobile fraction of water molecules derived from the jump diffusion model. The results from the present study are compared with those from the literature.

Temperature (K)	D_t (10^{-9} m^2 s^{-1}) τ_0 (ps)	MCM-41 3.6 nm	A-PMO 3.5 nm	BP-PMO 3.5 nm	DVB-PMO 4.1 nm	Bulk[a]	Ph-PMO[c] 3 nm	SBA-15[d] 6.6 nm	MCM-41[e] 3.8 nm	MCM-41[d] 2.9 nm	MCM-41[d] 2.4 nm
300	D_t	1.98	1.97	2.01	2.24	2.3[b] (298 K)	1.7	2.0	1.7	1.5	1.2
	τ_0	2.9	3.9	4.3	2.8	1.1[b] (298 K)	2.6	3.3	2.6	5.3	7.3
278	D_t	1.14	1.20	1.10	1.30	1.30	1.1 (273 K)		0.77 (273 K)		
	τ_0	4.5	6.1	7.2	4.6	2.3	8.7 (273 K)		6.6 (273 K)		
258	D_t	0.56	0.71	0.57	0.64	0.56					
	τ_0	12.0	12.4	17.0	11.0	8.9					
243	D_t	0.26	0.57	0.47	0.32	0.42 (253 K)					
	τ_0	23.7	28.6	66.6	33.9	22.7 (253 K)					

[a]: data from Teixeira et al.[22], [b]: data from Bellissent-Funel et al.[4], [c]: data from Aso et al.[25], [d]: data from Baum et al.[7], and [e]: data from Takahara et al.[5]

Bearing in mind these possible limitations, it is, however, possible to compare the values of D_T and τ_0 that were obtained from the quasielastic linewidth. Similar conclusions can be made from these previous evaluations of D_T, which values remain similar or marginally smaller than that of the bulk water whenever the pore diameter is larger or equal to 3 nm. An enhanced slowdown of the translational dynamics is observed for a pore size smaller than 3 nm (Table III-2).

5. Interfacial translational water dynamics - high resolution neutron backscattering study:

In the previous section, the translational dynamics of confined water has been discussed in terms of two populations: an interfacial layer of thickness $e_{non-mob}$ in the range 1-5 Å, with a highly reduced dynamics due to the interaction with the pore surface, and a liquid region at the pore center with a 'bulk-like' dynamics with moderate slowdown and marginal effect of the pore chemistry. It is noteworthy that the interfacial dynamics is likely not frozen on a longer time scale. The fraction of molecules named 'non-mobile' rather corresponds to the long-time tail of the broad distribution of dynamics.[37]

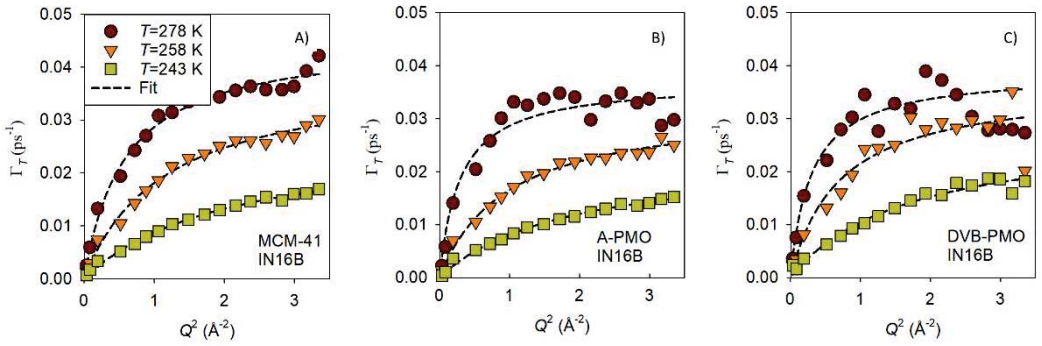

Figure III-12 Evolutions of the half width at half-maximum Γ_T of the Lorentzian as a function of Q2 obtained from the fitting of QENS spectra measured on IN16B for confined water in the 3 matrices (A) MCM-41, (B) A-PMO, and (C) DVB-PMO at three temperatures 278 K, 258 K, and 243 K (filled symbols). Fits using the jump diffusion model (dashed lines).

This simplified bimodal description is widely used to account for the dynamics that is slower than the cut-off introduced by the energy resolution of the instrument. To get a better insight on the dynamics of the interfacial molecules, which are expected to be more influenced by the nature of the water/surface interaction, we have used the higher resolution of the neutron backscattering spectrometer IN16B, i.e. 0.75 μeV compared to 22 μeV on IN5B. The resulting observable timescale is thus extended from about 30 ps to 1 ns. In the meantime, the dynamical range covered on IN16B is much reduced, which means that the broad quasielastic intensity shown for IN5B is mostly hidden in the background on IN16B (i.e. the local motion and possibly the fastest part of the translation).

The line width of the quasielastic intensity measured on IN16B was fitted with a jump-diffusion model, as illustrated in Figure III-12. The diffusion coefficients and residences times derived from these fits are illustrated in Figure III-13, and also given in Table III-3. The diffusion coefficient and the residence time of bulk water are added in Figure III-13,

which recalls the presentation made in Figure III-10 for IN5B results. The diffusion coefficients measured on IN16B are systematically smaller (by a factor of 1.2 to 2) than those measured on IN5B for the same water filled matrices. Also, the residence times are longer.

Table III-3: Comparison of the translation diffusion coefficient DT and the residence time τ_0 of water molecules derived from the jump diffusion model for two different experimental resolutions

Temperature (K)	D_t (10^{-9} m^2 s^{-1}) τ_0 (ps)	MCM-41		A-PMO		DVB-PMO	
		IN5B (30 ps)	IN16B (1 ns)	IN5B (30 ps)	IN16B (1 ns)	IN5B (30 ps)	IN16B (1 ns)
278	D_t	1.14	0.78	1.20	0.72	1.30	1.03
	τ_0	4.5	22	6.1	27	4.6	23
258	D_t	0.56	0.34	0.71	0.33	0.64	0.52
	τ_0	12.0	26	12.4	31	11.0	27
243	D_t	0.26	0.13	0.57	0.13	0.32	0.17
	τ_0	23.7	37	28.6	44	33.9	35

This confirms that the fraction of the water molecules, which was denoted as non-mobile on IN5B, comprises particles that actually diffuse but much more slowly. We inferred from IN5B results that the molecules performing 'bulk-like' spatially restricted motions, were located in the center of the pore. Accordingly, we relate the sharpest quasielastic contribution observed on IN16B to a slower diffusion process, which corresponds to molecules interacting with the interface of water filled matrices. Importantly, the diffusivity of these interfacial water molecules depends on the matrix chemistry. The largest reduction of translational mobility is obtained for the two hydrophilic matrices (MCM-41 and A-PMO).

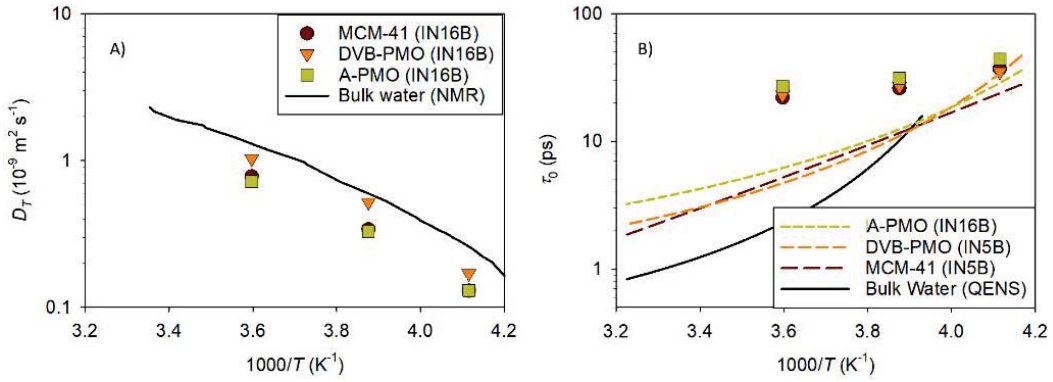

Figure III-13 (a) Translational diffusion coefficient DT and (b) residence time τ_0 of water evaluated from the fit of IN16B spectra with a jump-diffusion model for water confined in MCM-41 and two PMOs as a function of the inverse temperature (symbols). In panel a, the NMR diffusion coefficient of bulk water from Price et al.[35] (solid line). In panel b, the residence time of water confined in the same matrices fitted from IN5B spectra (dashed line) and the residence time of bulk water from Teixeira et al.[22] (solid line)

For purely siliceous MCM-41, this slowdown of the diffusion of interfacial water molecules is classically attributed to the formation of H-bonds between water and silanols. For A-PMO, silanol adsorption sites are dispersed on the pore surface due to the bridging organic units that impose a separation distance of 1.2 nm between silica units in the direction parallel to the pore axis. However, this effect is balanced by the presence of amino groups between silica units, which act as secondary H-bonding sites for interfacial water molecules. This is supported by the observation by NMR of strong interfacial correlations between water, and both silica and organic units.[15]

For water filled DVB-PMO, intermediate values of the diffusivity that stand between the bulk and the hydrophilic confinement situation are observed. Again, this points to an effect of the dilution of silica units, which are regularly spaced every 1.2 nm along the pore channel axis. Unlike A-PMO, this reduction of the number of H-bonding silanol groups is not counterbalanced by the DVB organic spacers that have no polar groups and cannot act as secondary adsorbing sites. This interpretation is in line with the observation of depleted regions in the vicinity of the aprotic organic bridging units.[15]

As a whole, the relation between surface chemistry and interfacial layer mobility, although studied for a limited number of materials, agrees with the evaluation of the relative surface hydrophilicity made for series of PMOs and quantified in terms water capillary pressure and surface water coverage prior to capillary condensation.[38]

Some important differences can be underlined from the comparison of the diffusivities obtained in the present QENS study and those derived from PFG NMR on similar samples.[11] A greater reduction of the diffusivity with respect to bulk water was obtained in the latter case, as well as a larger dependence on the nature of the porous sample (by up to two orders of magnitude). The apparent disagreement between the diffusivities measured by the two methods is intriguing. As mentioned in the introduction part, the diffusivities measured by both methods are averaged on very different molecular displacements (i.e. ~ 1 Å for QENS and ~ 1 µm for PFG NMR). The latter displacement exceeds notably the size of each individual porous gain. As thoroughly explained in this PFG NMR study, the obtained long-range diffusivities result from the migration of water molecules in the pores, but also on the outer surface of the porous grains and in the interparticle space. The transport behavior depends on the rate exchange between these different phases and their physical states (liquid or gaseous).

Under the same filling conditions as those used in the QENS study (i.e. absence of liquid excess) and for loosely agglomerated particles (such as MCM-41), it was concluded that the average diffusivity D_{av} was barely related to the liquid phase D_l but dominated by properties of the vapor phase with $D_{av} = p_v D_v$, where $p_v \ll 1$ and $D_v \gg D_l$ are the relative fraction and the diffusivity of water in the vapor phase. On the contrary, for agglomerated particles (such as A-PMO), or when an excess of bulk water has crystallized in the interparticle space, it was concluded that the long range transport of water molecules was occurring in a liquid thin film covering the external surface on the grains. In this case, the measured slow diffusive component was shown to be an effective value that depends on the macroscopic rather than nanoporous structure of the sample in terms of particle morphology and their agglomeration.

On the contrary, the short-range diffusivities measured by QENS probe the transport of water molecule inside a single pore. As such, they are intrinsic properties of the confined liquid phase, which were shown to be affected by the pore size, and the surface interaction. However, they bring no information on the macroscopic transport mechanisms of water

across the porous materials, which is important in many natural processes and for technological applications where fluid flow and imbibition occur. In this sense, we emphasize that the combination of PFG-NMR and QENS methods to study the dynamics of confined water in PMOs provides crucial information on the two sides of the same coin.

IV. Conclusion

We performed a systematic QENS study of the dynamics of liquid water confined in mesoporous silica (MCM-41) and organosilicas (PMOs) with different surface chemistries in a temperature range spanning from 243 to 300 K. Two high-flux spectrometers with complementary energy resolution were combined so as to cover an extended dynamical range. Following recent recommendations made for bulk water, a model free analysis of the incoherent dynamic structure factor was applied for the first time to confined water.

The analysis of IN5B results points towards the existence of two distinct dynamics: a fast local motion (typical time varying from 1 to 3 ps), which implies all the water molecules and translational diffusion dynamics attributable only to a fraction of molecules.

The EISF of the former component is consistent with the isotropic rotational diffusion of the water molecule at 300 K. However, this interpretation is questioned at lower temperature. Based on the concept of intra-basin local relaxation introduced for bulk water, our result suggests a reduction of the spatial amplitude of this local motion on cooling. The second quasielastic relaxation is attributed to translational diffusion. It concerns only a fraction of mobile molecules, which are most probably located at the pore center.

Deviations from the Fick's law at large Qs were accounted by the jump-diffusion model and at low Qs by transient spatial restriction effects. The obtained values of the diffusion coefficient D_T and the residence time τ_0 indicate a 'bulk-like' behavior. The slowing down of translational diffusion due to confinement is moderate. It is within 10% for D_T but it is more marked for τ_0 that is up to four times longer than for bulk water. The EISFs demonstrate that the translational diffusion is spatially restricted on the instrumental timescale, which differs from bulk water.

The radius R_T of the sphere confining the translational diffusion of the mobile molecules decreases from 9 to 5 Å, during cooling from 300 to 243 K. It is not strictly related to the pore size itself. We consider that it rather emerges from the hindrance due to the surrounding molecules that are influenced by the pore interface. This is supported by the increase on cooling of the fraction p of molecules that are dynamically frozen (i.e. not diffusing on the timescale of IN5B), and that are most likely located at the interface. It is about 10-20% at 300 K, and reaches values as large as 40-50% at 243 K, which corresponds to a thickness of the 'non-mobile' layer in the range of 1-5 Å. This fraction also varies as a function of the nature of the matrix, illustrating the effect of the surface interaction on the dynamics of the interfacial layer.

Finally, our study using the high-resolution spectrometer (IN16B) demonstrates that interfacial molecules are dynamically active on a longer timescale. Their motion could be described by a jump-diffusion model as well. However, the corresponding characteristic parameters D_T and τ_0 demonstrate a significantly slower process than that of the liquid located in the pore center. Moreover, the diffusivity of interfacial water molecules shows

dependence on the nature of the confining matrix. The largest slowdown is obtained for hydrophilic matrices (MCM-41 and A-PMO) with respect to the more hydrophobic one (DVB-PMO).

As a whole, this study indicates that, on the ps-to-ns timescale and for a pore size of about 3.5 nm, the details of the water/surface interaction (*i.e.* matrix hydrophilicity, and presence of silanol or amino H-bonding sites) hardly affect the generic confinement effects that involve the water molecules located in the core of the pore but they are important in determining the translational motion of the water molecules located at the interface.

REFERENCES

1. *Zanotti JM, Gibrat G, Bellissent-Funel MC. Hydration water rotational motion as a source of configurational entropy driving protein dynamics. Crossovers at 150 and 220 K. Physical Chemistry Chemical Physics 2008;10(32): 4865-70.*

2. *Garnier L, Szymczyk A, Malfreyt P, Ghoufi A. Physics behind Water Transport through Nanoporous Boron Nitride and Graphene. Journal of Physical Chemistry Letters 2016;7(17): 3371-76.*

3. *Swenson J, Bergman R, Howells WS. Quasielastic neutron scattering of two-dimensional water in a vermiculite clay. Journal of Chemical Physics 2000;113(7): 2873-79.*

4. *Bellissentfunel MC, Chen SH, Zanotti JM. SINGLE-PARTICLE DYNAMICS OF WATER-MOLECULES IN CONFINED SPACE. Physical Review E 1995;51(5): 4558-69.*

5. *Takahara S, Nakano M, Kittaka S, et al. Neutron scattering study on dynamics of water molecules in MCM-41. Journal of Physical Chemistry B 1999;103(28): 5814-19.*

6. *Faraone A, Liu L, Mou CY, Shih PC, Copley JRD, Chen SH. Translational and rotational dynamics of water in mesoporous silica materials: MCM-41-S and MCM-48-S. Journal of Chemical Physics 2003;119(7): 3963-71.*

7. *Baum M, Rieutord F, Jurany F, Rey C, Rebiscoul D. Dynamical and Structural Properties of Water in Silica Nanoconfinement: Impact of Pore Size, Ion Nature, and Electrolyte Concentration. Langmuir 2019;35(33): 10780-94.*

8. *Beck JS, Vartuli JC, Roth WJ, et al. A NEW FAMILY OF MESOPOROUS MOLECULAR-SIEVES PREPARED WITH LIQUID-CRYSTAL TEMPLATES. Journal of the American Chemical Society 1992;114(27): 10834-43.*

9. *Grun M, Lauer I, Unger KK. The synthesis of micrometer- and submicrometer-size spheres of ordered mesoporous oxide MCM-41. Advanced Materials 1997;9(3): 254-&.*

10. *Hoffmann F, Cornelius M, Morell J, Froba M. Silica-based mesoporous organic-inorganic hybrid materials. Angewandte Chemie-International Edition 2006;45(20): 3216-51.*

11. *Mietner BJ, Froba M, Valiullin R. Water Transport in Periodic Mesoporous Organosilica Materials. Journal of Physical Chemistry C 2018;122(24): 12673-80.*

12. *D MM, Appel M, Busch B, Frick M, Fröba P, Huber A, Jani J, Ollivier. In Water dynamics in mesoporous with periodically alternating surface interaction. Institut Laue-Langevin (ILL).*

13. *D, Morineau, M B, M F, P H, J O. In Water dynamics in mesoporous with periodically alternating surface interaction. Institut Laue-Langevin (ILL).*

14. *Appel M, Frick B. Note: One order of magnitude better signal-to-noise ratio for neutron backscattering. Review of Scientific Instruments 2017;88(3).*

15. *Mietner JB, Brieler FJ, Lee YJ, Froba M. Properties of Water Confined in Periodic Mesoporous Organosilicas: Nanoimprinting the Local Structure. Angewandte Chemie-International Edition 2017;56(40): 12348-51.*

16. *Arnold O, Bilheux JC, Borreguero JM, et al. Mantid-Data analysis and visualization package for neutron scattering and mu SR experiments. Nuclear Instruments & Methods in Physics Research Section a-Accelerators Spectrometers Detectors and Associated Equipment 2014;764: 156-66.*

17. *Richard D, Ferrand M, Kearley GJ. Analysis and Visualisation of Neutron-Scattering Data. 4. Institut Laue-Langevin, BP156, 38042 Grenoble, Cedex 09, France: Journal of Neutron Research; 1996:33-39.*

18. *Qvist J, Schober H, Halle B. Structural dynamics of supercooled water from quasielastic neutron scattering and molecular simulations. Journal of Chemical Physics 2011;134(14).*

19. *Laage D, Hynes JT. A molecular jump mechanism of water reorientation. Science 2006;311(5762): 832-35.*

20. *Qvist J, Mattea C, Sunde EP, Halle B. Rotational dynamics in supercooled water from nuclear spin relaxation and molecular simulations. Journal of Chemical Physics 2012;136(20).*

21. *Chen SH, Teixeira J, Nicklow R. INCOHERENT QUASI-ELASTIC NEUTRON-SCATTERING FROM WATER IN SUPERCOOLED REGIME. Physical Review A 1982;26(6): 3477-82.*

22. *Teixeira J, Bellissentfunel MC, Chen SH, Dianoux AJ. EXPERIMENTAL-DETERMINATION OF THE NATURE OF DIFFUSIVE MOTIONS OF WATER-MOLECULES AT LOW-TEMPERATURES. Physical Review A 1985;31(3): 1913-17.*

23. *Cavatorta F, Deriu A, Dicola D, Middendorf HD. DIFFUSIVE PROPERTIES OF WATER STUDIED BY INCOHERENT QUASI-ELASTIC NEUTRON-SCATTERING. Journal of Physics-Condensed Matter 1994;6: A113-A17.*

24. *DiCola D, Deriu A, Sampoli M, Torcini A. Proton dynamics in supercooled water by molecular dynamics simulations and quasielastic neutron scattering. Journal of Chemical Physics 1996;104(11): 4223-32.*

25. *Aso M, Ito K, Sugino H, et al. Thermal behavior, structure, and dynamics of low-temperature water confined in mesoporous organosilica by differential scanning calorimetry, X-ray diffraction, and quasi-elastic neutron scattering. Pure and Applied Chemistry 2013;85(1): 289-305.*

26. *Takahara S, Sumiyama N, Kittaka S, Yamaguchi T, Bellissent-Funel MC. Neutron scattering study on dynamics of water molecules in MCM-41. 2. Determination of translational diffusion coefficient. Journal of Physical Chemistry B 2005;109(22): 11231-39.*

27. *Briman IM, Rebiscoul D, Diat O, et al. Impact of Pore Size and Pore Surface Composition on the Dynamics of Confined Water in Highly Ordered Porous Silica. Journal of Physical Chemistry C 2012;116(12): 7021-28.*

28. *Volino F, Dianoux AJ. NEUTRON INCOHERENT-SCATTERING LAW FOR DIFFUSION IN A POTENTIAL OF SPHERICAL-SYMMETRY - GENERAL FORMALISM AND APPLICATION TO DIFFUSION INSIDE A SPHERE. Molecular Physics 1980;41(2): 271-79.*

29. *Arbe A, de Molina PM, Alvarez F, Frick B, Colmenero J. Dielectric Susceptibility of Liquid Water: Microscopic Insights from Coherent and Incoherent Neutron Scattering. Physical Review Letters 2016;117(18).*

30. *Bée M. Quasielastic neutron scattering : principles and applications in solid state chemistry, biology, and materials science1988.*

31. *Findenegg GH, Jaehnert S, Akcakayiran D, Schreiber A. Freezing and Melting of Water Confined in Silica Nanopores. Chemphyschem 2008;9(18): 2651-59.*

32. *Jaehnert S, Chavez FV, Schaumann GE, Schreiber A, Schoenhoff M, Findenegg GH. Melting and freezing of water in cylindrical silica nanopores. Physical Chemistry Chemical Physics 2008;10(39): 6039-51.*

33. *Gruener S, Hofmann T, Wallacher D, Kityk AV, Huber P. Capillary rise of water in hydrophilic nanopores. Physical Review E 2009;79(6).*

34. *Hall PL, Ross DK. INCOHERENT NEUTRON-SCATTERING FUNCTIONS FOR RANDOM JUMP DIFFUSION IN BOUNDED AND INFINITE MEDIA. Molecular Physics 1981;42(3): 673-82.*

35. *Price WS, Ide H, Arata Y. Self-diffusion of supercooled water to 238 K using PGSE NMR diffusion measurements. Journal of Physical Chemistry A 1999;103(4): 448-50.*

36. *Ediger MD, Harrowell P. Perspective: Supercooled liquids and glasses. Journal of Chemical Physics 2012;137(8).*

37. *Richert R. Dynamics of Nanoconfined Supercooled Liquids. Annual Review of Physical Chemistry, Vol 62 2011;62: 65-84.*

38. *Mietner JB. Visiting Nanopores : the great potential of PMOs for studying the properties of water in nanopores of different polarity. Thesis. Universität Hamburg; 2018.*

CHAPTER IV

MODULATING SURFACE INTERACTION BY CONFINING BINARY MIXTURE IN A HYBRID PORE SYSTEM WITH A HYDROPHILIC/HYDROPHOBIC SURFACE: EFFECT ON THE STRUCTURE OF BINARY MIXTURE

ABSTRACT

In the present chapter we will focus on the effect of modulating the pore surface chemistry on inducing the hypothesized formation of nanostructures within the confined binary liquids that would differ from the core-shell structure obtained in a straight cylindrical nanochannels of mesoporous silicates.

We used DVB-PMO as a host matrix to investigate the effect of tuning the surface hydrophobicity with a hydrophobic bridging units (divinyl benzene) and Tert-butanol (TBA)/Toluene (TOL) as a model mixture, fully miscible which showed an induced microphase separation (core-shell) in MCM-41 and SBA-15 mesoporous.

We have used two different techniques, first is the dynamic vapor sorption (DVS) and second is the small/wide angle neutron scattering (SANS/WANS) experiments. DVS experiments allowed us to quantify the interaction with the two mixture components and eliminate the core-shell model. SANS/WANS experiments allowed us to gather structural information by following the scattered intensity evolution with the use of isotopic contrast variation effects indicating specific TBA adsorption of the silica units.

I. INTRODUCTION:

In mesoporous silicates (SBA-15[1] and MCM-41[2, 3]), a microphase separation has been actually observed for TBA-TOL mixtures. One parameter, controlling the tendency of TBA-TOL mixtures to form such structures is the amphiphilic nature TBA, which has been also related to the formation of supramolecular clusters in the bulk.[4]

In confinement, another key parameter is the strong and specific interaction between the pore wall and the H-bonded component molecules.[5-9] Going from silica to DVB-PMO, we aimed at tuning the surface hydrophobicity with a hydrophobic bridging units (divinyl benzene) and hydrophilic silica units. Therefore, it is required to better quantify the actual interactions involved by this modulation of the surface chemistry, and link them to possible liquid nanostructures. This is one objective of the study presented in the present chapter, based on binary gas adsorption experiments following approaches successfully applied to silica.[10]

The second objective is to characterize the structure of the confined mixtures and provide a microscopic structural description. For silica pores, core-shell tubular structures were demonstrated by SANS experiments.[1, 2] The same method has been applied, as discussed in the present chapter, to search for possible new kind of nanostructuring induced by modulating the pore surface chemistry.

II. METHODS

1. Gas adsorption experiments:

1-1- Instrument and measurement conditions :

The adsorption of binary gas mixture of TBA and toluene was carried out by the VTI–SA+ Vapour Sorption instrument from TA instruments, using nitrogen as a carrier gas by admitting that nitrogen is an inert bearing gas that does not adsorb in DVB-PMO at room temperature (as it is far above the critical point).[11] Dry nitrogen gas was connected to the setup and its pressure was maintained at 1.4 bar approximately in order to create a flow of the gas from the nitrogen cylinder to the apparatus. The two liquids, TBA and toluene were used pure and mixed together in a desired ratio and filled into the dedicated reservoir. To vaporize the contained liquid, the reservoir was permanently maintained at 30°C, which was sufficient since both liquids are highly volatiles.

The pure/binary gas located in the evaporator, forming an organic vapor is mixed and carried by a flow of nitrogen gas with a partial pressure corresponding to the binary liquid saturating pressure. This saturated gas flow is mixed for a second time with a dry flow nitrogen gas in order to modulate the resulting partial pressure. The mixture of dry nitrogen and pure/binary gas was sent to the sample chamber consisting of a microbalance with two

pans, one of which contained DVB-PMO powder, while the other was left empty as a reference for measuring the change in weight of the sample.

The concentration of the organic vapor in the gas stream reaching the sample is obtained by using mass flow controllers, one for dry nitrogen and the other for nitrogen saturated with organic vapor. A drying step prior to the adsorption process was carried out, where the powder was heated to 120 °C, at a heating rate of 2°C min^{-1} under dry nitrogen flux for 120 minutes to remove any possible remaining adsorbed solvents or water inside the pores. After the drying step, a mixture of binary gas and nitrogen could be sent to the sample.

The partial pressure steps which we denote by P/P_0, where P_0 is the saturating pressure for the pure/binary gas and P is the partial pressure of the binary/ gas, were increased from 0 to 0.95 and decreased from 0.95 to 0 again during the adsorption and desorption steps, respectively. The adsorption of gas on the DVB-PMO powder was quantified at equilibrium. The equilibrium criterion in our experiments before moving on from a certain partial pressure step to the next one was a change in weight of the sample lower than 0.0010 % during at least 5 minutes. Both the sample cell and reservoir (saturator) of liquid are maintained at the same temperature (30 ◦C), with an accuracy of a few degrees. The increase/decrease in mass of the sample during adsorption/desorption respectively was recorded as percentage-change in mass of the sample and was plotted against increasing/decreasing values of P/P_0. The liquid reservoir was filled with TBA and toluene mixtures in different compositions: 100, 60, 50, 20 and 0% on TBA volume fraction. Same experiments were carried with water by using the humidity sensor shown in the setup in Figure IV-1.

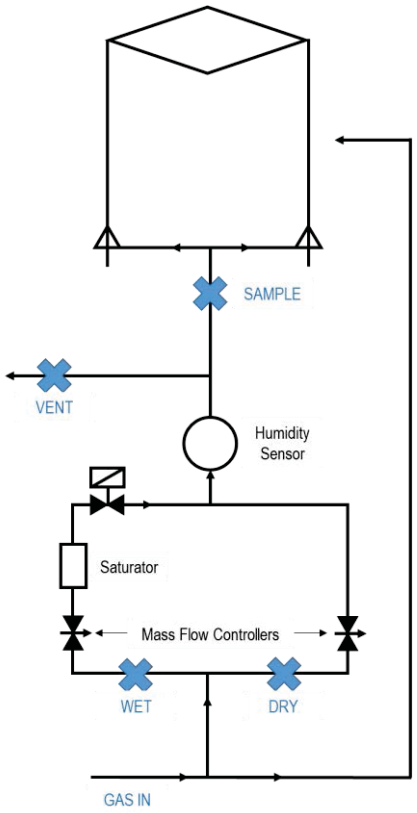

Figure IV-1: Schematic setup of vapor sorption experiment.

1-2- Multi-component BET model :

In the original work of Brunauer, Emmett, and Teller (1938), the type II nitrogen isotherms on various adsorbents was transformed to the "BET plot" using the BET equation

$$\frac{1}{N\left(\frac{P_0}{P}-1\right)} = \frac{1}{N_0\,K} + \frac{K-1}{N_0\,K}\,\frac{P}{P_0} \qquad (IV\text{-}1)$$

where N is the adsorbed amount, N_0 the monolayer capacity, $\frac{P}{P_0}$ is the relative pressure and K a BET constant which gives an indication of the order of magnitude of the attractive adsorbent–adsorbate interactions. And it was found that it presented a linearity over the approximate range $\frac{P}{P_0} = 0.05 - 0.35$. The specific surface area S_P can then be obtained from the monolayer capacity N_0 by the application of the simple equation: $S_P = a\,N_0$, where a the so-called cross-sectional area (the average area occupied by each molecule in a completed monolayer).

BET model application requires several precautions arising from the chemical and geometrical heterogeneity problems of the surface and the porosity. It appears that in the presence of micropores, the linear (BET) range is significantly shifted to lower relative pressures. Therefore, caution needs to be taken in the data selection for the surface area analysis, in which the capillary condensation rather than multilayer adsorption may take place in the above pressure region, especially for small pores (2-3 nm in diameter) or poorly ordered materials.[12, 13] Consequently, adding the capillary condensation data may lead to a significant overestimation of the monolayer capacity and obviously that of the specific surface area.

This model can be straightforwardly extended to multicomponent gases,[14] leading to the following prediction for the adsorbed average number of molecules of type i:

$$\langle N_i\rangle = N_0\,y_i\,\frac{\frac{P}{P_0}}{\left(1-\frac{P}{P_0}\right)}\,\frac{K_i\left(1-\frac{P}{P_0}\right)+K_iq_i+K_jq_j}{\left(1-\frac{P}{P_0}\right)+K_iq_i+K_jq_j} \qquad (IV\text{-}2)$$

Where i, j = 1, 2 for referring to TBA and TOL, $\langle N_i\rangle$ and K_i are respectively the average number and the BET constants of adsorbed molecules of type i. Consequently, the total number of adsorbed particles $\langle N\rangle = \langle N_i\rangle + \langle N_j\rangle$. The y_i is the ith component volume (or mole) fraction in the gas mixture which were not determined directly by experiment, but were calculated from volume fraction x_i of the liquid solution. $q_{i,j}$ is the relative partial pressure of the ith,jth component as $q_{i,j} = y_{i,j}\frac{P}{P_0}$. Since the specific surface area $S_P = 864\ m^2\ g^{-1}$ is obtained from the N_2 adsorption isotherms of DVB-PMO,[15] then we can re-write (IV-2) based on S_P and the total specific surface area of the sample and a, the average effective surface area of the adsorbing particles

$$\langle N_i\rangle = \frac{S_P}{a}\,y_i\,\frac{\frac{P}{P_0}}{\left(1-\frac{P}{P_0}\right)}\,\frac{K_i\left(1-\frac{P}{P_0}\right)+K_iq_i+K_jq_j}{\left(1-\frac{P}{P_0}\right)+K_iq_i+K_jq_j} \qquad (IV\text{-}3)$$

2. Small-Wide Angle Neutron Scattering (SANS-WANS) experiments:

2-1- Isotopic contrast method:

The scattered intensity from an assembly of nuclei is defined by the differential cross section $\frac{d\Sigma}{d\Omega}$ were $d\Omega$ is a differential solid angle and Σ is the scattering cross section, which can be written as a function of the individual scattering cross section σ of all the atoms, and their relative positions. For each isotope, σ is also related to its neutron scattering length b as

$$\sigma = 4\pi\, b^2 \qquad (IV\text{-}4)$$

Therefore, the scattered intensity is related to the scattering length of each atom composing the sample.

It's important to recall that the total scattering cross section $\frac{d\Sigma}{d\Omega}$ is a sum of coherent and incoherent scattering cross section $\frac{d\Sigma}{d\Omega_{coh}}(\vec{q})$ and $\frac{d\Sigma}{d\Omega_{incoh}}$, respectively, then $\frac{d\Sigma}{d\Omega} = \frac{d\Sigma}{d\Omega_{coh}}(\vec{q}) + \frac{d\Sigma}{d\Omega_{incoh}}$. The coherent scattering depends on $\vec{q}$ and contains structural information whereas it originates from scattering of different nuclei at the same time even so incoherent scattering contains dynamical information whereas it originates from the self-scattering of a unique nuclei at different times. Therefore, in this structural study we consider $\frac{d\Sigma}{d\Omega_{coh}}(\vec{q})$.

The relative contribution of each atom the coherent and incoherent parts of the total differential scattering cross of a sample is determined by its individual cross section : $\sigma = \sigma_{coh} + \sigma_{incoh}$. $\sigma_{coh} = 4\pi\, b_{coh}^2$, where b_{coh} is the coherent neutron scattering length which can vary between isotopes of the same atom. The most significant is the case of Hydrogen ($b_{coh}^H = -0{,}374\ 10^{-12} cm$) and its isotope Deuterium ($b_{coh}^D = 0{,}667\ 10^{-12} cm$).

This significant difference, exclusive power of neutron diffraction, allowed to create the isotopic contrast method which helps on studying complex systems by changing the contribution of one or many components by a simple adjusting contrast factor $\Delta(\rho\bar{b})$ since the scattering intensity I $\alpha\ \Delta(\rho\bar{b})^2$ where ρ is the molecular density and $\bar{b}$ is the is the sum of all the coherent scattering lengths of the atoms in the molecule and $(\rho\bar{b})$ is the molecular scattering length density. In aqueous solution of A and B, for example, replacing H_2O solvent by a H_2O/D_2O mixture with $(\rho\bar{b})_{mix} = (\rho\bar{b})_B$ to keep only the scattering coming from A.

In the case of DVB-PMO empty/filled matrix, the resulting scattering intensity

$$I = k\,[\,(\rho\bar{b})_{DVB-PMO} - (\rho\bar{b})_{Liq}]^2 \qquad \text{(IV-5)}$$

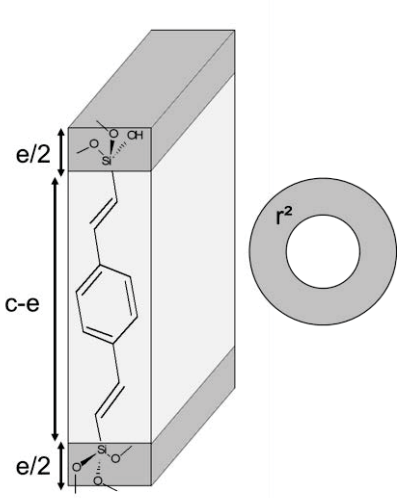

Figure IV-2: The unit cell structure that builds the pore wall of DVB-PMO. With c is its total length, e is the total length of the two silica units ($2\ x\ \frac{e}{2}$) and c-e is the length of the bridging unit. Inset: top view of the pore, showing the surface r² of the pore wall.

From Figure IV-2, which presents the unit cell structure that builds the pore wall, we can give a stoichiometry 2 and 1 to the silica units ($SiO_{1,5}$) and the bridging organic units, respectively. This allows as to calculate the DVB-PMO molecular density $\rho_{DVB-PMO}$ as a function of the number of the silica units (N_{Si}) and the bridging organic units (N_{BU}) by total volume of the unit cell $v = r^2c$

$$\rho_{DVB-PMO} = \frac{N_{Si}}{2\,v} = \frac{N_{BU}}{v} \qquad (\text{IV-6})$$

Following the same analogy, we can calculate the molecular density of the Silica unit ρ_{Si} as a function of N_{Si} by unitary volume of the silica part $v^{Si} = r^2e$

$$\rho_{Si} = \frac{N_{Si}}{v^{Si}} \qquad (\text{IV-7})$$

Then we can rewrite equation (IV-6) with replacing N_{Si} from equation (IV-7)

$$\rho_{DVB-PMO} = \frac{\rho_{Si}}{2} * \frac{v^{Si}}{v} = \frac{\rho_{Si}}{2} * \frac{e}{c} \qquad (\text{IV-8})$$

Now we just multiply the molecular scattering density of DVB-PMO $\rho_{DVB-PMO}$ by its average coherent neutron scattering length $\bar{b}_{DVB-PMO}$ to obtain the molecular scattering length density $\left(\rho\bar{b}\right)_{DVB-PMO}$ as

$$\left(\rho\bar{b}\right)_{DVB-PMO} = \frac{\rho_{Si}}{2} * \frac{e}{c} * (b_{BU} + 2\, b_{Si}) \qquad \text{(IV-9)}$$

With $\frac{e}{c}$ is the volume occupied by the silica units relative to the total pore area which is equal to 0,24 and ρ_{Si} can be calculated by developing equation (IV-9) as

$$\rho_{Si} = \frac{N_{Si}}{v^{Si}} = \frac{N_A * \rho_{Si}^{w}}{M_{Si}} \qquad \text{(IV-10)}$$

Where, N_A is the Avogadro constant, M_{Si} is the molar mass of silica unit ($SiO_{1,5}$ molecule) and ρ_{Si}^{w} is the mass density of silica units in DVB-PMO pore wall that we assume equal to that of amorphous silica in bulk (assumption often made for porous silica such as MCM-41).

Then,

$$\rho_{Si}^{w} = 2{,}2\ g\ cm^{-3}$$

Subsequently,

$$\left(\rho\bar{b}\right)_{DVB-PMO} = 19{,}12\ 10^{9}\ cm^{-1}$$

A special case is obtained when we choose an isotopic composition so that the scattering length density of the liquid becomes equal to that of the pore walls $\left(\rho\bar{b}\right)_{DVB-PMO} = \left(\rho\bar{b}\right)_{Liq} = 19{,}12\ 10^{9}\ cm^{-1}$. The liquid is then in a contrast matching condition (CM) with the matrix and the intensity is expected to vanish.

2-2- Samples preparation:

DVB-PMO of a pore diameter D=4.1nm was synthesized according to the procedure described in Chapter-I. A preliminary matrix drying was performed by heating at 120 °C under vacuum for 24h before performing experiments.

The mesoporous materials (DVB-PMO) was filled into a Hellma quartz cell of 1mm of thickness and simultaneously compacted to obtain a homogeneous dispersion of the powder in the cell with a measured amount to can determine the injected volume of liquid that completely fill the pore volume of the confinement matrix which was determined by adsorption isotherm measurements (V_P = 0,75 $cm^3\ g^{-1}$). The porous medium height in Hellma cell was between 20 and 25mm, around 3 time larger than the diameter of the neutron beam (7.6mm).

Table IV-1: different binary mixture samples studied and their corresponding H/D compositions

	Volume fraction (%)	*Volume injected (µL)*	$\left(\boldsymbol{\rho\bar{b}}\right)_{\boldsymbol{Liq}}$
TBAD/TOLH	20/80	7.67	20.15
TBAH/TOLD	62/38	9.71	19.90

TBA/TOL was the binary system studied in this work with two samples with one component deuterated and the second hydrogenated each prepared with a specific H/D composition so that the total scattering length density be equal to that of DVB-PMO (i.e. in CM condition with the matrix). It was then injected into porous medium with the adequate volume amount. Table IV-1 illustrates the different binary mixture samples studied and their corresponding H/D compositions, their injected volume amount and their scattering length density.

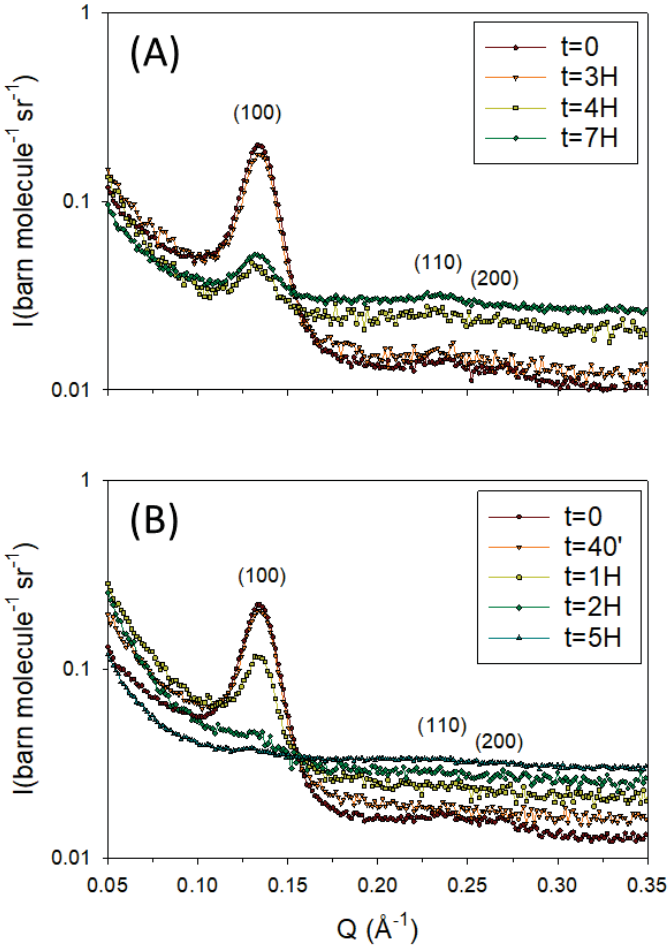

Figure IV-3: Evolution of the scattered intensity of DVB-PMO filled with (A) TBAD/TOLH and (B) TBAH/TOLD in contrast matching condition with a volume fraction of 20/80 and 62/38, respectively, as a function of time.

Immediately after the injection of liquid into the empty matrix, the imbibition kinetics were followed through the variation in the measured intensity with time at room temperature. Figure IV-3 shows the evolution for contrast matched TBAH/TOLD mixture versus time. As observed in the figure, the adsorption of the liquid in DVB-PMO and the filling of the pores over time is accompanied by a fast decrease in the Bragg intensity to a stable value reached after 4 to 5h indicating that the density in the pores has reached a state of equilibrium corresponding to the complete filling of the pores.

2-3- Measurements and data treatments:

SANS/WANS experiments were performed on the high resolution diffractometer D-16 at the Institut Laue Langevin in Grenoble-France with a resolution provided by a $\Delta\lambda/\lambda = 0.01$. The measurement was conducted at a wavelength $\lambda = 4.51$ Å. A sample to detector distance of 900 mm was employed using three detector angles at 11°, 24°, and 45°, giving rise to a Q range of 0.05−1.26 Å^{-1} devised on 3 regions as presented in Table IV-2. The momentum transfer Q is defined as

$$Q = \frac{4\pi}{\lambda} sin(\theta/2) \qquad \text{(IV-11)}$$

where θ is the scattering angle and λ is the incident neutron wavelength.

The data treatment was done with LAMP,[16] the spectra were corrected from the empty cell contribution (transmission corrections), normalized to the right amount of DVB-PMO and corrected for detector efficiency (through the normalization to a constant incoherent diffuser: H_2O) to eventually obtain intensities in absolute units.

Table IV-2 The three regions of the scattering angle θ and momentum transfer Q.

	θ (deg °)	***Q (Å^{-1})***
Fist Detector (11°)	2 - 20	0.05 – 0.48
Second Detector (24°)	19 - 37	0.46 – 0.88
Third Detector (45°)	36 - 54	0.86 – 1.26

III. RESULTS AND DISCUSSION

1. Gas adsorption experiments:

Figure IV-4 shows a complete cycle of adsorption and desorption, proof of a highly ordered DVB-PMO matrix. The two branches of adsorption and desorption are almost completely superposed with small hysteresis before reaching a plateau at high pressure as shown by a double arrow for pure TBA curve. To simplify our analysis, only the adsorption branch will be discussed below.

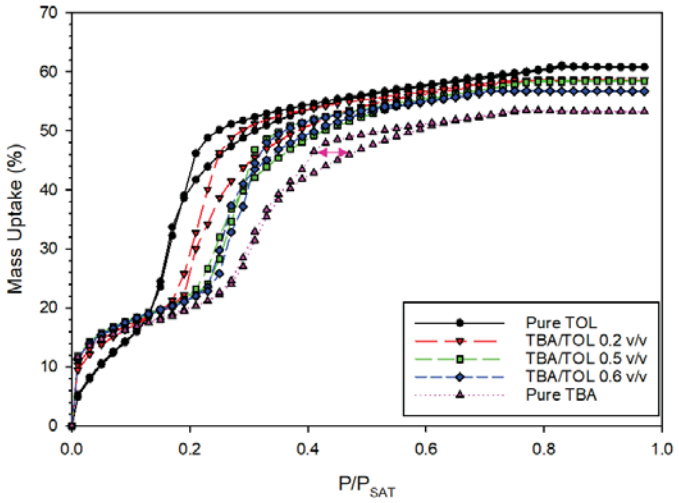

Figure IV-4: Vapor sorption isotherms (adsorption and desorption branches) of TBA/TOL mixtures in DVB-PMO measured at 30 ◦C for different volume fractions from pure toluene to pure TBA (magenta). The small hysteresis between the two branches of adsorption and desorption is shown by a double arrow only for pure TBA.

A common three regions can be distinguished from all adsorption isotherms presented in Figure IV-5. The first region, is that of low partial-pressure with $^{P}/_{P_{SAT}} \leq 0.1$ characteristic of formation of few first adsorbed gas monolayers which present about 20% weight increase of the powder. By the condensation beginning of the adsorbed gas molecules into liquid, a step-rise of mass uptake is occurred marking the second region of isotherm. The third region is determined by reaching a plateau beyond which the weight of the porous powder does not increase any more owing to completely filled pores. Next step will be dedicated to the study of the three regions separately.

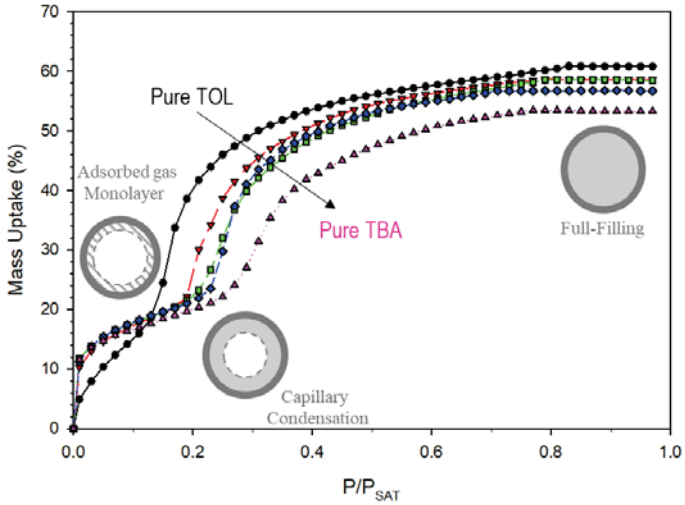

Figure IV-5: Vapor sorption isotherms (adsorption branch) of TBA/TOL mixtures in DVB-PMO measured at 30◦C for different volume fractions from pure toluene (black) to pure TBA (magenta) following the arrow direction. Three regions can be distinguished from all.

1-1- Low partial pressure region :

As discussed above, the treatment of adsorption data at low pressures could be performed with the BET model extended to multicomponent gases based on the expression (IV-13) to express the % mass uptake

$$\langle \%mass\ uptake \rangle = \frac{100}{\mathcal{N} w_m} \left(M_i \langle N_i(a, y_i, K_i) \rangle + M_j \langle N_j(a, y_j, K_j) \rangle \right) \quad (IV\text{-}12)$$

Where i, j = 1, 2 for referring to TBA and TOL, $N_{i,j}$, $y_{i,j}$, $M_{i,j}$ and $K_{i,j}$ are respectively the average number, volume (or mole) fraction in the gas, the molecular weights and the BET constants of adsorbed molecules of type i and j. $\mathcal{N}$ is the Avogadro number ($6.023e^{-23}$ mol^{-1}) and w_m is the empty matrix weight.

Figure IV-6, shows the best fits of experimental points in the adsorption isotherm (symbols) by equation (IV-13) with fixing the value of S_P to 864 $m^2\ g^{-1}$ and taking a single set of K_i and K_j respectively obtained from the fit of pure TBA and pure TOL adsorption isotherms and then fixed to fit all curves. The effective molecular area a is adjusted for each concentration and it takes different value.

The best fit of the curves gives a set of BET constants K_{TBA} and K_{TOL} plotted in Figure IV-7-(A) and average molecule area a for each TBA/TOL mixture plotted in Figure IV-7-(B) as a function of TBA fraction in the liquid mixture called $x^{In\ mixture}$. We find that K_{TBA} is 10 time larger than K_{TOL}. This indicates a much higher thermodynamic affinity of DVB-PMO to TBA molecules compared to TOL. The values of BET constants K_{TBA} and K_{TOL} obtained from[10] for MCM-41 are presented on the same graph to investigate the effect of surface chemistry on thermodynamic affinity to adsorbed molecules.

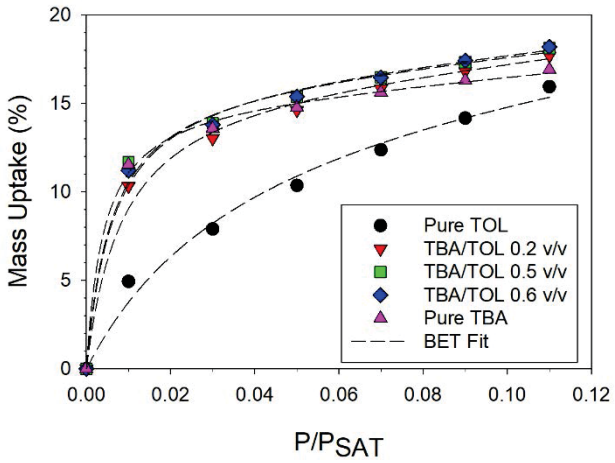

Figure IV-6: Multi-component BET fits (dashed lines) of adsorption isotherms (symbols) for $P/P_{SAT} \leq 0.12$ at different TBA/TOL mixtures.

We found that the affinity of TBA is 10 times more important to MCM-41 compared to that of DVB-PMO, while we keep the same tendency towards toluene molecule with a very close BET constant. This is consistent with the hypothesis which assumes that interactions

between TBA molecules and pore surface are insured by H-bond with the silanol groups. Hence, it is obvious that $K_{TBA}^{DVB-PMO} \ll K_{TBA}^{MCM-41}$ since the surface of DVB-PMO has a lower number of adsorption sites (lower density of silanol groups) than the surface of MCM-41 for equivalent pore sizes.

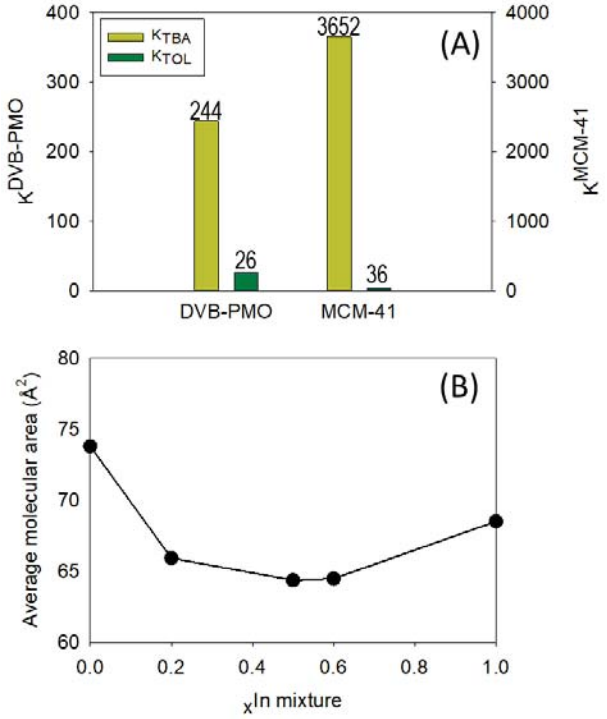

Figure IV-7: A) Best fit values of BET constants K_{TBA} and K_{TOL} for TBA/TOL mixtures in DVB-PMO (obtained from this work) and in MCM-41 (obtained from[10]). (B) Best fit values of the effective molecular area versus TBA composition of the liquid mixture in the reservoir ($x^{In\ mixture}$).

The effective BET molecular area as a function of $x^{In\ mixture}$ is shown in Figure IV-7-(B) it is higher at very low TBA concentrations, where toluene is dominant, and decreases with TBA concentration however it makes a jump at the highest concentration of TBA. We reach here the limits of the simple BET approach, which relates a low density of adsorption sites to a high effective molecular area. Hence, a possible densification of the molecular layer due to specific interactions between neighboring adsorption sites is not taking into account. Also the proposed multi-component BET model does not take into consideration any molecular interactions difference between the two components, while this is the case for TBA with H-bond interactions and TOL with a mix of van der Waals and aromatic potential interactions.

Another evidence of the high affinity of pore surface to TBA molecules can be obtained from Figure IV-8 which present the composition of the first monolayer formed on DVB-PMO pore surface against TBA fraction in the liquid mixture ($x^{In\ mixture}$): from a TBA concentration $x^{In\ mixture} = 0.2$, the first adsorbed monolayer is almost saturated with TBA (>80%).

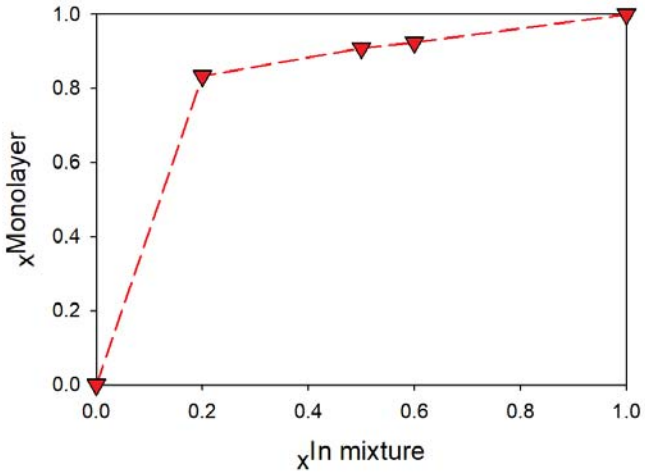

Figure IV-8: Composition of the first monolayer ($x^{Monolayer}$) versus the composition of liquid mixture in the reservoir ($x^{In\ mixture}$) on TBA.

1-2- Capillary condensation region :

After building the first monolayer at low partial pressure, the number of adsorbed molecules continue on growing up with the gradual increase of gas partial pressure. This ensures a progressive building of the adsorbed film which maintains in equilibrium with the gas flow around it. However, as the film gets thicker, it loses its thermodynamic equilibrium, leading to a more favorable physical state by condensation.

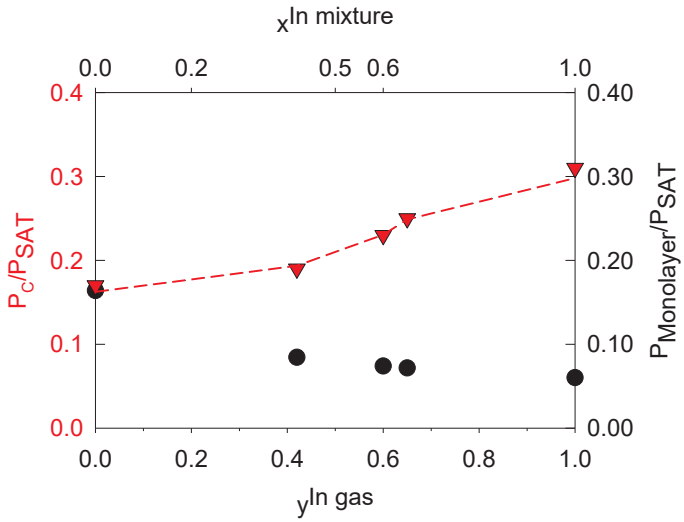

Figure IV-9: Experimental relative partial pressures of TBA/TOL mixtures in DVB-PMO at the capillary condensation Pc/P_{sat} (red symbols) and monolayer formation $P_{Monolayer}/P_{sat}$ (black symbols) versus TBA composition of the gas ($y^{In\ gas}$) or liquid ($x^{In\ mixture}$) solution. The solid line is the best fit according to the modified Kelvin equation (IV-14).

This phase transition generates a liquid inside the pores leading to a sharp increase in the weight of the sample characteristic of this region (see Figure IV-4). This capillary condensation step is linked to a particular pressure value; we denote it as the capillary condensation pressure P_c. We present in Figure IV-9 the P_c/P_{sat} at different TBA composition in the gas phase ($y^{In\ Gas}$) and their corresponding $x^{In\ mixture}$ values to found that this pressure increase with increasing TBA concentration on the binary mixture. On the same graph, we have added the partial pressure at which the first monolayer was formed which we called P_{mono}/P_{sat}.

We find by calculating the pressure ratio $P_c/P_{monolayer}$, that the capillary condensation pressures are higher than that of monolayer formation (pressure ratio>2), giving a clear indication that capillary condensation does not occur directly after monolayer formation except in the case of pure toluene where $P_c/P_{monolayer}\approx1$ as shown in Figure IV-10 with black symbols. The mass uptake ratio of the capillary condensation on the mass uptake at the monolayer formation variates between 1,5 to 2 which is considered as a second indication that capillary condensation occurs after the monolayer formation.

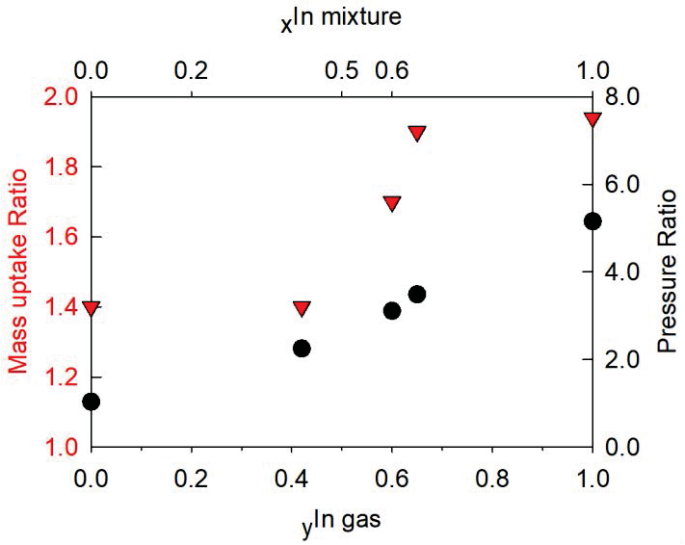

Figure IV-10: The Ratio of the mass uptake uptake at capillary condensation and the mass at the monolayer formation (Red symbols and right axis) and the ratio of the pressure at the monolayer formation and pressure at capillary condensation (black symbols and left axis) for different TBA composition of the liquid solution ($x^{In\ mixture}$).

The capillary condensation relative pressure within cylindrical nanopores can be related to the bulk liquid surface tension at the liquid–gas interface σ_{lg} through an alternative expression of the Kelvin equation proposed by Celestini[17] and Pellenq et al.[18]

$$\frac{P_C}{P_{sat}} = exp\left(-\frac{\sigma_{lg}}{k_B\,T\,\rho\,(R_p-\delta)}\right) \qquad \text{(IV-13)}$$

where P_C is the capillary condensation partial pressure of the adsorbing gas, R_p is the pore radius, δ is a correction term to take into account the adsorbed film thickness t and some nanometric length measuring the correlation between the solid–film and film–gas interfaces

λ and ρ is the number density of the adsorbed film related to mass density ρ_m and molar mass M by $\rho = \frac{N}{M}\rho_m$.

The surface tension σ_{lg} and number density ρ values of bulk liquid mixtures of TBA composition $x^{In\ mixture}$ at 30°C were used along with known radius of DVB-PMO pores ($R_p = 2{,}05$ nm known by DFT) keeping only the term δ as the adjustable parameter. The best fit presented in Figure IV-9 with red dashed line is obtained for δ = 1,45 nm. This value was slightly higher than what was obtained for MCM-41 matrix (pore diameter d=3,4 nm known by N_2 sorption) were δ=1,14 nm.[10] This amounts to saying that at capillary condensation only 65% of the pore volume is occupied by vapor and with the comparison made with MCM-41, we saw that this percentage is almost the same. Although this method succeeds in providing us with the value of δ, which is quite comparable to the literature, it remains unable to provide any indication on the relative contributions of the film thickness t and the correlation length λ which leads us to rely on assumptions.

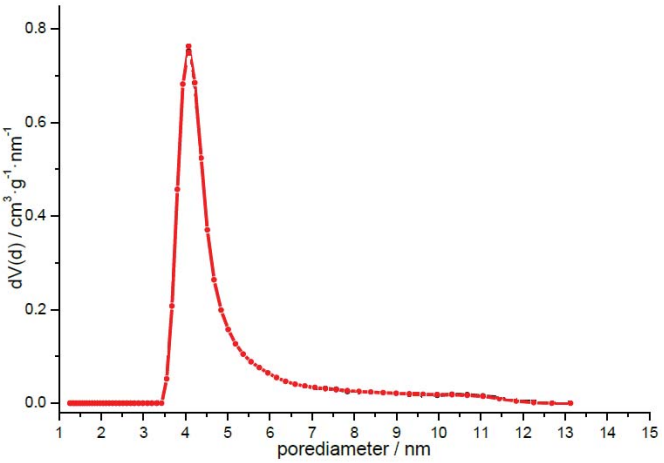

Figure IV-11: NLDFT pore size calculation of the of the DVB-PMO materials.[15]

First is assuming that at capillary condensation two monolayers are adsorbed, then $t \approx 0.9$ nm, subsequently $\lambda \approx 0{,}55$ nm. This may simply be related to the uncertainties on the pore size of DVB-PMO (i.e. uncertainties of the N_2 sorption technique itself, based on the volume occupied by nitrogen molecules while TBA and TOL molecules are more voluminous, or to uncertainties related to the pore size distribution as show the Figure IV-11).

If we neglect all uncertainties related to R_p, the obtained $\lambda \approx 0{,}55$ nm is relatively higher to what was obtained for MCM-41 ($\lambda \approx 0$) by taking the same t value.[10] This difference may be interpreted by the fact that pore wall surface is not isolated with a well building TBA monolayer however it still containing some available adsorption sites giving the possibility of making interactions with incoming molecules which is completely opposite to MCM-41 case.

An explanation for this may be the presence of organic units with a lower interaction with TBA molecules (comparing to H-bonds created with silica units) which present a 'door' allowing the access of vapor molecules. Second is assuming that at capillary condensation three monolayers are adsorbed, then λ would be close to zero which amounts to saying that the surface of DVB-PMO is isolated by a wall of 3 monolayers. This second assumption is less reasonable, because the mass uptake at the capillary condensation is much less than that of 3 monolayers howbeit, it corresponds, approximately, to 2 monolayers (see Figure IV-10).

1-3- High partial pressure region:

At high partial pressures, the adsorption curves reach a plateau implying that the pores are completely filled with a binary mixture of TBA and TOL. The final mass of the adsorbed material at a TBA composition $x^{\text{In mixture}}$, $w_f(x^{\text{In mixture}})$ can be related to the final composition x^{Final} of the liquid filling the pore as

$$x^{Final} = \frac{w_f\left(x^{In\ mixture}\right) - w_f\left(x^{In\ mixture}=0\right)}{w_f\left(x^{In\ mixture}=1\right) - w_f\left(x^{In\ mixture}=0\right)} \qquad \text{(IV-14)}$$

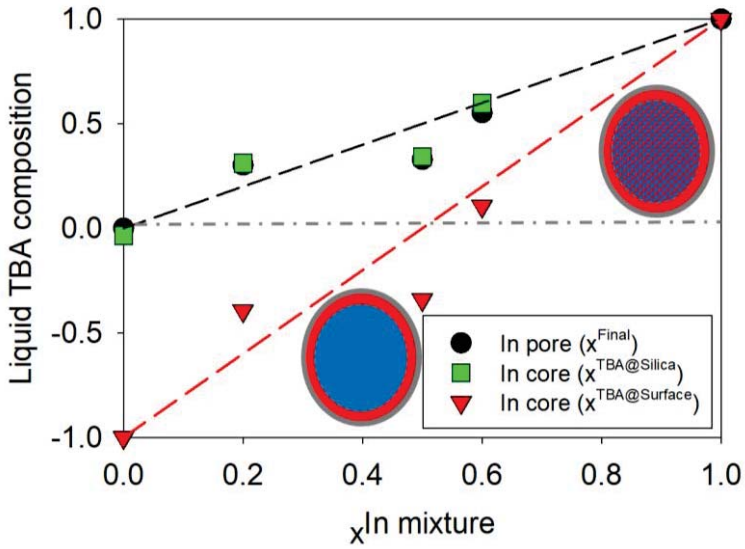

Figure IV-12: Final composition x^{Final} of the liquid filling the pore at high pressure versus the original composition $x^{In\ mixture}$ (black circles). The red down-triangles show the deduced composition on TBA of the liquid in the core of the pore within the frame of a monolayer of core-shell model (TBA adsorbed at all the pore surface) $x_{core}^{Core-Shell\ Model}$. The green squares show the deduced composition on TBA of the liquid in the core of the pore within the frame of a monolayer of TBA adsorbed, only, at Silica groups model $x_{core}^{TBA@Silica}$. The black dashed line indicates the composition of the original liquid mixture, and the red dashed line is a guide to the eye to follow the average pace of the red curve. Dash dotted line indicates the limit of physical deduced composition of the liquid with positive values; below this line, the initial TBA composition is not sufficient to form a monolayer of TBA over the entire surface (the core contains only toluene (blue for TOL) as shows the sketch). In return, above this line, with the initial TBA composition we can create a core shell structure with a positive composition on TBA in the core (as shows the sketch (red for TBA)).

Figure IV-12, shows the variation of x^{Final} as a function of $x^{In\ mixture}$ (black dots). We notice that its volume fraction inside the pore is almost equal to its corresponding composition in the mixture at liquid state (following the black dashed line) which is equivalent to say that the surface effect on the mixture demixing is not too strong. This was not the case for MCM-41 matrix, as presented in Figure IV-13, where the final average composition in the pore deviates from the initial mixture composition (black dots vs dashed line) indicating that there is a strong mixture demixing in the pores. This difference, which was interpreted by the strong affinity between MCM-41 surface and TBA molecules via H-bond interactions, was significantly reduced by using the core-shell model (red dots vs dashed line).

This is the reason why we tried to apply this model (core-shell) to our data and we calculated its corresponding composition of the core $x_{core}^{Core-Shell\ Model}$ by the following equation:

$$x_{core}^{Core-Shell\ Model} = \frac{x^{Final} - \Phi_{Monolayer}^{TBA@Surface}}{1 - \Phi_{Monolayer}^{TBA@Surface}} \qquad \text{(IV-15)}$$

With $\Phi_{Monolayer}^{Core-Shell\ Model}$, is the volume fraction of pore occupied by the shell (a monolayer of TBA of a thick E=D_{TBA}=0,43 nm) calculated as:

$$\Phi_{Monolayer}^{TBA@Surface} = 1 - \left(\frac{R_p - E}{R_p}\right)^2 \approx 0.37 \qquad \text{(IV-16)}$$

The calculated $x_{core}^{Core-Shell\ Model}$, presented with red symbols in Figure IV-12, deviates completely from physical meaning by obtaining negative values. This is quite expected since the core-shell model assumes the presence of strong interactions between the DVB-PMO surface and TBA molecule, which is not the case due to the low number of silanol groups which ensure strong H-bonds interactions.

Hence, we proposed an alternative model of TBA@Silica (a monolayer of TBA adsorbed, only, at Silica groups), and we calculated its corresponding composition of the core by the following equation:

$$x_{core}^{TBA@silica} = \frac{x^{Final} - \Phi_{Monolayer}^{TBA@Silica}}{1 - \Phi_{Monolayer}^{TBA@Silica}} \qquad \text{(IV-17)}$$

With $\Phi_{Monolayer}^{TBA@Silica}$, is the volume fraction of pore occupied by the monolayer of TBA adsorbed at Silica groups with a thickness D_{TBA}=0,43 nm) which can be related to $\Phi_{Monolayer}^{Core-Shell\ Model}$ by the following relation:

$$\Phi_{Monolayer}^{TBA@Silica} = \frac{\%Silica\ in\ Surface}{100}\ x\ \Phi_{Monolayer}^{Core-Shell\ Model} \qquad \text{(IV-18)}$$

with $\%Silica\ in\ Surface$ is the percentage of area occupied by silica groups relative to the total pore area which is calculated, from the length of silica group, that we denote e, and

the length of the regular unit that composes the DVB-PMO pore wall, that we denote c, by the relation

$$\%Silica\ in\ Surface = \frac{e}{c}\ x\ 100\ \approx 24\%$$

Thus,

$$\Phi_{Monolayer}^{TBA@Silica} \approx 0.1$$

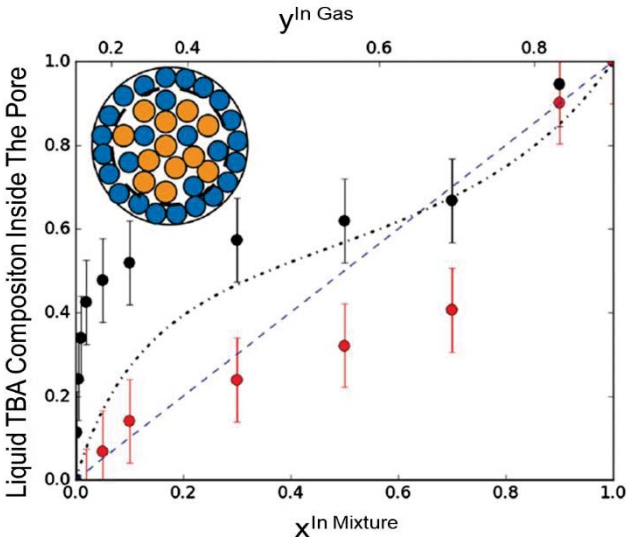

Figure IV-13: Final TBA composition of the liquid inside the MCM-41 pores after capillary condensation versus the original composition $x^{In\ Mixture}$ (black circles). The red circles show the deduced composition of the liquid in the core of the pore within the frame of a core–shell model (with only TBA at the surface). As a guide to the eye: the dashed line indicates the composition of the original liquid mixture, and the dash-dotted line indicates the composition of the gas phase. Inset: Scaled schematic representation of the completely filled MCM pore in the frame of a core–shell model with blue to indicate tert-butanol molecules and orange for toluene ones.

The calculated $x_{core}^{TBA@silica}$, presented with green symbols in Figure IV-12, superposes with the final composition x^{Final} of the liquid filling homogenously the pore. This means that, in the case of the TBA@Silica model, the mixture in the core is relatively homogeneous and that the number of silica groups in DVB-PMO surface (only 24%) can't assure a significant demixion. This makes quite difficult to distinguish between the TBA@Surface model and the homogeneous model with the gas sorption technique, however it allows us to eliminate the core-shell model which is an interesting result showing the high effect of surface interaction on the liquid structure.

1-4- Conclusion:

The vapor sorption method allowed us to quantify the interactions of the DVB-PMO matrix with TBA and TOL molecules. The different information that was been obtained

using this technique, provides a better idea on the confinement effect on the nano-structuration of the mixture. Indeed, the fit of the low partial region of different adsorption isotherms with the multi component BET model (shown in Figure IV-13) gave us a set of BET constants K_{TBA} and K_{TOL} which indicate the magnitude of pore surface/ TBA and TOL interactions, respectively. We have found that K_{TBA} is 10 times larger than K_{TOL}, which indicates a much higher thermodynamic affinity of DVB-PMO surface to TBA molecules compared to that of TOL.

Additionally, we showed the effect of surface chemistry on the thermodynamic affinity to adsorbed molecules by comparing DVB-PMO results with those obtained with MCM-41 matrix. We found that the affinity of MCM-41 to TBA molecules is 10 times more important to that of DVB-PMO (clear in Figure IV-7-(A)). We interpreted this result by the fact that interactions between TBA molecules and pore surface are insured by H-bond with the silanol groups and since the surface of DVB-PMO contains a small number of silanol groups (only 24% of the total surface) then its interaction with TBA would be lower. However, this low adsorption sites are sufficient to insure the creation of a high saturated 1st monolayer on TBA (> 80%). At the capillary condensation, the mass uptake is approximately twice of that at the monolayer formation, which indicates that the adsorbed layer at P=Pc is composed, at most, of two monolayers (referring to Figure IV-10). The fit of Pc/PSat with the modified Kelvin equation (IV-14), provides a $\delta = t + \lambda = 1{,}45$ nm.

If two monolayers are adsorbed, which is best consistent with mass uptake increase, then t≈0,9 nm, subsequently λ≈0,55 nm. Assuming λ≈0 nm implies that three monolayers are adsorbed at Pc, which is unlikely, because the corresponding mass uptake would be inconsistent with the adsorption isotherm. Apart from the possible origin due to the uncertainties on the exact value of R_p, which cannot be totally excluded, a possible interpretation of λ≈0,55 nm is that on approaching Pc, the pore wall surface is not isolated from the gas by the formation of a homogeneous molecular film. A reason for that is the presence of organic units, with a lower interaction with the adsorbed molecules, thus creating a 'door' allowing the access of vapor molecules to the pore surface which increases the correlation length between different interfaces.

At high pressure region (at the saturation), we have calculated x^{Final}, the average composition of the mixture filling the pore, which compared rather well with the initial composition of the liquid mixture in the evaporator. We also evaluated the composition in the core of the pore in the case of two inhomogeneous structures having the same average composition as the experimental one: first is the core-shell model, which considers that a monolayer of pure TBA is adsorbed over the entire pore surface. The second case is the TBA@Silica model, which considers that the TBA monolayer is only adsorbed on the silica units and the rest of the mixture is homogeneously distributed all-over the pore.

We find that the mixture in the TBA@Silica model cannot be distinguished from the totally homogeneous case under the experimental conditions of this study (pore size, composition, bridging-unit size). In particular, this is due to the low number of adsorption sites of silica groups in the DVB-PMO surface (only 24%), as situation that is radically from MCM-41 matrices where a total core-shell structure was observed. This makes quite difficult to distinguish between the TBA@Surface model and the homogeneous model with the gas sorption technique, however it allows us to exclude the core-shell model. In order to better understand the nanostructuring structure of mixture into DVB-PMO nanopores, we

performed SANS/WANS experiments (method details are described in the paragraph 'METHODS'), which will make the subject of the next part.

2. SANS / WANS experiments:

2-1- Filling Effect on Bragg peak intensities:

In the small Q range, the structure factor of empty DVB-PMO shows three Bragg peaks with Miller indexes (100), (110), and (200) as shown in Figure IV-14.

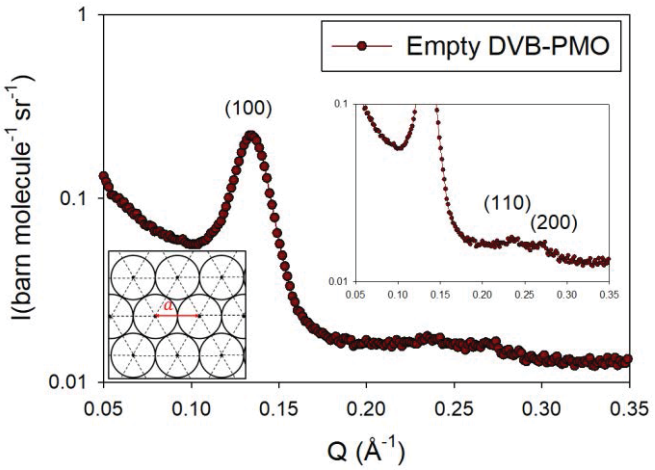

Figure IV-14: The scattered intensity of empty DVB-PMO at low Q region which shows the 3 Bragg peaks corresponding to the hexagonal arrangement of the pores. Inset at lower left of the figure: interplanar distance a between two neighboring pores.

These peaks correspond to the organization of the pore channels in hexagonal lattice. Their Bragg peak positions Q_{hk} is obtained by

$$Q_{hk0} = \frac{4\pi}{\sqrt{3}\,a}\sqrt{h^2 + k^2 + hk} \qquad \text{(IV-19)}$$

With a is the unit cell distance which is related to the center-center distance of two neighboring pores and directly related to the most intense peak (10) as

$$a = \frac{4\pi}{\sqrt{3}\,Q_{100}} = 53.74\text{Å} \approx 5.4nm \qquad \text{(IV-20)}$$

The theoretical positions of the three Bragg peaks are compared to experimental ones in the Table-IV-3.

Table IV-3: Theoretical and experimental positions for the three Bragg peaks.

$Q_{hk0}(Å^{-1})$ \ (hk0)	(100)	(110)	(200)
Theoretical	0.135	0.234	0.270
Experimental	0.135	0.240	0.270

It is noted that the intensity of the Bragg peaks decreases with Q. We interpret this by the fact that at higher distance, a structural disorder in the hexagonal network of DVB-PMO shows-up, releasing the Bragg peak intensity till their distinction. This limits the (hk0) peaks' number to only 3.

In addition to the characteristic hexagonal peaks, DVB-PMO reveals a supplementary Bragg peak (002) at Q_{002}=1,05 $Å^{-1}$, as shown in Figure IV-15. This peak characterizes the regular modulation of silica and divinyl benzene units along the pore axis a unique feature of the PMO family. The (002) Bragg peak offers a direct access to the length c of the unit cell that composes the pore wall of DVB-PMO (as shown previously in Figure IV-2) by:

$$c = \frac{4\pi}{Q_{002}} = 11.9\ Å \approx 1.2\ nm \qquad \text{(IV-21)}$$

By comparing with the results obtained from XRD experiments (Figure IV-16), we find that we miss the peak (001) although the peak (002) is clearly visible. This is quite confusing, because, according to the explanation we did above, the peak (002) should be less intense than the (001) one. The possible explanation that we propose, is that in neutrons the molecular form factor falls to zero (or is very weak) at Q_{001}, contrary to X-ray form factor.

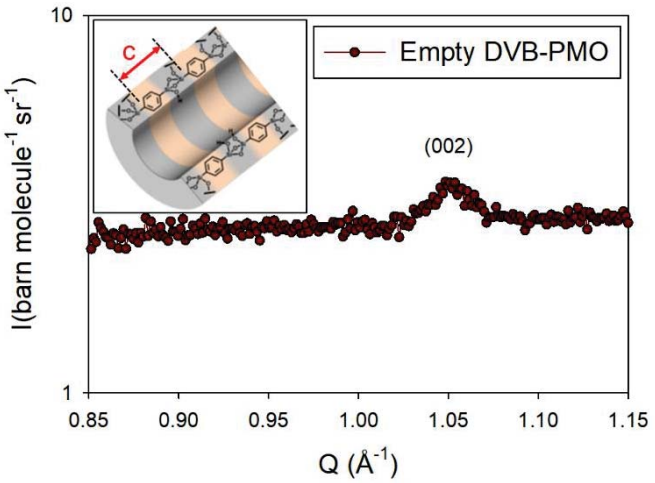

Figure IV-15: The scattered intensity of empty DVB-PMO at high Q region which shows the (002) Bragg peaks corresponding to lateral arrangement of the pore. Inset at upper left of the figure: the repeating unit (composed by silica and DVB units) length c.

Now, since we have identified the different Bragg peaks of empty matrix, we will study the filling effect on their behavior. Indeed, filling the empty DVB-PMO does not change the position of the different Bragg peaks but only their intensity due to the contrast effect. According to the equation (IV-5), defined later in SANS/WANS Methods paragraph, we are able to estimate the intensity variation as a function of the isotopic mixture composition.

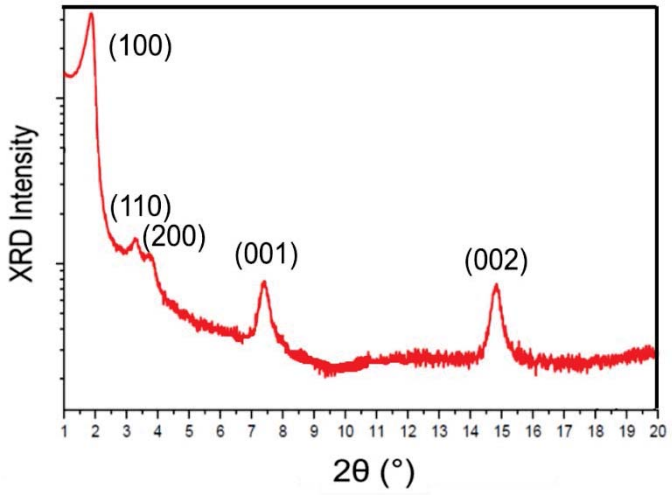

Figure IV-16: XRD patterns of the DVB-PMO. It shows three (hk0) and two (00l) Bragg peaks.

We have chosen to use two different binary mixtures which we have presented in Table-1. The first one is composed of hydrogenated tert-butanol and deuterated toluene (TBAH/TOLD) and the second one of deuterated tert-butanol and hydrogenated toluene (TBAD/TOLH) with the scattering length densities of both mixtures is almost equal to that of pore wall of DVB-PMO $\left(\rho\bar{b}\right)_{DVB-PMO} = 19{,}12\ 10^{9}\ cm^{-1}$ (calculated earlier). Since the two binary mixtures are in a contrast matching condition (CM), we aim to study the contrast effect by comparing the experimental scattered intensity of the filled DVB-PMO to that of empty matrix.

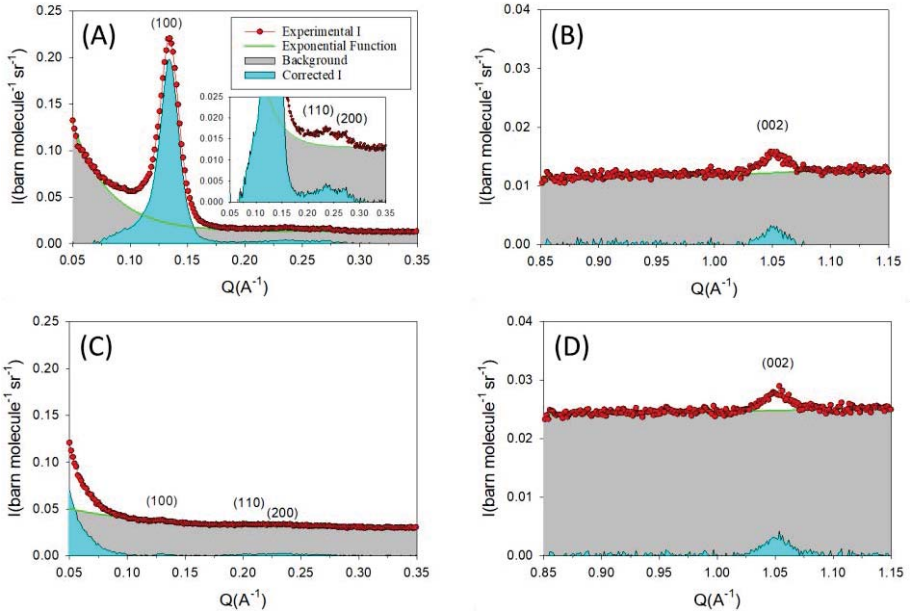

Figure IV-17: The background corrected intensity of empty (upper panels) and filled DVB-PMO with (CM) TBAH/TOLD (lower panels). The three Bragg peaks (100,110,200) at the low Q region of both mixtures are presented in left panels and the (002) Bragg peak of the high Q region are presented in the right panels.

In order to get a better comparison, we have, first of all, correct the background with a decreasing exponential function. The correction was done using Sigmaplot software where the position, width, and height of the peaks were kept free. The use of this functional form to describe the background is not theoretically motivated. It was chosen as it performed well compared to others, such as Porod or Guinier's laws. The raw experimental data, best fits and background corrected data are plotted in Figure IV-18 for DVB-PMO empty and filled with TBAH/TOLD and, in Figure IV-19 for DVB-PMO empty and filled with TBAD/TOLH.

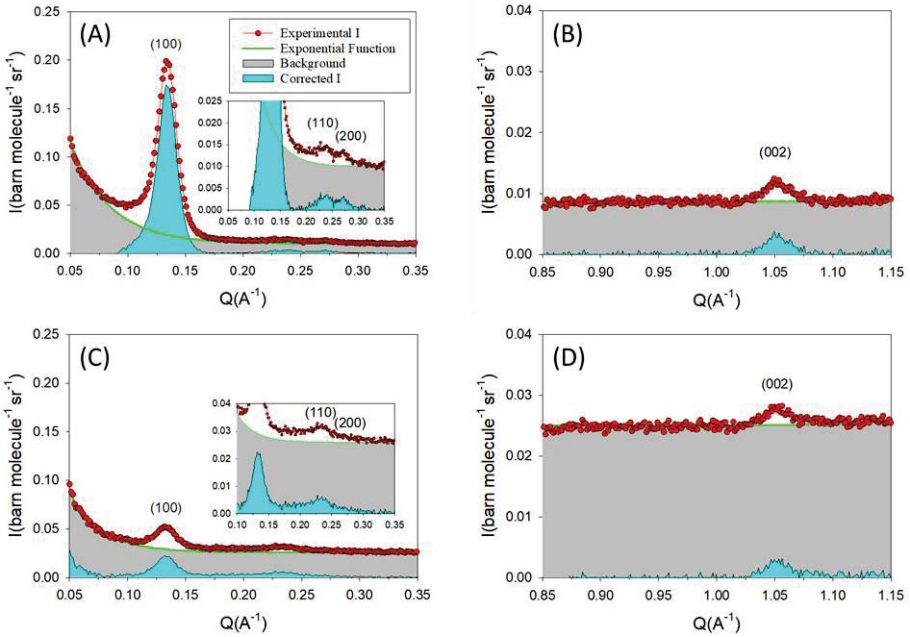

Figure IV-18: The background corrected intensity of empty (upper panels) and filled DVB-PMO with (CM) TBAD/TOLH (lower panels). The three Bragg peaks (100,110,200) at the low Q region of both mixtures are presented in left panels and the (002) Bragg peak of the high Q region are presented in the right panels.

In Figure IV-19, we summarize the filling effect on the corrected intensity. The figure shows that no Bragg peak extinction is observed in the case of the contrast matched binary mixtures. In contrary, the peak intensity (110) of DVB-PMO filled with the D/H mixture is even higher than that of the empty matrix and almost constant with H/D mixture. Moreover, there is a significant difference in the intensity modulation between the two mixtures as shown in Figure IV-20, in fact the 1st peak vanishes, almost completely in the case of H/D mixture (ratio≈100) while it persists in the case of D/H mixture (ratio≈10). The 2nd peak decreases in the case of H/D mixture (ratio≈2) while it increases in the case of D/H mixture (ratio≈0.6). A strong increase in the 3rd in the case of D/H mixture (ratio≈10) however it is almost constant in the case of H/D mixture (ratio≈1). Concerning the 4th no effect is observed in both mixtures.

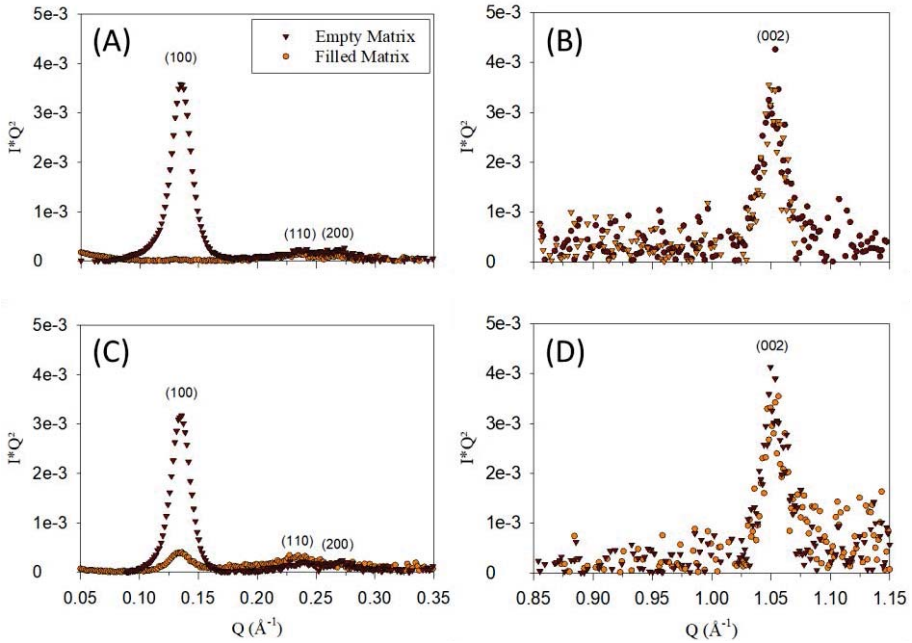

Figure IV-19: The intensity of empty and filled DVB-PMO with (CM) TBAH/TOLD (upper panels) and with (CM) TBAD/TOLH (lower panels). The three Bragg peaks (100,110,200) at the low Q region of both mixtures are presented in left panels and the (002) Bragg peak of the high Q region are presented in the right panels.

This observation is quite remarkable because it provides a direct evidence that the binary mixture does not homogeneously fill the pores. Furthermore, it indicates the existence of a heterogeneous distribution of the concentration of the mixture, which is at the origin of the form factor modulation. In reference to other works, which were interested on studying the same system confined in MCM-41[2] and SBA-15[1], similar observations have been interpreted by the nanosegregation of TBA to the pore surface leading to a core-shell structure.

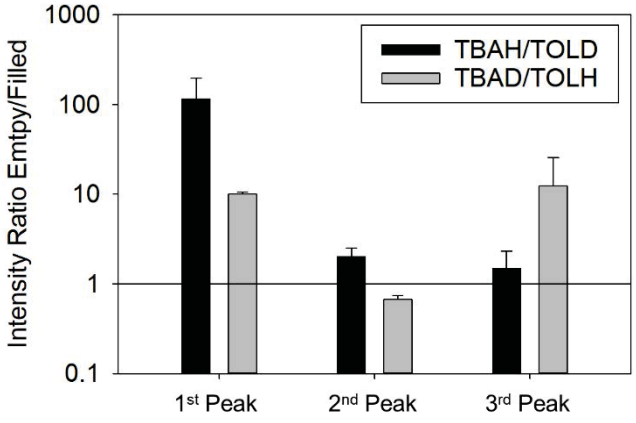

Figure IV-20: The ratio of Empty/Filled intensities of the 3 Bragg peaks (100),(110) and (200), consecutively. The vertical bars describe the intensity ratio of DVB-PMO filled with TBAH/TOLD mixture (Black) and with TBAD/TOLH (Grey).

The aim of the latter is to reveal the effect of changing the surface chemistry, more specifically in the case of DVB-PMO modulating the surface interaction along the pore axis, on the nature of the nano-structuring in confinement to see how well the core-shell structure can be linked to the presence of H-bonding elements and reveal, if it exists, the difference between the behavior of TBA/TOL mixtures in silica and organosilicas mesopore. To achieve this target, we have developed a theoretical model, described in the following paragraphs, to predict quantitatively the Bragg peak intensity for a different conceived models with diverse structures in order to estimate how the radial and lateral concentration is distributed within the pores.

2-2- Theoretical model development:

The intensity measured by neutron scattering is proportional to the product of the form factor $F(Q)$ of the object (pore) and the structure factor $S(Q)$ (pore distribution) using the formula

$$I(Q) = K\, S(Q)\, |F(Q)|^2 \qquad \text{(IV-22)}$$

where K is a constant normalization term.

The structure factor S(Q), for a perfect 2-D hexagonal array of cylindrical pores, can be written as

$$S(Q) = \frac{1}{Q^2} \sum_{hk} M_{hk}\ \delta(Q_{hk}) \qquad \text{(IV-23)}$$

Where M_{hk} is the line multiplicity, with $M_{hk} = 6$ for h0 or hh and 12 otherwise. Q is the scattering vector and $\delta(Q_{hk})Q_{hk0} = \frac{4\pi}{\sqrt{3}\,a}\sqrt{h^2 + k^2 + hk}$ (*IV-19* are Dirac (δ) functions at the Bragg peak positions obtained by (IV-20) described earlier.

To take into account any possible disorder in the 2-D hexagonal crystalline lattice, we can use the Debye-Waller Factor (DWF) approximated by the harmonic approximation that counts-on the frozen random disorder in the pore position with respect to the ideal lattice. The DWF which contains $\langle u^2 \rangle$, the mean square displacement of the cylinders from the regular lattice site, can be introduced in the structure factor term as

$$S(Q) = \frac{1}{Q^2} \sum_{hk} M_{hk}\, exp\left(-\frac{\langle u^2 \rangle}{2}\, Q^2 \right) \qquad \textit{(IV-24)}$$

As an example, for MCM-41 (D = 3.65 nm) used in the following reference,[2] the obtained value of the MSD is $\langle u^2 \rangle = 0.12$ nm², that corresponds to small displacements with respect to pore diameter.

In the case of an empty matrix:

$$F^{Empty}(Q) = \frac{(\rho\bar{b})_{DVB-PMO}\, R_{pore}^2\, Z(QR_{pore})}{(\rho\bar{b})_{DVB-PMO}\, R_{pore}^2} \qquad \text{(IV-25)}$$

Where $Z(QR_{pore}) = \frac{2\,J_1(QR_{pore})}{QR_i}$ (J_1 being a first order Bessel function). In this approach we made the choice to normalize F(Q) to the total number of scatters of the empty matrix, i.e. F(0)=1.

We can now rewrite the intensity measured by neutron scattering in (IV-23) with $M_{hk} = 6$ as

$$I(Q) * Q^2 = 6K \left| \frac{(\rho\bar{b})_{DVB-PMO}\, R_{pore}^2\, Z(QR_{pore})}{(\rho\bar{b})_{DVB-PMO}\, R_{pore}^2} \right|^2 exp(-\frac{\langle u^2 \rangle}{2}\, Q^2\,) \quad \text{(IV-26)}$$

The different intensities of Bragg peaks are presented with dots in Figure IV-21. We can notice that their intensity is highly modulated from one position to the other. Knowing that the structure factor gives a constant intensity at a well-defined Bragg peak positions, this modulation is due to the form factor fluctuation. The different fits of the 3 Bragg peaks intensities with equation (IV-27), are presented in Figure IV-21 with lines.

To limit the fit parameters, I chose to impose the pore geometry with R_p=2,05 nm (obtained from N_2-physisorption) and I also assumed that the chemical composition is homogeneous in the pore wall which allowed me to consider the density as an average value $(\rho\bar{b})_{DVB-PMO}$. Therefore, the two parameters which remained adjustable are <u²> and K. However, we cannot achieve a quantitative description of the experimental data. Indeed, the fit does not, ideally, follow the intensity fluctuation. Moreover, by releasing <u²> it risks having negative values which have no physical meaning (see solid line) and by setting it to zero, the fit still, always, not ideal.

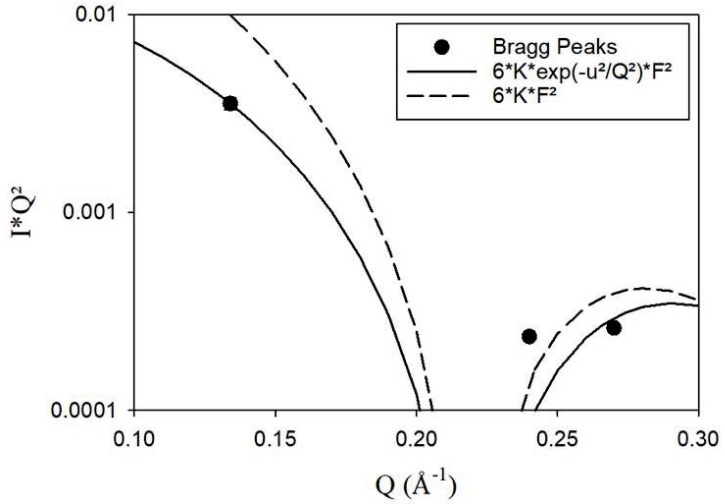

Figure IV-21: Fit of Bragg peaks intensity of empty DVB-PMO with equation (III 19) with a fixed pore radius R_p=2.05 nm and $(\rho\bar{b})_{DVB-PMO} = 19.12\ 10^9\ cm^{-1}$.

Given that the adjustable parameters are both related to the structure factor and the latter does not vary by filling, we can resolve the problem by limiting our study to the intensity ratio between Empty and Filled matrices (IV-28). This quantity will depend only on the form factor term $|F(Q)|^2$, which limits all the uncertainties related to S(Q). This method will assure a predictive calculations of the various model of mixture structure inside the pore without making any fits.

$$\frac{I^{Empty}}{I^{Filled}} = \frac{|F^{Empty}(Q)|^2}{|F^{Filled}(Q)|^2} \qquad \text{(IV-27)}$$

Therefore, we define the expression of each form factor in the case of filled matrix $F^{Filled}_{Model}(Q)$ corresponding to a model of mixture structure inside the pore in the different sub-paragraphs below:

- ***Model 1: Homogenous Filling:***

This model assumes no segregation. The radial and lateral density profile into pore is constant and equal to that of initial injected CM mixture, as presented in Figure IV-22. In this case, for a perfectly contrast-matched liquid, the intensity of all peaks is predicted to go to zero which is, obviously, not the experimental case. This model is just used to make a comparison between the homogeneous and non-homogeneous hypothesis.

The associated form factor is

$$F^{Filled}_{Model1}(Q) = \frac{[(\rho\bar{b})_{MIXTURE} - (\rho\bar{b})_{DVB-PMO}]R^2_{pore}\, Z(QR_{pore})}{(\rho\bar{b})_{DVB-PMO}\, R^2_{pore}} =$$

$$\frac{[(\rho\bar{b})_{MIXTURE} - (\rho\bar{b})_{DVB-PMO}]}{(\rho\bar{b})_{DVB-PMO}}\, F^{Empty}(Q) \qquad \text{(IV-28)}$$

Where the scattering length densities $(\rho\bar{b})_{MIXTURE} = (\rho\bar{b})_{Shell} = (\rho\bar{b})_{Core}$

for both CM mixtures can be calculated as:

$$(\rho\bar{b})_{MIXTURE(H/D)} = (\rho\bar{b})_{Shell} = (\rho\bar{b})_{Core} = V^{Shell}_{TBA} * (\rho\bar{b})_{TBAH} + (1 - V^{Shell}_{TBA}) * (\rho\bar{b})_{TOLD}$$

$$= 19{,}8\ 10^9\ cm^{-1}$$

$$(\rho\bar{b})_{MIXTURE(D/H)} = (\rho\bar{b})_{Shell} = (\rho\bar{b})_{Core} = V^{Shell}_{TBA} * (\rho\bar{b})_{TBAD} + (1 - V^{Shell}_{TBA}) * (\rho\bar{b})_{TOLH}$$

$$= 20{,}2\ 10^9\ cm^{-1}$$

With V^{Shell}_{TBA} and V^{Core}_{TBA} are the volume fraction of TBA in the shell and in the core, respectively, and we give the different values in the summary Table IV-4.

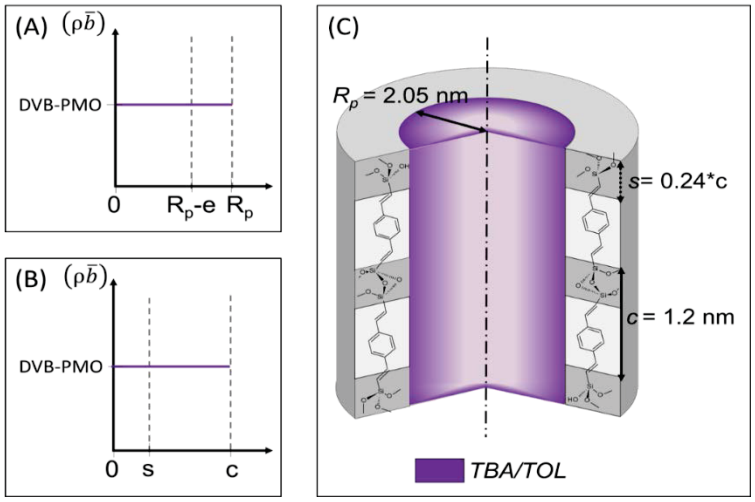

Figure IV-22: The radial (A) and lateral (B) scattering length density profile into pore. (C) Schematic representation of the 1st filling model with R_p is the pore radius, c is the unit cell (Silica+BU) length and s is the silica unit length.

- ***Model 2: only TBA@Silica and only TOL@Bridging-unit:***

This second model assumes a specific interaction between tert-butanol and silica units via H-bond and between toluene and divinyl benzene which leads to the formation of a mono-layer (the shell) on the surface of the pore with a thickness e = 0.6 nm. Based on the core-shell form factor in reference[2] and to the geometrical information presented on Figure IV-23-E, we have described the associated form factor as

$$F_{Model2}^{Filled}(Q) = \frac{1}{(\rho\bar{b})_{DVB-PMO}\, R_{pore}^2} \left\{ \left[(\rho\bar{b})_{Shell} - (\rho\bar{b})_{DVB-PMO} \right] R_{pore}^2\, Z(QR_{pore}) + \left[(\rho\bar{b})_{Shell} - (\rho\bar{b})_{Core} \right] R_{pore}^2\, Z(QR_{pore}) \right\} \quad \textit{(IV-29)}$$

Where the scattering length densities $(\rho\bar{b})_{Shell}$ and $(\rho\bar{b})_{Core}$ for both CM mixtures can be calculated as:

$$(\rho\bar{b})_{Shell} = V_{TBA}^{Shell} * (\rho\bar{b})_{TBAH} + (1 - V_{TBA}^{Shell}) * (\rho\bar{b})_{TOLD} = 42{,}7\ 10^9\ cm^{-1}$$

$$(\rho\bar{b})_{Shell} = V_{TBA}^{Shell} * (\rho\bar{b})_{TBAD} + (1 - V_{TBA}^{Shell}) * (\rho\bar{b})_{TOLH} = 22{,}3\ 10^9\ cm^{-1}$$

$$(\rho\bar{b})_{Core} = V_{TBA}^{Core} * (\rho\bar{b})_{TBAH} + (1 - V_{TBA}^{Core}) * (\rho\bar{b})_{TOLD} = -3{,}2\ 10^9\ cm^{-1}$$

$$(\rho\bar{b})_{Core} = V_{TBA}^{Core} * (\rho\bar{b})_{TBAD} + (1 - V_{TBA}^{Core}) * (\rho\bar{b})_{TOLH} = 18{,}1\ 10^9\ cm^{-1}$$

With V_{TBA}^{Shell} and V_{TBA}^{Core} are the volume fraction of TBA in the shell and in the core, respectively, and we give the different values in the summary Table IV-4. The radial and lateral density profile into pore is presented in Figure IV-23 for both CM mixtures.

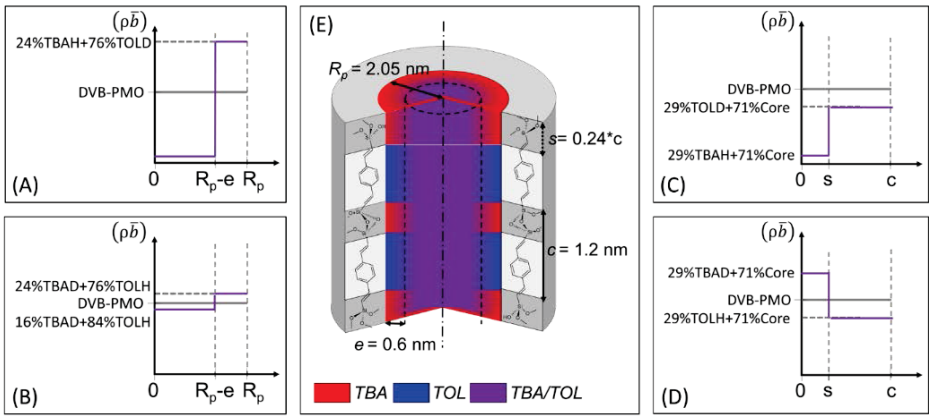

Figure IV-23: The radial (A,B) and lateral (C,D) scattering length density profile into pore for both CM mixtures. (E) Schematic representation of the 2nd filling model with R_p is the pore radius, c is the unit cell (Silica+BU) length and s is the silica unit length.

- ***Model 3: only TBA@Silica:***

This third model assumes only a specific interaction between tert-butanol and silica units which leads to the formation of a mono-layer of pure TBA on the surface of the silica units of a thickness e = 0.6 nm. Referring to the geometrical information presented on Figure IV-24-E, we have described the associated form factor as

$$F_{Model3}^{Filled}(Q) = \frac{1}{(\rho\bar{b})_{DVB-PMO}\, R_{pore}^2} \left\{ \left[(\rho\bar{b})_{Shell} - (\rho\bar{b})_{DVB-PMO} \right] R_{pore}^2\, Z(QR_{pore}) + \left[(\rho\bar{b})_{Shell} - (\rho\bar{b})_{Core} \right] R_{pore}^2\, Z(QR_{pore}) \right\} \quad \text{(IV-30)}$$

Where the scattering length densities $(\rho\bar{b})_{Shell}$ and $(\rho\bar{b})_{Core}$ for both CM mixtures can be calculated as:

$$(\rho\bar{b})_{Shell} = V_{TBA}^{Shell} * (\rho\bar{b})_{TBAH} + (1 - V_{TBA}^{Shell}) * (\rho\bar{b})_{TOLD} = 16{,}6\ 10^9\ cm^{-1}$$

$$(\rho\bar{b})_{Shell} = V_{TBA}^{Shell} * (\rho\bar{b})_{TBAD} + (1 - V_{TBA}^{Shell}) * (\rho\bar{b})_{TOLH} = 26{,}0\ 10^9\ cm^{-1}$$

$$(\rho\bar{b})_{Core} = V_{TBA}^{Core} * (\rho\bar{b})_{TBAH} + (1 - V_{TBA}^{Core}) * (\rho\bar{b})_{TOLD} = 22{,}9\ 10^9\ cm^{-1}$$

$$(\rho\bar{b})_{Core} = V_{TBA}^{Core} * (\rho\bar{b})_{TBAD} + (1 - V_{TBA}^{Core}) * (\rho\bar{b})_{TOLH} = 14{,}4\ 10^9\ cm^{-1}$$

With V_{TBA}^{Shell} and V_{TBA}^{Core} are the volume fractions of TBA in the shell and in the core, respectively, and we give the different values in the summary Table IV-4. The radial and lateral density profile into pore is presented in Figure IV-24 for both CM mixtures.

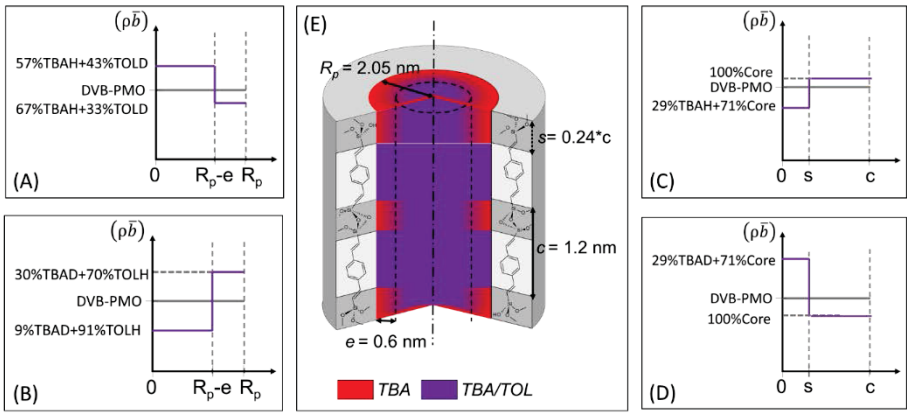

Figure IV-24: The radial (A,B) and lateral (C,D) scattering length density profile into pore for both CM mixtures. (E) Schematic representation of the 3rd filling model with R_p is the pore radius, c is the unit cell (Silica+BU) length and s is the silica unit length.

- ***Model 4: Core-Shell:***

This fourth model assumes a high and equivalent interaction between tert-butanol and Silica/BU units which leads to the formation of a mono-layer of pure TBA on the pore surface of a thickness e=0.8 nm in the case of CM TBAH/TOLD and e=0.6 nm in the case of CM TBAD/TOLH. Referring to the geometrical information presented on Figure IV-25-E, we have described the associated form factor as

$$F_{Model3}^{Filled}(Q) = \frac{1}{(\rho\bar{b})_{DVB-PMO}\, R_{pore}^2} \left\{ \left[(\rho\bar{b})_{Shell} - (\rho\bar{b})_{DVB-PMO} \right] R_{pore}^2\, Z(QR_{pore}) + \left[(\rho\bar{b})_{Shell} - (\rho\bar{b})_{Core} \right] R_{pore}^2\, Z(QR_{pore}) \right\} \quad \text{(IV-31)}$$

Where the scattering length densities $(\rho\bar{b})_{Shell}$ and $(\rho\bar{b})_{Core}$ for both CM mixtures can be calculated as:

$$(\rho\bar{b})_{Shell} = V_{TBA}^{Shell} * (\rho\bar{b})_{TBAH} + (1 - V_{TBA}^{Shell}) * (\rho\bar{b})_{TOLD} = -3{,}2\ 10^9\ cm^{-1}$$

$$(\rho\bar{b})_{Shell} = V_{TBA}^{Shell} * (\rho\bar{b})_{TBAD} + (1 - V_{TBA}^{Shell}) * (\rho\bar{b})_{TOLH} = 30{,}9\ 10^9\ cm^{-1}$$

$$(\rho\bar{b})_{Core} = V_{TBA}^{Core} * (\rho\bar{b})_{TBAH} + (1 - V_{TBA}^{Core}) * (\rho\bar{b})_{TOLD} = 57{,}2\ 10^9\ cm^{-1}$$

$$(\rho\bar{b})_{Core} = V_{TBA}^{Core} * (\rho\bar{b})_{TBAD} + (1 - V_{TBA}^{Core}) * (\rho\bar{b})_{TOLH} = 9{,}5\ 10^9\ cm^{-1}$$

With V_{TBA}^{Shell} and V_{TBA}^{Core} are the volume fraction of TBA in the shell and in the core, respectively, and we give the different values in the summary Table IV-4. The radial and lateral density profile into pore is presented in Figure IV-25 for both CM mixtures.

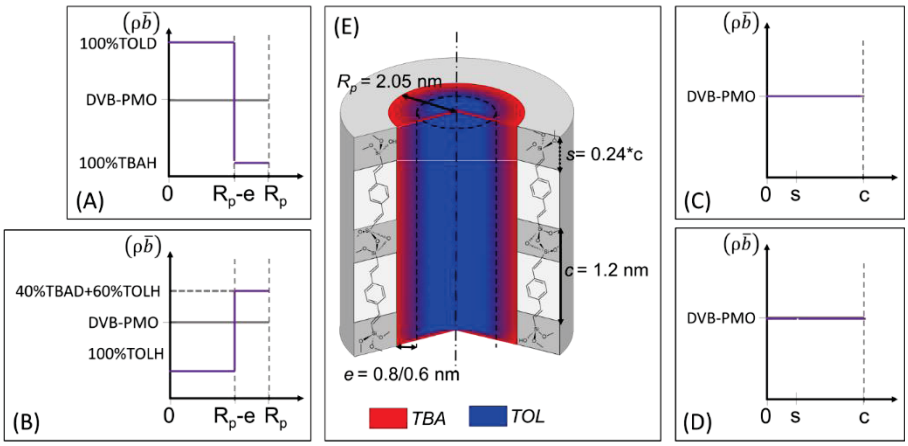

Figure IV-25: The radial (A,B) and lateral (C,D) scattering length density profile into pore for both CM mixtures. (E) Schematic representation of the 4th filling model with R_p is the pore radius, c is the unit cell (Silica+BU) length and s is the silica unit length.

Table IV-4: The volume fraction of TBA in the shell and in the core V_{TBA}^{Shell} and V_{TBA}^{Shell} respectively, for both CM mixtures.

62/38 TBAH/TOLD				
	1st Model	2nd Model	3rd Model	4th Model
V_{TBA}^{Shell}	0.62	0.24	0.67	1
V_{TBA}^{Core}	0.62	1	0.57	0
20/80 TBAD/TOLH				
	1st Model	2nd Model	3rd Model	4th Model
V_{TBA}^{Shell}	0.2	0.24	0.3	0.4
V_{TBA}^{Core}	0.2	0.16	0.09	0

The Figure IV-26, shows the form factor of the different models which were calculated from the equations described above for the two CM mixtures 62TBAH/38TOLD (Figure IV-26-A) and 20TBAD/80TOLH (Figure IV-26-B). The form factor of the 1st model is almost zero that is why it is not visible in the figure. Concerning the 3 other models, we notice a great difference of the form factor; first between the different models for the same mixture and second between the different mixtures for the same model. These observations are in qualitative agreement with experimental intensity which showed, also, a significant difference between the two mixtures as shown previously in Figure IV-20.

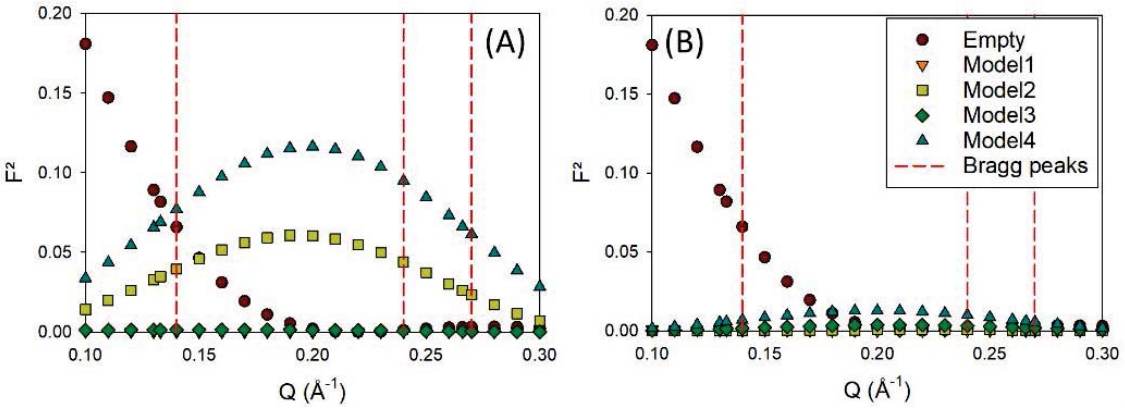

Figure IV-26: The form factor of empty matrix and the 4 different models for the two CM mixtures 62TBAH/38TOLD (A) and 20TBAD/80TOLH (B).

2-3- Experimental intensities VS Predicted Models:

In this last step, we will compare the experimental results with those calculated for the different models. In Figure IV-27, we present the fit method which allowed us to obtain the intensities relating to each of the three Bragg peaks. We can clearly see that the fit, mostly for the two less intense peaks (110) and (200), is not ideal and this is due firstly to the quality of the spectrum and secondly to the simplicity of the fit model that we have chosen (3 Gaussians). Nevertheless, we must keep in mind that the only target of this fit is to obtain the relative intensity for each Bragg peak and this fit, despite its non-ideality, satisfies this target. As the ratio of the experimental Empty/Filled intensities is equal to the ratio of its form factors (as explained in the previous part), we present in Figure IV-28 both together. This allows as to predict which model shows the best agreement with the experimental Bragg intensity and best describe the nanostructuring of confined mixtures.

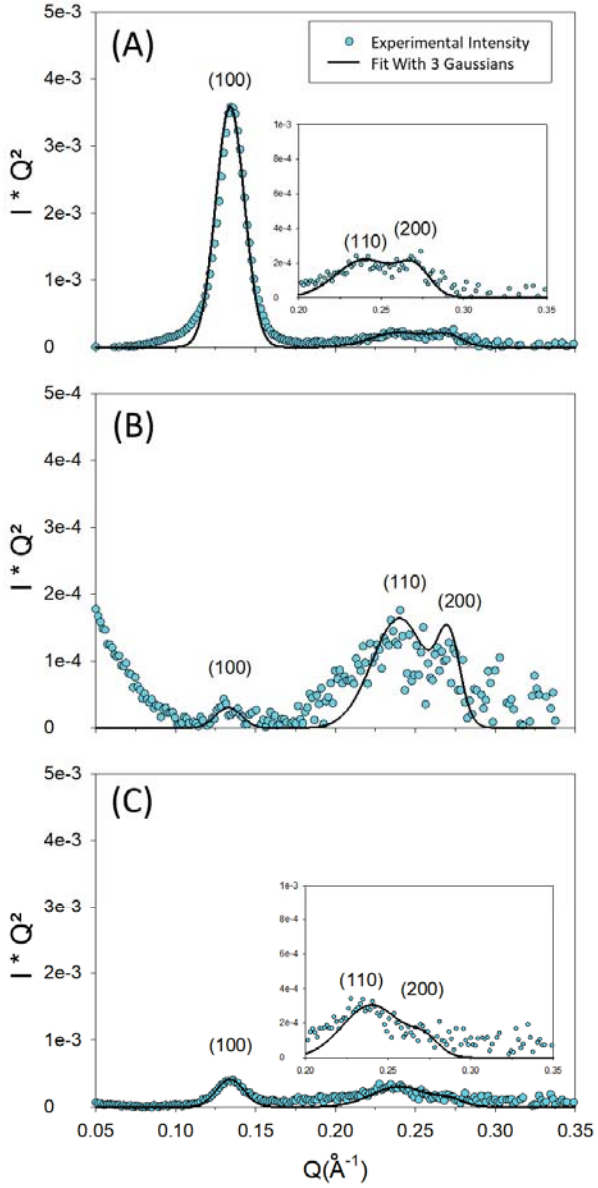

Figure IV-27: Best fit (3 Gaussians) of the experimental intensity after background correction of empty matrix (A), filled matrix with CM TBAH/TOLD (B) and CM TBAD/TOLH (C).

First of all, it is clear that the homogeneous model (Model 1) is not consistent with the experimental results and does not follow the intensity modulation of the peaks. All the three other models anticipate a higher intensity ratio of the first order Bragg peak, a lower for the second and intermediate for the third which is not qualitatively the same as experimental results. Indeed, for the TBAH/TOLD CM mixture Figure IV-28-A) the intensity ratio of the 3rd order Bragg peak is the lower and it's the higher for the TBAD/TOLH CM mixture (Figure IV-28-B). This can be linked to the large error related to the fit of the 3rd peak because of its weak intensity. Then we will focus, preferably, on the first two Bragg peaks. Remarkably, in the case of TBAH/TOLD CM mixture (Figure IV-28-A) the 3rd Model is the only model in a good agreement with experiments for all Bragg peaks with a higher deviation of the 3rd order Bragg peak. However, it seems to be less straightforward in the case of TBAD/TOLH CM mixture.

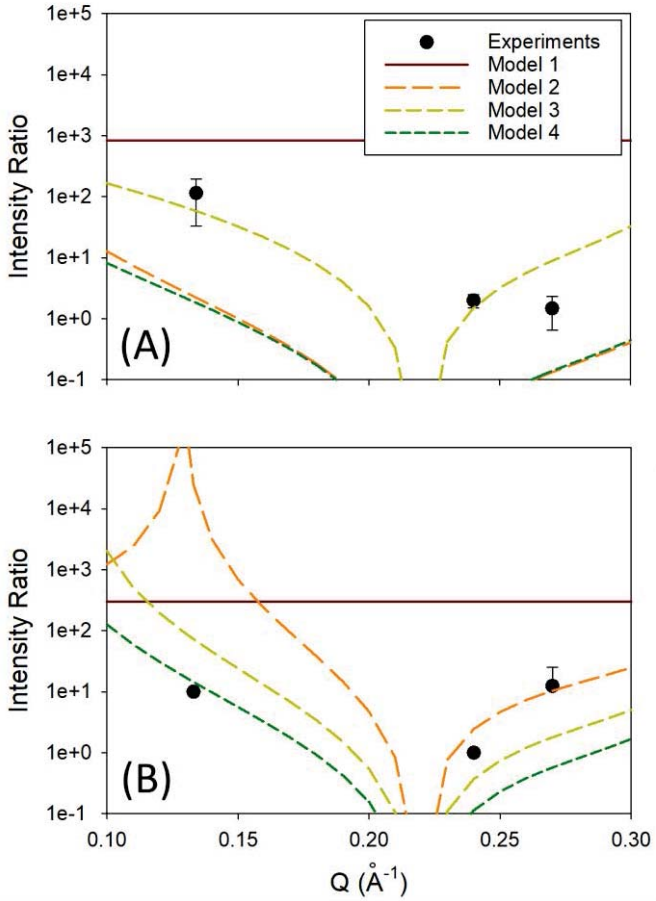

Figure IV-28: Model predictions (lines) and experimental Bragg (circles) intensities ratio Empty/Filled for (A): (CM) TBAH/TOLD and (B): (CM) TBAD/TOLH.

Preeminently, it does not seem easy to understand this kind of observation, howbeit by going back to Table IV-4, which presents the volume fractions of TBA (hence of TOL) in the core and in the interface of pore, we can, obviously, see that in the case of TBAD/TOLH mixture the difference between the different models is not too great relatively to that of TBAH/TOLD mixture and this is clear by comparing different volume fractions in the shell or in the core, respectively V_{TBA}^{Shell} and V_{TBA}^{Core} (Horizontal view of Table IV-4).

To conclude, the TBAH/TOLD mixture seems to be more discriminative and therefore, the Model 3, qualitatively, better predicts experimental results. As a reminder, this model assumes that only the silica unit is selective towards the tert-butanol molecules, which leads to build a TBA monolayer at the surface of all the non-organic units. Regarding the rest of the mixture is homogeneously distributed in the rest of the pore (i.e. the core and the bridging-unit)

2-4- Conclusion :

As a continuation of the results obtained with vapor sorption experiments, which showed that DVB-PMO matrix has an affinity 10 times greater with TBA molecules than TOL molecules and that this affinity is due to the presence of silanol groups in the silica units which ensures this strong interaction. So the SANS experiments allowed us to better understand the structuring of TBA and TOL molecules into the pore cavity.

To achieve this goal, we have taken a step-by-step process. In the first step, we were able to understand our experimental results and identify all the observed Bragg peaks which are 4 in total: (100), (110), (200) and (002) thus giving an explanation for the disappearance of (210) peak. Through this identification, we were able to calculate the lattice distance 'a' and the regular modulation distance along the pore axis between silica and divinyl benzene units 'c'.

In the second step, we succeeded in finding a method which ensures a predictive calculations of the scattering intensity of various models of nanostructuration of TBA/TOL mixture structure inside the pore without making any fits and avoid all the uncertainties related to the structure factor S(Q). This method consists on studying the Empty/Filled intensity ratio which is equal to the Empty/Filled ratio of squared form factor as designated in the relation (IV-28). The Empty/Filled intensity ratio is an experimental output and the Empty/Filled ratio of squared form factor we have calculated for each of the 4 structural models we have proposed.

We calculated the different form factors relating to the two studied H/D and D/H mixtures and which are both in contrast-matching condition with the DVB-PMO matrix. As for the D/H mixture, we noticed that the predicted intensity by the different models are very similar. In fact, for this specific mixture, it appears that, whatever the model chosen, the volume fractions of TBA in the shell and in the core are very comparable. (Horizontal view of Table IV-4) and much better visible in Figure IV-26-B which shows the great similarity of the form factor of the different models for this same mixture.

While the D/H mixture cannot be totally decisive in making a clear distinction between the different models, a different situation was shown when adding insights from the H/D system. As the whole, the predicted intensities from the 3rd model were found to present the best consistency with the all set of experimental data. This model assumes that only the silica unit is selective towards the tert-butanol molecules leading to the formation of a TBA monolayer at their surface and the rest of the mixture is homogeneously distributed in the rest of the pore (i.e. the core and the bridging-unit), providing thus a microscopic, though probably simplified, picture of the nanoconfined liquid mixture in PMO.

REFERENCES

1. *Mhanna R, Hamid ARA, Dutta S, et al. More room for microphase separation: An extended study on binary liquids confined in SBA-15 cylindrical pores. Journal of Chemical Physics 2017;146(2).*

2. *Hamid ARA, Mhanna R, Lefort R, et al. Microphase Separation of Binary Liquids Confined in Cylindrical Pores. Journal of Physical Chemistry C 2016;120(17): 9245-52.*

3. *Hamid ARA, Mhanna R, Catrou P, Bulteau Y, Lefort R, Morineau D. Multiple Glass Transitions of Microphase Separated Binary Liquids Confined in MCM-41. Journal of Physical Chemistry C 2016;120(20): 11049-53.*

4. *Mhanna R, Lefort R, Noirez L, Morineau D. Microstructure and concentration fluctuations in alcohol-Toluene and alcohol-Cyclohexane binary liquids: A small angle neutron scattering study. Journal of Molecular Liquids 2016;218: 198-207.*

5. *Mizukami M, Kurihara K. Alcohol cluster formation on silica surfaces in cyclohexane. Adsorption and Nanostructures 2002;117: 13-17.*

6. *Mizukami M, Kurihara K. Ethanol cluster formation on silicon oxide surface in cyclohexane-ethanol binary liquids. Chemistry Letters 2000(3): 256-57.*

7. *Mizukami M, Kurihara K. Hydrogen-bonded macrocluster formation of 1-propanol and 2-propanol on silica surfaces. Australian Journal of Chemistry 2003;56(10): 1071-80.*

8. *Mizukami M, Moteki M, Kurihara K. Hydrogen-bonded macrocluster formation of ethanol on silica surfaces in cyclohexane. Journal of the American Chemical Society 2002;124(43): 12889-97.*

9. *Mizukami M, Nakagawa Y, Kurihara K. Surface induced hydrogen-bonded macrocluster formation of methanol on silica surfaces. Langmuir 2005;21(21): 9402-05.*

10. *Dutta S, Lefort R, Morineau D, et al. Thermodynamics of binary gas adsorption in nanopores. Physical Chemistry Chemical Physics 2016;18(35): 24361-69.*

11. *Zhou L, Bai SP, Zhou YP, Yang B. Adsorption of nitrogen on silica gel over a large range of temperatures. Adsorption-Journal of the International Adsorption Society 2002;8(1): 79-87.*

12. *Sing KSW, Everett DH, Haul RAW, et al. REPORTING PHYSISORPTION DATA FOR GAS SOLID SYSTEMS WITH SPECIAL REFERENCE TO THE DETERMINATION OF SURFACE-AREA AND POROSITY (RECOMMENDATIONS 1984). Pure and Applied Chemistry 1985;57(4): 603-19.*

13. *S.J G, K.S.W S. Adsorption, Surface Area and Porosity. Academic Press, London, ; 1982.*

14. *Park J. Extension of the Brunauer-Emmett-Teller Equation to Mixtures. Journal of Chemical Engineering of Japan 2015;48(11): 927-32.*

15. *Mietner JB. Visiting Nanopores : the great potential of PMOs for studying the properties of water in nanopores of different polarity. Thesis. Universität Hamburg; 2018.*

16. *Richard D, Ferrand M, Kearley GJ. Analysis and Visualisation of Neutron-Scattering Data. 4. Institut Laue-Langevin, BP156, 38042 Grenoble, Cedex 09, France: Journal of Neutron Research; 1996:33-39.*

17. *Celestini F. Capillary condensation within nanopores of various geometries. Volume 228, Issues 1–2 , 31 March 1997 , Pages 84-90. Physics Letters A; 1997.*

18. *Pellenq RJ-M, Coasne B, O Denoyel R, Coussy O. Simple phenomenological model for phase transitions in confined geometry. 2. Capillary condensation/evaporation in cylindrical mesopores. Langmuir 2009;Feb 3;25(3):1393-402.*

CHAPTER V

MODULATING SURFACE INTERACTION BY CONFINING BINARY MIXTURE IN A HYBRID PORE SYSTEM WITH A HYDROPHILIC/HYDROPHOBIC SURFACE: EFFECT ON THE DYNAMICS OF BINARY MIXTURE

ABSTRACT

In the present chapter we will focus on the dynamics of a fully miscible binary liquids combining a polar H-bonded (Tert-butanol) and an aprotic weakly polar (Toluene) molecule confined in periodic mesoporous organosilicas matrix DVB-PMO (divinyl-Benzene periodic mesoporous organosilicas).

We aimed at highlighting any specific behavior, in terms of distinct dynamics or dynamical heterogeneities, which would indicate microphase separation either induced by the radial confinement effects or by the axial modulation of the interfacial interaction. Furthermore, we have investigated the mixing effects on the relative dynamics of each constituent and we have compared the bulk and confined situations.

We have used the quasielastic neutron scattering (QENS) technique to study the microscopic molecular dynamics. We applied isotopic contrast variation effects to highlight the dynamics of the hydrogenated component (TBAH or TOLH) in the mixture, due to its high incoherent cross section, and minimize the contribution of the complementary deuterated molecule (resp. TOLD or TBAD).

I. INTRODUCTION:

Since the pioneering studies of the early 1990s[1-5] that have shown that geometrical nanoconfinement have a significant effect on the dynamics of liquids, researchers from many technological and industrial fields[6] (catalysis, chromatography or membrane separation) have performed studies on this effect in various confined geometries and for various molecular liquids. A wealth of fundamental properties has been collected for pure liquids[7-16] and specifically for water[17-34], which is fairly justified by their general interest and their relative simplicity.

A different situation is encountered for multicomponent liquid mixtures, which are expected to exhibit more complex behaviors, and which have been less frequently studied in confined geometry so far. A prototypical example illustrating the interest of studying more complex systems is given by fully miscible binary liquids confined in mesostructured porous matrixes. Besides their relevance for applications, they offer new perspectives for the emergence of original, and possibly tunable behaviors that markedly differ from those of their individually confined components and bulk states.

Binary mixtures of tert-butanol−aprotic solvents and their pure components have recently attracted much attention, and have been thoroughly investigated in the bulk[35, 36] and confined states.[37, 38] It has been evidenced the possible microphase separation in a confined environment, which links to the effects of different interfacial interactions.[39, 40] For tert-butanol−toluene mixtures, this phenomenon also explains the observation of distinct dynamics, attributed to molecules located at the liquid-solid interface (shell-region) and into the center of the pores (core-region)[37, 41], as well as their dependency on the concentration[42, 43].

In the previous chapter of this thesis, significant adsorption of TBA molecules at the porous interface of PMO compared to TOL molecules were observed. In addition, on the contrary to the pure silica porous interface of MCM-41, the organization observed for DVB-PMO pores is different from a simple core-shell structure. It is more consistent with a partial nanosegregation with an increase of the concentration of TBA at the pore surface. More specifically, this conclusion is supported by the better agreement obtained for the model that assumes that only the silica units are selective towards the tert-butanol molecules leading to the formation of a TBA monolayer at their surface and that the rest of the mixture is homogeneously distributed in the rest of the pore (i.e. in the core and at surface of the organic bridging-units). This implies that the large difference between the tert-butanol-silica and the toluene-silica interaction strengths plays a dominant role in the microscopic structure of the nanoconfined liquid mixture in PMO. It therefore emerges the question of the impact of a different balance between the two liquid-surface interactions, as well as the effect of having a spatially modulated surface interaction on the dynamics of binary mixture molecules.

Hence, the ultimate goal of the study reported in the present chapter was, first, to investigate the mixing effects on the relative dynamics of each constituent. Second, to compare the bulk and confined situations to highlight any dynamical specific behavior, in terms of distinct dynamics or dynamical heterogeneities, which would be related to the specific microphase separation observed in last chapter.

To do so, we have studied and compared the dynamics of TBA-TOL binary mixtures in the bulk and confined in divinyl-Benzene periodic mesoporous organosilicas (DVB-PMO)..

We have used the quasielastic neutron scattering (QENS) technique to study the microscopic molecular dynamics on a broad temperature range from 315 to 220 K. We applied isotopic contrast variation effects to highlight the dynamics of the hydrogenated component in the mixture, due to its high incoherent cross section, and minimize the contribution of the complementary deuterated molecule. Therefore, we varied the concentration of hydrogenated TBA (TBAH) and hydrogenated TOL (TOLH), as well as their deuterated counterparts.

II. METHODS

1. Samples

The hydrogenated solvents TBA and TOL (>99%) were purchased from Sigma-Aldrich, and the fully deuterated solvents TBA ($C_4D_{10}O$, 99.8%) and TOL (C_7D_8,99.5%) were obtained from Eurisotop and used directly, without further purification.

The DVB-PMO periodic mesoporous organosilicates were prepared according to the synthesis procedure described in Chapter-II. The synthesis product (a powder), was characterized by different methods in order to control its pore size and crystal network structure as also described in Chapter-II. Before experiments, the matrix powder was dried at 120°C under primary vacuum for 12h. Liquid binary mixtures were prepared in volume fraction for different isotopic and concentration compositions (given later in Table V-2). They were added to empty matrix (previously well dried) using a calibrated micropipet.

Table V-1: Composition of DVB-PMO matrix after 12H under saturated vapor of pure TBA and pure TOL.

Liquid Confined in DVB-PMO	Mass PMO (mg)	Mass Liq (mg)	Filling ratio[a] (cm^3/g)	Pore volume[b] (cm^3/g)	Filling fraction[c] (cm^3/g)
Pure TBA	3.06	1.17	0.49	0.99	0.68
Pure TOL	2.45	0.86	0.40	0.99	0.69

[a] defined as the amount of mass uptake of matrix after 12h in contact of liquid vapor at P_{Sat}, [b] evaluated from the nitrogen physisorption isotherms, [c] derived from the analysis of adsorption isotherms by dynamic vapor sorption methods.

The targeted filling was equal to amount of TOL or TBA at full pore loading determined from the analysis of adsorption isotherms by dynamic vapor sorption methods as explain in chapter IV. It corresponds to a liquid volume per mass of confining matrix ($V_L = 0{,}68\ cm^3\ g^{-1}$), which is smaller than the total porous volume derived from nitrogen physisorption experiments ($V_p = 0{,}99\ cm^3\ g^{-1}$). This illustrates that a fraction of the

porosity probed by N_2 is not fully accessible to TOL and TBA molecules due to their significantly larger size. Note that similar observations were made for water-filled PMOs as discussed in chapter II, with loading ratios (i.e. V_L/V_p) found in the range 42 to 60%. Note that it the latter case, the hydrophobicity of the pore surface additionally affected (reduced) these quantities. To check the filling status of the matrixes differential scanning calorimetry (DSC) experiments were performed with a Q-20 TA Instrument equipped with a liquid nitrogen cooling system and using T_{zero} hermetic aluminum pans. The melting transition of an indium sample was used for calibration of temperature and heat flux. Temperature scanning rates of 10 K·min^{-1} were applied during an initial cooling ramp and a subsequent heating ramp.

For DSC experiments, DVB-PMO matrix, of a mass m_p, was exposed to sample vapor (at its saturated vapor pressure P_{Sat}) for 12h to ensure filling. Composition of the DVB-PMO filled samples is described in Table V-1. The obtained filling ratio (0.5 and 0.4 respectively for TBA and TOL) is smaller than the one derived from the analysis of adsorption isotherms. For both liquids, the thermal events that characterize their bulk state, disappeared under confinement. In fact, only the glass transition appears in the bulk thermograms which means that filled samples (in this filling conditions) do not contain any bulk excess liquid outside the porosity.

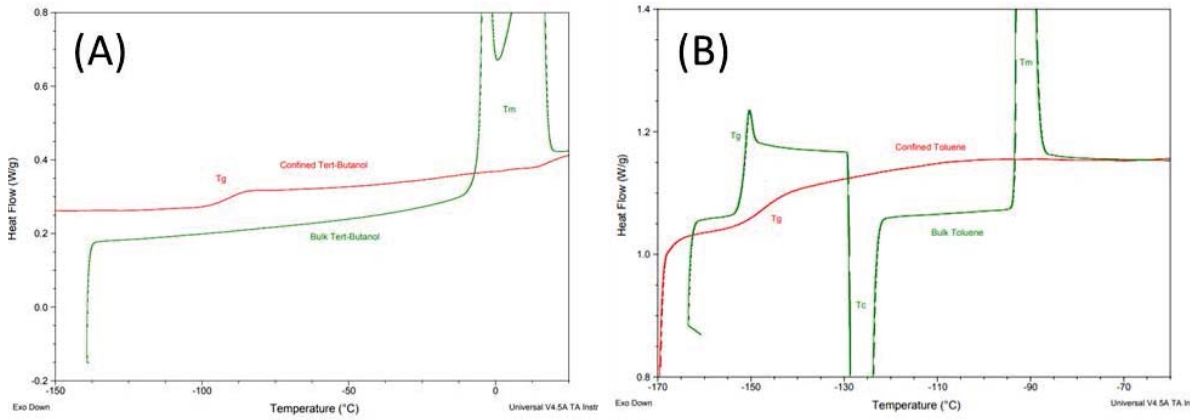

Figure V-1: A: DSC scans (endotherm up) of bulk (green) and confined (red) pure TBA. B: DSC scans (endotherm up) of bulk (green) and confined (red) pure TOL. The thermograms were recorded on heating with a temperature scanning rate of 10 K min^{-1}.

2. Quasielastic Neutron Scattering (QENS)

The Quasielastic Neutron Scattering data were measured on the time-of-flight spectrometer IN6-SHARP at the Institut Laue Langevin in Grenoble, France. The experiments were performed with an incident neutron wavelength of 5.12 Å and an elastic energy resolution ΔE of 70 μeV (FWHM) to give access to dynamics timescale ($t = \bar{h}/\Delta E$) of about 10 ps.

Data were collected for bulk and confined TBA and TOL mixtures at selected temperatures in the range 220-315K, as indicated in Table V-2. For each sample, an acquisition time of 2h was performed after thermal equilibration at each temperature, separated by cooling steps of about 40 min proceeded with a typical rate of 1 K/min.

Background scattering from the empty sample holder was measured for 2 h at three different temperatures 2 K, 220 K and 315K, and a vanadium standard was measured at 315 K for 2 h for normalization and to determine the instrument resolution function. Data were processed by using Mantid and LAMP software packages[45] and analyzed using QENSH software.[46] The corrected spectra were then normalized to the intensity measured for a vanadium foil.

Table V-2 Summary of the different temperatures, isotopic and chemical compositions of the measured samples, including bulk liquids, confined liquids and empty matrices.

	H/D ISOTOPIC and %vol COMPOSITION	**TEMPERATURES (K)**
EMPTY MATRIX	-	*2 - 220 - 315*
FILLED MATRIX	*TBAH*	*220 - 250 – 280 - 315*
	50/50 TBAH/TOLD	
	30/70 TBAH/TOLD	
	TOLH	*220 - 250 - 280 - 315*
	50/50 TOLH/TBAD	
BULK	*TBAH*	*250 – 315*
	50/50 TBAH/TOLD	
	TOLH	
	50/50 TOLH/TBAD	

Sample preparation was similar for all the confined samples. A constant amount of the mesoporous materials (DVB-PMO) was filled into a standard flat aluminum cell which was also used for bulk samples. After liquid injection, the cells were immediately sealed and the samples were allowed to equilibrate for a few hours to ensure the homogeneous filling of the different pores, in accordance with the SANS kinetic measurements for a different mesoporous material (SBA-15).[38] An indium wire was used to seal the sample cell. The sample cells were weighted at each different steps of the preparation and also checked after each QENS measurement to verify the measurable loss of sample.

In order to optimize signal intensity while reducing multiple scattering effects, the thickness of the sample was chosen to be 2 mm for the confined samples and 0,2 mm for the bulk liquids. The absence of crystallization in confined samples was checked with DSC experiments and was not observed during QENS experiments. This validates our filling method (described in previous *Samples* paragraph (II.1)), which was also used in previous studies to fill SBA-15 and MCM-41 matrices.[38, 41, 47]

3. Incoherent vs coherent scattering

The QENS signal of hydrogenated samples is often linked to the incoherent scattering function $S_{incoh}(Q, \omega)$, allowing to probe the self-correlation of the individual dynamics of the scattering particles. This is due to the high incoherent cross-section of Hydrogen compared to incoherent and coherent contributions of most of the other atoms composing organic molecules. In the case of pure hydrogenated samples, such as TBAH and TOLH (Figure V-2), the coherent cross-section contribution is less than 8% which can be, therefore, neglected. However, this may not be evident with the presence of deuterated components with a significant coherent contribution. To solve this issue, we calculated the coherent/incoherent contribution of deuterated molecules in the total cross-section.

As shown in Figure V-2, for binary mixtures the coherent contribution does not exceed 16% of the total cross section even with the presence of deuterated component in the mixture. The coherent contribution related only to deuterated molecule (red area) does not exceed 10% of the total cross-section and it presents around 60% of the total coherent contribution. This keep the incoherent approximation always valid.

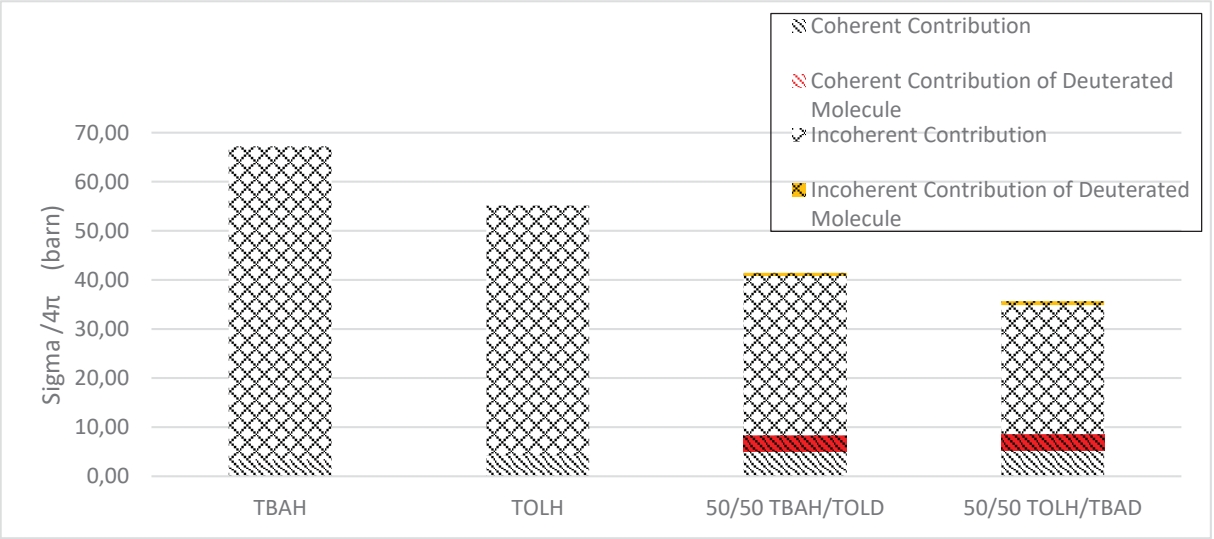

Figure V-2 Coherent/Incoherent scattering cross sections of hydrogenated and deuterated components of different isotopic mixtures.

Regarding the incoherent contribution of the deuterated component (yellow area), it is around 3% of the total incoherent signal of the mixture. It should be also mentioned that the intensity of the coherent contribution is Q-modulated by $S_{coh}(Q)$, while $S_{incoh}(Q) = \int S_{incoh}(Q, \omega) d\omega$ is constant. This makes that the coherent contribution depends firstly on Q (Figure V-3-A) and secondly on confinement (Figure V-3-B). Consequently, this could modify the incoherent/coherent contribution ratio. However, based on the previous discussion, on the ratios between the incoherent and coherent cross sections, it can be considered to a good level of approximation that for the systems and compositions studied, the scattered intensity arises to a large extent from the incoherent scattering of the hydrogenated component. This allows probing the self-correlation related to the individual dynamics of the hydrogenated components within the mixtures.

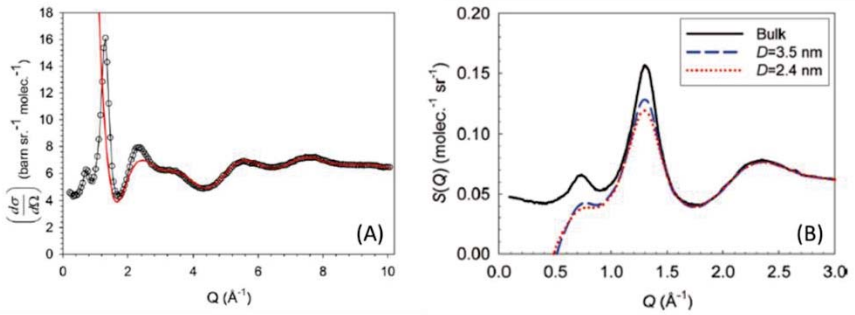

Figure V-3 (A) Q-dependency of experimental coherent intensity of TBAD (99.8% D) at T = 303 K.[35] (B) Confinement effect on the simulated structure factor S(Q) of TBA bulk and confined in nanochannels of pore size D = 2.4 nm and D=3.5 nm.[13]

III. RESULTS AND DISCUSSION

1. General features

The Q-dependence of QENS scattering intensity is shown in Figure V-4 for bulk and confined TBAH and TOLH in DVB-PMO for a selected temperature T=315K. By following the black arrow on Figure V-4-A that shows the Q-increasing, we observed a reduction of the intensity contained in the elastic resolution combined with a broadening of the quasielastic line.

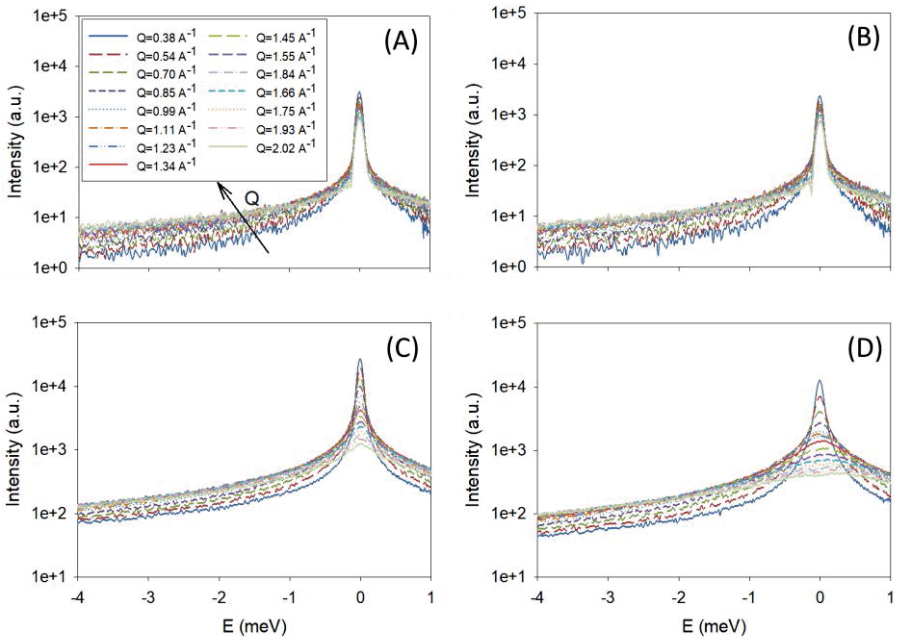

Figure V-4 Q-dependence of the scattering intensity of confined (above panels) and bulk (bellow panels) TBAH (right panels) and TOLH (left panels). QENS spectra presented for a common temperature of 315K. The black arrow on (A) shows the Q-variation direction.

This Q-dependence probably arises from the combination of different effects, which are classically observed in QENS studies of liquids. It includes the effect of dispersive modes (e.g. translational diffusion) and the modulation of the elastic intensity due to vibrations (Debye Waller factor) or local quasielastic modes (rotation, libration), which comprise an elastic incoherent structure factor (EISF). A continuous sharpening of the quasielastic peak was observed for all confined mixtures and presented for confined TBAH and TOLH in Figure V-5 by decreasing the temperature from 315K to 220K following the black arrow in Figure V-5-A.

On a qualitative level, the width of the quasielastic scattering is inversely proportional to the typical timescale of motion of particles. Therefore, this sharpening indicates that the molecule dynamics slows down gradually with cooling. The absence of a sharp increase of the elastic signal confirms that TBAH and TOLH remained liquid on the entire studied temperature range. It allows excluding the hypothetical presence of excess liquid outside the pores and the crystallization of in-pore liquid, which is in agreement with the DSC experiment as described, previously, in this chapter in paragraph *Samples* (III-1).

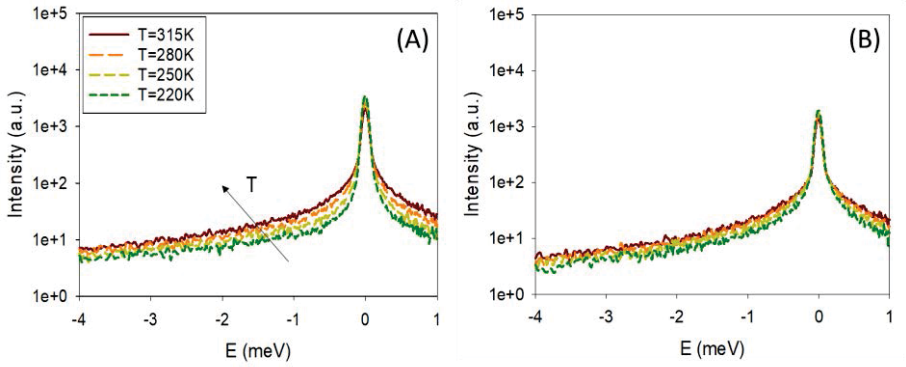

Figure V-5: *T-dependence of the scattering intensity of confined TBAH (A) and TOLH (B) in DVB-PMO. QENS spectra presented for a common Q=1.1 Å-1. The black arrow on (A) shows the T-variation direction.*

Bulk and confined mixtures spectra were fitted individually at each Q with a model comprising a sum of three Lorentzian functions (3L) and a model comprising a sum of two Lorentzian functions and one elastic component, i.e. a Dirac function $\delta(\omega)$ (2L+E), respectively. The elastic contribution, of confined mixtures, arising from the pore wall atoms was accounted for by adding the scattered experimental intensity of the empty matrix of DVB-PMO to the theoretical functions. This means that the persistent elastic contribution is actually ascribed to hydrogenated molecules. The best fit (red solid line) and the experimental QENS spectra (symbol) for bulk and confined TBAH and TOLH in DVB-PMO is shown in Figure V-6. The additional curves in this figure present the decomposition of the total fitted intensity (I^{Fit}) into Dirac (Elastic peak) and Lorentzian (sharp, intermediary and broad) functions components.

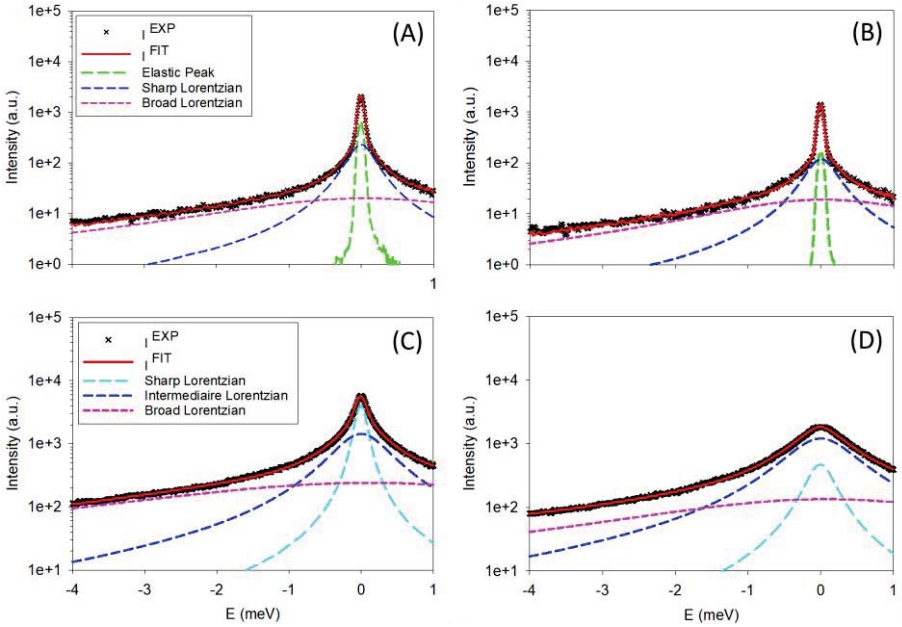

Figure V-6: QENS spectra (symbols), fitted function (red solid lines) and its comprising Lorentzian functions and elastic peak (dashed lines) measured for confined TBAH (A), confined TOLH (B), bulk TBAH (C) and bulk TOLH (D).

2. Confined mixtures

As the width of the quasielastic scattering is inversely proportional to the typical time scale of motion of particles we related the broad and sharp quasielastic components of confined mixtures spectra to fast (F) and slow (S) motions, respectively.

The fitted intensity comprising an elastic and two Lorentzian quasielatic components (2L+E) can be written as:

$$I^{2L+E}(Q,\omega) = K\begin{bmatrix} I_{EL}(Q)\delta(\omega) + I_S(Q)L_S(Q,\omega,\Gamma_S) \\ +I_F(Q)L_F(Q,\omega,\Gamma_F) \end{bmatrix} \quad (V\text{-}1)$$

In our QENS study of water (chapter III), the dynamics of confined water was interpreted by the coexistence of two independent relaxations, corresponding to local-fast motions and translational jump diffusion with the presence of a non-mobile (slower than 10ps) molecule fraction.[17] We retained a similar approach for confined TBA/TOL mixtures, assuming two independent dynamical modes. In this case, the dynamic structure factor should write as

$$S(Q,\omega) = K\left[A_S(Q)\delta(\omega) + \big(1 - A_S(Q)\big)L_S(Q,\omega,\Gamma_S)\right]\otimes\left[A_F(Q)\delta(\omega) + \big(1 - A_F(Q)\big)L_F(Q,\omega,\Gamma_F)\right]\otimes R(Q,\omega) \quad (V\text{-}2)$$

where $A_i(Q)$ is the elastic incoherent structure factor (EISF) describing the geometry of motions and L_i is a Lorentzian function with a half width half maximum Γ_i. The values of $A_i(Q)$ can be evaluated from the fitted intensities $I_i(Q)$. In particular, assuming a decoupling

of both timescales (i.e. $\Gamma_F \gg \Gamma_S$, being actually a condition that will be verified in the next paragraph), equation $S(Q,\omega) = K\left[A_S(Q)\delta(\omega) + \big(1 - A_S(Q)\big)L_S(Q,\omega,\Gamma_S)\right]\otimes A_F(Q)\delta(\omega) + \big(1 - A_F(Q)\big)L_F(Q,\omega,\Gamma_F)\otimes R(Q,\omega)$ (V-2) writes as:

$$S(Q,\omega) = K\left[A_S(Q)A_F(Q)\delta(\omega) + \big(1 - A_S(Q)\big)A_F(Q)L_S(Q,\omega,\Gamma_S) + \big(1 - A_F(Q)\big)L_F(Q,\omega,\Gamma_F)\right]\otimes R(Q,\omega) \qquad (V\text{-}3)$$

So that, $I_{EL}(Q) = A_S(Q)A_F(Q)$, $I_S(Q) = \big(1 - A_S(Q)\big)A_F(Q)$, and $I_F(Q) = \big(1 - A_F(Q)\big)$.

In Figure V-7, we show the different intensities obtained from the fit of QENS spectra by equation (V-3) for different TBAH and TOLH mixtures.

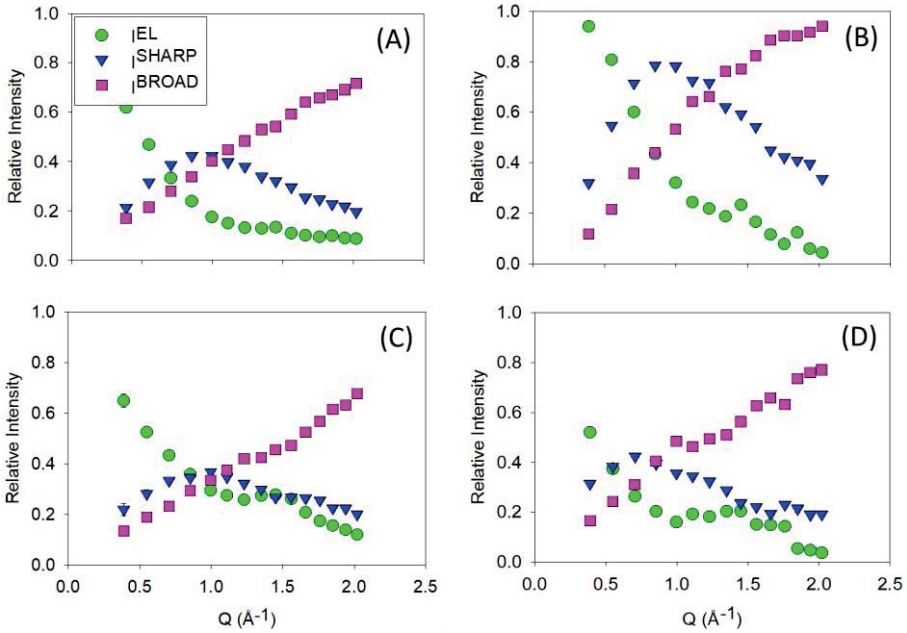

Figure V-7: The experimental intensities obtained by the fit of the QENS spectra for pure TBAH (A), pure TOLH (B), 50/50 TBAH/TOLD (C) and 50/50 TOLH/TBAD (D) confined in DVB-PMO matrix at a temperature of 315K.

2-1- TBAH/TOLD Confined Mixtures: Effect of TOL on the Dynamics of TBA

In Figure V-8, we show the two relaxation times τ_S and τ_F related to Γ_S and Γ_F, respectively, obtained from the fit with (2L+E) model as a function of Q^2 at the four studied temperatures and for three different mixtures of TBAH/TOLD with various volume fraction of TBAH (x = 1, 0.5 and 0.3). τ_S and τ_F are readily separable and they differ by a factor of 10 to 15, which allowed to talk about two distinct dynamics slow and fast. Their values

fluctuate slightly around average values that we mentioned to it in Figure V-8 by different black dashed lines and we illustrated it in Table V-3.

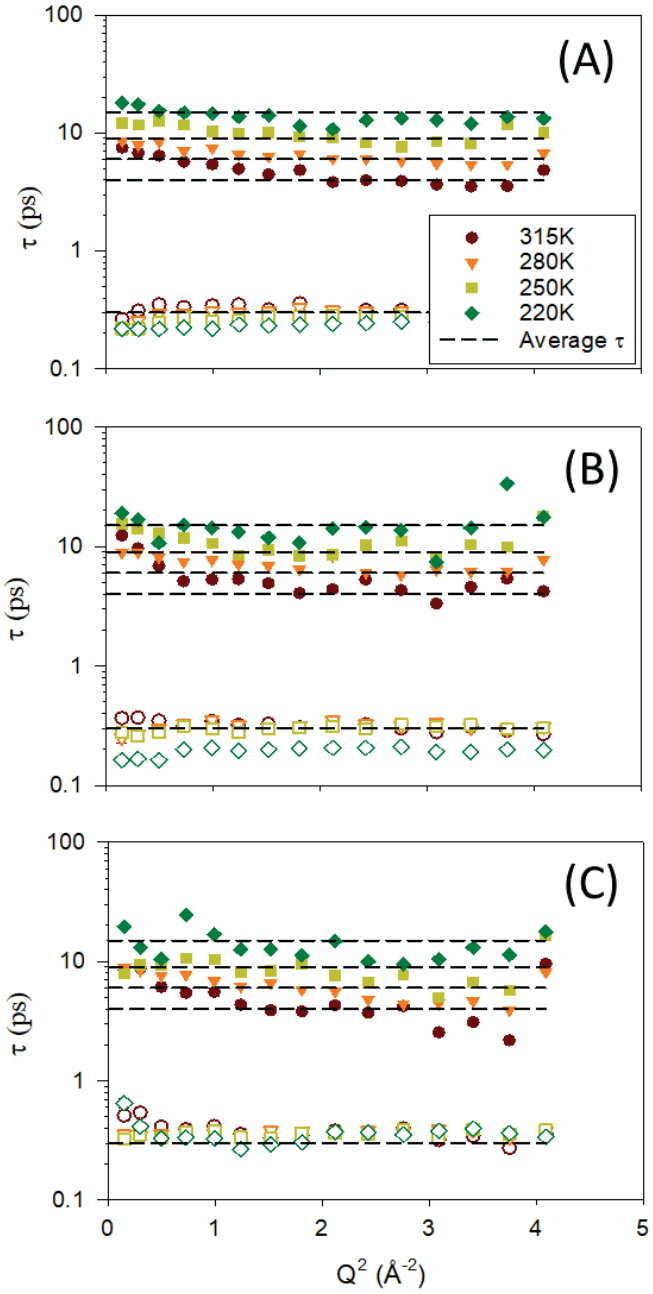

Figure V-8: The characteristic time of slow (filled symbol) and fast (open symbols) motion as a function of Q² at different temperatures values and for three different mixtures of TBAH/TOLD (100/0 (A), 50/50 (B) and 30/70(C)) confined in DVB-PMO matrix. The average time values are presented with dashed lines.

The relaxation time τ_F attributed to the fast motion is almost not affected by temperature and by the addition of TOLD to TBAH (see Figure V-9). It remains generally is the range from 0.26 ps to 0.34 ps, indicating a single average value for all temperatures and mixtures to be about $\tau_F^* = 0.3$ ps.

Table V-3: Average values of different relaxation times τ_S and τ_F for different temperatures and TBAH/TOLD mixtures confined in DVB-PMO matrix.

	% TBAH IN CONFINED MIXTURE					
	100		***50***		***30***	
	τ_F ***(ps)***	τ_S ***(ps)***	τ_F ***(ps)***	τ_S ***(ps)***	τ_F ***(ps)***	τ_S ***(ps)***
315K	*0.32*	*4.63*	*0.33*	*5.11*	*0.34*	*4.25*
280K	*0.31*	*6.52*	*0.32*	*7.08*	*0.33*	*5.86*
250K	*0.30*	*9.87*	*0.31*	*10.56*	*0.32*	*7.99*
220K	*0.26*	*13.64*	*0.27*	*13.65*	*0.28*	*12.91*

Regarding the longest relaxation time τ_S, attributed to a slower motion, we noticed a temperature dependence for the three TBAH/TOLD mixtures. The motion slowed down by cooling and it varied from an average value $\tau_S^* =$ 4 ps at 315K to 14 ps at 220K. We could deduce an activation energy of $E_a = 7.9$ KJ mol^{-1} (cf. Figure V-10).

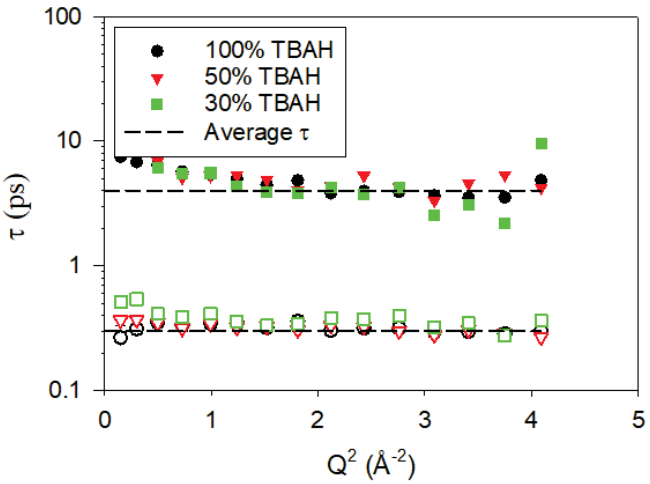

Figure V-9 Effect of TBAH fraction on the relaxation time of slow (filled symbols) and fast (open symbols) dynamics at a common temperature of 315K. Average values of τ are presented with black long-dashed lines.

By comparing different mixtures, τ_S was very similar. These results might appear surprising, since with the addition of toluene (which is less viscous than TBA) an acceleration of the dynamics of TBAH molecules could have been expected. On the other hand, it can be rationalized if one consider the hypothetical formation of a microphase separated system, as already demonstrated for the same mixture confined in silica mesopore

with a very similar pore size.[37, 38, 47, 48] Indeed, if two phases; one rich in TBA and second rich in TOL are present in two different regions in the pores, their mutual influence is reduced. In other words, the dynamics of both molecules will behave independently of the composition. Further results are needed to firmly confirm this hypothesis. Concerning dynamics for instance, one should verify if the dynamics of TOLH is also independent of the TBA fraction. Moreover, by comparison with the bulk, it should be checked if this phenomenon is specific to the confined state or not.

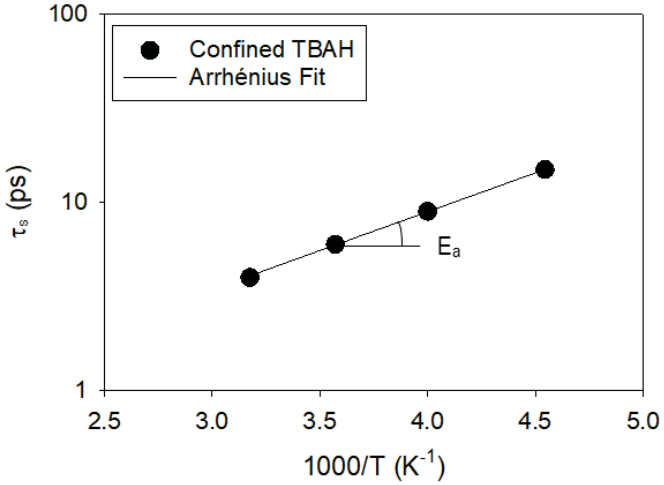

Figure V-10. Relaxation time of slow dynamics against 1000/T for pure TBAH confined on DVB-PMO matrix. Solid line presents a fit with Arrhenius equation as $ln(\tau_S) = A - (1000/T)\ E_a/R$ used to obtain the activation energy $E_a = 7.9\ KJ\ mol^{-1}$.

No clear dependency of τ_S and τ_F on Q was found. It implies that these motions can be considered, to a large extent, as non-dispersive. This result is different from what was obtained for water[17] and which was presented in CHAP-II. In the latter case, the slow dynamics was clearly dispersive and attributed to translational diffusion.

We have considered the possibility that in TBA/TOL confined mixtures, the translational mode was indeed slower than the motion attributed to τ_S If so, it would therefore appear as a third quasielastic very thin line, that light have been missed by the fitted model. As a test, we replaced the elastic component by a sharp Lorentzian, and fitted the obtained alternative function formed by three Lorentzian (3L) instead of the (2L+E) model.

In Figure V-11, we present the half width at half-maximum Γ_T, as a function of Q^2 obtained from (3L) fit. Although Γ_T is actually dispersive as expected for translational diffusion, its value is well below the elastic resolution of the instrument. Most probably, the translational dynamics is so slow that its quasielastic intensity mostly appears as an elastic line within the relaxed resolution of IN6. Accordingly, we abandoned this method of fit and keep the (2L+E) fit method.

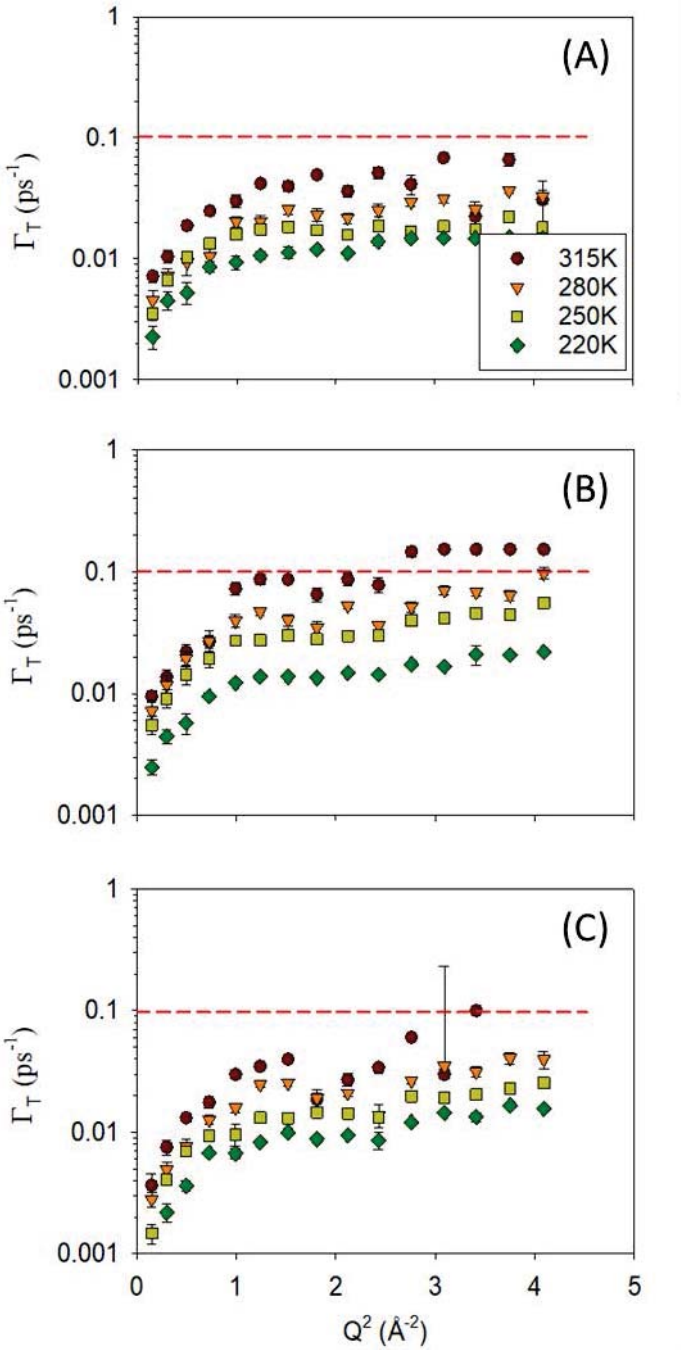

Figure V-11: Evolutions of the half width at half-maximum Γ of the sharp Lorentzian obtained from (3L) fit method of QENS spectra as a function of Q^2 for pure TBAH (A), 50/50 TBAH/TOLD (B) and 30/70 TBAH/TOLD (C) mixtures confined in DVB-PMO matrix at four temperatures, from top to bottom 300 K, 280 K, 250K and 220 K. Red long-dashed lines show the resolution limits.

Slow and fast motions are most likely related to rotational or conformational dynamics, but this cannot be assured at this level. To solve this issues and get a better understanding of the geometry of the trajectory related to each motion, a fit of their corresponding EISFs has been performed.

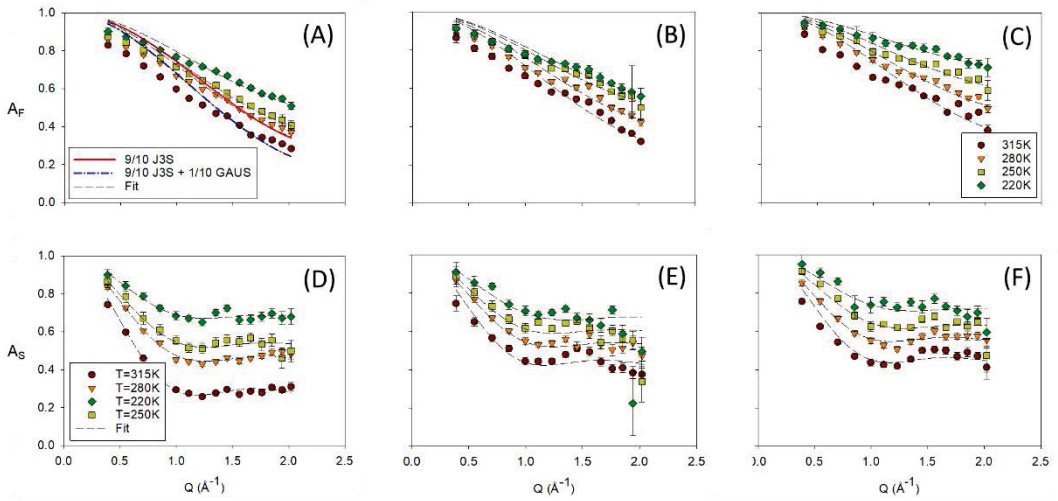

Figure V-12: *Elastic incoherent structure factor (symbols) A_F of fast (above panels) and A_S of slow (below panels) quasielastic relaxation motion at four different temperatures (different colors) for three different TBAH fraction from left to right 0, 0.5 and 0.3 confined in DVB-PMO. Fits with expression (V-5) and (V-6) is presented with dashed-lines for fast and slow dynamics. For comparison, two different approaches describing the broadest quasielastic are presented in the panel (A): (red solid line) model with only jump between 3 sites of the three hydrogens of methyl groups and (blue dash-point line) model described with expression (V-5) with radii R_{J3S} and R_G fixed to 1Å.*

Figure V-12, shows experimental EISFs A_S and A_F of slow and fast mode, respectively, at different temperatures (symbols) and for the three different TBAH/TOLD mixtures. Both A_S and A_F were fitted with a model that incorporates a fraction p of non-mobile molecules (i.e., dynamically frozen on the timescale of the instrument) and a fraction $(1-p)$ of mobile ones.

First of all, we have chosen a general fit model which describes the geometry trajectory as a Gaussian sphere of a diameter R_G as mentioned in the following expression

$$A(Q) = p\,\delta(\omega) + (1-p)\,[exp(-(Q\,R_G)^2)] \quad (V\text{-}4)$$

We used this model, to can obtain a preliminary idea on the typical dimensions of each motion. For the fast mode, we obtained an average radius of $R_G = 1$Å which depends slightly on temperature and on TBAH fraction in the mixture. Thus, we related the obtained value to the C–H and O-H bond length of methyl and hydroxyl groups of TBA molecule. As this motion was very fast and with a local geometry then our reflection was directed towards conformational motion that match with our results. Hence, we have proposed a model which describes the hydrogen movement of the 3 methyl groups by a jump process between 3 sites (discontinuous rotation) of a free radius R^F_{J3S} and the hydrogen of hydroxyl group by a small Gaussian sphere of a fixed radius $R^F_G = 1$ Å as mentioned in the following:

$$A_F(Q) = p^F\,\delta(\omega) + (1-p^F)\,[\frac{9}{10}\,(\frac{1}{3}\,(1+2\,j_0(\sqrt{3}\,Q\,R^F_{J3S})) + \frac{1}{10}\,(e^{-(Q\,R^F_G)^2})] \quad (V\text{-}5)$$

The obtained radius of mobile fraction $(1 - p^F)$ from the fit with this model is $R_{j3S}^F = 1 \pm 0.3$ Å. Concerning now the slow dynamics with a larger amplitude, it rather suggested the overall motion of the entire molecule. We have described it as an isotropic rotation of all hydrogen atoms of TBA molecule on the surface of a sphere (continuous rotation) according to the following expression:

$$A_S(Q) = p^S\,\delta(\omega) + (1 - p^S)\,[j_0(QR_{Rot}^S)]^2 \qquad (V\text{-}6)$$

The obtained radius of mobile fraction $(1 - \mathrm{p^S})$ from the fit with this model is $R_{Rot}^S = 2.6 \pm 0.1$Å,which is consistent with the molecule geometry.The radii of both dynamics are only slightly dependent on temperature and on TBAH concentration in the mixtures. On the other hand, a remarkable effect is deduced on the immobile fraction $\mathrm{p^S}$ and $\mathrm{p^F}$ of slow and fast modes.

In Figure *V-13*, we reveal both temperature and concentration dependence of the immobile fractions. A systematic increase in p with decreasing temperature reflects the larger number of dynamically frozen atoms on cooling. However, this does not necessarily mean a slowing down of the dynamics of the mobile fraction $(1 - \mathrm{p})$ since we have already seen that relaxation time of fast motion τ_F was not dependent on temperature. A 40% increase of the fraction $\mathrm{p^S}$ is associated to a temperature drop of 95 K (from 315K to 220K). On the same temperature range, the fraction $\mathrm{p^F}$ increases by about 30 to 40%.

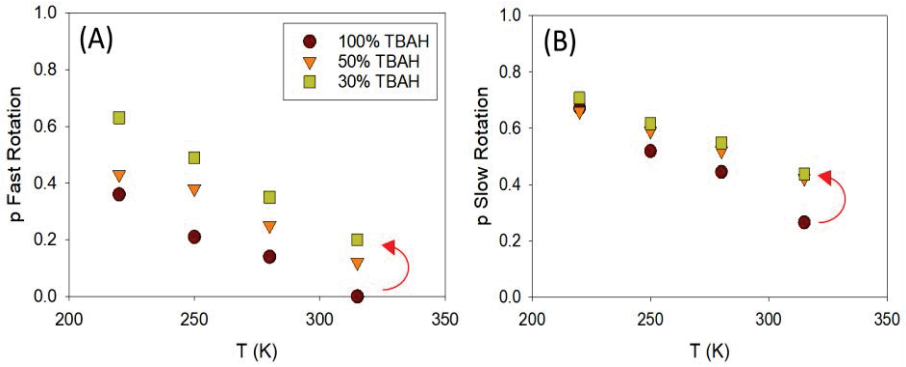

Figure V-13: *TBAH fraction in mixture effect on immobile fractions p^F (A) and p^S (B) of fast and slow motions, respectively as a function of temperature.*

We also noticed a dependence of p on the concentration of mixtures with a systematic increase (red arrow in Figure V-13) with the addition of toluene. The smallest value of p was obtained for 0% TOLD mixture with a raise of 1.5 to 20% for the TBAH/TOLD mixture with *x*=50%. Again, the increase of the fraction of non-mobile TBA with increasing TOL is apparently counterintuitive, since it is opposite to the expected plasticizing effects of TOL. On the other hand, in line with the hypothesis of microphase separation, this could be related to the segregation of TBA molecules at the pore-wall with the addition of toluene. Among all the TBA molecules present in the pore, the fraction of pore-surface adsorbed molecules that obviously present restricted dynamics would therefore increase with increasing the amount of TOL.

Comparing both the fraction of non-mobile atoms, and the characteristic times of the mobile ones, we can formulate the interesting conclusion: on the one hand, the immobile

parts p^S and p^F, that we assumed related to the adsorbed film to the pore interface, increase by the addition of TOL (decrease of TBA fraction). On the other hand, the dynamics of the mobile fraction of TBA molecules that are weakly interacting with the pore surface, and possibly located close to the pore center are barely affected by the amount of TOL.

2-2- TBAD/TOLH Confined Mixtures: Effect of TBA on the Dynamics of TOL

As in the case of TBAH/TOLD mixtures discussed above, the choice of fit with 2L+E was taken after having also tried a model with 3L. The latter model allowed us to have access to a very sharp (very slow) quasielastic line.

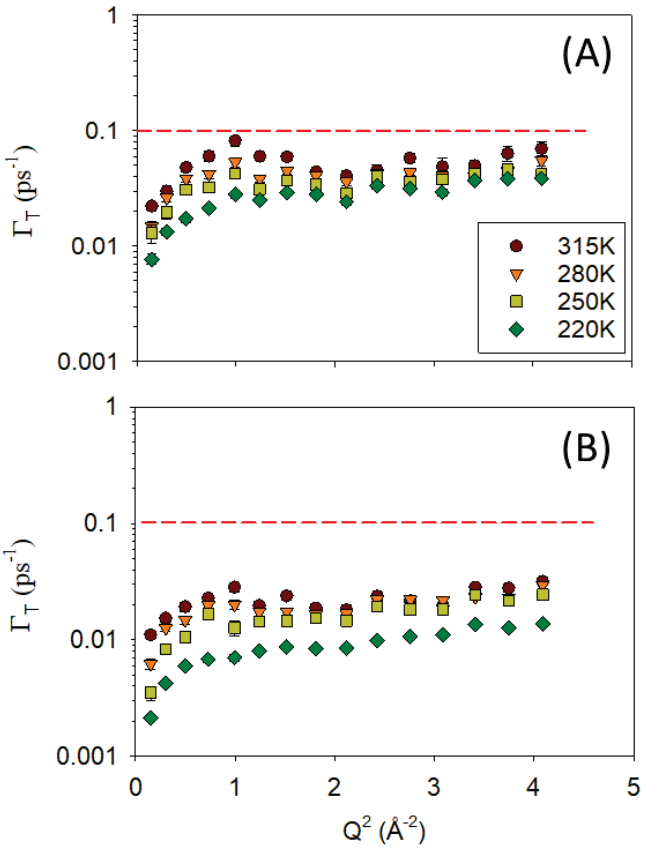

Figure V-14: *Evolutions of the half width at half-maximum Γ of the sharp Lorentzian obtained from (3L) fit method of QENS spectra as a function of Q^2 for pure TOLH (A) and 50/50 TOLH/TBAD mixture (B) confined in DVB-PMO matrix at four temperatures, from top to bottom 300 K, 280 K, 250K and 220 K. Red long-dashed lines show the resolution limits.*

However as shown in Figure V-14, the width of the sharpest Lorentzian was clearly much smaller than the resolution, which was not found safe. We rather considered the existence of a purely elastic component, i.e. 2L+E model, adding a true Dirac function δ(ω) broadened after convolution with the resolution.

In Figure V-15, we show the two relaxation times τ_S and τ_F related to Γ_S and Γ_F, respectively, obtained from the fit with (2L+E) model as a function of Q^2 at the four studied temperatures and for two different mixtures of TOLH/TBAD with various volume fraction of TOLH 1 and 0,5. τ_S and τ_F are readily separable and they differ by a factor of 10, which allowed to talk about two distinct dynamics, i.e. slow and fast. The average values of τ_S and τ_F are illustrated in Figure V-15 by dashed lines since they vary slightly as a function of Q.

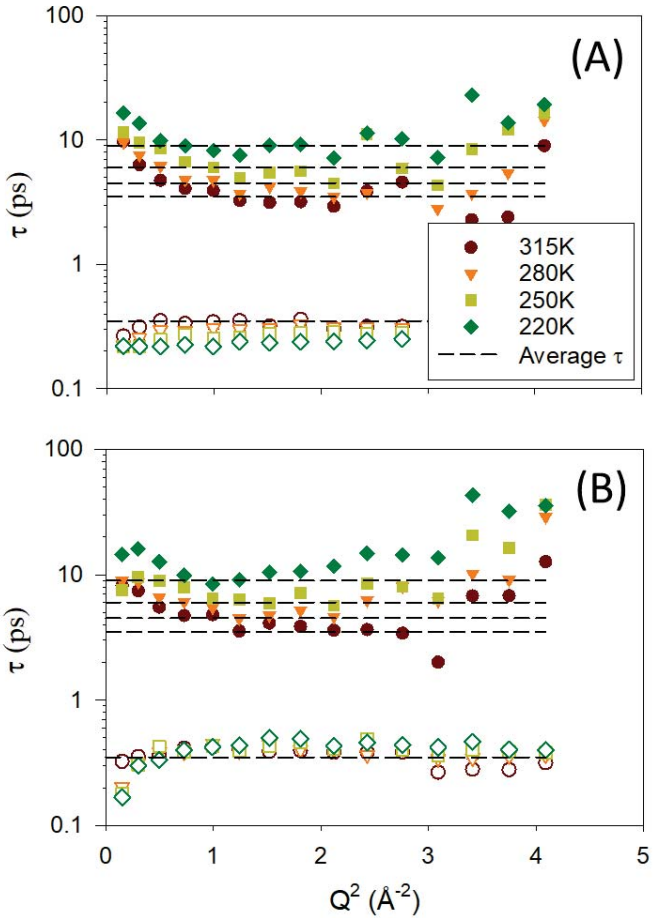

Figure V-15: *The characteristic time of slow (filled symbol) and fast (open symbols) motion as a function of Q² at the four studied temperatures (315K, 280K, 250K and 220K) for two different mixtures of TOLH/TBAD (100/0 (A) and 50/50 (B)). The average time values are presented with long-dashed lines.*

At large Q ($Q^2 > 2\text{Å}^2$) we attributed the greater fluctuation to the drop in intensity of the sharp Lorentzian, as shown in Figure V-7. We indicated the average values of τ_S and τ_F in Table V-4.

Table V-4: Average values of different relaxation times τ_F and τ_F for different temperatures and TOLH/TBAD mixtures confined in DVB-PMO matrix.

	% TOLH IN CONFINED MIXTURE			
	100		***50***	
	τ_F *(ps)*	τ_S *(ps)*	τ_F *(ps)*	τ_S *(ps)*
315K	*0.35*	*3.52*	*0.38*	*4.46*
280K	*0.36*	*4.72*	*0.39*	*6.64*
250K	*0.37*	*6.92*	*0.39*	*8.30*
220K	*0.38*	*10.32*	*0.41*	*13.58*

Both τ_S and τ_F are not affected by TOLH fraction (see Figure V-16). Within statistical fluctuations as a function of Q (in the range from 0.2 ps to 0.5 ps), τ_F does not exibit significant and systematic temperature dependence. A single average value was estimated to be $\tau_F^* = 0.35$ ps for all temperatures and mixtures compositions.

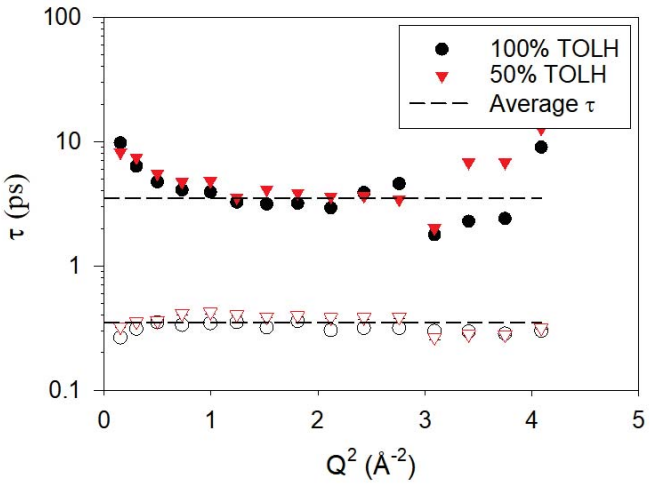

Figure V-16: *Effect of TOLH fraction on the relaxation time of slow (filled symbols) and fast (open symbols) dynamics at a common temperature of 315K. Average values of τ are presented with black long-dashed lines.*

Regarding the slow motion, it was slowed down by cooling going from an average value $\tau_S^* =$ 3.5 ps at 315K to 9 ps at 220K with an activation energy of $E_a = 5.85$ KJ mol^{-1} (cf. Figure V-17).

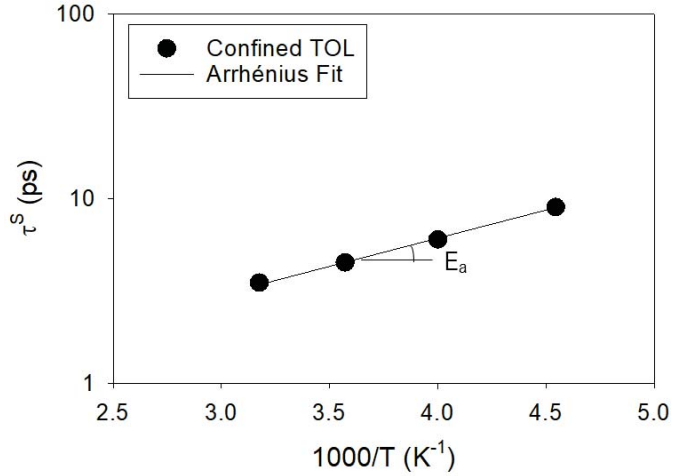

Figure V-17: *Relaxation time of slow dynamics against 1000/T for pure TBAH confined on DVB-PMO matrix. Solid line presents a fit with Arrhenius equation as ln(τ_S) = A - (1000/T) E_a/R used to obtain the activation energy E_a = 5.85 KJ mol^{-1}.*

According to this analysis of the relaxation times of the two quasielastic modes, we can conclude that, although more viscous than TOL, the addition of tert-butanol does not induce a measurable slow-down of the TOLH molecules dynamics. This is again consistent with the hypothesis of phase separation of the two molecules under confinement. The geometry of the trajectories of the slow and fast modes of TOLH were analyzed from the two EISFs A_S and A_F presented in Figure V-18.

After different trials, the most acceptable description, in terms of fit quality and physical meanings, were obtained these two expressions

$$A_F(Q) = p^F\delta(\omega) + (1 - p^F)\left[\frac{3}{8}\left(\frac{1}{3}\left(1 + 2\,j_0(\sqrt{3}\,Q\,R_{j3S}^F)\right) + \frac{5}{8}\left(e^{-(Q\,R_G^F)^2}\right)\right]\right. \quad (V\text{-}7)$$

$$A_S(Q) = p^S\delta(\omega) + (1 - p^S)\,[j_0(QR_{Rot}^S)]^2 \quad (V\text{-}8)$$

In these two expressions (V-7) and (V-8), the hydrogens trajectory is described as a combination of methyl rotation, described by a jump process between 3 sites of a radius $R_{J3S}^F = 1 \pm 0.1$Å for the 3 hydrogens of methyl group and a tumbling mode of the 5 hydrogens of the phenyl group localized in a Gaussian sphere of a radius $R_G^F = 1$Å .

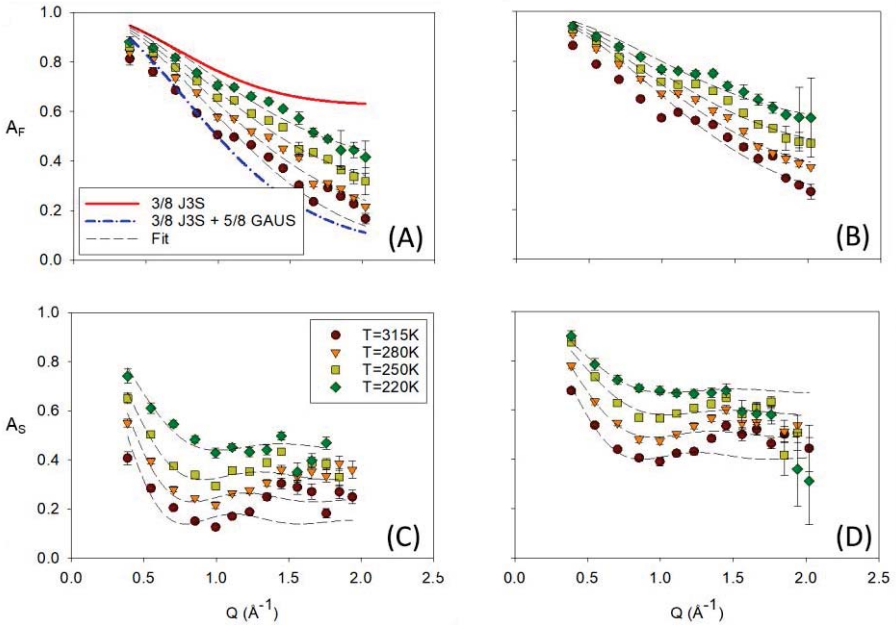

Figure V-18: Elastic incoherent structure factor (symbols) A_F of fast (above panels) and A_S of slow (below panels) quasielastic relaxation motion at four different temperatures (different colors) for three different TOLH fraction from left to right 0 and 0.5 confined in DVB-PMO. Fits with expression (V-7) and (V-8) is presented with dashed-lines for fast and slow dynamics. For comparison, two different approaches describing the broadest quasielastic are presented in the panel (A): (red solid line) model with only the three hydrogens of methyl made a jump between 3 sites and (blue dash-point line) model described with expression (V-7) with radii R^F_{J3S} and R^F_G fixed to 1Å.

We compared with two alternative views; in first (red continues line in Figure V-18-A) we checked the case when only the three hydrogens of methyl made a jump between 3 sites. The second is similar to our fit model but with radii R^F_{J3S} and R^F_G fixed to 1Å. Concerning hydrogens performing the slow mode, their EISF match well with the isotropic rotation model on the surface of a sphere of radius $R^S_{Rot} = 3.5 \pm 0.5$ Å. At this level, we have been able to get a better description of the mobile fraction $(1 - p^S)$ and $(1 - p^F)$ of slow and fast motions, respectively. Upcoming, we will focus on the non-mobile part p^S and p^F related to the elastic part of both dynamics.

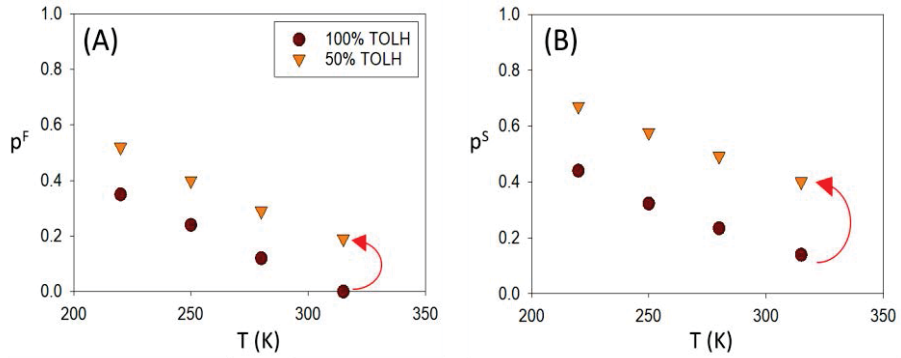

Figure V-19: Effect of TOLH fraction on immobile fractions p^F(A) and p^S (B) of fast and slow motions, respectively as a function of temperature.

In Figure V-19, we reveal both temperature and concentration dependence of the immobile fractions. A systematic increase in p with decreasing temperature reflects the larger number of dynamically frozen molecules on cooling. However, this does not necessarily mean a slowing down of the dynamics of mobile fraction $(1-\mathrm{p})$ since we have already seen that relaxation time of fast motion τ_F was not dependent on temperature. A 40% increase of the fraction $\mathrm{p^F}$ is associated to a temperature drop of 95K (from 315K to 220K) and a 20 to 30% increase of the fraction $\mathrm{p^S}$. We also noticed a dependence of p on the concentration of mixtures with a systematic increase (red arrow in Figure V-19) with TBA adding. The smallest value of p was obtained for 0% TBAD mixture with a raise of 20% for 50% TBAD mixture.

3. Bulk mixtures

Unlike confined mixtures, the dynamic structure factors of bulk liquids did not present a purely elastic component. However, three Lorentzian functions were needed to reproduce the quasielastic broadening. The absence of elastic line implies a complete loss of density-density correlations on the timescale of the instrument, which is conceivable in case of a non-local mode, such as translational diffusion. Bulk spectra were fitted by (3L) model which includes a sharp, an intermediate and a broad Lorentzian. The broad and intermediate Lorentzian were related to Fast and Slow local motions, respectively, (i.e. involving a non-zero EISF), while the sharp one was tentatively related to translational motion (i.e. a purely quasielastic line with a vanishing EISF). Hence, the fitted intensity with (3L) model can be written as:

$$I^{3L}(Q,\omega) = \left[I_{Sharp}(Q)L_{Sharp}\left(Q,\omega,\Gamma_{Sharp}\right) + I_{Inter}(Q)L_{Inter}(Q,\omega,\Gamma_{Inter}) + I_{Broad}(Q)L_{Broad}(Q,\omega,\Gamma_{Broad})\right]\otimes R(Q,\omega) \quad (V\text{-}9)$$

The corresponding physical model, assuming that the three different motions are independent, writes as

$$S(Q,\omega) = K\,[L_T(Q,\omega,\Gamma_T)]\otimes\left[A_S(Q)\delta(\omega) + \left(1-A_S(Q)\right)L_S(Q,\omega,\Gamma_S)\right]\otimes\left[A_F(Q)\delta(\omega) + \left(1-A_F(Q)\right)L_F(Q,\omega,\Gamma_F)\right]\otimes R(Q,\omega) \quad (V\text{-}10)$$

Owing to the fact that $\Gamma_T \ll \Gamma_S \ll \Gamma_F$, it was approximated to,

$$S(Q,\omega) = K\left[A_S(Q)A_F(Q)[L_T(Q,\omega,\Gamma_T)] + \left(1-A_S(Q)\right)A_F(Q)L_S(Q,\omega,\Gamma_S) + \left(1-A_F(Q)\right)L_F(Q,\omega,\Gamma_F)\right]\otimes R(Q,\omega) \quad (V\text{-}11)$$

Comparing the latest equation with the fitted function allowed us to determine the EISFs $A_S(Q)$ and $A_F(Q)$ of the slow and fast local modes, as well as the quasielastic broadening of the three dynamics $\Gamma_T, \Gamma_S,$ and Γ_F. In Figure V-20, we show the different intensities obtained from the fit of QENS spectra by equation (V-11) for different TBAH and TOLH mixtures.

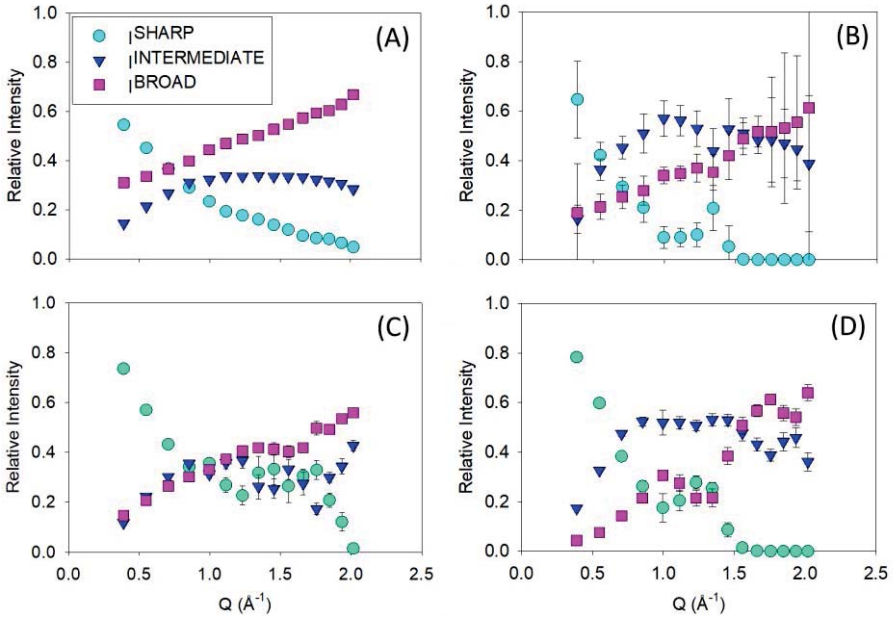

Figure V-20: The experimental intensities obtained by the fit of the QENS spectra for bulk: pure TBAH (A), pure TOLH (B), 50/50 TBAH/TOLD (C) and 50/50 TOLH/TBAD (D) at a temperature of 315K.

3-1- Fast and Slow Dynamics

Figure V-21, shows relaxation time τ as a function of Q^2 for bulk mixtures of TBAH and TOLH at the studied temperatures. As the melting point of TBA in the bulk state is 298K, only the highest temperature 315K was studied for pure TBAH, as well as for its corresponding mixture TBAH/TOLD.

The melting point of bulk TOL being 178K, we measured TOLH, and its associated mixture TBAD/TOLH at two different temperatures 250K and 315K. The relaxation time of slow and fast dynamics τ_S and τ_F, respectively are separable by a factor of 10. τ_F is quite independent on Q, however, we notice a greater dispersion of τ_S. This suggests that this mode actually comprises a distribution of relaxation time, possibly related to different degrees of freedom that are difficult to disentangle experimentally.

This situation might be favored in the bulk case by the possible diffusion of the molecule center of mass on the studied timescale. Due to this distribution of τ_S, we have extracted an average value τ^*_S presented by a black dashed-line in the figure, to allow a simplified discussion on its dependence on the temperature and composition. The variations with Q of τ_F were much smaller, which better justified the discussion based on its average value. The relaxation time of the fast motion τ_F=0.3±0.1 ps for TOLH in TBAD/TOLH mixtures and 0.2±0.05 ps for TBAH in TBAH/TOLD mixtures and no temperature effect is noticed. The

relaxation time of the slow motion is τ_S=1.1±0.5 ps for TOLH in TBAD/TOLH mixtures and 1.05±0.5 ps for TBAH in TBAH/TOLD mixtures with a small slow-down of the toluene dynamics with cooling.

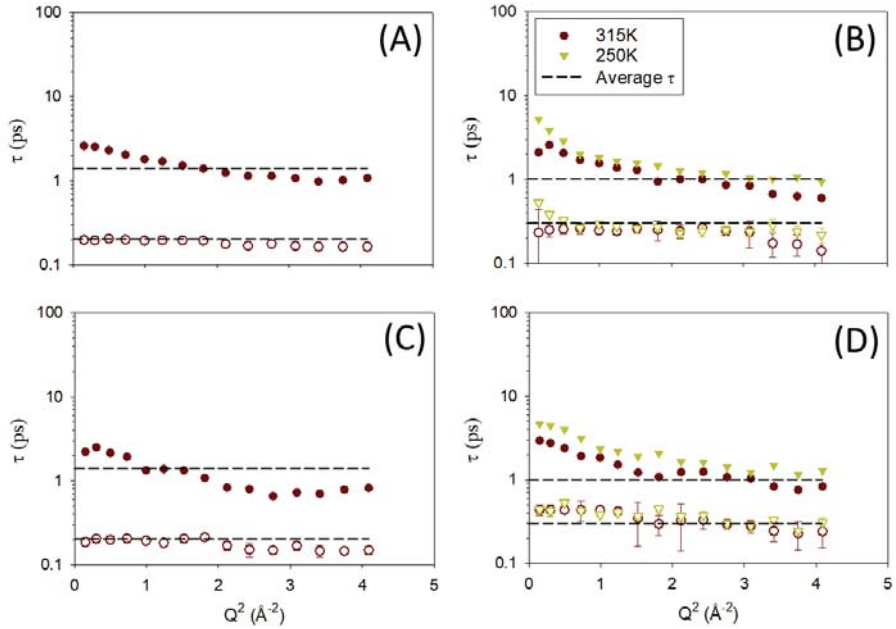

Figure V-21: *The characteristic time of slow (filled symbol) and fast (open symbols) motion as a function of Q² at the studied temperatures: only at 315K for TBAH (A) and 50%TBAH (C) and at 315K and 250K for 100% TOLH (B) and 50% TOLH (D). The average time values are presented with long-dashed lines.*

When comparing the dynamics of each pure liquid, one can notice a slight difference in their own relaxation times (Figure V-21-(A vs B)). However, the important point is that this difference between TBAH and TOLH fast dynamics remained about the same, even in the mixtures (Figure V-21-(C vs D)). In other words, concerning the mixing effects, no visible differences were seen in the fast dynamics of each component (TBAH and TOLH) as a function of the concentration studied. This conclusion made for the bulk mixtures, goes along with that already made for the confined ones.

At first sight, this could suggest that, in the confined state, the dynamics of the mobile fraction of molecules performing slow and fast local dynamics is in fact reminiscent of the bulk mixtures, and not specific to the confined phases. This fraction of mobiles molecules is likely located in the pore center, which would make sense. Although sensible at a qualitative level, a different conclusion must be formulated at the quantitative level. Confinement obviously induces an important slowdown of the dynamics, as illustrated in by the averaged relaxation times measured at T=315K in Table V-5.

The reduction of mobility is especially important for the slower process of TBA molecules (by a factor of 4), and to a less extend for the slower process TOL molecules (about a factor of 3). The fast processes, which are related to conformational degrees of freedom are, as expected, less affected by confinement. Considering the errors bars, the slowdown, if any, should not exceed 20% in the latter case.

Table V-5: Average values of the two relaxation times τ_S and τ_F at T=315K, for TOLH, TBAH in the bulk liquid and confined in DVB-PMO matrix.

	TBAH		**TOLH**	
	τ_F (ps)	τ_S (ps)	τ_F (ps)	τ_S (ps)
Bulk	0.2 ±0.05	1.05 ±0.1	0.3 ±0.1	1.1 ±0.5
Confined	0.3 ±0.05	4 ±1	0.35 ±0.05	3.5 ±1

Following this part dedicated to the discussion of the relaxation times of the two local modes, we now consider the nature of their spatial trajectories. To do so, we have fitted their EISFs A_F and A_S by the same expressions as used for the confined mixtures cf. (V-5), (V-6) and (V-7), (V-8). The case of TBA is considered first. The EISFs of TBAH in the pure bulk liquid and in the TBAH/TOLD bulk mixture are shown in Figure V-22. We remind here that a unique temperature, T=315K, is considered due to crystallization of bulk TBA.

The fitted fraction of non-mobile atoms (i.e. remaining elastic term), p^F and p^S are null in the present case. This means that all TBA molecules perform both fast and slow dynamics. In the fit of A_F with expression (V-5), we set the rotation radius R_G of hydroxyl hydrogen to 1 Å and obtained a value of R_{J3S}=0.76 Å regardless of TBAH fraction (x_{TBA}) in the mixture.

For comparison, two other models are presented in Figure V-22-A; in first (red solid line in Figure V-22-A) we proposed that only the three hydrogens of methyl made a jump between 3 sites. We also computed the predictions from a model similar to our fitted equation, but with radii R_{J3S}^F and R_G^F fixed to 1Å. Interestingly, the EISF and the deduced trajectories related to the fast relaxation of bulk TBA and bulk TBAH/TOLD mixtures are very similar to those obtained for the same liquids in the confined stated, as discussed in the 2nd part of this chapter. This supports their attribution to conformational dynamics that are mostly determined by the molecule shape, and to a much lesser extent to the local environment.

A different observation was made for the slow dynamical process. Indeed, from the fit of A_S with expression (V-6), we obtained R_{Rot}^S=1.25 Å and R_{Rot}^S=1.17 Å for pure TBAH and 50/50 TBAH/TOLD, respectively. These radii are much smaller than the values obtained in the case of confined liquids (R_{Rot}^S=2.6±0.1Å,). To illustrate this important difference, we have shown (solid red line) on the same graph (Figure V-22-B) the model of rotation on a surface of a sphere of a radius of 2.6 Å (mean radius obtained in the case of confined TBAH) with $p^S = 0$.

On the contrary to confined TBA, it is obvious for bulk TBA that the obtained parameter R_{Rot}^{S}=1.17-1.25 Å cannot be linked to the geometrical distance between the H atoms and the mass center of the TBA molecule. From this point of view, it has lost part of its physical meaning. The reason for that probably stems from the necessary simplifications made in the dynamical model we applied, that assumes only two independent, and perfectly determined, local modes (i.e. methyl and isotropic molecule rotation). Although very well–suited for confined TBA, it obviously misses part of the dynamical complexity of bulk liquids. A possible explanation of the success in describing the rotational dynamics of TBA in confinement is the freezing, on the experimental timescale, of the translational diffusion. In the bulk liquid, the observation of translational dynamics (as analyzed in the next section) provides additional degrees of freedom and paths for towards structural relaxation that may also couple to local dynamics.

We now consider the local dynamics of the TOLH molecules. In Figure V-23, we show A_F and A_S for pure and 50% mixture of TOLH at two different temperatures 315K and 250K. At the higher studied temperature 315K, p^F and p^S are null which means that all molecules perform both fast and slow dynamics. On cooling from 315K to 250K, p^S and p^F of pure TOLH increase from zero to, respectively, 0.24 and 0.32 with an increase, for both p^S and p^F, of a value of 0.1, approximately, by adding 50% of TBAD to the mixture.

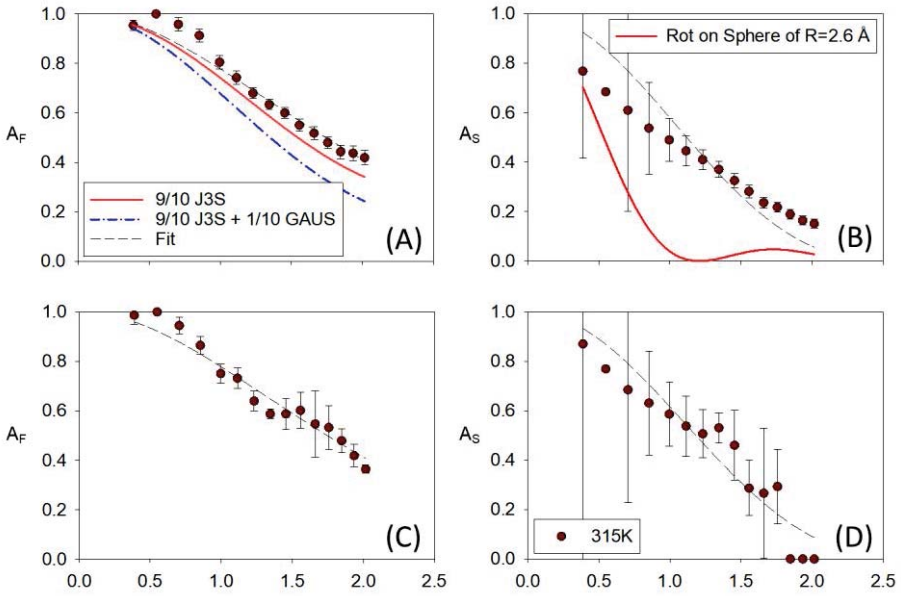

Figure V-22: Elastic incoherent structure factor (symbols) A_F of fast (left panels) and A_S of slow (right panels) quasielastic relaxation motion at 315K for bulk pure TBAH (above panels) and bulk 50/50 TBAH/TOLD (below panels). Fits with expression (V-5) and (V-6) is presented with dashed-lines for fast and slow dynamics, respectively. For comparison, two different approaches describing the broadest quasielastic are presented in the panel (A): (red solid line) model with only the three hydrogens of methyl making a jump between 3 sites and (blue dash-point line) model described with expression (V-5) with radii R_{J3S} and R_G fixed to 1Å. Panel (B): (red solid line) model of a rotation on a sphere of a radius R=2.6 Å as in the case of confined TBAH mixtures.

From the fit of A_F with expression (V-5), with an average radius $R^* = \frac{5}{8} R_G + \frac{3}{8} R_{J3S} =$ 0.8Å, regardless of TOLH fraction (x_{TOL}) in the mixture. For comparison two other models are presented in Figure V-23-A; first (red solid line) we proposed that only the three hydrogens of methyl made a jump between 3 sites and in second is similar to our fit model but with radii R^F_{J3S} and R^F_G fixed to 1Å. In the fit of A_S with expression (V-8), we obtained R^S_{Rot}=1.62 Å, regardless of TOLH fraction (x_{TOL}) in the mixture. Again, like for TBA, this radius is much smaller than the value obtained in the case of confined TOLH.

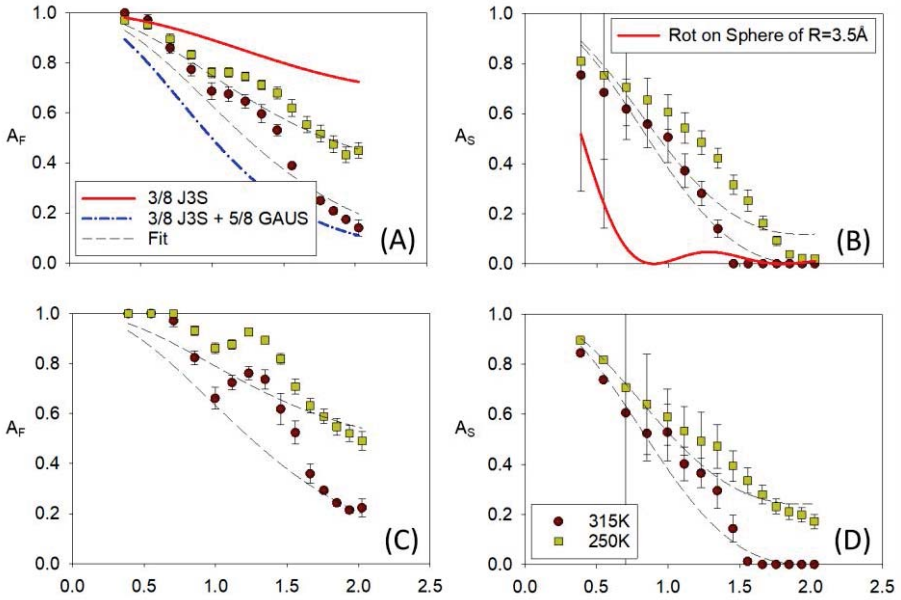

Figure V-23: Elastic incoherent structure factor (symbols) A_F of fast (left panels) and A_S of slow (right panels) quasielastic relaxation motion at 315K and 250K for bulk pure TOLH (above panels) and bulk 50/50 TOLH/TBAD mixture (below panels). Fits with expression (V-7) and (V-8) is presented with dashed-lines for fast and slow dynamics, respectively. For comparison, two different approaches describing the broadest quasielastic are presented in the panel (A): (red solid line) model with only the three hydrogens of methyl made a jump between 3 sites and (blue dash-point line) model described with expression (V-7) with radii R_{J3S} and R_G fixed to 1Å. And in panel(B): (red solid line) model of a rotation on a sphere of a radius R=3.5 Å as in the case of confined TOLH mixtures.

To highlight this important difference, we have shown (continuous red line) on the same graph (Figure V-23-B) the model of rotation on a surface of a sphere of a radius of 3.5 Å (mean radius obtained in the case of confined TOLH) with p^S= 0. As discussed in the previous section for TBA, it appears that the freezing-in of the translation for confined TOL allowed us to better identify the rotational dynamics, while the more complex dynamics of bulk TOL on the experimental timescale cannot be catched by a simple model of independent modes. A very different strategy could have also been used, such as a fit with a Kohlrausch (stretched exponential) function. This type of analysis, though often applied to glassforming molecular liquids, would have provided effective parameters (relaxation time and stretching exponent) but not additional physical insights into the nature of microscopic dynamics as already obtained from the model we used.

3-2- Translational Dynamics

We present in Figure V-24, the linewidth of the sharpest lorentzian Γ_T obtained from the I^{3L} fit model (V-9). It is presented as a function of Q^2 for bulk TBAH and TOLH, in the pure liquids and in 50/50 mixtures. At small Q, Γ_T increases linearly with Q^2, which conforms the normal Fick translational diffusion law. However, a deviation occurs at large Q, where Γ_T bends and tends asymptotically towards a constant value denoted $1/\tau_0$. In fact, the Fickian diffusion model assumes a continuous motion process.

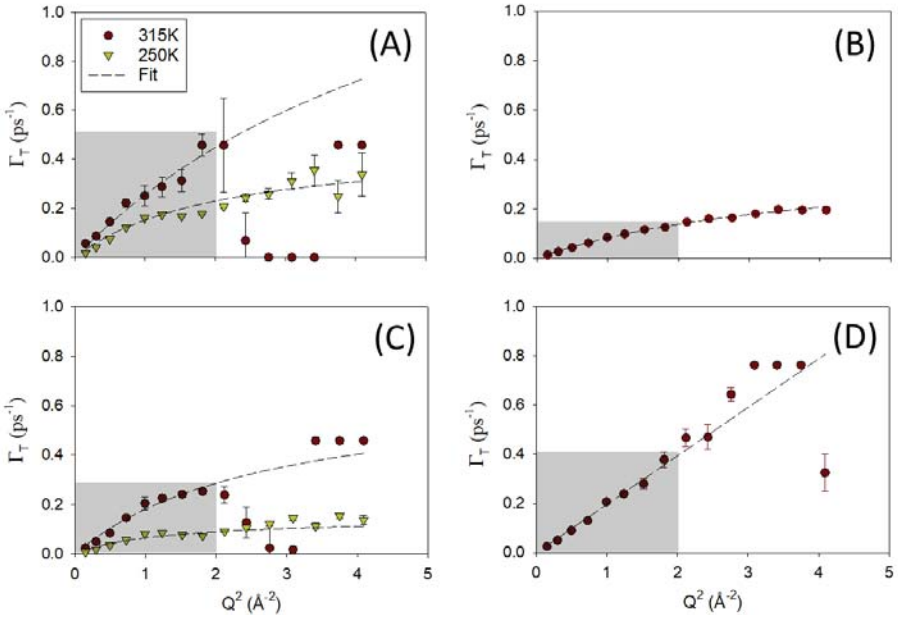

Figure V-24: Evolutions of the half width at half-maximum Γ_T of the sharp Lorentzian obtained from (3L) fit method of QENS spectra as a function of Q^2 for bulk pure TOLH (A), pure TBAH (B), 50/50 TOLH/TBAD (C) and TBAH/TOLD (D) mixtures at the studied temperatures. The fit of region $Q^2 < 2$ Å^2 with equation (V-12) is presented by long-dashed lines.

Deviation from this assumption is observed when considering small displacements (*i.e.* for Q larger than the inverse particle distance), where a discontinuous mechanism is related to the finite molecular size and the local order in the liquid. The linewidth was modelled by the well-known jump-diffusion model, which assumes that the translation motion proceeds by successive elementary jumps. Between two jumps, the particle remains localized for a typical time τ_0 on a molecular site, with a spatial extension limited to the amplitude of vibrational modes. Applying the usual assumptions that the jump can be regarded as instantaneous with respect to the delay τ_0 spent by the particle on a site, and that the jump length l is much larger than the spatial extension of each site, the linewidth of the sharpest Lorentzian was fitted with:

$$\Gamma_T(Q) = \frac{D_T\, Q^2}{1+\tau_0 D_T\, Q^2} \qquad (V\text{-}12)$$

where D_T is the diffusion coefficient and τ_0 the mean jump time the fit.

We fitted the model to the region $Q^2 < 2Å^2$. Above this value, the linewidths presented large unphysical fluctuations. This is simply due to the fact that the intensity of the quasielastic Lorentzian attributed to translation is dumped by the EISFs of the local modes (cf. (V-11)). As such, it decays to zero for $Q>1.5$ $Å^{-1}$, as illustrated in Figure V-20, making the estimation of its width very difficult. The prediction from the model was extended to the entire Q range for information. As expected, toluene is more diffusive than tert-butanol with a D_T of 3.0 ±0.1 10^{-9} m^2 s^{-1} and 1.0 ±0.1 10^{-9} m^2 s^{-1}, respectively. A large temperature effect on the translational mode is noted in the case of toluene with a decrease in its diffusion coefficient with cooling.

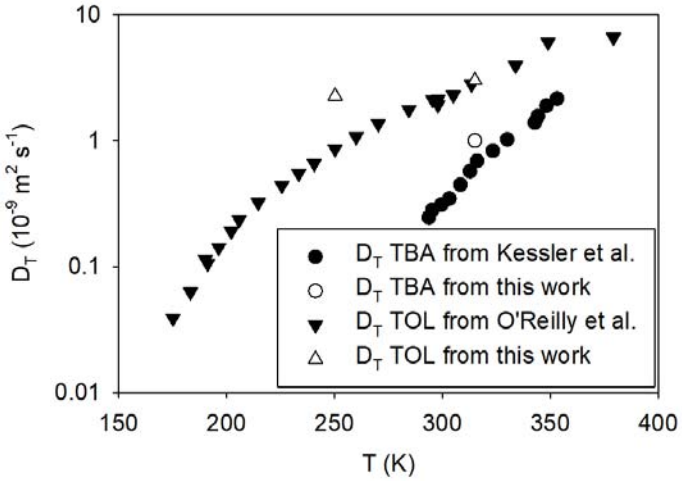

Figure V-25: Comparison of D_T obtained from this work with literature results obtained for bulk TBA and TOL with steady field pulsed NMR diffusion measurements from Kessler et al. (1967) and O'Reilly and Peterson (1972).

In Figure V-25, we compared our results with diffusion coefficients obtained from steady field pulsed NMR diffusion measurements from Kessler et al. (1967) and O'Reilly and Peterson (1972) for TBA and TOL, respectively. At 315K, the two diffusion coefficients are close to those obtained from the literature. On the other hand, we noticed a deviation at 250K in the case of toluene.

From Figure V-26, we noticed that in the mixtures the dynamics of TOL and TBA converged towards the same values with D_T= 2.3±0.1 10^{-9} m^2 s^{-1} both for TOLH in the TBAD/TOLH mixture and for TBAH in the TBAH/TOLD sister mixture. This indicates that the translational dynamics of both molecules, which have comparable sizes, is eventually determined by the overall viscosity of the mixture. This is expected to happen on length scales where the liquid mixture forms an homogenous phase.

Unfortunately, within the dynamical range covered by the IN6 spectrometer, we did not have access to the diffusion coefficients of the confined mixtures, and check this hypothesis. Being too slow, the translational dynamic appeared as an entirely elastic component, and no additional quantitative information can be extracted thereof. On the other hand, it appeared that also the local modes presented a fraction of non-mobile atoms, quantified by the p fraction. As a reminder, the immobile fraction p increases with the addition of TOLD to TBAH (see Figure V-13) which means a slowing down of TBAH molecules by adding toluene. This apparent anti-plasticizing effect was attributed to the segregation of TBA to

the pore wall. It is the opposite trend in the case of bulk, where TBA molecules are, as normally expected, accelerated by adding toluene.

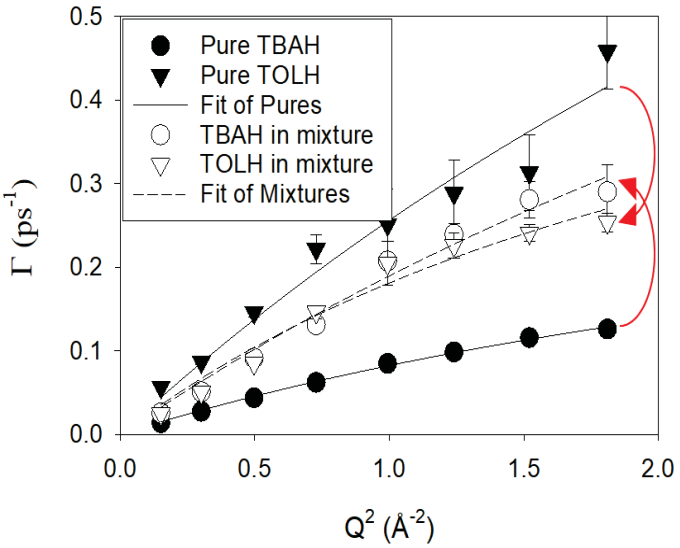

Figure V-26: Effect of mixing TOL and TBA on the translational dynamics for a common temperature of 315K.

IV. CONCLUSION

The QENS method allowed us to follow specifically the dynamics of the hydrogenated molecules, due to the significance of incoherent contribution, in isotopically labelled pure and binary mixtures of TBA and TOL molecules. We have compared bulk liquids and confined liquids in DVB-PMO matrix, and investigated different temperatures.

The experimental spectra of the confined mixtures were fitted by a 2 lorentzians and one elastic component (2L+E model) and those of bulk mixtures were all fitted by a 3 lorentzians (3L model). Therefore, we started our result and discussion part by giving both expressions of theoretical intensities (V-1) and (V-9) linked respectively to (2L + E) and (3L) fit models. We defined, as well, the different parameters of each theoretical model to allow a good understanding of their corresponding physical meaning. By following this approach, we have defined two independent local modes in the case of confined mixtures (slow mode (S) and fast mode (F)) and three independent modes in the case of bulk mixtures (translational mode (T), slow mode (S) and fast mode (F)).

The Figure V-27 gives a synthetic description of the observed confinement effects on the dynamics of the studied liquid mixture.

In the case of confined TBAH/TOLD (respectively TOLH/TBAD) mixtures, the fast mode (F) is characterized by a relaxation time τ_F which essentially remains in the range 0,3-0,4 ps (respectively 0,2-0,5 ps), when decreasing temperature from 315 K to 220 K. The slow mode (S) is characterized by a relaxation time τ_S which exhibits a noticeable temperature dependence, going from 4 ps to 15 ps (respectively from 3,5 ps to 9 ps) on cooling on the same temperate range. We found that the temperature variation of τ_S follows an Arrhenius law with an activation energy Ea = 7,90 kJ mol^{-1} (respectively 5,85 kJ mol^{-1}).

The fact that τ_F is quite independent on temperature, concentration and on the molecule nature (TBA or TOL) is consistent with its attribution to conformational fluctuations. Indeed, we have related them to methyl group rotation and aromatic ring tumbling. Additionally, we observed no clear effect of concentration on the value of τ_S, which might appear a bit more surprising, as it was related to some motions of larger amplitude, such as molecule rotation. Hence, it seems that the local rotational dynamics of each distinct molecule occur in a local environment that does not significantly change with composition.

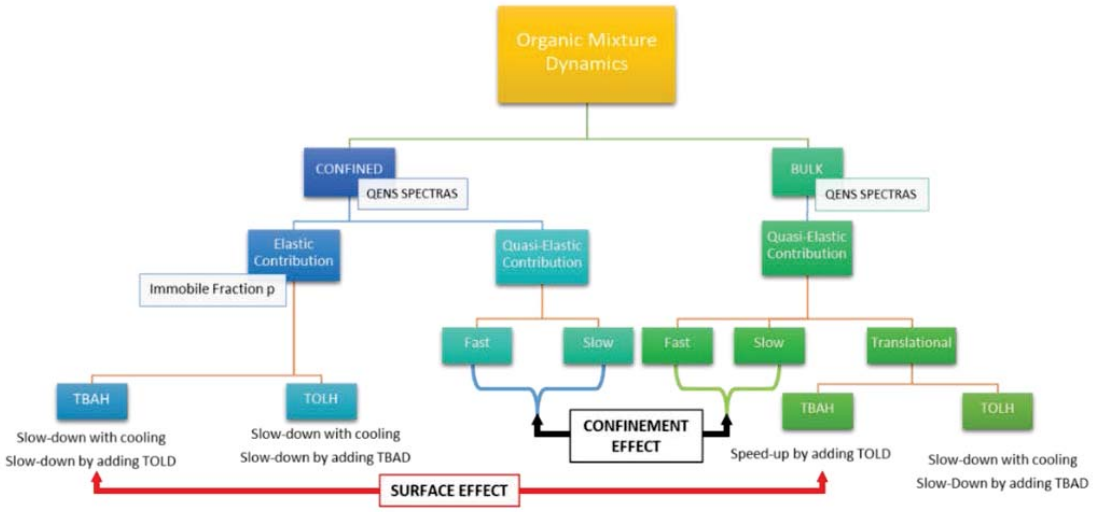

Figure V-27: Synthetic view on the study of confinement effect on the organic mixture dynamics by QENS technique.

At first sight, this appeared to us as a hint for the existence of a microphase demixing phenomenon under confinement in DVB-PMO amphiphilic pores, while such observation was so far limited to hydrophilic pores that are characterized by a much higher TBA-surface interaction (i.e. core-shell structure in SBA-15[38] and MCM-41[37, 47]). However, comparing the dynamics of confined and bulk mixtures, we showed that, in any cases, the relaxation time τ_S associated to the local dynamics was not sensitive enough to the average mixture composition to properly answer this question about the hypothetical microphase separation in DVB-PMO. Interestingly, we also quantified a significant confinement-induced slowdown of the rotational dynamics, by a factor of 3 to 4, for TOL and TBA molecules, respectively.

We also succeeded in describing the spatial trajectory of the two different local modes with a fairly good agreement with experimental data for confined liquids. The same model performed in an approximated manor for bulk liquids due to the overlap of additional degrees of freedom, provided by translational diffusion on the studied experimental timescale. The trajectory geometry of the fast mode was described with a model of a jump between 3 sites (for methyl hydrogens rotation) and a rotation in a Gaussian sphere (for the rest of the hydrogens). The obtained characteristic radii were in the range of 1 Å ± 0.1 Å which is in agreement with the molecule geometry. Regarding the slow local mode, we have described it by an isotropic rotation on the surface of a sphere of radius 2,6 Å ± 0,5 Å and 3,5 Å ± 0,5 Å respectively for TBAH and TOLH molecules. This mode is therefore attributed to the overall isotropic rotation of the molecule around its center of mass.

Moreover, in the confined states, we defined a non-mobile fraction (relative to instrumental time scale) p for each local mode (S) and (F). For TBAH mixtures, we found that the increase in the values of p^S and p^F with cooling from 320K to 220K, were respectively 0.4 and about 0.2-0.3. For TOLH mixtures, the same temperature variation led to the increase in the values of p^S and p^F of respectively 0.4 and about 0.3-0.4.

Strikingly, we also found that, for both TOLH and TBAH, the immobile fractions p increase when going for the pure liquid to the binary mixture. This unexpected phenomenon observed for the local modes could not be investigated for the translational diffusion. Indeed, the latter type of motion was considerably reduced due to confinement effects and entered the elastic energy resolution of the instrument. On the contrary for the bulk liquids, the diffusion coefficients could be evaluated. It showed a very different behavior, with the slowdown of TOLH diffusion when adding to it the more viscous TBA liquid. Symmetrically, an acceleration of the TBA diffusion was observed when adding to it the non-H-bonded and weakly polar TOL liquid. As a result, the diffusion coefficients of both constituents merge in the mixture, as expected for homogeneous phases of non-interacting molecules with comparable sizes.

In confinement, the increase of the fraction of non-mobile TBA molecules during its dilution with TOL does not follow this trend, and rather indicates an anti-plasticizing effect. This would be consistent with the preferential adsorption of TBA molecules at the interface, as indicated by small angle neutron diffraction and dynamical vapor sorption experiments.

REFERENCES

1. *Jackson CL, McKenna GB. THE GLASS-TRANSITION OF ORGANIC LIQUIDS CONFINED TO SMALL PORES. Journal of Non-Crystalline Solids 1991;131: 221-24.*

2. *Granick S. MOTIONS AND RELAXATIONS OF CONFINED LIQUIDS. Science 1991;253(5026): 1374-79.*

3. *Zhang J, Liu G, Jonas J. EFFECTS OF CONFINEMENT ON THE GLASS-TRANSITION TEMPERATURE OF MOLECULAR LIQUIDS. Journal of Physical Chemistry 1992;96(8): 3478-80.*

4. *Arndt M, Stannarius R, Gorbatschow W, Kremer F. Dielectric investigations of the dynamic glass transition in nanopores. Physical Review E 1996;54(5): 5377-90.*

5. *Schuller J, Melnichenko YB, Richert R, Fischer EW. DIELECTRIC STUDIES OF THE GLASS-TRANSITION IN POROUS-MEDIA. Physical Review Letters 1994;73(16): 2224-27.*

6. *Scheidler P, Kob W, Binder K. The relaxation dynamics of a confined glassy simple liquid. European Physical Journal E 2003;12(1): 5-9.*

7. *Christenson HK. Confinement effects on freezing and melting. Journal of Physics-Condensed Matter 2001;13(11): R95-R133.*

8. *Morineau D, Xia YD, Alba-Simionesco C. Finite-size and surface effects on the glass transition of liquid toluene confined in cylindrical mesopores. Journal of Chemical Physics 2002;117(19): 8966-72.*

9. *Alba-Simionesco C, Dosseh G, Dumont E, et al. Confinement of molecular liquids: Consequences on thermodynamic, static and dynamical properties of benzene and toluene. European Physical Journal E 2003;12(1): 19-28.*

10. *Morineau D, Alba-Simionesco C. Liquids in confined geometry: How to connect changes in the structure factor to modifications of local order. Journal of Chemical Physics 2003;118(20): 9389-400.*

11. *Alcoutlabi M, McKenna GB. Effects of confinement on material behaviour at the nanometre size scale. Journal of Physics-Condensed Matter 2005;17(15): R461-R524.*

12. *Alba-Simionesco C, Coasne B, Dosseh G, et al. Effects of confinement on freezing and melting. Journal of Physics-Condensed Matter 2006;18(6): R15-R68.*

13. *Morineau D, Alba-Simionesco C. Does Molecular Self-Association Survive in Nanochannels? Journal of Physical Chemistry Letters 2010;1(7): 1155-59.*

14. *Richert R. Dynamics of Nanoconfined Supercooled Liquids. Annual Review of Physical Chemistry, Vol 62 2011;62: 65-84.*

15. *Huber P. Soft matter in hard confinement: phase transition thermodynamics, structure, texture, diffusion and flow in nanoporous media. Journal of Physics-Condensed Matter 2015;27(10).*

16. *Audonnet F, Brodie-Linder N, Morineau D, Frick B, Alba-Simionesco C. From the capillary condensation to the glass transition of a confined molecular liquid: Case of toluene. Journal of Non-Crystalline Solids 2015;407: 262-69.*

17. *Jani A, Busch M, Mietner JB, et al. Dynamics of water confined in mesopores with variable surface interaction. Journal of Chemical Physics 2021;154(9).*

18. *Demuth D, Sattig M, Steinrucken E, Weigler M, Vogel M. H-2 NMR Studies on the Dynamics of Pure and Mixed Hydrogen-Bonded Liquids in Confinement. Zeitschrift Fur Physikalische Chemie-International Journal of Research in Physical Chemistry & Chemical Physics 2018;232(7-8): 1059-87.*

19. *Lederle C, Sattig M, Vogel M. Effects of Partial Crystallization on the Dynamics of Water in Mesoporous Silica. Journal of Physical Chemistry C 2018;122(27): 15427-34.*

20. *Weigler M, Brodrecht M, Buntkowsky G, Vogel M. Reorientation of Deeply Cooled Water in Mesoporous Silica: NMR Studies of the Pore-Size Dependence. Journal of Physical Chemistry B 2019;123(9): 2123-34.*

21. *Swenson J, Cerveny S. Dynamics of deeply supercooled interfacial water. Journal of Physics-Condensed Matter 2015;27(3).*

22. *Milischuk AA, Ladanyi BM. Structure and dynamics of water confined in silica nanopores. Journal of Chemical Physics 2011;135(17).*

23. *Gallo P, Rovere M, Chen SH. Water confined in MCM-41: a mode coupling theory analysis. Journal of Physics-Condensed Matter 2012;24(6).*

24. *Kuon N, Milischuk AA, Ladanyi BM, Flenner E. Self-intermediate scattering function analysis of supercooled water confined in hydrophilic silica nanopores. Journal of Chemical Physics 2017;146(21).*

25. *Bellissentfunel MC, Chen SH, Zanotti JM. SINGLE-PARTICLE DYNAMICS OF WATER-MOLECULES IN CONFINED SPACE. Physical Review E 1995;51(5): 4558-69.*

26. *Zanotti JM, Bellissent-Funel MC, Chen SH. Relaxational dynamics of supercooled water in porous glass. Physical Review E 1999;59(3): 3084-93.*

27. *Takahara S, Nakano M, Kittaka S, et al. Neutron scattering study on dynamics of water molecules in MCM-41. Journal of Physical Chemistry B 1999;103(28): 5814-19.*

28. *Faraone A, Liu L, Mou CY, Shih PC, Copley JRD, Chen SH. Translational and rotational dynamics of water in mesoporous silica materials: MCM-41-S and MCM-48-S. Journal of Chemical Physics 2003;119(7): 3963-71.*

29. *Takahara S, Sumiyama N, Kittaka S, Yamaguchi T, Bellissent-Funel MC. Neutron scattering study on dynamics of water molecules in MCM-41. 2. Determination of translational diffusion coefficient. Journal of Physical Chemistry B 2005;109(22): 11231-39.*

30. *Liu L, Chen SH, Faraone A, Yen CW, Mou CY. Pressure dependence of fragile-to-strong transition and a possible second critical point in supercooled confined water. Physical Review Letters 2005;95(11).*

31. *Faraone A, Liu L, Mou CY, et al. Dynamics of supercooled water in mesoporous silica matrix MCM-48-S. European Physical Journal E 2003;12: S59-S62.*

32. *Briman IM, Rebiscoul D, Diat O, et al. Impact of Pore Size and Pore Surface Composition on the Dynamics of Confined Water in Highly Ordered Porous Silica. Journal of Physical Chemistry C 2012;116(12): 7021-28.*

33. *Aso M, Ito K, Sugino H, et al. Thermal behavior, structure, and dynamics of low-temperature water confined in mesoporous organosilica by differential scanning calorimetry, X-ray diffraction, and quasi-elastic neutron scattering. Pure and Applied Chemistry 2013;85(1): 289-305.*

34. *Baum M, Rieutord F, Jurany F, Rey C, Rebiscoul D. Dynamical and Structural Properties of Water in Silica Nanoconfinement: Impact of Pore Size, Ion Nature, and Electrolyte Concentration. Langmuir 2019;35(33): 10780-94.*

35. *Hamid ARA, Lefort R, Lechaux Y, et al. Solvation Effects on Self-Association and Segregation Processes in tert-Butanol-Aprotic Solvent Binary Mixtures. Journal of Physical Chemistry B 2013;117(35): 10221-30.*

36. *Mhanna R, Lefort R, Noirez L, Morineau D. Microstructure and concentration fluctuations in alcohol-Toluene and alcohol-Cyclohexane binary liquids: A small angle neutron scattering study. Journal of Molecular Liquids 2016;218: 198-207.*

37. *Hamid ARA, Mhanna R, Lefort R, et al. Microphase Separation of Binary Liquids Confined in Cylindrical Pores. Journal of Physical Chemistry C 2016;120(17): 9245-52.*

38. *Mhanna R, Hamid ARA, Dutta S, et al. More room for microphase separation: An extended study on binary liquids confined in SBA-15 cylindrical pores. Journal of Chemical Physics 2017;146(2).*

39. *Dutta S, Lefort R, Morineau D, et al. Thermodynamics of binary gas adsorption in nanopores. Physical Chemistry Chemical Physics 2016;18(35): 24361-69.*

40. *Essafri I, Morineau D, Ghoufi A. Microphase separation of a miscible binary liquid mixture under confinement at the nanoscale. Npj Computational Materials 2019;5.*

41. *Mhanna R, Catrou P, Dutta S, et al. Dynamic Heterogeneities in Liquid Mixtures Confined in Nanopores. Journal of Physical Chemistry B 2020;124(15): 3152-62.*

42. *Swenson J, Elamin K, Chen G, Lohstroh W, Sakai VG. Anomalous dynamics of aqueous solutions of di-propylene glycol methylether confined in MCM-41 by quasielastic neutron scattering. Journal of Chemical Physics 2014;141(21).*

43. *Elamin K, Jansson H, Swenson J. Dynamics of aqueous binary glass-formers confined in MCM-41. Physical Chemistry Chemical Physics 2015;17(19): 12978-87.*

44. *Kresge CT, Leonowicz ME, Roth WJ, Vartuli JC, Beck JS. ORDERED MESOPOROUS MOLECULAR-SIEVES SYNTHESIZED BY A LIQUID-CRYSTAL TEMPLATE MECHANISM. Nature 1992;359(6397): 710-12.*

45. *Richard D, Ferrand M, Kearley GJ. Analysis and Visualisation of Neutron-Scattering Data. 4. Institut Laue-Langevin, BP156, 38042 Grenoble, Cedex 09, France: Journal of Neutron Research; 1996:33-39.*

46. Zanotti, JM. INSTALLING IDL AND QENSH. 2018.

47. Hamid ARA, Mhanna R, Catrou P, Bulteau Y, Lefort R, Morineau D. Multiple Glass Transitions of Microphase Separated Binary Liquids Confined in MCM-41. Journal of Physical Chemistry C 2016;120(20): 11049-53.

48. Ramona M. Confinement-induced nano-segregation of binary liquids with amphiphilic interactions DOCTEUR DE L'UNIVERSITÉ DE RENNES 1. UNIVERSITÉ DE RENNES 1; 2015.

CHAPTER VI

GENERAL CONCLUSION & PERSPECTIVES

In addition to offering fundamental opportunity to understand new physical properties at the nanoscale, confinement is taking day after day an important place in many industrial applications owing to advances in nanotechnology. These applied fields point to a high number of challenges related to the manipulation of complex liquids, nanofiltration, gas extraction, energy storage, health, and food science. This explains the high research progress in this field over the past decade. Fundamentally, the inability of many established descriptions of bulk systems to encompass specificities of matter at the nanoscale have motivated researchers to take further interest in this topic. Indeed, confinement induces drastic modification of dynamical and structural properties of molecular systems with respect to their bulk counterparts. This phenomenon was mainly related to the finite size and the strong interfacial effects dominating on scales comparable to a few molecular diameters.

In particular, this PhD thesis project has been motivated by the growing number of observations of microphase separation induced by nanoporous confinement in liquid mixtures which are otherwise fully miscible under normal bulk conditions. A comprehensive description of a microphase-separated core−shell organization was achieved for the prototypical tert-Butanol (TBA)−toluene (TOL) binary mixtures confined in mesostructured porous material silicas from the structural and dynamical point of views. Among many fascinating confinement effects, the formation of new liquid structures in nanochannels is quite remarkable and raises several questions about its physical origin. In recent studies, this novel surface-induced nanosegregation (core−shell structure) was related to liquid-surface interaction with a preferential interaction of alcohol with silicate.

Inspired by these studies, we aimed at getting a better understanding on how we could modify/control physical properties (in particular dynamics and structure) through the nanoscale control of surface chemistry. We achieved this goal by using periodic mesoporous organosilicas (PMOs) system with a hybrid surface characterized by hydrophobic/hydrophilic modulated units which opens the door to the modulation of surface interactions.

In a first part of the PhD project, we have investigated the dynamics of liquid water confined in mesostructured porous silica (MCM-41) and periodic mesoporous organosilicas (PMOs) by incoherent quasielastic neutron scattering experiments.[1] The effect of tuning the water/surface interaction from hydrophilic to more hydrophobic on the water mobility, while keeping the pore size in the range 3.5-4.1 nm, was assessed from the comparative study of three PMOs comprising different organic bridging units and the purely siliceous MCM-41 case. An extended dynamical range was achieved by combining time-of-flight (IN5B) and backscattering (IN16B) quasielastic neutron spectrometers providing complementary energy resolutions. Due to confinement effects, water was effectively maintained in the liquid phase on an extended temperature range (from 300 K to 243 K), where its dynamics was studied. We were able to highlight the existence of two independent motions resulting from fast local motion around the average molecule position and the confined translational jump diffusion of its center of mass. All the molecules performed local relaxations, whereas the translational motion of a fraction of molecules was frozen on the experimental timescale. We provided, also, a comprehensive microscopic view on the dynamics of liquid water confined in mesopores, with distinct surface chemistries, in terms of non-mobile/mobile fraction, self-diffusion coefficient, residence time, confining radius, local relaxation time, and their temperature dependence. Importantly, we demonstrated that the strength of the water/surface interaction determines the long-time tail of the dynamics, which we attributed to the translational diffusion of interfacial molecules, while the water dynamics in the pore center is barely affected by the interface hydrophilicity.

Following this study on water dynamics, it turned out to be especially interesting to extend the study towards much longer times and lower temperature, where a single interfacial molecularly-thick film between the pore and the ice persists. This perspective study was part of the postdoctoral project led by Benjamin Malfait in our team and with whom I have a collaboration opportunity. This work is described in a publication reporting on dielectric spectroscopy experiments.[2]

In a second part of the PhD project, the effect of modulating the liquid-liquid and liquid-surface interactions on the strcutre and the dynamics of fully miscible binary liquids was addressed. Extending preceding studies in silica mesopores with the same liquids, we selected amphiphilic mixtures formed by a polar H-bonded (Tert-butanol) and an aprotic weakly polar (Toluene) molecule.

To investigate the static properties of the confined binary liquids, we have performed a structural study and quantified the molecules-surface interaction by small angle neutron diffraction and dynamical vapor sorption experiments.

The vapor sorption method allowed us to quantify the interactions of the DVB-PMO matrix with TBA and TOL molecules. We have demonstrated the much higher thermodynamic affinity of DVB-PMO surface to TBA molecules (10 time larger) compared to that of TOL. Additionally, we showed the effect of surface chemistry on the thermodynamic affinity to adsorbed molecules by comparing DVB-PMO results with those obtained with MCM-41 matrix. We found that the affinity of MCM-41 to TBA molecules is 10 times more important to that of DVB-PMO. Being able to exclude the two extreme possible structures (i.e. homogeneous mixing and fully phase-separated core-shell model), our results have pointed to another inhomogeneous model for PMO-filled systems that assumes only a specific interaction between tert-butanol and silica units.

The SANS experiments allowed us to better understand the structuring of TBA and TOL molecules into the DVB-PMO pore cavity. By making predictive calculations of the scattering intensity of various models of nanostructuration inside the pore, we have found a best consistency with the same model as that was previously proposed for DVS experiments. This model assumes that only the silica unit is selective towards the tert-butanol molecules leading to the formation of a TBA monolayer at their surface and the rest of the mixture is homogeneously distributed in the rest of the pore (i.e. the core and the bridging-unit), providing a microscopic, though probably simplified, picture of the nanoconfined liquid mixture in PMO.

These structural studies were complemented by experimental investigations of their microscopic molecular dynamics. Since these mixtures do not crystallize anymore in confined geometry, QENS experiments were successfully performed in the liquid state on a broad temperature range from 315 to 220 K. We applied isotopic contrast variation effects to highlight the dynamics of the hydrogenated component in the mixture and minimize the contribution of the complementary deuterated molecule. Therefore, we varied the concentration of hydrogenated TBA (TBAH) and hydrogenated TOL (TOLH), as well as their deuterated counterparts. We have investigated the mixing effects on the relative dynamics of each constituent and we have compared the bulk and confined situations. For confined mixtures, we have defined two independent local modes performed by hydrogenated molecules (slow mode (S) and fast mode (F)) and three independent modes for hydrogenated molecules in bulk mixtures (translational mode (T), slow mode (S) and fast mode (F)). The fast mode (F) is characterized by a relaxation time τ_F which exhibits a

low temperature, concentration and molecule dependence and essentially remains in the range 0,2-0,5 ps. However, the slow mode (S) is characterized by a relaxation time τ_S which exhibits a noticeable temperature dependence, going from 4 ps to 15 ps in the case of TBAH and from 3,5 ps to 9 ps in the case of TOLH on cooling on the temperate range from 315 K to 220 K.

We also succeeded in describing the spatial trajectory of the two different local modes with a fairly good agreement with experimental data for confined liquids. The same model performed in an approximated manor for bulk liquids due to the overlap of additional degrees of freedom, provided by translational diffusion on the studied experimental timescale. The trajectory geometry of the fast mode was described with a model of a jump between 3 sites (for methyl hydrogens rotation) and a rotation in a Gaussian sphere (for the rest of the hydrogens). The obtained characteristic radii were in the range of 1 Å ± 0.1 Å which is in agreement with the molecule geometry. Regarding the slow local mode, we have described it by an isotropic rotation on the surface of a sphere of radius 2,6 Å ± 0,5 Å and 3,5 Å ± 0,5 Å respectively for TBAH and TOLH molecules. This mode is therefore attributed to the overall isotropic rotation of the molecule around its center of mass.

We have evaluated, the diffusion coefficients of TBAH and TOLH in bulk mixtures which showed a very different behavior, with the slowdown of TOLH diffusion when adding to it the more viscous TBA liquid. Symmetrically, an acceleration of the TBA diffusion was observed when adding to it the non-H-bonded and weakly polar TOL liquid. Very interestingly, this in on contrary to the confined state, which exhibited an apparently counterintuitive increase of the fraction of non-mobile TBA molecules during its dilution with TOL. This “anti-plasticizing effect” was related to the specific adsorption of TBA molecules at the porous interface.

To our knowledge, this study that examined thoroughly the effect of the modulation of surface interaction on physical properties of water and confined binary miscible mixtures is definitely original with respect to the existing literature. With this work we have provided an overview of the phenomenon from structural and dynamical points of view. Therefore, we consider this work as a support to the development of future studies combining different families of mesostructured porous materials and complex liquid mixtures, which would give provide new opportunities in the control of supermolecular structuring and solvents properties. Beyond the case of prototypical amphiphilic mixtures, like those studied in the present thesis, we anticipate that confining new classes of alternative solvents should be particularly relevant for technological applications, but also scientifically challenging. In this perspective, I had the opportunity to be involved in a new perspective project that extended beyond the initial scope of the thesis, and which focused on a very promising and actively studied emerging class of liquids mixtures, named deep eutectic solvents (DESs). As a first step towards their study in confined geometry, we have initiated investigations of their long-range order and concentration fluctuations in bulk state,[3] their ionic conductivity and dipolar reorientational dynamics[4] as well as their phase behavior in aqueous solutions[5]. For information, the reference of the publications resulting from this perspective work are provided in the following.

REFERENCES

1. *Jani A, Busch M, Mietner JB, et al. Dynamics of water confined in mesopores with variable surface interaction. Journal of Chemical Physics 2021;154(9).*

2. *Malfait B, Jani A, Mietner JB, et al. Influence of Pore Surface Chemistry on the Rotational Dynamics of Nanoconfined Water. Journal of Physical Chemistry C 2021;125(30): 16864-74.*

3. *Percevault L, Jani A, Sohier T, et al. Do Deep Eutectic Solvents Form Uniform Mixtures Beyond Molecular Microheterogeneities? Journal of Physical Chemistry B 2020;124(41): 9126-35.*

4. *Jani A, Malfait B, Morineau D. On the coupling between ionic conduction and dipolar relaxation in deep eutectic solvents: Influence of hydration and glassy dynamics. Journal of Chemical Physics 2021;154(16): 164508.*

5. *Jani A, Sohier T, Morineau D. Phase behavior of aqueous solutions of ethaline deep eutectic solvent. Journal of Molecular Liquids 2020;304: 112701-06.*

ANNEX-I

QUASI-ELASTIC NEUTRON SCATTERING (QENS)

I. GENERALITY ON QENS

In order to assess the confinement effect, it is necessary to have a probe that covers the spatio-temporal region specific to the confinement scale. Neutron scattering is one of the most appropriate methods for studying both the structure and the dynamics of condensed matter. It has gradually become an exceptional and in some cases the unique tool to evaluate the interactions of atoms and molecules at the molecular level and in a variety of systems (e.g. liquids, crystalline materials, glasses, metals, superconductors, polymers, gels, etc. biological objects). This experimental method is complementary to numerical methods, such as molecular dynamics simulation, which cover the same time and length scales. In this chapter, a brief overview about QENS is given. The general principles of neutron scattering methods have been established in many text books[1-3]. The readers are invited to refer to these documents if they intend to get a comprehensive view on the subject. However, the following part provides brief overview about QENS to apprehend the studies of confined liquids that are reported thereafter.

Quasi-elastic Neutron Scattering is a spectroscopic method, where the momentum and the corresponding energy transfer of neutrons are measured. This transfer arises when neutrons are impinged ($\lambda_{inc} \approx 1 - 10$ Å normally well adapted to the interatomic distances) onto a sample and interact with the atoms in it. The momentum transfer Q, also called scattering vector depicts the difference before and after penetration the sample and can be used to obtain information about the dynamics in the sample.

II. THEORETICAL BASIC NOTIONS OF NEUTRON SCATTERING

A free neutron moving at the speed v can be considered either as a particle of mass m, or as a plane wave of momentum vector

The magnitude of the momentum vector is related to the wavelength λ of the neutron plane wave by

$$k = |k| = 2\pi\lambda \qquad (2)$$

Neutrons can be generated for example by the fission process of a heavy nucleus and their kinetic energy E can be expressed using the following equation:

$$E = \frac{1}{2}mv^2 = \frac{\hbar^2 k^2}{2m} \qquad (3)$$

Thermal neutrons produced by interaction with a moderator at room temperature (T ≈ 300 K) having an energy centered about $E = 25\ meV$ and a wavelength about $\lambda = 1.8$ Å are perfectly scale with the intermolecular interactions and the interatomic distance in condensed matter, respectively. The neutron energy value can be modulated by tuning the temperature of the moderator and by selecting (filtering) some slices out of the distribution of neutron speed in a range that spans from 0.5 to 8 Å. This tool gives to users a more flexibility in choosing energy range and make it perfect to study both the dynamics (collective excitations, self-diffusion, rotation, conformation changes etc.) and the structure in liquids and solids.

A neutron scattering experiment consists in measuring two different quantities. First is the energy transfer, $\hbar\omega$, between the initial energy, E, and the final energy, E_0, of the neutrons that correspond to

$$\hbar\omega = E - k\,E_0 = \frac{\hbar^2}{2m\,(k^2 - k_0^2)} \qquad (4)$$

And second is the scattering vector Q as

$$Q = k - k_0 \qquad (5)$$

where k and k_0 are the corresponding wave vectors. The typical set-up for neutron scattering experiments is described in Figure 1 where a monochromatic beam is sent into a sample the scattering process takes place. The detector positioned in a given angle allows the counting of the scattered intensity.

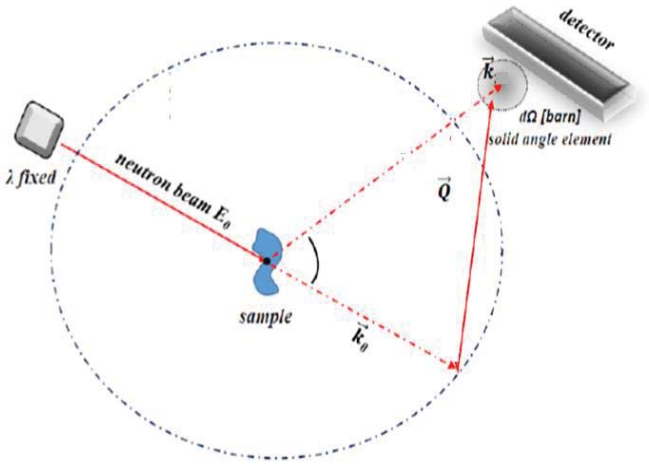

Figure-1: Schematic overview of QENS experiment showing the wave vector transfer Q = k - k0 at constant scattering angle.

The neutron can be either absorbed or scattered by atoms. Apart for specific systems, thermal neutron absorption is small and we will focus only on the scattering process. The interaction between neutrons and atoms is highly localized by comparison to their wavelength, so that the plane waves are scattered as spherical waves by each atom (cf. Figure-2). The amplitude of the spherical wave is given by the scattering length b. The imaginary part of b corresponds to the absorption, and the real part corresponds to the scattering process itself and its scattering events Is expressed by the equation:

$$Is = I_0 \, \sigma_s \qquad (6)$$

where I_0 and σ_s are corresponding to incident current of neutrons and the cross section. In this equation the cross section represents the dimension of a surface (typically indicated by 1 barn = 10-24 cm²). The probability of a neutron with energy E_0, leaving the sample in the solid angle element $\partial\Omega$ (see Figure-1) with an energy exchange is given by the double differential cross section:

$$\frac{\partial^2\sigma}{\partial\Omega\partial E} = \frac{1}{\hbar}\frac{\partial^2\sigma}{\partial\Omega\partial\omega} \qquad (7)$$

Concerning the scattering length varies according to the isotopic nature of each atom, and also the spin state of the atom-neutron system. This generally induces a stochastic variation of the relative amplitude of the scattered waves from one atomic site to the other. Therefore,

each isotope is allocated an average scattering length over the different spin states and called the coherent scattering length bcoh. Only a fraction of the waves scattered by the different atoms will develop interferences weighted by b_{coh}, this former process is denoted coherent scattering. The average value over all isotopes is called coherent scattering length $\langle b_i \rangle$. The fluctuations of b around b_{coh} lead to an additional scattering signal that does not arise from interferences between waves, this latter process is denoted incoherent scattering. That means that, the incoherent scattering length b_i^{inc} can be defined as the root mean square deviation of bi from $\langle b_i \rangle$

$$b_i^{coh} = \langle b_i \rangle \qquad (8)$$

$$b_i^{incoh} = [b_i^2 - \langle b_i \rangle^2]^{1/2} \qquad (9)$$

Using these for defining the scattering length one can also introduce the so-called total bound scattering cross section, which are expressed in the following equations. Either here there is both a coherent and incoherent contribution

$$\sigma = \sigma coh + \sigma inc \qquad (10)$$

$$\sigma coh = 4\pi \langle b \rangle 2 \qquad (11)$$

Generally, the coherent scattering provides information on collective properties (structure or phonons), while the incoherent scattering provides information of the individual dynamics.

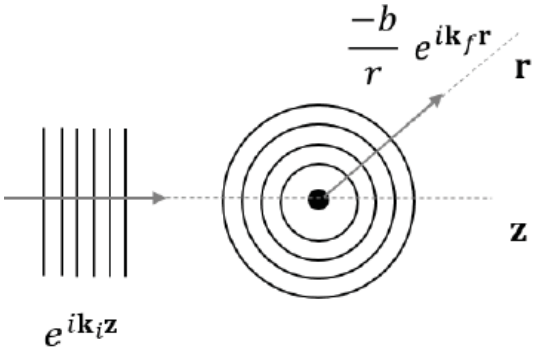

Figure-2: Sketch of the scattering of an incident neutron plane wave of momentum vector ki by a single atom, leading to the creation of a spherical wave of momentum vector kf and amplitude - b.

In Table-, we give the value of the coherent scattering length of a selection of usual atoms and the two different cross sections σ_{coh} and σ_{inc} expressed in barn. The values of scattering cross sections deserve some important comments: it is noteworthy that they do not vary in a simple manner as a function of the position of the element in the periodic table. This is very different from X-rays (see the fifth column of σ_{abs}) that interact with atoms as a function of the charge number Z. Indeed, neutrons are sensitive to some light elements, especially hydrogens, which are omnipresent in organic and soft matter. A second point of interest is the isotopic effect, which is remarkable for hydrogen. The pure isotope ^{1}H has a negative coherent scattering length and a dominant incoherent scattering cross section. At variance, the deuterium isotope ^{2}H (D) has a positive scattering length and a dominant coherent cross section.

This allows tuning the average scattering length by mixing in well-suited proportion hydrogenated/deuterated forms of the same molecule to match the scattering length of any other constituent (contrast matching experiments). Moreover, it is possible to highlight the incoherent part of the scattering from hydrogenated sites in otherwise deuterated samples. This method is widely used to label the individual (self) dynamics of tagged molecules or chemical groups of a given molecule.

Table-1: Scattering length and cross sections of usual atoms

Atom	b_{coh} (fm)	σ_{coh} (barn)	σ_{incoh} (barn)	σ_{abs} (barn)
^{1}H	-3.74	1.76	80.3	0.333
^{2}H	6.67	5.59	2.05	0.0005
C	6.65	5.55	0.001	0.003
N	9.36	11.0	0.50	1.90
O	5.81	4.23	0.001	0.0002

Making the link between the double differential cross section and the position within the sample of each atom at a time t, referred by the position vector $Ri(t)$ is the key point of neutron scattering. This relation writes as

$$\frac{\partial^2\sigma}{\partial\Omega\,\partial\omega} = \frac{kf}{ki}\,\frac{1}{2\pi}\,\frac{1}{N}\sum_i\sum_j\int_{-\infty}^{+\infty}\langle e^{iQ.Ri(t)}e^{-iQ.Ri(0)}e^{-i\omega t}\rangle\,dt \qquad (12)$$

where $\langle\ \rangle$ express the thermal average and it is performed for the elements of the double sum over the N atoms of the sample.

To simplify the expression, the case of a sample formed by an assembly of N identical isotopes will be considered below. Therefore, the double differential cross section can be split into a coherent and an incoherent term

$$\frac{\partial^2\sigma}{\partial\Omega\,\partial\omega} = \frac{kf}{ki}\,\frac{1}{2\pi}\,\frac{1}{N}\left(\sigma_{coh}\,S(Q,\omega) + \sigma_{incoh}\,S_{incoh}(Q,\omega)\right) \qquad (13)$$

where $S(Q,\omega)$ and $S_{incoh}(Q,\omega)$ are the scattering function (also denoted dynamic structure factor) and the incoherent scattering function, respectively.

Interestingly, the scattering functions are related to two other important functions by single or double Fourier transformation (thus relating the transfer of energy to time and the transfer of momentum to space).

They are the intermediate scattering functions:

$$I\ (Q,t) = \frac{1}{2\pi}\int_{-\infty}^{+\infty} S\ (Q,\omega)\,e^{i\omega t}\,d\omega \qquad (14)$$

$$I_{incoh}(Q,t) = \frac{1}{2\pi}\int_{-\infty}^{+\infty} S_{incoh}(Q,\omega)\,e^{i\omega t}\,d\omega \qquad (15)$$

and the pair correlation functions

$$G(r,t) = \frac{1}{(2\pi)^3}\int_{-\infty}^{+\infty} I\ (Q,t)\,e^{-iQr}\,dQ \qquad (16)$$

$$G_{incoh}(r,t) = \frac{1}{(2\pi)^3}\int_{-\infty}^{+\infty} I_{incoh}(Q,t)\,e^{-iQr}\,dQ \qquad (17)$$

From these relations, it turns out that in the classical limits, the intermediate scattering functions can be simply expressed with respect to the atomic positions:

$$I\ (Q,t) = \frac{1}{N}\sum_i\sum_j\langle e^{iQ.Ri(t)}e^{-iQ.Rj(0)}\rangle \qquad (18)$$

$$I_{incoh}(Q,t) = \frac{1}{N}\sum_i\sum_j\langle e^{iQ.Ri(t)}e^{-iQ.Rj(0)}\rangle \qquad (19)$$

It is noteworthy that the incoherent scattering by two atoms does not produce interferences so that it merely involves the same atom at two successive times. This is obvious in (19) that comprises a single sum over all atoms.

For comprehensiveness, we finally recall the signification of the pair correlation $G\ \ (r,t)$ and the self-correlation function $G_{incoh}(r,t)$ that are related to the intermediate scattering functions by equation (16) and (17).

Classically, these two correlation functions can be write as

$$G\ \ (r,t)\ = \sum_i \langle \partial(r + R0(0) - Ri(t)) \rangle \qquad (20)$$

$$G_{incoh}(r,t)\ = \sum_i \langle \partial(r + R0(0) - Ri(t)) \rangle \qquad (21)$$

$G\ \ (r,t)$ can be expressed as the probability of finding a particle at the time t and the position r from the position of a particle at time t = 0. Note that it does not matter whether the two particles considered at time 0 and t are different or identical. This is unlike $G_{incoh}(r,t)$ that expresses the probability of finding the same particle at time t and at the position r from its initial location.

III. REFERENCES

1. Lovesey, S., Theory of Neutron Scattering from Condensed Matter. 1984.

2. Dianoux, A. J.; Lander, G., Neutron Data Booklet. 2001.

3. Bée, M., Quasielastic neutron scattering : principles and applications in solid state chemistry, biology, and materials science. 1988.

ANNEX-II

Influence of Pore Surface Chemistry on the Rotational Dynamics of Nanoconfined Water

Authors

Benjamin Malfait, Aicha Jani, Jakob Benedikt Mietner, Ronan Lefort, Patrick Huber, Michael Fröba,and Denis Morineau

Abstract

These studies were carried out as part of the postdoctoral fellowship of B. Malfait.

- *Study of the dynamics of water confined in mesostructured porous silicas and PMOs by dielectric relaxation spectroscopy.*
- *Relaxation processes attributed to the rotational motions of non-freezable water located in the vicinity of the pore surface were studied in the temperature range from 140 to 225 K.*
- *Two distinct situations were achieved depending on the hydration level:*
    - *at low humidity (33% RH), water formed a non-freezable layer adsorbed on the pore surface.*
    - *At 75% RH, water formed an interfacial liquid layer sandwiched between the pore surface and the ice crystallized in the pore center.*

  In these two cases, the study revealed different water dynamics and different dependence on the surface chemistry.
- *The respective importance of water−water and water−surface interactions in determining the dynamics of the interfacial liquid-like water and the adsorbed water molecules as well as the nature of the different H-bonding sites present on the pore surface.*

THE JOURNAL OF PHYSICAL CHEMISTRY C
A JOURNAL OF THE AMERICAN CHEMICAL SOCIETY

pubs.acs.org/JPCC

Article

Influence of Pore Surface Chemistry on the Rotational Dynamics of Nanoconfined Water

Benjamin Malfait, Aicha Jani, Jakob Benedikt Mietner, Ronan Lefort, Patrick Huber,* Michael Fröba,* and Denis Morineau*

Cite This: https://doi.org/10.1021/acs.jpcc.1c05502

Read Online

ACCESS | Metrics & More | Article Recommendations | Supporting Information

ABSTRACT: We have investigated the dynamics of water confined in mesostructured porous silicas (SBA-15, MCM-41) and four periodic mesoporous organosilicas (PMOs) by dielectric relaxation spectroscopy. The influence of water−surface interaction has been controlled by the carefully designed surface chemistry of PMOs that involved organic bridges connecting silica moieties with different repetition lengths, hydrophilicity, and H-bonding capability. Relaxation processes attributed to the rotational motions of nonfreezable water located in the vicinity of the pore surface were studied in the temperature range from 140 to 225 K. Two distinct situations were achieved depending on the hydration level: at low relative humidity (33% RH), water formed a nonfreezable layer adsorbed on the pore surface. At 75% RH, water formed an interfacial liquid layer sandwiched between the pore surface and the ice crystallized in the pore center. In these two cases, the study revealed different water dynamics and different dependence on the surface chemistry. We infer that these findings illustrate the respective importance of water−water and water−surface interactions in determining the dynamics of the interfacial liquid-like water and the adsorbed water molecules as well as the nature of the different H-bonding sites present on the pore surface.

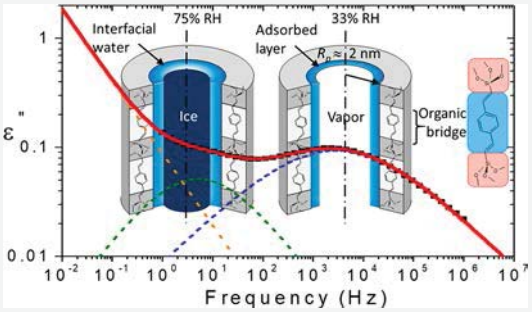

1. INTRODUCTION

Water is undoubtedly one of the most important substances due to its central role as a solvent in an extensive number of natural and industrial processes. In most frequent situations, water is found as spatially confined or in an interfacial state rather than forming a bulk phase. This is the case for a number of geological materials (zeolites, clays...) and related applications for environmental remediation and wastewater treatment.[1] Confined water is also crucial in energy technology, including proton−exchange membrane fuel cells,[2,3] and many other perspectives for water−energy technologies that were opened by the emergence of nanofluidics.[4] In biological systems as well, water molecules interacting closely with the surface of biomolecules form a hydration layer (0.4−0.8 nm)[5] that differs from bulk water[6] and can be considered as a confined phase.[7] Water dynamics in this layer is partly determined by the interactions between the water and the functional groups of the macromolecule.[6,8−10]

From a fundamental point of view, confining water at the nanoscale in prototypical porous solids has turned out to be particularly adequate in order to better understand the unusual behavior of interfacial water. For pore diameter $d < 2.5$ nm,[11] crystallization of confined water is suppressed by inhibition of the nucleation process,[12,13] which was considered as an opportunity to study anomalous physical properties of liquid water in a wide temperature range.[7,14] Among several types of confinement, including clay,[15] graphite oxide,[16] zeolite,[17] or porous silica glasses,[18,19] the mesostructured SBA-15[20] and MCM-41[21] are particularly suited hosts due to their well-defined porous geometry formed by ordered cylindrical channels.[22,23] Dynamics of confined supercooled water in MCM-41 has been studied with various experimental techniques such as dielectric relaxation spectroscopy (DRS),[21] nuclear magnetic resonance (NMR),[24] and quasi-elastic neutron scattering (QENS).[25]

The impact of the pore size, surface chemistry, or filling fraction has been reviewed in the literature and remains a matter of discussion.[7,20] In the high-temperature region (ca. above 240 K), the main structural relaxation α-process varies markedly with the size of confinement. Notably, when decreasing the pore diameter, the temperature dependence of the relaxation time evolves from a non-Arrhenius toward a more Arrhenius-like behavior.[26] At lower temperature, a crossover was detected at around 225 K from non-Arrhenius behavior at high temperature to Arrhenius-like behavior at low

Received: June 22, 2021
Revised: July 19, 2021

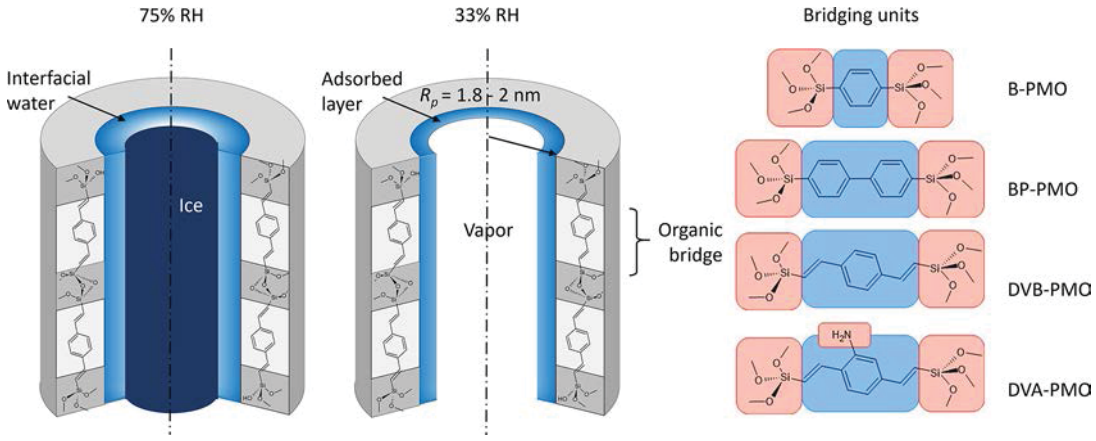

Figure 1. Sketch of the different mesoporous materials and confined conditions studied. Left panel: sample filled at 75% RH, interfacial liquid coexists with ice. Middle panel: sample filled at 33% RH, water forms an adsorbed liquid layer. Right panel: different organic bridging units studied, with the hydrophilic and hydrophobic regions highlighted, respectively, by red and blue boxes.

temperature. This feature was detected for different confinement sizes, also corresponding to circumstances where water was present in different physical states, namely: (i) liquid water coexisting with ice for SBA-15 (pore size 6 nm),[20] (ii) liquid with partial crystallization occurring in the crossover region for MCM-41 (pore size from 2.4 to 3.6 nm),[20,27−29] and (iii) entirely nonfreezing liquid for pore size smaller than 2.4 nm.[29−31] In the low-temperature regime, the reorientation dynamics of water molecules hardly depends on the pore size, suggesting that it reflects an intrinsic property of interfacial water.[7,20,28,32] This can be rationalized when noting that for sufficiently large pores ice formation further restricts the interfacial volume accessible to the liquid phase.[26,27] In this situation, the geometrical confinement is determined by the thickness of the interfacial layer itself, and it is no longer related to the pore size. Concerning the surface chemistry, ^{2}H NMR experiments revealed similar reorientation dynamics of water molecules confined in modified and unmodified MCM-41 (with equivalent pore size),[26] which supports that it reflects a universal character of the relaxation dynamics of water. However, this observation was shown to depend strongly on the degree of pore filling. For partially filled pores, the reorientation dynamics of the adsorbed water layer is significantly faster (three decades) than the interfacial water when the pore center is entirely filled.[27,29] This demonstrates the critical importance of the nature of interfacial interactions (water−vapor, water−water, and water pores), which are promoted when considering partially or capillary filled samples.[7]

The emerging question from all these results concerns the influence of the surface chemistry of the pore on the dynamics of surface water. In order to extend current knowledge, which has so far been based on a few studies on grafted silicas, we are contemplating new opportunities offered by the molecular-scale imprint of the water−surface interaction. Periodic mesoporous organosilicas (PMOs) are particularly well-suited, though barely used in water studies so far. Their pore wall is formed by a periodic repetition of inorganic and organic bridging units, with tunable hydrophilicity and H-bonding tendency.[33] Unlike postsynthesis surface-grafted porous silicas,[34] PMOs allow a stoichiometric control of the periodically alternating surface chemistry along the pore channel (i.e., one organic bridge per silica inorganic unit).[35]

A multidimensional solid-state NMR study has shown that the specific surface chemistry of PMOs caused different spatial arrangements of the interfacial water.[35] Strong correlations between water and the surface of the pore were observed in the vicinity of inorganic units that present H-bonding silanol groups. This was also the case near hydrophilic organic bridges when they comprise amino groups that act as alternative H-bonding sites. On the contrary, a depression of the interfacial layer of water around hydrophobic organic bridging units was indicated by the absence of spatial correlation.[35] Very recently, QENS experiments were carried out to investigate the dynamics of liquid water confined in PMOs, above the melting point, in the relatively high-temperature range of 243−300 K.[36] This study concluded on the spatial heterogeneity of the translational dynamics across the pore diameter. Moderate confinement effects on the translational dynamics were observed for the fraction of most mobile molecules, which were likely located in the pore center and thus were not affected by the nature of the pore surface. However, the interaction strength determined the longtime tail of the time dependence of the translational dynamics, corresponding to interfacial water molecules close to the surface wall.[36]

The above-mentioned observations made for water-filled PMOs underline the interest in focusing on the dynamics of only the few-molecule layers that interact with the pore surface and also in extending the experimental dynamical range to a longer time. In the present study, we have selected two different experimental conditions that fulfill this requirement: (i) by loading the pores at 33% RH below the capillary condensation pressure to ensure that water is adsorbed on the surface, leaving the pore center empty, and (ii) by decreasing the temperature of saturated pores at 75% RH to allow crystallization of the pore center. Indeed, in the latter case, it is expected that an interfacial layer of liquid water remains, with a thickness of about 0.6 nm,[37] which is also comparable with the hydration layer (0.4−0.8 nm).[6] We have applied dielectric relaxation spectroscopy, taking advantage of its higher sensibility and wider accessible time scale (microsecond to second), to study the low-temperature and longtime rotational dynamics of interfacial or monolayer water molecules.

https://doi.org/10.1021/acs.jpcc.1c05502
J. Phys. Chem. C XXXX, XXX, XXX−XXX

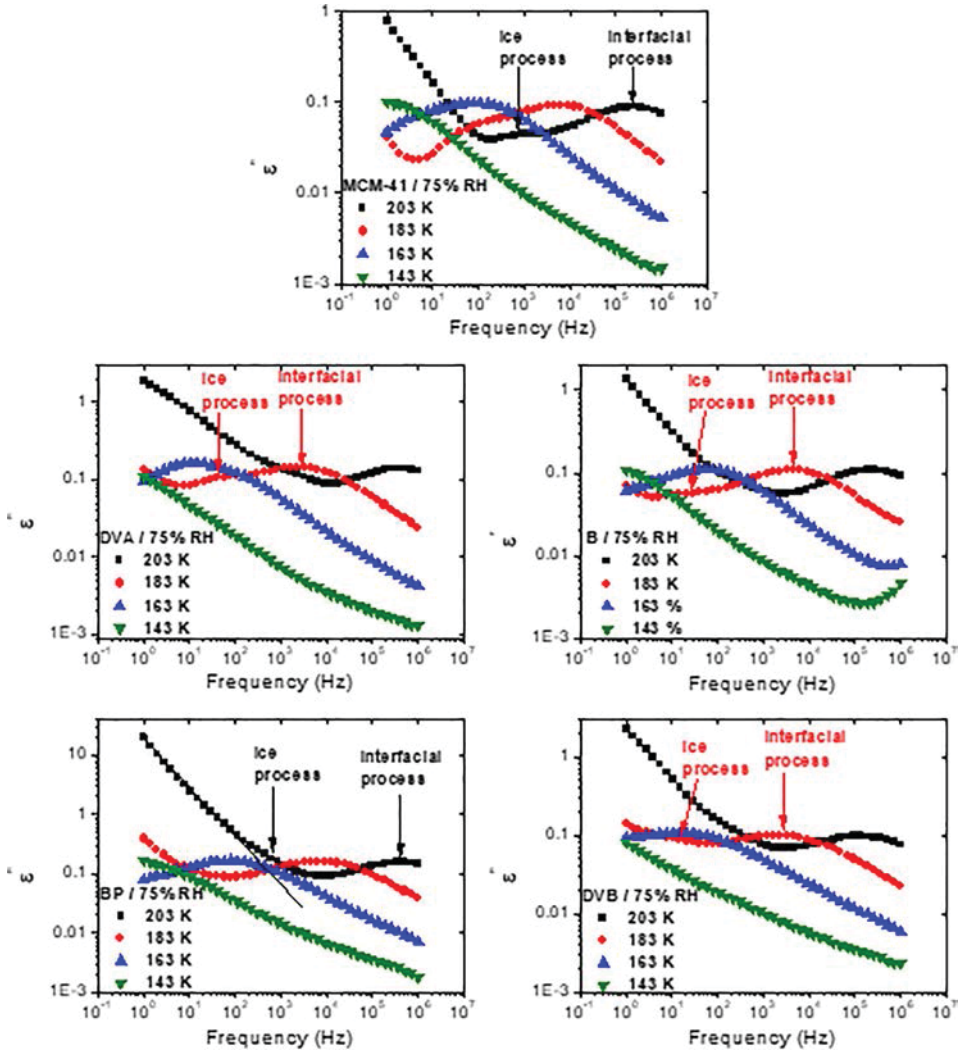

Figure 2. Dielectric loss spectra $\varepsilon''(\omega)$ of water confined within the five matrices: MCM-41, DVA-PMO, B-PMO, BP-PMO, and DVB-PMO at different temperatures. Loading was carried out at 75% RH, ensuring the full loading of nanochannels by capillary condensation. Ice and interfacial processes are identified by arrows, and the low-frequency contribution is associated with MWS and/or conductivity.

2. RESULTS AND DISCUSSION

2.1. Samples and Methods. We used four different periodic mesoporous organosilicas (PMOs) with different organic bridging groups: divinylbenzene (DVB), divinylaniline (DVA), benzene (B), and biphenyl (BP), with mean pore diameter D in the range 3.5−4.1 nm. Comparing results obtained with these PMOs allows studying both the effect of hydrophobicity of the organic bridge (DVA-PMO vs DVB-PMO) and repetition distances of silica/organic units along the pore axis that is related to the length of the organic unit (B-PMO vs BP-PMO), as illustrated in Figure 1. These materials were complemented by purely siliceous matrices with comparable mesoporous geometry (MCM-41, D = 3.65 nm) or larger pore size (SBA-15, D = 8.3 nm). Further details concerning the porous materials preparation and characterization are given in Section S1. The physical states of confined water corresponding to the two different hydration levels studied (75% and 33% RH) are also sketched in Figure 1. Based on water sorption isotherms[35] and previous DSC studies[36] (see also Section S2 for details on the hydration method), the porosity is completely filled with water for the larger RH value, while water is adsorbed at the pore surface, leaving an empty pore center for the lower RH value.

The complex dielectric function $\varepsilon^*(f) = \varepsilon'(f) - i\varepsilon''(f)$, where f is the frequency of the applied oscillating electrical field and ε' and ε'' are the real and imaginary parts, respectively, is measured from 1 to 10^6 Hz in the temperature range from 143 to 277 K for the different hydrated samples. Data acquisition and fitting procedures are detailed in Section S3.

2.2. Capillary-Filled Porous Matrices at 75% RH. The dielectric loss $\varepsilon''(\omega)$ of the different water-filled PMOs and MCM-41 porous matrices is presented for a selection of four temperatures in Figure 2. Isochronal representations of the dielectric loss as a function of the temperature $\varepsilon''(T)$ are illustrated in Figures S1 and S2.

Two major processes were detected in these spectra, as indicated by arrows in Figure 2. Moreover, three additional components should be mentioned, attributed to dc conductivity, fast local water relaxation, and Maxwell−Wagner−Sillars polarization. The dc conductivity is visible in Figure 2 at 203 K in the range of frequency below 10^2 Hz. The fast local water relaxation emerged as a weak signal on the high-frequency side of the relaxation peak at the lowest temperatures (ca. below 155 K) as illustrated in Figure S3 for water-

https://doi.org/10.1021/acs.jpcc.1c05502
J. Phys. Chem. C XXXX, XXX, XXX−XXX

Table 1. HN Parameters of the Two Processes Obtained from the Fit of the Loss Part of the Dielectric Function of Water-Filled MCM-41 and PMOs (75% RH) Measured at T = 183 K[a]

process	HN parameter	MCM-41	DVA-PMO	B-PMO	BP-PMO	DVB-PMO
ice	$\Delta\varepsilon$	0.0634	0.095	0.072	0.172	0.205
	α_{HN}	0.8	0.9	0.8	0.6	0.6
	β_{HN}	1	1	1	1	1
interfacial	$\Delta\varepsilon$	0.438	0.636	0.5	0.742	0.501
	α_{HN}	0.5	0.53	0.51	0.5	0.46
	β_{HN}	1	1	1	1	1
$\Delta\varepsilon$(interfacial)/$\Delta\varepsilon$(ice)		6.9	6.7	6.9	4.3	2.4

[a] $\Delta\varepsilon$ is the dielectric strength, and α_{HN} and β_{HN} ($0 < \alpha_{HN}$; $\alpha_{HN}\beta_{HN} \leq 1$) are fractional parameters describing, respectively, the symmetric and asymmetric broadening of the complex dielectric function and characterizing the relaxation heterogeneity.[41]

filled MCM-41 and discussed in ref 28. Due to its small contribution to the dielectric function, over a limited temperature range, we refrained from performing a fit of this extra signal. Maxwell–Wagner–Sillars polarization appeared on the lowest-frequency side of the spectra in the temperature range 195–210 K and also in isochronal representations of the dielectric loss (Figures S1 and S2). This process was already observed in similar samples[27,29] and related to the heterogeneous character of the porous media.[38,39]

The two major relaxation processes can be related to the physical state of confined water. According to water physisorption isotherms, the entire porosity was filled after equilibrium with water vapor at 75% RH.[35,40] Moreover, the two relaxation processes entered the instrumental frequency range ($1–10^6$ Hz) for temperatures ranging from 143 to 223 K. This is below the freezing point of water confined in these matrices, that is, in the range 227–237 K according to calorimetry.[36] In MCM-41, it has been shown that an interfacial layer of nonfreezable water coexists with ice localized in the center of the pore.[27,37] This situation is likely to exist in PMOs too. Therefore, we attribute the two relaxation processes seen in water-filled PMOs to ice and interfacial water, in line with studies on porous silicas.[20,29,32] The slow process is associated with ice and the faster one to interfacial water. Further support to this interpretation is provided by the present study from the effect of the pore size on the relative dielectric strength of both processes. This point is addressed in section S6 (cf. Figures S4 and S5), where water-filled SBA-15 (D = 8.3 nm) and MCM-41 (D = 3.65 nm) are compared.

A model implying two Havriliak–Negami functions (HN functions) and dc conductivity was fitted to the data. Very good fits were obtained for all the samples in the temperature range 143–223 K, as shown in Figure S4 and Figure S6 for MCM-41 and PMOs. The fitted HN parameters obtained are summarized in Table 1.

The two HN exponents α_{HN} and β_{HN} did not vary significantly with temperature and were thereafter considered as temperature-independent fitting parameters. Moreover, for the interfacial liquid water, they did not depend on the type of porous material with $\alpha_{HN} \approx 0.5$ and $\beta_{HN} \approx 1$. The most noticeable feature concerns the value of the dielectric strength of the interfacial water process relative to that of the ice process $\Delta\varepsilon$(interfacial)/$\Delta\varepsilon$(ice). Its value presented a systematic dependence on the nature of the matrix. The value of $\Delta\varepsilon$(interfacial)/$\Delta\varepsilon$(ice) averaged over the temperature range 173–203 K is illustrated in Figure 3. It was about 7 for MCM-41, DVA-PMO, and B-PMO and reduced to, respectively, 4 and 3 for BP-PMO and DVB-PMO. For SBA-15, the value is

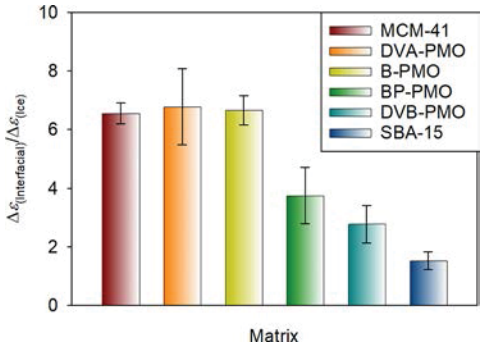

Figure 3. $\Delta\varepsilon$(Interfacial)/$\Delta\varepsilon$(ice) averaged over the temperature range 173–203 K for water confined in matrices loaded at 75% RH. Error bars illustrate the maximum temperature variations

further decreased to 1.5, which may find a specific interpretation related to the much smaller surface-to-volume ratio of SBA-15 compared the other matrices. Notwithstanding the fact that absolute values of the dielectric permittivity are inaccessible due to the heterogeneous nature of the sample (cf. discussion in section S6), the large variation of the relative dielectric strength observed for PMOs suggests that the amount of water involved in the interfacial layer may depend not only on the pore size but also on the pore surface chemistry and the resulting interaction with water.

Two parameters controlling the water–surface interaction have been identified in previous studies of PMOs based on water physisorption[40] and multidimensional solid-state NMR spectroscopy studies.[35] The first is the length of the organic bridges that act as spacers between H-bonding silica units, as sketched in Figure 1. It was shown that decreasing the length of hydrophobic bridging units, which was the case when comparing divinylbenzene (DVB-PMO) and benzene (B-PMO), results in a more hydrophilic material.[40] The second parameter is the intrinsic hydrophilicity of the bridging unit and especially its capability to form H-bonds. In the present study, this applies only for divinylaniline (DVA-PMO) that comprises an H-bonding amino group. This makes it more hydrophilic than divinylbenzene (DVB-PMO) and biphenyl (BP-PMO) bridging units that have comparable size but no polar group.[35] Based on these two parameters, Mietner et al. rationalized the relative hydrophilicity of a series of PMO matrices as quantified by the relative amount of adsorbed water below capillary condensation.[42] Interestingly, the systematic evolution of the ratio between the relative dielectric strengths of the interfacial water and the ice relaxation processes shown in Figure 3 follows a similar trend. It indicates that the fraction of water involved in the nonfreezing interfacial layer is

https://doi.org/10.1021/acs.jpcc.1c05502
J. Phys. Chem. C XXXX, XXX, XXX–XXX

maximum for the more hydrophilic matrices (i.e., pure silica and PMOs with a small hydrophobic bridging unit or long H-bonding bridging unit) and gradually decreases with the PMO hydrophilicity for large nonpolar bridging units.

We now discuss the temperature dependence of reorientational dynamics of water confined in the five matrices (75% RH). The relaxation times assigned to the ice- and interfacial water processes, as well as the Maxwell–Wagner process when detected, are shown in Arrhenius representation in Figure 4.

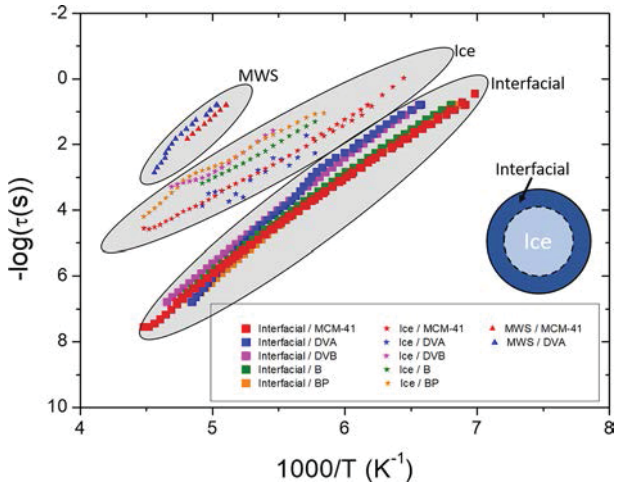

Figure 4. Temperature dependence of relaxation times of the MWS-, ice- and interfacial-processes of water confined into the five matrices: MCM-41, DVA, B, BP and DVB. Loading was carried out at 75% RH, ensuring the complete filling of nanochannels by capillary condensation. Unless specified, errors bars are smaller than the symbol size.

The two relaxation processes were grouped in gray areas in the relaxation map. For the two porous silicas (MCM-14 and SBA-15) our data were found in quantitative agreement with results from literature, as illustrated Figure S7.[27]

The dynamics of ice confined in MCM-41 and PMOs is only 2–3 orders of magnitude slower than the interfacial liquid in the temperature range analyzed and faster than bulk ice. It is worth mentioning that the nature of the confined ice (hexagonal/cubic, stacking disordered) is still under ongoing discussion.[43] However, assuming that the dynamics of confined ice involves mechanisms that are similar to the bulk (i.e., orientational or ionic defects),[44] its higher mobility is likely attributable to significant structural distortion. Also, there is a large dispersion among the relaxation times of the ice process in the different matrices. This is probably due to different levels of disorder in the ice. However, the relaxation times all retained an Arrhenius-like temperature dependence with a comparable activation energy E_a which was in the range from 40 to 42 kJ mol^{-1} (±4 kJ mol^{-1} for DVA-PMO and ±0.5 kJ mol^{-1} for the other systems), suggesting that the underlying dynamic process in confined ice is barely affected by the nature of the matrix.

The second relaxation process, attributed to the reorientational dynamics of the interfacial water, was also found to be similar for the different confining matrices. It does not follow a unique Arrhenius dependence in the entire temperature range but displays a cusp around 180 K. For MCM-41, this observation has been discussed in terms of a crossover from an α-like relaxation above 180 K to a β-like process below 180 K, although this issue is still a matter of active debate that goes beyond the scope of the present study.[7,14] However, we have adhered to the commonly held idea that the strictly Arrhenius behavior of deeply undercooled water is rather a characteristic feature of the lowest-temperature region (i.e., below the crossover at 180 K). It was conjectured by Cerveny et al.[15] that this revealed the universal nature of the low-temperature dynamics of confined water. Therefore, Arrhenius fits of the data were carried out in the temperature region below the crossover at about 180 K, and the obtained parameters are presented in Table 2.

Table 2. Arrhenius Parameters of the Interfacial Water Relaxation Time Obtained by Fitting the Temperature Region below 180 K

porous matrix label	τ_∞ (s)	E_a (kJ mol^{-1})
MCM-41	~10^{-22}	50 ± 0.5
DVA-PMO	~10^{-18}	50 ± 0.5
B-PMO	~10^{-19}	51 ± 0.5
BP-PMO	~10^{-20}	51 ± 0.5
DVB-PMO	~10^{-19}	53 ± 0.5

The values of pre-exponential factor τ_∞ are very small (10^{-18}–10^{-22} s) compared to the expected relaxation times that describe the high-temperature limits of local orientation fluctuations in the liquid state (approximatively 10^{-13}–10^{-14} s).[45] The similar observations of unphysical values of the pre-exponential factor τ_∞ of the dielectric relaxation of confined water have been reported by different groups.[27,29] This indicates that the molecular origin of the relaxation process attributed to the interfacial water might change at higher temperature. This phenomenon has been shown for water-filled MCM-41, which presents a crossover at 225 K as illustrated in Figure S7.[27]

Despite large variations in the pre-exponential factor, the values of the activation energy remained comparable, in the range from 50 to 53 ± 0.5 kJ mol^{-1} for all five samples. This indicates that the surface chemistry has no significant influence on the relaxation process of the interfacial layer. This important finding extends previous conclusions made from ^{2}H STE NMR experiments on water confined in surface-modified MCM-41.[26] More generally, this supports a number of studies relating to confined water in different pore sizes[29,31] and to water mixtures.[46,47] Despite very different conditions, they all converge to the existence of the same relaxation process that appears for temperatures below a dynamical crossover located at around 180 K. As such, this relaxation process could be indicative of the universal character of the corresponding dynamics of water.[46]

In light of this interpretation, one may conclude that the dynamics of water in the liquid interfacial region is governed by water–water interactions and is less sensitive to water–pore surface interactions. In fact, the value of the activation energy corresponds to the energy required for breaking at least two hydrogen bonds.[26] In the interfacial phase, a water molecule can interact with either another interfacial water molecule or with a water molecule from the ice phase. In this case, the water–pore surface interaction seems to play a secondary role, as demonstrated by the negligible influence of the matrix surface chemistry.

Different observations were made in a recent NMR study of D_2O confined in SBA-15 comprising surfaces functionalized

https://doi.org/10.1021/acs.jpcc.1c05502
J. Phys. Chem. C XXXX, XXX, XXX–XXX

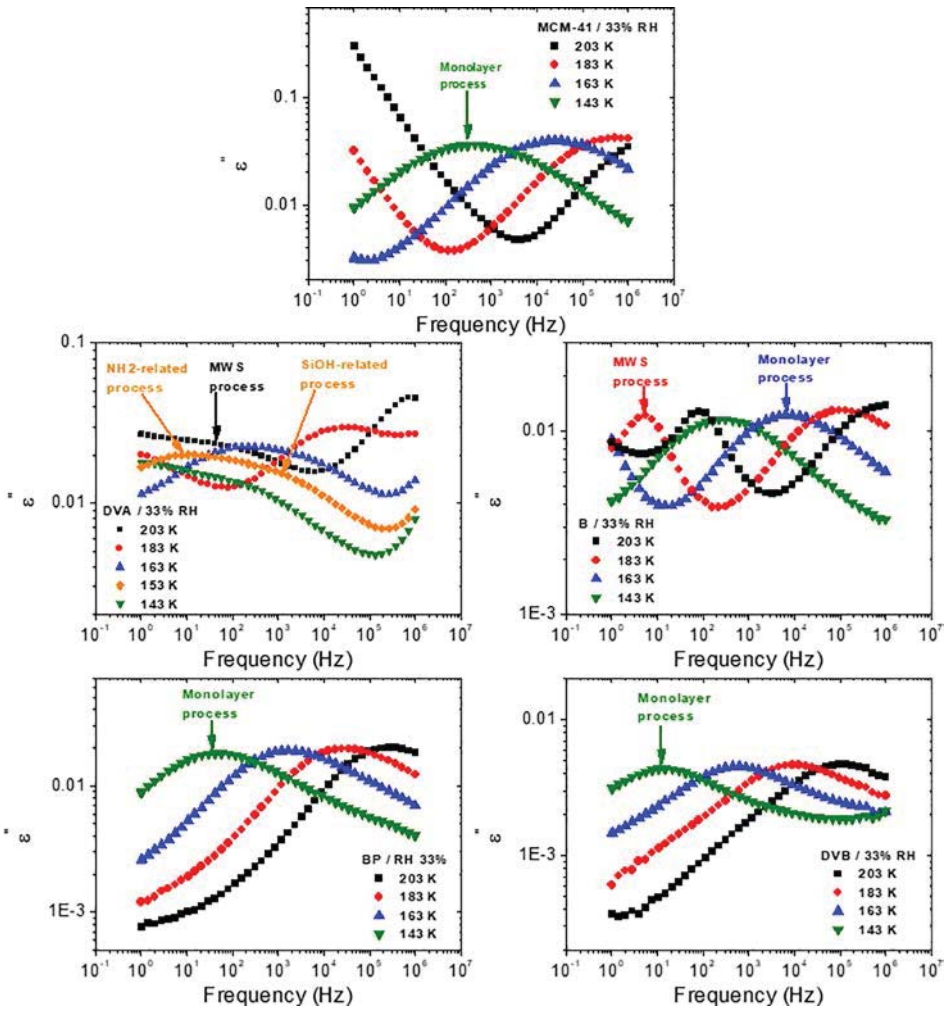

Figure 5. Dielectric loss spectra $\varepsilon''(\omega)$ of water confined within the five matrices: MCM-41, DVA-PMO, B-PMO, BP-PMO, and DVB-PMO at different temperatures. Loading was carried out at 33% RH, below the capillarity condensation, resulting in a monolayer of water at the inner surface and empty center. MWS and monolayer processes are identified by arrows.

with different amino acids.[48] The value of the correlation times for the reorientation dynamics was found to increase systematically with the acidic character of the residue, while, as in the present study, the corresponding activation energies barely changed. It should be stressed that the study was performed in the temperature range above 200 K, i.e., above the crossover usually seen in confined water.[28] Also, the surface treatment was achieved by chemical grafting of relatively long chains inducing softness in the confining medium, while the organic bridging units of PMOs are incorporated into the matrix walls. From the valuable comparison of both works, it emerges that the degree of coupling between the dynamics of interfacial water and the pore surface must depend on several parameters, in particular the softness of the confinement, the flexibility, polarity, and ionic charge of the surface functional groups, and the temperature range. A different situation is also expected when water forms an adsorbed monolayer.

2.3. Adsorbed Water on the Pore Surface of PMOs (33% RH). The dynamics of water adsorbed on the surface of MCM-41 and PMOs was studied for samples loaded at a reduced relative pressure (33% RH). According to the water physisorption isotherms,[35,40] this condition ensures being situated before the capillary condensation filling. Thus, only a layer of adsorbed water can be formed on the pore wall, leaving the pore center empty.

The dielectric loss $\varepsilon''(\omega)$ of water adsorbed at 33% RH on the surface of the different matrices is illustrated in Figure 5 for a selection of four temperatures. Isochronal representations of $\varepsilon''(T)$ are also presented in Figure S8. Compared to the completely filled matrices, the low-frequency dc conductivity was reduced, which is easily conceivable due to the restricted translation mobility of adsorbed molecules. A low-frequency process attributed to Maxwell−Wagner polarization was also observed. Most importantly, water-filled DVA-PMO additionally exhibited two relaxation processes, while only one relaxation process was observed for all the other systems. The corresponding dielectric losses were fitted by, respectively, two and one HN functions (cf. Figure S9). It is worth noting that the shape parameters α_{HN} and β_{HN} are smaller for the partially filled matrices compared to the completely filled matrices (Figure S6 and Table 1). It can be related to broader distribution relaxation times, arising from dynamic inhomogeneity and different environments.[49] The reduced value of β_{HN} for the partially filled samples (except DVA) could also indicate the emergence of a secondary high-frequency process. However, this hypothesis is not confirmed by masterplot curves (Figure S10) that are rather consistent with the

https://doi.org/10.1021/acs.jpcc.1c05502
J. Phys. Chem. C XXXX, XXX, XXX−XXX

presence of only one relaxation process. The resulting relaxation times are shown in Figure 6. As shown in Figure S11, the present results fully agree with previous findings for partially water-filled silica pores.[27,29]

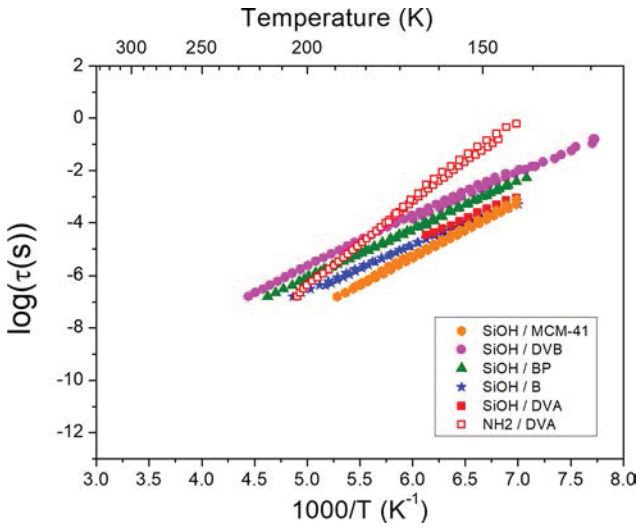

Figure 6. Temperature dependence of relaxation times of water adsorbed on the pore surface of the five matrices: MCM-41, DVB-PMO, BP-PMO, B-PMO, and DVA-PMO. Loading was carried out at 33% RH, below the capillarity condensation, resulting in a monolayer of water at the inner surface and empty center. Unless specified, errors bars are smaller than the symbol size.

We first discuss the systems showing a single relaxation mode, i.e., MCM-41, B-PMO, BP-PMO, and DVB-PMO. The relaxation mode of each system appeared on a comparable time scale and exhibited a qualitatively similar temperature dependence. This suggests that they have a common origin. This unique relaxation process is consistent with the presence of a single phase formed by the surface layer adsorbed at the pore wall.[29] In line with the nomenclature often used in the literature,[27,29] the process arising from the adsorbed surface layer is later designated as the monolayer process. This does not imply that the microscopic picture of water forming a single molecular layer that uniformly covers the pore surface is strictly valid. Indeed, the existence of water clusters on the silica surface cannot be ruled out, a situation which would also be likely for PMOs due to the modulated surface chemistry.

Interestingly, this monolayer process cannot be confused with the interfacial water process seen in the samples loaded at 75% RH. First, it is about 2−3 decades faster than the interfacial water process, as also illustrated in Figure S10.[27,29] Moreover, the relaxation time of the monolayer processes presents an Arrhenian temperature dependence in the entire temperature range analyzed. The Arrhenius fitting parameters are summarized in Table 3. Importantly, this analysis reveals that the nature of the water−surface interactions, which is controlled by the pore chemistry of PMOs, differently affects the monolayer and interfacial water processes. Indeed, the activation energy is reduced to values in the range from 33 to 35 ± 0.5 kJ mol^{-1} for PMOs compared to 40 ± 0.5 kJ mol^{-1} for MCM-41.

We infer that the activation energy reflects the different environments around the adsorption sites found in MCM-41 and PMOs. Due to their polarity and their ability to form H-bonds, silanols are the preferential adsorption sites for water

Table 3. Arrhenius Parameters of Monolayer Processes for Confined Water in the Five Matrices at 33% RH

porous matrix label	τ_∞ (s)	E_a (kJ mol^{-1})
MCM-41	~10^{-18}	40 ± 0.5
DVA-PMO[a]	~10^{-23}	57 ± 0.5
DVA-PMO[b]	~10^{-16}	33 ± 0.5
B-PMO	~10^{-16}	33 ± 0.5
BP-PMO	~10^{-16}	35 ± 0.5
DVB-PMO	~10^{-15}	34 ± 0.5

[a]Process related to water interacting with the amine groups. [b]Process related to water interacting with the silanol groups.

molecules. This was confirmed by quantum mechanical calculations for a model silica surface by Saengsawang et al.[50] Among different possible configurations, this study has shown that the strongest binding energy was achieved for clusters formed by a water interacting with two silanols. This configuration is also likely to occur on the pore surface of MCM-41 silica matrices. However, it must be rarer for PMOs due to the larger average distance between silanols. More precisely, considering that the organic and silica bridging units are alternately occupying periodic positions along the pore z-axis, it might still be possible for a water molecule to be bounded to two silanols that occupy radially adjacent positions.

However, this is impossible for two axially adjacent silanols because they are spatially separated by an organic bridging unit. Indeed, we recall that the repetition distance of silica units along the z-axis (cf. Figure 1) is Δz = 0.76 nm for B-PMO and Δz = 1.2 nm for BP-PMO and DVB-PMO, which exceeds the size of a single water molecule. In PMOs, a single water bound to silanol is still possible but energetically weaker,[50] which we designate as the possible origin of the smaller activation energy for the dipolar relaxation mode. This interpretation also rationalizes the fact that, despite a different repetition distance, a similar relaxation process was observed for the three PMOs.

We finally consider the specific case of water adsorbed in DVA-PMO, which presented two distinct relaxation processes. It is obvious from Figure 6 that the time scale of the fastest process agrees well with that of the single relaxation process discussed above for the three other PMOs. This is also true for the value of the activation energy, which equals 33 kJ mol^{-1}. We therefore attribute this process to the rotational motion of the water molecules adsorbed on the silanols of the silica unit. The activation energy of the second relaxation process (57 kJ mol^{-1}) is almost twice as large as the first one and also larger than the monolayer process for MCM-41.

It is worth noting that the coexistence of two relaxation peaks was also reported in a previous study for MCM-41 with comparable pore size (D = 3.6 nm).[27] This situation was obtained for intermediate levels of hydration, and the two relaxation processes were attributed to a coexisting adsorbed water monolayer and capillary condensed water. In this study, the samples were hydrated by exposing them to 100% RH, but the hydration step was limited to a water load below complete filling. The level of hydration H was expressed in terms of water mass uptake per mass of dry sample, which should not be confused with RH. Only a monolayer relaxation was observed at the hydration level (H = 8%), while the second relaxation emerged at H = 15%. Although the hydration method used in that study complicates the estimation of the actual RH, it is very likely that the hydration level (H = 15%), where two

https://doi.org/10.1021/acs.jpcc.1c05502
J. Phys. Chem. C XXXX, XXX, XXX−XXX

relaxation processes were reported for MCM-41, was indeed located within the hysteresis loop of the capillary condensation. This could explain the coexistence of capillary filled pores with other pore surfaces only covered with a monolayer.

In the present study, the two values of the relative humidity (33% and 75% RH) were selected to be properly situated outside the hysteresis loop of the capillary condensation, that is to say, in two regions of the water adsorption isotherm where both the adsorption and desorption branches were superimposed. This excludes the possible coexistence of unfilled and capillary filled regions and also the hypothetical formation of metastable states. In fact, based on the water physisorption isotherms of PMOs (cf. Supporting Information in ref 35), we could estimate that the hydration level for DVA-PMO (33% RH) was H = 7%, which is comparable to H = 8% in the above-mentioned study, where only a single monolayer process was observed for MCM-41.[27]

Therefore, the case of DVA-PMO requires another interpretation. In order to attribute this additional process, two useful remarks can be done: (i) compared to the other PMOs, and especially DVB-PMO, the only specificity of DVA-PMO arises from the presence of an amine H-bonding group, and (ii) the activation energy of this second process is approaching the value obtained for the interfacial water in the case of capillary filled samples (i.e., 75% RH). According to (i), it seems natural to associate this process to the presence of a secondary adsorption site located on the bridging unit. In fact, the existence of two different adsorption sites in DVA-PMO has been demonstrated for capillary filled samples by 2D ^{1}H−^{29}Si and ^{1}H−^{13}C HETCOR NMR.[35] In these experiments, two sets of NMR cross peaks revealed that water closely interacted with the organic unit and with the silica part of the pore surface of DVA-PMO. In contrast, for a non-H-bonded organic bridging unit, i.e., BP-PMO, the cross peaks were restricted to water−silica interactions. This supports the hypothesis that the second relaxation process actually arises from water molecules interacting with the amine sites. Although interesting, this picture alone does not provide a clear explanation for the large value of the activation energy (ii). In fact, nitrogen being less electronegative than oxygen, the strength of the H-bond associated with this second adsorption site is expectedly weaker than that associated with silanol. In our opinion, the most sensible interpretation not only involves an individual adsorbed molecule but also requires the formation of clusters of water molecules on the pore surface before capillary condensation. This phenomenon can obviously be favored by the spatial modulation of the surface interaction, induced by the specific surface chemistry of PMO. The higher conformational flexibility of the organic bridging units with respect to surface silanols may also confer a stabilizing effect on the H-bonding amino groups of the DVA moieties. In contrast to the adsorbed monolayer, water clusters involve both water−surface and water−water interactions, which are consistent with the larger value of the activation energy of the corresponding relaxation process.

3. CONCLUSIONS

We performed a systematic DRS study on the reorientation dynamics of water confined in mesoporous silica with different pore diameters (SBA-15, MCM-41) and four organosilicas (PMOs) with different surface chemistries and surface interactions. Two values of the filling fractions were achieved by controlling the value of the relative humidity maintained during the hydration process. The first condition (75% RH) stands above the completion of the capillary condensation, which ensures a full loading of the porous volume with water and no bulk excess. The second (33% RH) is located below the onset of capillary condensation, which implies that water molecules are adsorbed on the inner surface of the channels, leaving the center of the pores empty.

For completely filled pores, partial crystallization occurred in the temperature range studied. Two relaxation processes were attributed, respectively, to ice and to unfreezable interfacial water that is sandwiched between the pore surface and the surface of distorted ice, in line with previous findings.[20,27−29] Geometrical considerations based on the relative variation of the dielectric strength of these modes as a function of the pore size of the two silicas (D = 8.3 and 3.6 nm) were found to be consistent with the estimated thickness of the interfacial layer ($e \approx 0.6$ nm). This value corresponding to about two molecular sizes agrees with the thickness derived from thermoporometric studies.[37]

For capillary filled PMOs (75% RH) with comparable pore sizes but different surface chemistry, a systematic evolution of the dielectric strength of the interfacial layer relative to ice was observed. A simplified description, based on the ratio of the relative dielectric strengths of the two relaxation processes, indicated a correlation between the amount of water involved in the interfacial layer and the chemistry of the pore surface. As a general trend, the contribution from the interfacial layer was found to decrease with increasing surface hydrophobicity. Nevertheless, no significant influence of the surface chemistry was found on the water reorientation dynamics in the interfacial layer, in terms of relaxation time and activation energy. This indicates that the dynamics of water molecules forming the interfacial layer between ice and the pore surface is governed by water−water interactions and that the surface chemistry plays a secondary role.

This finding contrasts with the case of water molecules adsorbed on the pore surface at low partial pressure (33% RH). In this case, depending on the surface chemistry, we have identified three distinct situations. (i) For MCM-41, a single Arrhenius-like relaxation process was observed. The value of its relative dielectric strength was about half that of the interfacial process measured at full loading, which is consistent with the formation of an adsorbed monolayer. Its faster dynamics and its smaller activation energy (40 kJ mol^{-1}) further demonstrate that the nature of the monolayer is obviously different from the interfacial water discussed above. In MCM-41, rather than water−water interaction, the rotational dynamics of monolayer molecules is determined by the H-bond interaction with the surface silanols. (ii) For PMOs, a similar relaxation process was also observed, but its activation energy was reduced to 33−35 kJ mol^{-1} compared to 40 kJ mol^{-1} for MCM-41. While H-bonding silanols are still present on the surface of PMOs, they are distributed periodically along the pore axis. We have shown that the repetition distance, determined by the length of the organic bridging unit, hinders the formation of multiple H-bonds with adsorbed water molecules. As a result, we infer that the smaller energy required to break the water−surface binding interaction consequently reduces the activation energy of the rotational dynamics of adsorbed water. (iii) For DVA-PMO, an additional relaxation process with Arrhenius-like temperature dependence was observed. It was attributed to the specific capability of DVA to act as a second H-bonding adsorption site for surface water molecules, due to the presence of an amine

https://doi.org/10.1021/acs.jpcc.1c05502
J. Phys. Chem. C XXXX, XXX, XXX−XXX

group. The relatively large value of the activation energy (57 kJ mol^{-1}) of this second process points to the formation of clusters of H-bonded water molecules in the vicinity of the DVA units. The stabilization of water clusters could benefit from the higher conformational flexibility of DVA organics with respect to silanols. At present, this interpretation still needs to be supported by additional sets of data and would greatly profit from a microscopic picture as offered by molecular simulation. Interestingly, this picture definitively contrasts with the simplified view of adsorbed water molecules, forming a uniformly distributed monolayer on the pore surface, which was suggested for MCM-41.

This highlights the new possibility of controlling the properties of confined liquids thanks to the spatial modulation of the surface interaction, induced by the specific surface chemistry of PMOs, with regard to both the equilibrium and nonequilibrium transport behavior.[51] In particular, the exploration of capillarity-driven flow phenomena,[52,53] where the surface modulation affects the resulting Laplace pressures and effective viscosities and thus hydraulic permeabilities, could be rewarding in the future.

■ ASSOCIATED CONTENT

Supporting Information

The Supporting Information is available free of charge at https://pubs.acs.org/doi/10.1021/acs.jpcc.1c05502.

Further information on materials (Section S1, Table S1); sample hydration method (Section S2); dielectric spectroscopy method (Section S3.); dielectric loss of water confined in MCM-41 and PMOs loaded at 75% RH (Figure S1, Figure S2); secondary weak process of water-filled MCM-41 (Figure S3); pore size effects on water-filled MCM-41 and SBA-15 silicas (Figure S4, Figure S5, Table S2, Table S3); dielectric fitted functions for water-filled PMOs (Figure S6); temperature dependence of the different relaxation times for water-filled MCM-41 and SBA-15 (Figure S7); dielectric loss of water adsorbed in PMOs at 33% RH (Figure S8); dielectric fitted functions for water adsorbed in PMOs at 33% RH (Figure S9); masterplot curves of the monolayer process in the five matrices (Figure S10); temperature dependence of the different relaxation times for water adsorbed in mesoporous MCM-41 silicas at two RH (Figure S11); highlighting crystallization and melting processes in SBA-15 loaded at 75% RH (Figure S12); and references (Section S14) (PDF)

■ AUTHOR INFORMATION

Corresponding Authors

Patrick Huber − *Institute for Materials and X-ray Physics, Hamburg University of Technology, 21073 Hamburg, Germany; Centre for X-Ray and Nano Science CXNS, Deutsches Elektronen-Synchrotron DESY, 22603 Hamburg, Germany; Centre for Hybrid Nanostructures CHyN, Hamburg University, 22607 Hamburg, Germany;* orcid.org/0000-0002-2126-9100; Email: patrick.huber@tuhh.de

Michael Fröba − *Institute for Materials and X-ray Physics, Hamburg University of Technology, 21073 Hamburg, Germany*; Email: froeba@chemie.uni-hamburg.de

Denis Morineau − *Institute of Physics of Rennes, CNRS-University of Rennes 1, UMR 6251, F-35042 Rennes, France;* orcid.org/0000-0002-8784-3021; Email: denis.morineau@univ-rennes1.fr

Authors

Benjamin Malfait − *Institute of Physics of Rennes, CNRS-University of Rennes 1, UMR 6251, F-35042 Rennes, France*

Aicha Jani − *Institute of Physics of Rennes, CNRS-University of Rennes 1, UMR 6251, F-35042 Rennes, France*

Jakob Benedikt Mietner − *Institute of Inorganic and Applied Chemistry, University of Hamburg, 20146 Hamburg, Germany*

Ronan Lefort − *Institute of Physics of Rennes, CNRS-University of Rennes 1, UMR 6251, F-35042 Rennes, France*

Complete contact information is available at: https://pubs.acs.org/10.1021/acs.jpcc.1c05502

Notes

The authors declare no competing financial interest.

■ ACKNOWLEDGMENTS

This work was conducted in the frame of the DFG-ANR collaborative project (Project NanoLiquids No. ANR-18-CE92-0011-01, DFG Grant No. FR 1372/25-1 Project number 407319385, and DFG Grant No. Hu850/11-1 Project number 407319385), which is acknowledged. Support was received from Rennes Metropole and Europe (European Regional Development Fund - CPER PRINT2TAN). We thank Dr. Malina Bilo for providing the B-PMO sample. It is a pleasure to acknowledge Prof. Andreas Schönhals for fruitful discussions and critical reading of the manuscript. We also acknowledge the scientific exchange and support of the Center for Molecular Water Science (CMWS).

■ REFERENCES

(1) Babel, S. Low-Cost Adsorbents for Heavy Metals Uptake from Contaminated Water: A Review. *J. Hazard. Mater.* **2003**, *97* (1−3), 219−243.

(2) Kusoglu, A.; Weber, A. Z. New Insights into Perfluorinated Sulfonic-Acid Ionomers. *Chem. Rev.* **2017**, *117* (3), 987−1104.

(3) Martinez, N.; Morin, A.; Berrod, Q.; Frick, B.; Ollivier, J.; Porcar, L.; Gebel, G.; Lyonnard, S. Multiscale Water Dynamics in a Fuel Cell by Operando Quasi Elastic Neutron Scattering. *J. Phys. Chem. C* **2018**, *122* (2), 1103−1108.

(4) Bocquet, L. Nanofluidics Coming of Age. *Nat. Mater.* **2020**, *19* (3), 254−256.

(5) Middendorf, H. D. Neutron Studies of the Dynamics of Biological Water. *Phys. B* **1996**, *226*, 113−127.

(6) Bagchi, B. Water Dynamics in the Hydration Layer around Proteins and Micelles. *Chem. Rev.* **2005**, *105* (9), 3197−3219.

(7) Cerveny, S.; Mallamace, F.; Swenson, J.; Vogel, M.; Xu, L. Confined Water as Model of Supercooled Water. *Chem. Rev.* **2016**, *116* (13), 7608−7625.

(8) Wohlfromm, T.; Vogel, M. On the Coupling of Protein and Water Dynamics in Confinement: Spatially Resolved Molecular Dynamics Simulation Studies. *J. Chem. Phys.* **2019**, *150* (24), 245101.

(9) Bizzarri, A. R.; Cannistraro, S. Molecular Dynamics of Water at the Protein-Solvent Interface. *J. Phys. Chem. B* **2002**, *106* (26), 6617−6633.

(10) Laage, D.; Elsaesser, T.; Hynes, J. T. Water Dynamics in the Hydration Shells of Biomolecules. *Chem. Rev.* **2017**, *117* (16), 10694−10725.

(11) Findenegg, G. H.; Jähnert, S.; Akcakayiran, D.; Schreiber, A. Freezing and Melting of Water Confined in Silica Nanopores. *ChemPhysChem* **2008**, *9* (18), 2651−2659.

(12) Jackson, C. L.; McKenna, G. B. Vitrification and Crystallization of Organic Liquids Confined to Nanoscale Pores. *Chem. Mater.* **1996**, *8* (8), 2128−2137.
(13) Malfait, B.; Correia, N. T.; Ciotonea, C.; Dhainaut, J.; Dacquin, J.; Royer, S.; Tabary, N.; Guinet, Y.; Hédoux, A. Manipulating the Physical States of Confined Ibuprofen in SBA-15 Based Drug Delivery Systems Obtained by Solid-State Loading: Impact of the Loading Degree. *J. Chem. Phys.* **2020**, *153* (15), 154506.
(14) Gallo, P.; Amann-Winkel, K.; Angell, C. A.; Anisimov, M. A.; Caupin, F.; Chakravarty, C.; Lascaris, E.; Loerting, T.; Panagiotopoulos, A. Z.; Russo, J.; et al. Water: A Tale of Two Liquids. *Chem. Rev.* **2016**, *116* (13), 7463−7500.
(15) Cerveny, S.; Schwartz, G. A.; Bergman, R.; Swenson, J. Glass Transition and Relaxation Processes in Supercooled Water. *Phys. Rev. Lett.* **2004**, *93* (24), 245702.
(16) Cerveny, S.; Barroso-Bujans, F.; Alegría, Á.; Colmenero, J. Dynamics of Water Intercalated in Graphite Oxide. *J. Phys. Chem. C* **2010**, *114*, 2604−2612.
(17) Pahlke, B. H.; Lusceac, S. A.; Geil, B.; Fujara, F. NMR Study of Local and Long Range Dynamics of Adsorbed Water in Zeolite NaY (Br). *Z. Phys. Chem.* **2012**, *226* (11−12), 1093−1113.
(18) Ryabov, Y.; Gutina, A.; Arkhipov, V.; Feldman, Y. Dielectric Relaxation of Water Absorbed in Porous Glass. *J. Phys. Chem. B* **2001**, *105* (9), 1845−1850.
(19) Soprunyuk, V.; Schranz, W.; Huber, P. Dynamic Mechanical Analysis of Supercooled Water in Nanoporous Confinement. *EPL (Europhysics Lett.* **2016**, *115* (4), 46001.
(20) Weigler, M.; Brodrecht, M.; Buntkowsky, G.; Vogel, M. Reorientation of Deeply Cooled Water in Mesoporous Silica: NMR Studies of the Pore-Size Dependence. *J. Phys. Chem. B* **2019**, *123* (9), 2123−2134.
(21) Hedström, J.; Swenson, J.; Bergman, R.; Jansson, H.; Kittaka, S. Does Confined Water Exhibit a Fragile-to-Strong Transition? *Eur. Phys. J.: Spec. Top.* **2007**, *141* (1), 53−56.
(22) Feuston, B. P.; Higgins, J. B. Model Structures for MCM-41 Materials: A Molecular Dynamics Simulation. *J. Phys. Chem.* **1994**, *98* (16), 4459−4462.
(23) Beck, J. S.; Vartuli, J. C.; Roth, W. J.; Leonowicz, M. E.; Kresge, C. T.; Schmitt, K. D.; Chu, C. T. W.; Olson, D. H.; Sheppard, E. W.; McCullen, S. B.; et al. A New Family of Mesoporous Molecular Sieves Prepared with Liquid Crystal Templates. *J. Am. Chem. Soc.* **1992**, *114* (27), 10834−10843.
(24) Sattig, M.; Reutter, S.; Fujara, F.; Werner, M.; Buntkowsky, G.; Vogel, M. NMR Studies on the Temperature-Dependent Dynamics of Confined Water. *Phys. Chem. Chem. Phys.* **2014**, *16*, 19229−19240.
(25) Liu, L.; Chen, S.; Faraone, A.; Yen, C.; Mou, C. Pressure Dependence of Fragile-to-Strong Transition and a Possible Second Critical Point in Supercooled Confined Water. *Phys. Rev. Lett.* **2005**, *95*, 117802.
(26) Weigler, M.; Brodrecht, M.; Breitzke, H.; Dietrich, F.; Sattig, M.; Buntkowsky, G.; Vogel, M. 2H NMR Studies on Water Dynamics in Functionalized Mesoporous Silica. *Z. Phys. Chem.* **2018**, *232* (7−8), 1041−1058.
(27) Lederle, C.; Sattig, M.; Vogel, M. Effects of Partial Crystallization on the Dynamics of Water in Mesoporous Silica. *J. Phys. Chem. C* **2018**, *122* (27), 15427−15434.
(28) Swenson, J.; Cerveny, S. Dynamics of Deeply Supercooled Interfacial Water. *J. Phys.: Condens. Matter* **2015**, *27*, 033102.
(29) Sjöström, J.; Swenson, J.; Bergman, R.; Kittaka, S. Investigating Hydration Dependence of Dynamics of Confined Water: Monolayer, Hydration Water and Maxwell-Wagner Processes. *J. Chem. Phys.* **2008**, *128* (15), 154503.
(30) Sattig, M.; Vogel, M. Dynamic Crossovers and Stepwise Solidification of Confined Water: A 2 H NMR Study. *J. Phys. Chem. Lett.* **2014**, *5* (1), 174−178.
(31) Jansson, H.; Swenson, J. Dynamics of Water in Molecular Sieves by Dielectric Spectroscopy. *Eur. Phys. J. E: Soft Matter Biol. Phys.* **2003**, *12* (S1), 51−54.
(32) Swenson, J. Possible Relations between Supercooled and Glassy Confined Water and Amorphous Bulk Ice. *Phys. Chem. Chem. Phys.* **2018**, *20* (48), 30095−30103.
(33) Hoffmann, F.; Cornelius, M.; Morell, J.; Fröba, M. Silica-Based Mesoporous Organic-Inorganic Hybrid Materials. *Angew. Chem., Int. Ed.* **2006**, *45* (20), 3216−3251.
(34) Iliade, P.; Miletto, I.; Coluccia, S.; Berlier, G. Functionalization of Mesoporous MCM-41 with Aminopropyl Groups by Co-Condensation and Grafting: A Physico-Chemical Characterization. *Res. Chem. Intermed.* **2012**, *38*, 785−794.
(35) Mietner, B. J.; Brieler, F. J.; Lee, Y. J.; Fröba, M. Properties of Water Confined in Periodic Mesoporous Organosilicas: Nano-imprinting the Local Structure. *Angew. Chem., Int. Ed.* **2017**, *56*, 12348−12351.
(36) Jani, A.; Busch, M.; Mietner, J. B.; Ollivier, J.; Appel, M.; Frick, B.; Zanotti, J.-M.; Ghoufi, A.; Huber, P.; Fröba, M.; et al. Dynamics of Water Confined in Mesopores with Variable Surface Interaction. *J. Chem. Phys.* **2021**, *154* (9), 094505.
(37) Jähnert, S.; Vaca Chávez, F.; Schaumann, G. E.; Schreiber, A.; Schönhoff, M.; Findenegg, G. H. Melting and Freezing of Water in Cylindrical Silica Nanopores. *Phys. Chem. Chem. Phys.* **2008**, *10* (39), 6039.
(38) Richert, R. Dielectric Spectroscopy and Dynamics in Confinement. *Eur. Phys. J.: Spec. Top.* **2010**, *189* (1), 37−46.
(39) Mijovic, J. Dielectric Spectroscopy of Reactive Network-Forming Polymers. In *Broadband Dielectric Spectroscopy*; Kremer, F., Schönhals, A., Eds.; Springer Berlin Heidelberg: Berlin, Heidelberg, 2002; p 350.
(40) Thommes, M.; Morell, J.; Cychosz, K. A.; Fröba, M. Combining Nitrogen, Argon, and Water Adsorption for Advanced Characterization of Ordered Mesoporous Carbons (CMKs) and Periodic Mesoporous Organosilicas (PMOs). *Langmuir* **2013**, *29*, 14893−14902.
(41) Kothari, K.; Ragoonanan, V.; Suryanarayanan, R. Dielectric Spectroscopy of Small Molecule Pharmaceuticals—Effect of Sample Configuration. *J. Pharm. Sci.* **2014**, *103* (10), 3190−3196.
(42) Mietner, B. J. Visiting Nanopores: The Great Potential of PMOs for Studying the Properties of Water in Nanopores of Different Polarity. *Universität Hamburg-Doctoral dissertation*, 2018.
(43) Thangswamy, M.; Maheshwari, P.; Dutta, D.; Bera, A. K.; Singh, M. N.; Sinha, A. K.; Yusuf, S. M.; Pujari, P. K. Evolution of Confined Ice Nano Structures at Different Levels of Pore Filling: A Synchrotron Based X-Ray Diffraction Study. *Phys. Chem. Chem. Phys.* **2020**, *22*, 14309−14317.
(44) Popov, I.; Ishai, P. B.; Khamzin, A.; Feldman, Y. The Mechanism of the Dielectric Relaxation in Water. *Phys. Chem. Chem. Phys.* **2016**, *18*, 13941−13953.
(45) Kremer, F.; Schönhals, A. The Scaling of the Dynamics of Glasses and Supercooled Liquids. In *Broadband Dielectric Spectroscopy*; Kremer, F., Schönhals, A., Eds.; Springer: Berlin Heidelberg, 2003; pp 99−130.
(46) Cerveny, S.; Alegría, Á.; Colmenero, J. Universal Features of Water Dynamics in Solutions of Hydrophilic Polymers, Biopolymers, and Small Glass-Forming Materials. *Phys. Rev. E* **2008**, *77*, 031803.
(47) Elamin, K.; Jansson, H.; Swenson, J. Dynamics of Aqueous Binary Glass-Formers Confined in MCM-41. *Phys. Chem. Chem. Phys.* **2015**, *17* (19), 12978−12987.
(48) Steinrücken, E.; Wissel, T.; Brodrecht, M.; Breitzke, H.; Regentin, J.; Buntkowsky, G.; Vogel, M. 2 H NMR Study on Temperature-Dependent Water Dynamics in Amino-Acid Functionalized Silica Nanopores. *J. Chem. Phys.* **2021**, *154* (11), 114702.
(49) Kremer, F.; Schönhals, A. Theory of Dielectric Relaxation. In *Broadband Dielectric Spectroscopy*; Kremer, F., Schönhals, A., Eds.; Springer: Berlin Heidelberg, 2003; pp 1−34.
(50) Saengsawang, O.; Remsungnen, T.; Fritzsche, S.; Haberlandt, R.; Hannongbua, S. Structure and Energetics of Water-Silanol Binding on the Surface of Silicalite-1: Quantum Chemical Calculations. *J. Phys. Chem. B* **2005**, *109* (12), 5684−5690.

https://doi.org/10.1021/acs.jpcc.1c05502
J. Phys. Chem. C XXXX, XXX, XXX−XXX

(51) Huber, P. Soft Matter in Hard Confinement: Phase Transition Thermodynamics, Structure, Texture, Diffusion and Flow in Nanoporous Media. *J. Phys.: Condens. Matter* **2015**, *27* (10), 103102.
(52) Gruener, S.; Hofmann, T.; Wallacher, D.; Kityk, A. V.; Huber, P. Capillary Rise of Water in Hydrophilic Nanopores. *Phys. Rev. E* **2009**, *79* (6), 067301.
(53) Gruener, S.; Wallacher, D.; Greulich, S.; Busch, M.; Huber, P. Hydraulic Transport across Hydrophilic and Hydrophobic Nanopores: Flow Experiments with Water and n-Hexane. *Phys. Rev. E: Stat. Phys., Plasmas, Fluids, Relat. Interdiscip. Top.* **2016**, *93* (1), 013102.

https://doi.org/10.1021/acs.jpcc.1c05502
J. Phys. Chem. C XXXX, XXX, XXX−XXX

ANNEX-III

Do Deep Eutectic Solvents Form Uniform Mixtures Beyond Molecular Microheterogeneities?

Authors

Lucie Percevault, Aicha Jani, Thibaut Sohier, Laurence Noirez, Ludovic Paquin, Fabienne Gauffre, Denis Morineau

THE JOURNAL OF PHYSICAL CHEMISTRY B

pubs.acs.org/JPCB Article

Do Deep Eutectic Solvents Form Uniform Mixtures Beyond Molecular Microheterogeneities?

Lucie Percevault, Aicha Jani, Thibaut Sohier, Laurence Noirez, Ludovic Paquin, Fabienne Gauffre, and Denis Morineau*

Cite This: J. Phys. Chem. B 2020, 124, 9126–9135 Read Online

ACCESS | Metrics & More | Article Recommendations | Supporting Information

ABSTRACT: We have performed small-angle neutron scattering in a momentum transfer range ($0.05 < Q < 0.5$ Å^{-1}) to study long-range order and concentration fluctuations in deep eutectic solvents (DESs) and their aqueous solutions. Ethaline (choline chloride/ethylene glycol), glycerol/lactic acid, and menthol/decanoic acid mixtures were selected to illustrate individually the case of ionic, nonionic, and hydrophobic mixtures. Carefully designed isotopic labeling was used to emphasize selectively the spatial correlations between the different solvent components. For ethaline DESs and their aqueous solutions, a weak low-Q peak observed only for certain compositions and some partial structure factors revealed the mesoscopic segregation of ethylene glycol molecules that do not participate in the solvation of ionic units, either because they are in excess with respect to the eutectic stoichiometry (1:4 neat ethaline) or substituted by water (4w-ethaline and higher aqueous dilutions). For the nonionic hydrophilic solutions, such a mesoscopic segregation was not observed. This indicates that the better balanced interactions between the three nonionic H-bonded components (water, lactic acid, and glycerol) favor homogeneous mixing. For the hydrophobic DESs, we observed an excess of coherent scattering intensity centered at $Q = 0$, which could be reproduced by a model of noninteracting spherical domains. Local concentration fluctuations are not excluded either. However, unlike liquid mixtures with a tendency to demix, we have found no evidence of expansion of domains with different compositions to a large scale.

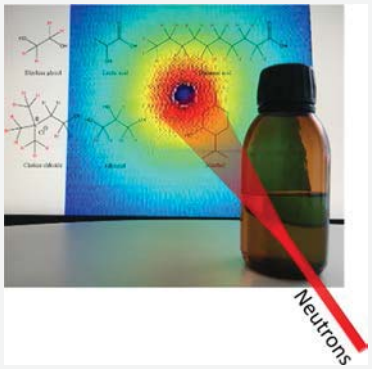

1. INTRODUCTION

Since their recent introduction as a promising alternative to classical solvents, the interest in deep eutectic solvents (DESs) has increased continuously.[1,2] They are considered as more affordable and usually less toxic variants of the room-temperature ionic liquids. In the meantime, they retain most of the advantages of their ionic counterparts, including low volatility and high solvating and extracting properties. The performances of DESs have been considered for practical applications in a growing number of industrial processes, including extraction, (bio)synthesis, catalysis, electrochemistry, and carbon dioxide capture.[3−5]

According to their initial description, DESs are formed by the mixing of an H-bond donor (HBD) with an H-bond acceptor (HBA) or with a molecular ionic species (such as a quaternary ammonium). The existence of an eutectic point in the phase diagram of the as-formed binary mixture induces a large depression of its melting point.[6,7] This forms a phase that remains in the liquid state below room temperature even though its constituents melt at a much higher temperature. It is also expected that the strong ionic and H-bonding interactions favor specific spatial correlations between the DES constituents.[8,9] The resulting non-ideal mixing effects could explain the exceptional lowering of the melting point of certain DESs.

In the quest of solvents with carefully designed functional properties, a series of different types of mixtures was prepared and studied, including nonionic, hydrophobic, or natural systems.[3−5] Accordingly, the attributes of DESs enounced in the initial definitions have been considered in a more loose way, with regard to non-ideal mixing and the relation to the eutectic composition. For practical reasons, aqueous solutions of DESs have been formulated and their physical properties, including excess properties, viscosity, and acoustic, structural, and optical properties have been studied thoroughly.[9−21] These works have also raised the question of the resilience of the specific local arrangement of DES during dilution with water and its evolution toward an aqueous solution of its constituents.[9−11,19,22]

The structure of DESs has attracted a lot of interest during the last four years. Hammond et al. performed wide-angle neutron scattering (WANS) experiments fitted to an empirical potential structure refinement (EPSR) model for reline (1:2

Received: July 10, 2020
Revised: August 21, 2020
Published: September 18, 2020

https://dx.doi.org/10.1021/acs.jpcb.0c06317
J. Phys. Chem. B 2020, 124, 9126−9135

choline chloride/urea).[23] This study showed that reline formed stoichiometric supramolecular ionic complexes, which are composed of H-bonded coordinating choline and urea strongly interacting with chloride anions. Complementing this pioneering work, WANS studies reported complexed ionic clusters for choline chloride-based DESs with different HBDs.[22,24,25] The principal role of the HBD−chloride anion interactions in controlling the formation of supramolecular solvated units was generally pointed out. However, it was shown that changing the composition or the temperature impacts the stability and stoichiometry, as well as the role of the choline cation as a secondary HBD participant. Fluorescence and infrared spectroscopy studies demonstrated that changing the hydrocarbon chain length of both HBA and HBD affects the spatial and dynamic heterogeneity of the ionic DESs.[26−28] This view is in line with conclusions from WANS on alkylammonium bromide/glycerol DESs[29] and molecular dynamics (MD) simulation of choline chloride derivatives/ethylene glycol (EG) DESs[30] that have related the microheterogeneous structure of DESs to the segregation of the apolar and polar groups of the cationic molecules into separated domains. The formation and the percolation of these domains are favored by larger chains, which reveal the role of the amphiphilic character of the cationic moieties. Interestingly, these supramolecular assemblies reflect the non-ideal character of DESs. In fact, it was concluded from a systematic studies of reline, glyceline (choline chloride/glycerol), and ethaline (choline chloride/EG) DESs by QM/MD (quantum mechanics/molecular dyanmics) simulation that the extension of the hydrogen bond network between the HBD and the ionic species was correlated with the enhanced depression of the melting point.[31] The effects of non-ideal mixing in both the structure and some physicochemical properties (e.g., the lowering of the melting point) of DESs and DES dilutions were stressed in recent studies of a ternary DES composed of ChCl, urea, and resorcinol diluted in either water or benzyl alcohol. Using both MD simulations and neutron scattering with isotopic substitution together with EPSR as well as Brillouin and NMR spectroscopies, these studies described how, in the so-called solvent-in-DES regime, solvent molecules participated in the H-bond complexes of the original DESs as an additional HBD.[32,33]

Another aspect of special interest is the observation of a low-Q peak centered about the momentum transfer $Q = 0.15-0.3$ Å^{-1} (also denoted as a prepeak) in the simulated neutron and X-ray scattering static structure factor of Li^+/ClO_4^-/alkylamide DES.[34,35] This prepeak is the fingerprint of intermediate range order, in line with similar observations commonly made for ionic liquids or alcohols.[36,37] For reline and ethaline, there is no noticeable prepeak in the total structure factor.[8,38] However, according to these MD simulations, this observation was due to cancellation effects.[8] In fact, prepeaks were observed in simulated partial structure factors, and they were attributed to the presence of unique intermediate range structural ordering. More specifically for ethaline, a prepeak predicted at about $Q = 0.5$ Å^{-1} was related to EG homomolecular correlations (i.e., EG−EG correlations).[8] Due to the lack of experimental scattering data for ethaline DES, this recent prediction has not been verified so far.

Compared to ion-based DESs, there is less literature on structural studies of DESs that do not comprise ionic salts or organic cations. We denote these systems as "nonionic DESs," notwithstanding the presence of carboxylic acid groups. Microheterogeneous structures produced by segregation of polar/nonpolar molecular groups forming nanoscopic domains have been evidenced by IR spectroscopy for *N*-methylacetamide/lauric acid DES.[39] There are also evidence that lauric acid molecules form micellar structures in DESs with a size corresponding to two lauric acids, which is further supported by the presence of a prepeak at $Q = 0.25$ Å^{-1} in the X-ray scattering intensity.[40]

Given the amphiphilic nature of many DES ingredients, the structure of their aqueous solutions is a particularly exciting topic. Neutron scattering experiments and MD simulation point out the preferential solvation of chloride by water in choline chloride-based DESs.[10,16,41,42] However, the supramolecular ionic clusters formed by the association of the initial DES components seem resistant to moderate hydration levels.[22,43] Although aqueous solutions of reline were demonstrated not to be classically phase-separated,[10] it is noteworthy that microphase segregation and the formation of co-continuous structures were evidenced by NMR and Brillouin spectroscopy in various water−DES mixtures.[18,19,44] The detailed nature of such microphase separated structure is still under discussion. On the one hand, the formation of large water clusters (e.g. 1 nm) was dismissed for malic acid/choline chloride/water (1:1:2), water rather forming a transient, wormlike aggregates that rarely exceed two molecules in width.[22] On the other hand, recent MD simulation of ethaline water mixtures revealed that the growth of long-range density fluctuations on increasing the hydration level was more specifically attributed to the segregation of the HBD molecules (i.e., EG) in the pool of the aqueous mixture.[9] This is supported by the existence of multimers composed of strongly H-bonded EG molecules in aqueous solution of ethaline, as demonstrated by infrared spectroscopy and density functional theory quantum calculations.[45] According to the above-mentioned predictions from MD simulation, the mesoscopic structural ordering of EG molecules during water addition should be evidenced by the raising of a low-Q component ($0.1 \le Q \le 0.25$ Å^{-1}) for the EG−EG partial structure factor, but it could not be seen in the total $S(Q)$ due to cancellation effects.[9] Experimentally, conventional X-rays and neutron diffraction methods provide a weighted sum of all partial structure factors, which is likely also affected by the cancellation effects. A small-angle neutron scattering (SANS) experiment with isotopic labeling offers a unique possibility to measure the partial structure factors and detect this low-Q component.

The aim of the present work is to study the large-scale structure of DESs from the analysis of the static structure factor in the range of low momentum transfer ($0.05 \le Q \le 0.5$ Å^{-1}), which has been barely investigated experimentally so far. This study benefited from the high resolution of SANS. Inspired by recent predictions made from molecular simulations for ethaline DES and ethaline DES aqueous solutions, we highlighted specifically intermolecular correlations by isotopic labeling in order to reveal partial structure factors.[8,9] Neutron scattering with isotopic substitution offers a unique method to achieve this molecular labeling, as illustrated by studies of the mesoscopic structure of classical liquid mixtures.[46] Different compositions and different types of solvents were studied, spanning from ionic to nonionic, hydrophobic to hydrophilic, as well as aqueous solutions in order to bring a broad view of possible long-range order in DES and related H-bonded liquid mixtures for a series of prototypical cases.

https://dx.doi.org/10.1021/acs.jpcb.0c06317
J. Phys. Chem. B 2020, 124, 9126−9135

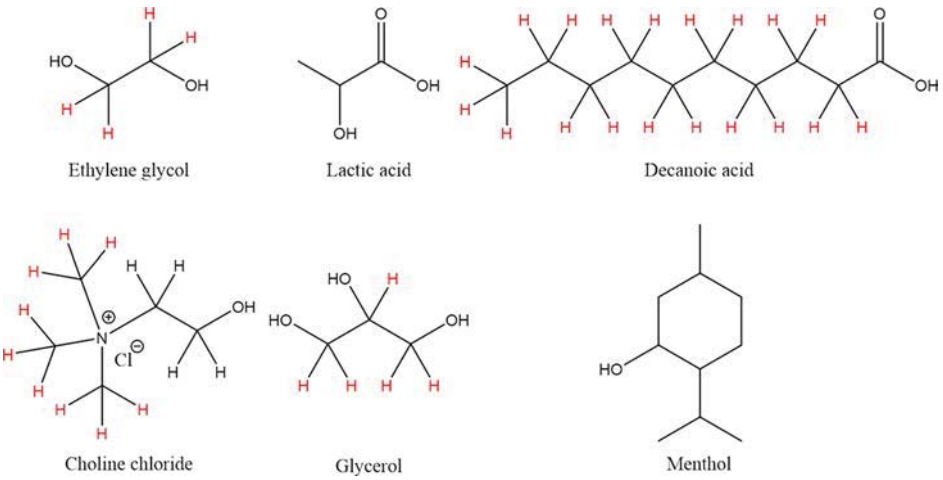

Figure 1. Molecular structure of the chemicals studied. The hydrogen sites that were isotopically labeled are colored in red.

Table 1. Composition of the DESs and Aqueous Solutions Studied

DES type	constituents	chemical composition	water mass fraction (% wt)	isotopic composition
neat ionic DES	ethylene glycol/choline chloride (ethaline)	(4:1), (3:1), (2.3:1)		(H_6:D_9H_5), (D_4H_2:H_{14})
ionic DES solution	ethylene glycol/choline chloride/water	(2:1:*w*) with *w* = 0, 0.8, 1.7, 2.7, 4, 6.5, 10	0, 5, 10, 15, 20, 30, 40	(D_4H_2:D_9H_5:H_2O), (H_6:D_9H_5:H_2O), (D_4H_2:H_{14}:H_2O)
nonionic H-bonded solution	lactic acid/glycerol/water	(1:2:*w*) with *w* = 0, 1, 2, 3, 30	0, 6, 10, 15, 66	(H_6:D_5H_3:H_2O)
hydrophobic DES	menthol/decanoic acid	(2:3), (1:1), (3:2), (2:1), (3:1), (4:1)		(H_{20}:$D_{19}H$)

Ethaline mixtures were selected as typical systems representing the class of ionic DESs. Mixtures of lactic acid with glycerol fall in the category of hydrophilic nonionic solutions. Both molecules have been used in the literature as HBD constituents of DESs formed by mixing with choline chloride,[47] and their mixtures have been applied for the treatment of biomass.[48] In the present work, we have studied lactic acid/glycerol mixtures by comparison to ethaline DESs in order to determine the impact of switching-off the electrostatic interactions. Indeed, apart from a small difference concerning the HBD (glycerol instead of EG), the main difference between these two systems is the substitution of HBA ionic choline chloride by nonionic (or partially ionic) H-bonded carboxylic acid. The effects of adding water to both of these hydrophilic solvents were also investigated. Finally, different menthol/decanoic acid mixtures were studied as members of the class of hydrophobic DES.[49,50]

2. METHODS

2.1. Samples. Fully hydrogenated choline chloride (>99%) and EG (anhydrous, 99.8%) and DL-menthol (≥95%) were purchased from Sigma-Aldrich and lactic acid (extra pure, SLR) from Fisher Scientific. Partially deuterated choline chloride (trimethyl D_9, 98% D), EG (1.1.2.2 D_4, 99% D), decanoic acid (D_{19}, 98%), and glycerol (1.1.2.3.3 D_5, 99% D) were purchased from Eurisotop. The structures of the molecules are illustrated in Figure 1, and the isotopically labeled sites are highlighted.

Mixtures were prepared by weighting and adding their constituents. The constituents were mixed by mechanical agitation at about 60 °C for duration between 30 min and 4 h until a clear homogeneous liquid phase was obtained and served as stock solutions. For hydrophilic solvents, series of aqueous solutions were prepared from the mother solutions by pipetting and addition of deionized water.

The chemical composition of the different systems is given in Table 1. It should be noted that different isotopic variants were also prepared for ethaline and ethaline DES aqueous solutions, as described later. Note that the labile hydroxyl and acid groups were not deuterated in order to avoid isotopic exchange with water.

2.2. SANS Experiments. SANS experiments were performed using the PAXY diffractometer (LLB, Saclay). The sample detector distance chosen was 1 m, and the neutron wavelength used was 5 Å allowing the measurement of the diffracted intensity in a momentum transfer range ($0.05 < Q < 0.5$ Å^{-1}). The measurements were conducted at room temperature with a thermal bath regulator set to 24.5 °C. Complementary measurements were also performed at 15 and 39 °C for comparison. The solutions were prepared in advance so the mixtures are thermodynamically at equilibrium. The solutions were filled in 1 mm thick quartz Hellma cells. The raw intensities were corrected from the empty cell contribution by subtraction of the filled and empty cell spectra, divided by the corresponding transmission. The correction of the systematic variation of the detector efficiency and normalization of $I(Q)$ to absolute unit was performed with respect to the measured intensity of a 1 mm thick hydrogenated water of known value of its incoherent cross section ($\Sigma_{incoh}/4\pi = 0.445$ cm^{-1}) using the data reduction software PASiNET from Laboratoire Léon Brillouin.

Particular attention has been paid to the use of contrast effects in order to reveal specific correlations stemming from partial structure factors. A large variation of the coherent neutron scattering of the different DESs components was

https://dx.doi.org/10.1021/acs.jpcb.0c06317
J. Phys. Chem. B 2020, 124, 9126−9135

Table 2. Neutron Coherent Scattering Length Density of the Components of Ethaline DES and Ethaline Aqueous Solutions for Three Different Isotopic Compositions[a]

Neutron scattering length density ρ_{SLD} (10^9 cm^{-2})	Ethylene glycol (EG)	Choline chloride (ChCl)	Water
ETHA-W(DDH) : $EG(D_4H_2)/ChCl(D_9H_5)$/Water (H_20)	47	47	-5
ETHA-W(HDH) : $EG(H_6)/ChCl(D_9H_5)$/Water (H_20)	2	47	-5
ETHA-W(DHH) : $EG(D_4H_2)/ChCl(H_{14})$/Water (H_20)	47	2	-5
ETHA(HD) : $EG(H_6)/ChCl(D_9H_5)$	2	47	
ETHA(DH) : $EG(D_4H_2)/ChCl(H_{14})$	47	2	

[a]The cell background colors indicate the highest scattering contrast between the different compounds.

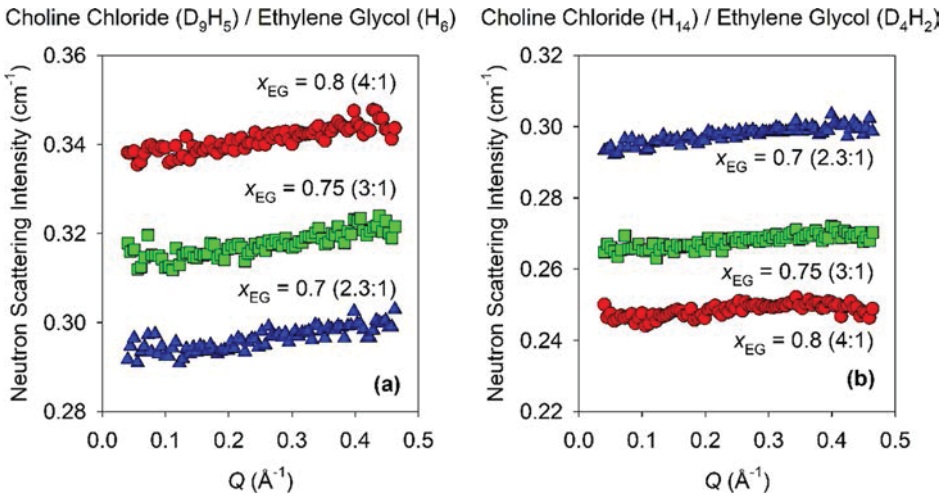

Figure 2. Neutron scattering intensity of ethaline DESs measured at 24.5 °C for three different compositions corresponding to EG/choline chloride in mol ratio 2.3:1, 3:1, and 4:1. The different panels correspond to different isotopic labeling of the two components of ethaline: (a) deuterated choline chloride ETHA(HD), (b) deuterated EG ETHA(DH).

achieved using D/H isotopic labeling, as indicated in Table 2 for the ethaline aqueous solutions, and discussed thereafter.

3. RESULTS AND DISCUSSION

3.1. Neat Ionic DES: Ethaline (EG/Choline Chloride).

Ethaline DES (EG/choline chloride) was studied in a molar ratio of 2.3:1, 3:1 and 4:1, which is in the region of maximum freezing depression.[51,52] In order to highlight the coherent scattering of one of the two components, two isotopic variants of each DESs were prepared mixing a deuterated component, which maximizes its coherent scattering with respect to the hydrogenated one [named ETHA(HD) and ETHA(DH)]. The values of the coherent scattering length density of each molecule are summarized in Table 2. They were determined according to the classical definition by $\rho_{SLD}=\sum b_i/v$, where b_i is the coherent scattering length of atom i, the sum being performed over all the atoms constituting one molecule, and v is the molecular volume. The two deuterated molecules have comparable scattering length density (47×10^9 cm^{-2}), while their fully hydrogenated forms (2×10^9 cm^{-2}) rather compare with water (-5.10^9 cm^{-2}). It is thus expected that the coherent scattering for ETHA(HD) and ETHA(DH) mostly reflect the partial structure factors arising respectively from choline chloride and EG.

The main effect of changing the EG/ChCl mol ratio (cf. Figure 2) consists in a net increase of the total scattered intensity with the fraction of hydrogenated molecules. This is obviously attributed to the incoherent scattering, which mostly arises from hydrogen contribution. The coherent scattering, which is Q-dependent, is weak in the studied Q-range. For ETHA(HD), illustrated in Figure 2a, we observed a monotonous decrease of the intensity from the medium (0.5 Å^{-1}) to small (0.05 Å^{-1}) Q values. This contribution is attributed to the low-Q side of the main diffraction peak arising from short range intermolecular order. According to recent computations of the structure factor, the maximum of the main diffraction peak is located around Q = 1.5 Å^{-1}, and thus outside the Q-range accessible to our SANS measurements.[8] In the absence of mesoscale heterogeneity, this intensity classically decreases to small values determined by the liquid compressibility in the limit of vanishing Q's. For ETHA(DH) however, we observed a deviation from this monotonous variation with the occurrence of a weak additional broad peak around Q = 0.35 Å^{-1} for EG/choline chloride (4:1) as illustrated in Figure 2b. Such a prepeak was recently witnessed in the EG−EG partial structure factor of ethaline, and attributed to long-range correlations dominated by EG molecules.[8] Our observation made for the specific isotopic composition that enhanced EG−EG correlations is consistent with this prediction. So far, MD simulations are restricted to one composition (2:1). The present SANS results suggest that this prepeak is mostly visible for larger amount of EG. We infer that having EG molecules in excess with respect to the stoichiometric composition of the DES favors their segregation

https://dx.doi.org/10.1021/acs.jpcb.0c06317
J. Phys. Chem. B 2020, 124, 9126−9135

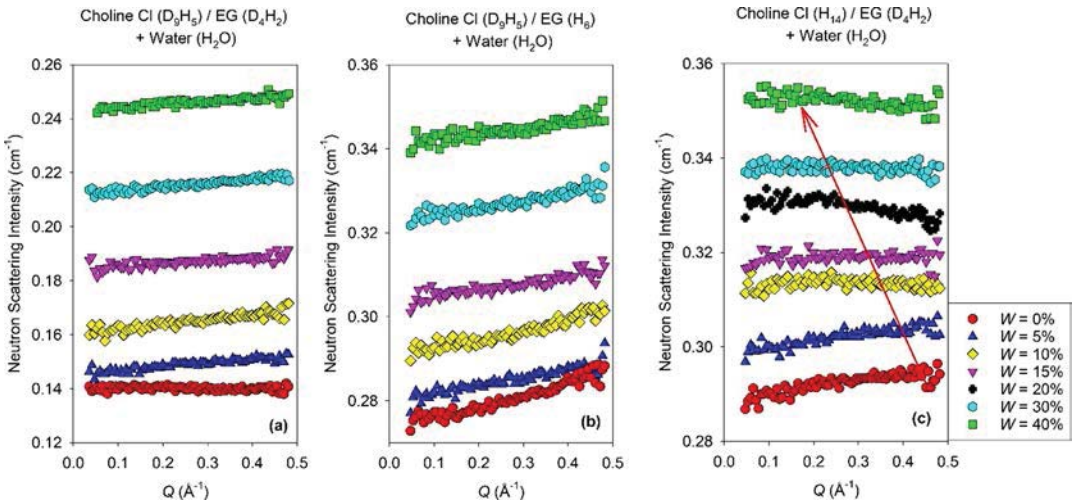

Figure 3. Neutron scattering intensity of ethaline DES aqueous solutions with EG/choline chloride in mol ratio 2:1, and for values of the water mass fraction W ranging from 0 to 40% from bottom to top. The different panels correspond to different isotopic labeling of the two components of ethaline: (a) deuterated choline chloride and deuterated EG ETHA-W(DDH), (b) deuterated choline chloride ETHA-W(HDH), (c) deuterated EG ETHA-W(DHH). The shift to low Q-values of the maximum intensity of the broad peak is indicated by the red arrow in panel c.

and the long-range extension of hydrogen bonding interactions among them. Finally, we can also conclude that the temperature effect is small on the range from 15 to 39 °C, as demonstrated by the weak variation of the neutron scattering intensity shown in Figure S1.

3.2. Aqueous Solutions of Ionic DES (EG/Choline Chloride). Aqueous solutions of ethaline are made of a ternary mixture (EG/choline chloride/water). In order to detect structural microheterogeneities; that is spatial correlations of the local concentration, it is therefore useful to label specifically each of the three compounds. Three different systems were considered composed of normal water (H_2O) and ethaline in which one or both components were partially deuterated. Therefore, the low-Q scattered intensity from ETHA-W(DDH), ETHA-W(HDH) and ETHA-W(DHH) should reflect the local inhomogeneity of concentration in ethaline as a whole, choline chloride, and EG, respectively. The contrast of coherent scattering between the different compounds is indicated in Table 2.

The effect of adding water was studied for one DES composition (x_{EG} = 0.67), which is EG/choline chloride in a constant 2:1 mol ratio that is in the vicinity of the eutectic point. The corresponding neutron scattering intensity is illustrated in Figure 3 for different values of the water mass fraction W (from 0 to 40%). Each of the three panels corresponds to a specific isotopic labeling. Adding water to the given DES consists in a net increase of the incoherent scattering. It was verified that the experimentally measured baseline of the scattered intensity was in quantitative agreement with the calculated incoherent scattering cross section of the different mixtures.

For ETHA-W(DDH), and ETHA-W(HDH) (Figure 3a,b), we observed a weakly decreasing intensity when Q decreased from medium (0.5 $Å^{-1}$) to small values (0.05 $Å^{-1}$), which is similar to the case of ETHA(HD) discussed in the previous part. Likewise, this profile is attributed to the low-Q side of the main diffraction peak. Only for ETHA-W(DHH) (Figure 3c), we observed an additional broad peak that shifted from medium to small Q values when the fraction of water increased. The peak is indicated by a red arrow in Figure 3c.

In order to highlight the effect of the isotopic labeling, we compared on the same graph the scattered intensity of ETHA-W(HDH) and ETHA-W(DHH) for the two limits of water fraction studied; that is, W = 0% in Figure 4a and W = 40% in

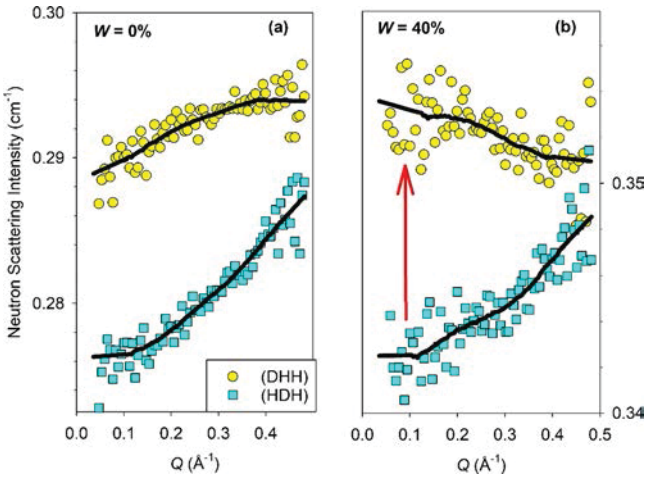

Figure 4. Use of a specific labeling to reveal the intermediate range structuration of EG in ethaline aqueous solutions. Deuterated choline chloride ETHA-W(HDH) (squares) and deuterated EG ETHA-W(DHH) (circles). The solid line is a smooth representation of the data. The value of the water mass fraction is (a) W = 0% and (b) W = 40%. The growth of a low-Q peak is indicated by a red arrow.

Figure 4b. The importance of isotopic contrast to reveal the low-Q peak is highlighted in Figure 4b from a comparison of ETHA-W(HDH) and ETHA-W(DHH) for W = 40%, where the prepeak revealed for ETHA-W(DHH) is underlined by a red arrow. The scattered intensity for all water fractions studied is illustrated in the Supporting Information.

The intensity remained small, which means that the heterogeneous character of the ethaline solution is not pronounced at the nanometer scale. Interestingly, our observation is in agreement with the simulated partial structure factor of ethaline–water solutions.[9] It was predicted that a prepeak shows up specifically in the EG–EG partial structure

https://dx.doi.org/10.1021/acs.jpcb.0c06317
J. Phys. Chem. B 2020, 124, 9126–9135

factor in the Q-range 0.1−0.25 Å^{-1}. In line with the present SANS data, it was shown that the intensity of this prepeak increases with increasing the water amount and shifts to small Q. In that study, the largest intensity was obtained for the more diluted solution (i.e., 5-w ethaline), corresponding to a prepeak position centered about 0.13 Å^{-1}. This is consistent with the result that we obtained experimentally for the closest studied composition W = 20% (i.e., 4-w ethaline).

We infer that the addition of water in ethaline (similarly to the presence of superstoichiometrical EG molecules in the neat DES) favors the preferential association between EG molecules. This could be the consequence of the preferential solvation of ionic species by water molecules, which compete with EGs that present a weaker HBD character.

3.3. Aqueous Solutions of Hydrophilic Nonionic H-Bonded Mixtures (Lactic acid/Glycerol). The mixture of lactic acid with glycerol falls in the category of hydrophilic nonionic H-bonded solvents. It can be viewed as a variant of ethaline, with a substitution of the ionic species by a second H-bonded molecule. Hence, we switched-off the interaction between HBD and ionic species, which is an important component of the ethaline DES properties. We used a mixture of deuterated glycerol with hydrogenated lactic acid and water [i.e., GLY-LA-W(DHH)]. This choice was made to emphasize the glycerol−glycerol correlations. In fact, this isotopic composition is similar to the case of ETHA(DH) and ETHA-W(DHH), for which prepeaks were observed.

Nonetheless, no prepeak could be detected in SANS, as illustrated in Figure 5. The entire intensity was dominated by

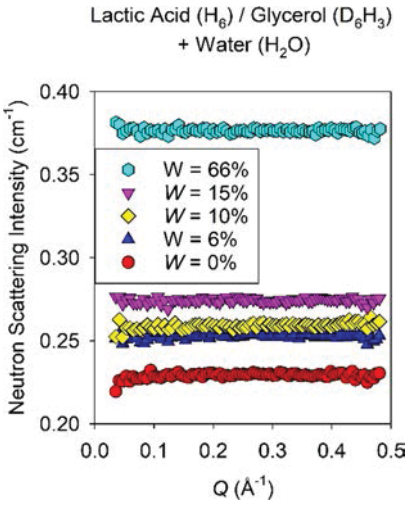

Figure 5. Neutron scattering intensity of lactic acid/deuterated glycerol aqueous solutions for values of the water mass fraction W ranging from 0 to 66% from bottom to top.

the flat incoherent scattering (cf. also Figure 6), with no measurable coherent contribution. Unlike ethaline, this demonstrates the fully homogeneous character of lactic acid/glycerol mixture and its aqueous solutions (W = 0−66%) at the mesoscale. For ethaline, it was argued that the formation of strongly H-bonded EG segregates was supplemented by the strongest affinity of water molecules with ions.[9] From that viewpoint, lactic acid and glycerol are much comparable molecules in terms of polarity, H-bonding tendency, and weak amphilicity. Both are composed of a short alkyl part with three carbons and contain three H-bonding functional groups.

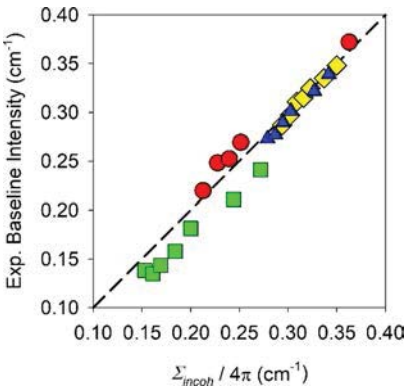

Figure 6. Comparison of the theoretical incoherent scattering cross section with the experimental neutron scattering intensity of different types of aqueous solutions and values of the water mass fraction. Ethaline with deuterated choline chloride and EG (green square), ethaline with deuterated choline chloride (blue triangle), ethaline with deuterated EG (yellow diamond), and lactic acid/deuterated glycerol (red circle) aqueous solutions.

Accordingly, we argue that the water affinity with one or the other components is more balanced. The propensity of lactic acid and glycerol to form either homomolecular or heteromolecular H-bonds is probably similar as well. This is confirmed by the SANS data that demonstrate the homogeneous mixing of the aqueous solutions down to the mesoscale.

3.4. Hydrophobic DES (Menthol/Decanoic Acid). Finally, we discuss the DES made by mixing menthol and decanoic acid. This system falls in the category of hydrophobic DESs.[49,50] For this reason, instead of the water composition, the relative amount of menthol and decanoic acid varied. The menthol molar fraction x ranged from 0.4 to 0.8, which corresponds to stoichiometric composition from 4:1 to 2:3. A unique isotopic composition was used, with a deuterated form of decanoic acid ($D_{19}H$) (ρ_{SLD} = 63 × 10^9 cm^{-2}) and hydrogenated glycerol (ρ_{SLD} = 6 × 10^9 cm^{-2}) in order to maximize the contrast between the two compounds. The SANS experiments revealed a significant increase of the scattered intensity toward the limit of low Q, as illustrated in Figure 7. This peak was relatively broad and covered the entire studied Q-range. Its maximum position was located below the smallest accessible momentum and seemingly centered at Q = 0. Similar observations were reported in the literature for binary liquids, including alcohol/alkane mixtures and aqueous solutions of classical solvents as well as ionic liquids.[36,46,53,54] They were attributed to concentration fluctuations that shows up at Q = 0, according to the theory of Kirkwood−Buff integrals. In other words, it suggests that the distribution of molecular species in the system is not fully homogeneous. Following the analysis made for binary liquids, we first fitted the scattered intensity by eq 1, which is composed by a Lorentzian centered at Q = 0 with a fitted correlation length ξ according to the Ornstein−Zernike theory and an incoherent scattering baseline determined from the liquid composition.

$$I(Q) = \frac{I_0}{1 + Q^2\xi^2} + \frac{\Sigma_{incoh}}{4\pi} \quad (1)$$

The scattered intensity at zero-Q, which is directly related to the Kirkwood−Buff integrals, exhibited a weak dependence on the composition, with a maximum that is perceived around the equimolar composition despite the limited number of studied

https://dx.doi.org/10.1021/acs.jpcb.0c06317
J. Phys. Chem. B 2020, 124, 9126−9135

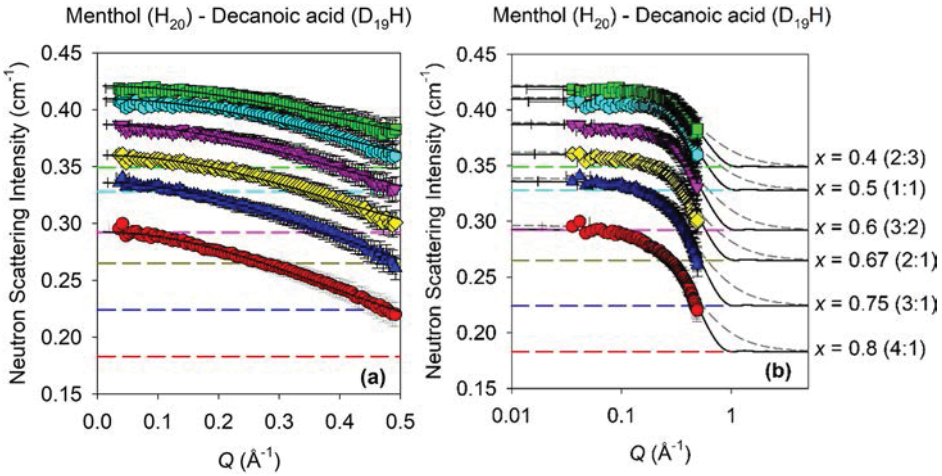

Figure 7. Neutron scattering intensity of menthol (H_{20}):decanoic acid (D_{19}) DES mixtures for values of the menthol molar fraction x ranging from 0.4 to 0.8 from top to bottom. (a) Linear scale, (b) semilog scale [the flat incoherent scattering cross section (long dashed line), the fits with the form factor of a spherical particle (solid line); and the Ornstein−Zernike model (short dashed line)].

compositions. This variation is emphasized in Figure 8 by a quadratic term $x(1-x)$, which suggests a symmetric behavior of the mixture with respect to the menthol and decanoic acid constituents.

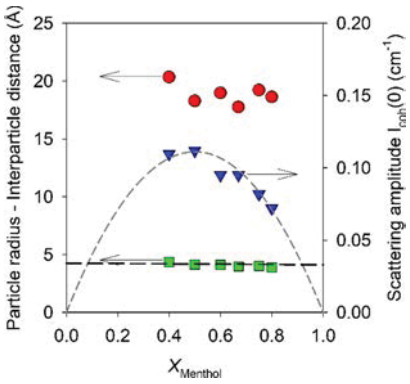

Figure 8. Parameters derived from the fitting of the neutron scattering intensity of menthol (H_{20}):decanoic acid (D_{19}) DES mixtures as a function of the menthol molar fraction x [the domain radius (green square, left axis), the interdomain distance (red circle, left axis), and the coherent scattering amplitude (blue triangle, right axis)]. The averaged molecule radius computed from the average molecular volume (long dashed line), and a symmetric quadratic guideline $x(1-x)$ scaled to the coherent scattering (short dashed line).

Although generally satisfying, this model failed to accurately reproduce the decay of the experimental intensity at medium Q (>0.4 $Å^{-1}$), as illustrated in short dashed lines in Figure 7b. For comparison, we opted for an alternative description, which applies for liquid comprising domains of well-defined geometry such as micellar aggregates rather than ill-defined fluctuating aggregates.[36,55] In the latter case, the scattered intensity is written as

$$I(Q) = n_d V_d^2 (\Delta\rho_{SLD})^2 P(Q) S(Q) + \frac{\Sigma_{incoh}}{4\pi} \quad (2)$$

where n_d and V_d are the number density of domains and the volume of each of domains, $\Delta\rho_{SLD}$ is the difference of scattering length density between the domains and the surrounding phase.[56] $P(Q)$ and $S(Q)$ are the form factor and the structure factor, which quantify the shape of each domain and their spatial correlations, respectively. Satisfactory fits shown as solid lines in Figure 7b were obtained by assuming that the domain shape is spherical with a radius R_d so that $P(Q)$ is given by eq 3. We further assumed that the interdomain interaction was negligible in this Q-range [i.e., $S(Q) = 1$], a point that was verified a posteriori as discussed later.

$$P(Q) = 9\left[\frac{\sin QR_d - QR_d \cos QR_d}{(QR_d)^3}\right]^2 \quad (3)$$

The obtained parameters are illustrated in Figure 8. The domains radius is varying from about 4.4 to 3.9 Å. These values are compared with the average radius of the molecules r_m, which was evaluated from the molecular volume ($v_m = 4/3\pi r_m^3$) neglecting corrections due to non-additivity of the partial volume (cf. long dashed line in Figure 8). The fact that these domains do not present strong interactions [justifying the assumption that $S(Q) = 1$ on the studied Q-range] was first supported by the absence of the correlation peak at finite Q. This was confirmed by the average distance between domains, which could be evaluated from their number density n_d that appears in eq 3 as a scaling factor. Indeed, the obtained values are typically 4 times larger than R_d, as illustrated in Figure 8.

This demonstrates that this DES clearly exhibits structural heterogeneity, however the segregation of the two components is spatially limited. This differs from binary liquids with strong demixing tendency, such as aqueous solutions of ionic liquids or aqueous solutions of large alcohols and pyridine derivatives for which the measured correlation lengths usually exceed 10 Å.[54,55,57] On the other hand, it compares reasonably with the values obtained for ionic liquids.[36,58]

Two alternative descriptions have been applied, either in terms of diluted well-shaped spherical aggregates such as micelles or in terms of shapeless concentration fluctuations, which are precursors of an underlying phase separation. However, due to the absence of interaction peaks and despite the slightly better fits obtained with the former model, we consider that the two descriptions can be acceptable. From this viewpoint, the mesoscale structure of DESs also deserves a comparison with the ionic liquids. Depending on the systems,

https://dx.doi.org/10.1021/acs.jpcb.0c06317
J. Phys. Chem. B 2020, 124, 9126−9135

the description of the low-Q scattering intensity in terms of monodisperse hard-sphere interacting pseudospherical aggregates or structureless concentration fluctuations was preferred.[36,58] The amphiphilic nature of the menthol and decanoic acid molecules comprising polar head and long aliphatic tail brings further support to the possible formation of micellar clusters. Variable temperature measurements could assess the presence of a miscibility gap and help resolve the physical origin of the observed mesoscopic structure in menthol/decanoic acid DES.

4. CONCLUSIONS

Despite the rapidly increasing number of studies on the short- and intermediate-range order of DESs, small-angle scattering techniques have been scarcely used to investigate their structures at longer distances. Important enough, recent molecular simulation studies have predicted the occurrence of low-Q correlation peaks in ethaline[8] and its aqueous solutions,[9] which called for a further experimental examination with SANS methods.

We selected three types of prototypical solutions: a classical DES formed by the association of an HBD and an ionic species, a hydrophilic nonionic mixture of H-bonded DES components, and a hydrophobic DES. Moreover, we studied the effect of adding different amounts of water in the two hydrophilic solutions. SANS experiments with isotopic labeling (H/D exchange) were carried out in order to vary the coherent scattering contrast between the different compounds and reveal mesoscopic static correlations in the partial structure factors for Q-values (0.05−0.5 $Å^{-1}$) located before the main diffraction peak.

For ethaline DES and its aqueous solutions, a low-Q coherent scattering was observed only when the EG−EG correlations were enhanced by specific deuteration. This excess intensity appeared as a weak peak located at about 0.35 $Å^{-1}$ for neat DES comprising superstoichiometrical EG. It appeared also during the gradual addition of water to the DES formed at the eutectic composition and shifted to smaller Q (~0.15 $Å^{-1}$). Albeit being a small effect, this observation points to the segregation of EG molecules. Supporting simulation studies, we suggest that the formation of strongly H-bonded EG segregates is promoted by the higher affinity of water molecules with the ionic species, which therefore competes with the solvation of ions by EG. We argue that the presence of EG in excess with respect to the stoichiometry required to form DES supramolecular ionic complexes could have a similar effect. The latter situation calls for further investigation including simulation methods.

Unlike ethaline, aqueous solutions of a hydrophilic H-bonded nonionic mixture (lactic acid/glycerol) appeared homogeneously mixed at the mesoscopic scale. We infer that this is favored by the marginal amphiphilic nature of the molecules (comprising small alkyl groups) that limits the microsegregation of polar and apolar groups. Moreover, the H-bonding functional groups of the two constituents are comparable, which implies that they interact likewise with one or the other H-bonded molecule.

For the hydrophobic DES (menthol/decanoic acid), molecular segregation was more obvious and it led to a significant low-angle additional scattering contribution. This coherent peak centered at Q = 0 was best fitted by a model, which assumed the presence of diluted or weakly interacting spherical aggregates of one compound embedded in its counterpart. However, we demonstrated that the size of such micelle-like domains remains small, typically at the molecular scale. An alternative description in terms of shapeless concentration fluctuations modeled by the Ornstein−Zernike theory cannot be definitively ruled out. However, there was no indication that the size of such precursors of a hypothetical phase separation extends to a larger scale as a function of the composition, and variable temperature experiments would certainly be useful.

In conclusion, we have demonstrated that some DESs and their aqueous solutions highlight the formation of supramolecular structures. However, none of them indicated that strong deviations from homogeneous mixing occur on a spatial scale that exceeds significantly a few molecular sizes. This conclusion was demonstrated for a selection of prototypical systems, which belong to three different classes of solvents. Although they cannot be necessarily generalized to all categorized DES systems, we consider that the conclusions from this work can help sorting the different properties, including ionic and H-bonding interactions, microheterogeneity, nonideality, and incomplete mixing, which could be considered as salient characters of DESs or rather considered as system-specific, with the aim to convert them into useful functionality.

■ ASSOCIATED CONTENT

Supporting Information

The Supporting Information is available free of charge at https://pubs.acs.org/doi/10.1021/acs.jpcb.0c06317.

Temperature effects on the neutron scattering intensity of ethaline DES and comparison of the neutron scattering intensity of ethaline DES aqueous solutions for two different isotopic labeling and for all the studied water mass fractions (PDF)

■ AUTHOR INFORMATION

Corresponding Author

Denis Morineau − *Institute of Physics of Rennes, CNRS-University of Rennes 1, UMR 6251, Rennes F-35042, France;* orcid.org/0000-0002-8784-3021; Email: denis.morineau@univ-rennes1.fr

Authors

Lucie Percevault − *Institute of Chemical Sciences of Rennes, CNRS-University of Rennes 1, UMR 6226, Rennes F-35042, France*

Aicha Jani − *Institute of Physics of Rennes, CNRS-University of Rennes 1, UMR 6251, Rennes F-35042, France*

Thibaut Sohier − *Institute of Physics of Rennes, CNRS-University of Rennes 1, UMR 6251, Rennes F-35042, France*

Laurence Noirez − *Laboratoire Léon Brillouin (CEA-CNRS), CEA-Saclay, Université Paris-Saclay, Gif-sur-Yvette F-91191, France*

Ludovic Paquin − *Institute of Chemical Sciences of Rennes, CNRS-University of Rennes 1, UMR 6226, Rennes F-35042, France*

Fabienne Gauffre − *Institute of Chemical Sciences of Rennes, CNRS-University of Rennes 1, UMR 6226, Rennes F-35042, France*

Complete contact information is available at: https://pubs.acs.org/10.1021/acs.jpcb.0c06317

https://dx.doi.org/10.1021/acs.jpcb.0c06317
J. Phys. Chem. B 2020, 124, 9126−9135

Notes

The authors declare no competing financial interest.

■ ACKNOWLEDGMENTS

Support from Rennes Metropole and Europe (FEDER Fund—CPER PRINT$_2$TAN) and the ANR (Project NanoLiquids no ANR-18-CE92-0011-01) is expressly acknowledged. This work is part of the PhD thesis of A.J. who benefits from a grant from the French Ministry of Higher Education, Research, and Innovation. The authors are grateful to the CNRS—network SolVATE (GDR 2035) for financial support and fruitful discussions.

■ REFERENCES

(1) Abbott, A. P.; Capper, G.; Davies, D. L.; Rasheed, R. K.; Tambyrajah, V. Novel solvent properties of choline chloride/urea mixtures. *Chem. Commun.* **2003**, 70−71.
(2) Abbott, A. P.; Boothby, D.; Capper, G.; Davies, D. L.; Rasheed, R. K. Deep eutectic solvents formed between choline chloride and carboxylic acids: Versatile alternatives to ionic liquids. *J. Am. Chem. Soc.* **2004**, *126*, 9142−9147.
(3) Zhang, Q.; De Oliveira Vigier, K.; Royer, S.; Jérôme, F. Deep eutectic solvents: syntheses, properties and applications. *Chem. Soc. Rev.* **2012**, *41*, 7108−7146.
(4) Smith, E. L.; Abbott, A. P.; Ryder, K. S. Deep Eutectic Solvents (DESs) and Their Applications. *Chem. Rev.* **2014**, *114*, 11060−11082.
(5) Ge, X.; Gu, C.; Wang, X.; Tu, J. Deep eutectic solvents (DESs)-derived advanced functional materials for energy and environmental applications: challenges, opportunities, and future vision. *J. Mater. Chem. A* **2017**, *5*, 8209−8229.
(6) Kollau, L. J. B. M.; Vis, M.; van den Bruinhorst, A.; Esteves, A. C. C.; Tuinier, R. Quantification of the liquid window of deep eutectic solvents. *Chem. Commun.* **2018**, *54*, 13351−13354.
(7) Martins, M. A. R.; Pinho, S. P.; Coutinho, J. A. P. Insights into the Nature of Eutectic and Deep Eutectic Mixtures. *J. Solution Chem.* **2019**, *48*, 962−982.
(8) Kaur, S.; Malik, A.; Kashyap, H. K. Anatomy of Microscopic Structure of Ethaline Deep Eutectic Solvent Decoded through Molecular Dynamics Simulations. *J. Phys. Chem. B* **2019**, *123*, 8291−8299.
(9) Kaur, S.; Gupta, A.; Kashyap, H. K. How Hydration Affects the Microscopic Structural Morphology in a Deep Eutectic Solvent. *J. Phys. Chem. B* **2020**, *124*, 2230−2237.
(10) Hammond, O. S.; Bowron, D. T.; Edler, K. J. The Effect of Water upon Deep Eutectic Solvent Nanostructure: An Unusual Transition from Ionic Mixture to Aqueous Solution. *Angew. Chem., Int. Ed.* **2017**, *56*, 9782−9785.
(11) Passos, H.; Tavares, D. J. P.; Ferreira, A. M.; Freire, M. G.; Coutinho, J. A. P. Are Aqueous Biphasic Systems Composed of Deep Eutectic Solvents Ternary or Quaternary Systems? *ACS Sustainable Chem. Eng.* **2016**, *4*, 2881−2886.
(12) Dai, Y.; Witkamp, G.-J.; Verpoorte, R.; Choi, Y. H. Tailoring properties of natural deep eutectic solvents with water to facilitate their applications. *Food Chem.* **2015**, *187*, 14−19.
(13) Yadav, A.; Trivedi, S.; Rai, R.; Pandey, S. Densities and dynamic viscosities of (choline chloride plus glycerol) deep eutectic solvent and its aqueous mixtures in the temperature range (283.15−363.15) K. *Fluid Phase Equilib.* **2014**, *367*, 135−142.
(14) Meng, X.; Ballerat-Busserolles, K.; Husson, P.; Andanson, J.-M. Impact of water on the melting temperature of urea plus choline chloride deep eutectic solvent. *New J. Chem.* **2016**, *40*, 4492−4499.
(15) Ma, C.; Laaksonen, A.; Liu, C.; Lu, X.; Ji, X. The peculiar effect of water on ionic liquids and deep eutectic solvents. *Chem. Soc. Rev.* **2018**, *47*, 8685−8720.
(16) Kumari, P.; Shobhna; Kaur, S.; Kashyap, H. K. Influence of Hydration on the Structure of Reline Deep Eutectic Solvent: A Molecular Dynamics Study. *ACS Omega* **2018**, *3*, 15246−15255.
(17) Lapeña, D.; Lomba, L.; Artal, M.; Lafuente, C.; Giner, B. Thermophysical characterization of the deep eutectic solvent choline chloride:ethylene glycol and one of its mixtures with water. *Fluid Phase Equilib.* **2019**, *492*, 1−9.
(18) Posada, E.; Roldán-Ruiz, M. J.; Jiménez Riobóo, R. J.; Gutiérrez, M. C.; Ferrer, M. L.; del Monte, F. Nanophase separation in aqueous dilutions of a ternary DES as revealed by Brillouin and NMR spectroscopy. *J. Mol. Liq.* **2019**, *276*, 196−203.
(19) Roldán-Ruiz, M. J.; Jiménez-Riobóo, R. J.; Gutiérrez, M. C.; Ferrer, M. L.; del Monte, F. Brillouin and NMR spectroscopic studies of aqueous dilutions of malicine: Determining the dilution range for transition from a "water-in-DES" system to a "DES-in-water" one. *J. Mol. Liq.* **2019**, *284*, 175−181.
(20) Ahmadi, R.; Hemmateenejad, B.; Safavi, A.; Shojaeifard, Z.; Shahsavar, A.; Mohajeri, A.; Heydari Dokoohaki, M.; Zolghadr, A. R. Deep eutectic-water binary solvent associations investigated by vibrational spectroscopy and chemometrics. *Phys. Chem. Chem. Phys.* **2018**, *20*, 18463−18473.
(21) Jani, A.; Sohier, T.; Morineau, D. Phase behavior of aqueous solutions of ethaline deep eutectic solvent. *J. Mol. Liq.* **2020**, *304*, 112701−112706.
(22) Hammond, O. S.; Bowron, D. T.; Jackson, A. J.; Arnold, T.; Sanchez-Fernandez, A.; Tsapatsaris, N.; Garcia Sakai, V.; Edler, K. J. Resilience of Malic Acid Natural Deep Eutectic Solvent Nanostructure to Solidification and Hydration. *J. Phys. Chem. B* **2017**, *121*, 7473−7483.
(23) Hammond, O. S.; Bowron, D. T.; Edler, K. J. Liquid structure of the choline chloride-urea deep eutectic solvent (reline) from neutron diffraction and atomistic modelling. *Green Chem.* **2016**, *18*, 2736−2744.
(24) Gilmore, M.; Moura, L. M.; Turner, A. H.; Swadźba-Kwaśny, M.; Callear, S. K.; McCune, J. A.; Scherman, O. A.; Holbrey, J. D. A comparison of choline: urea and choline: oxalic acid deep eutectic solvents at 338 K. *J. Chem. Phys.* **2018**, *148*, 193823.
(25) Turner, A. H.; Holbrey, J. D. Investigation of glycerol hydrogen-bonding networks in choline chloride/glycerol eutectic-forming liquids using neutron diffraction. *Phys. Chem. Chem. Phys.* **2019**, *21*, 21782−21789.
(26) Hossain, S. S.; Samanta, A. How do the hydrocarbon chain length and hydroxyl group position influence the solute dynamics in alcohol-based deep eutectic solvents? *Phys. Chem. Chem. Phys.* **2018**, *20*, 24613−24622.
(27) Hossain, S. S.; Paul, S.; Samanta, A. Liquid Structure and Dynamics of Tetraalkylammonium Bromide-Based Deep Eutectic Solvents: Effect of Cation Chain Length. *J. Phys. Chem. B* **2019**, *123*, 6842−6850.
(28) Cui, Y.; Kuroda, D. G. Evidence of Molecular Heterogeneities in Amide-Based Deep Eutectic Solvents. *J. Phys. Chem. A* **2018**, *122*, 1185−1193.
(29) McDonald, S.; Murphy, T.; Imberti, S.; Warr, G. G.; Atkin, R. Amphiphilically Nanostructured Deep Eutectic Solvents. *J. Phys. Chem. Lett.* **2018**, *9*, 3922−3927.
(30) Alizadeh, V.; Geller, D.; Malberg, F.; Sánchez, P. B.; Padua, A.; Kirchner, B. Strong Microheterogeneity in Novel Deep Eutectic Solvents. *ChemPhysChem* **2019**, *20*, 1786−1792.
(31) Stefanovic, R.; Ludwig, M.; Webber, G. B.; Atkin, R.; Page, A. J. Nanostructure, hydrogen bonding and rheology in choline chloride deep eutectic solvents as a function of the hydrogen bond donor. *Phys. Chem. Chem. Phys.* **2017**, *19*, 3297−3306.
(32) López-Salas, N.; Vicent-Luna, J. M.; Posada, E.; Imberti, S.; Madero-Castro, R. M.; Calero, S.; Ania, C. O.; Jiménez-Riobóo, R. J.; Gutiérrez, M. C.; Ferrer, M. L.; del Monte, F. Further Extending the Dilution Range of the "Solvent-in-DES" Regime upon the Replacement of Water by an Organic Solvent with Hydrogen Bond Capabilities. *ACS Sustainable Chem. Eng.* **2020**, *8*, 12120−12131.
(33) López-Salas, N.; Vicent-Luna, J. M.; Imberti, S.; Posada, E.; Roldán, M. J.; Anta, J. A.; Balestra, S. R. G.; Madero Castro, R. M.; Calero, S.; Jiménez-Riobóo, R. J.; Gutiérrez, M. C.; Ferrer, M. L.; del Monte, F. Looking at the "Water-in-Deep-Eutectic-Solvent" System:

https://dx.doi.org/10.1021/acs.jpcb.0c06317
J. Phys. Chem. B 2020, 124, 9126−9135

A Dilution Range for High Performance Eutectics. *ACS Sustainable Chem. Eng.* **2019**, *7*, 17565−17573.
(34) Kaur, S.; Gupta, A.; Kashyap, H. K. Nanoscale Spatial Heterogeneity in Deep Eutectic Solvents. *J. Phys. Chem. B* **2016**, *120*, 6712−6720.
(35) Kaur, S.; Kashyap, H. K. Unusual Temperature Dependence of Nanoscale Structural Organization in Deep Eutectic Solvents. *J. Phys. Chem. B* **2018**, *122*, 5242−5250.
(36) Russina, O.; Lo Celso, F.; Plechkova, N. V.; Triolo, A. Emerging Evidences of Mesoscopic-Scale Complexity in Neat Ionic Liquids and Their Mixtures. *J. Phys. Chem. Lett.* **2017**, *8*, 1197−1204.
(37) Hamid, A. R. A.; Lefort, R.; Lechaux, Y.; Moréac, A.; Ghoufi, A.; Alba-Simionesco, C.; Morineau, D. Solvation Effects on Self-Association and Segregation Processes in tert-Butanol-Aprotic Solvent Binary Mixtures. *J. Phys. Chem. B* **2013**, *117*, 10221−10230.
(38) Kaur, S.; Sharma, S.; Kashyap, H. K. Bulk and interfacial structures of reline deep eutectic solvent: A molecular dynamics study. *J. Chem. Phys.* **2017**, *147*, 194507.
(39) Xiaobing, C.; Yaowen, C.; Gobeze, H. B.; Kuroda, D. J. Assessing the Location of Ionic and Molecular Solutes in a Molecularly Heterogeneous and Nonionic Deep Eutectic Solvent. *J. Phys. Chem. B* **2020**, *124*, 4762−4773.
(40) Cui, Y.; Rushing, J. C.; Seifert, S.; Bedford, N. M.; Kuroda, D. G. Molecularly Heterogeneous Structure of a Nonionic Deep Eutectic Solvent Composed of N-Methylacetamide and Lauric Acid. *J. Phys. Chem. B* **2019**, *123*, 3984−3993.
(41) Weng, L.; Toner, M. Janus-faced role of water in defining nanostructure of choline chloride/glycerol deep eutectic solvent. *Phys. Chem. Chem. Phys.* **2018**, *20*, 22455−22462.
(42) Gontrani, L.; Bonomo, M.; Plechkova, N. V.; Dini, D.; Caminiti, R. X-Ray structure and ionic conductivity studies of anhydrous and hydrated choline chloride and oxalic acid deep eutectic solvents. *Phys. Chem. Chem. Phys.* **2018**, *20*, 30120−30124.
(43) Delso, I.; Lafuente, C.; Muñoz-Embid, J.; Artal, M. NMR study of choline chloride-based deep eutectic solvents. *J. Mol. Liq.* **2019**, *290*, 111236.
(44) Posada, E.; López-Salas, N.; Jiménez Riobóo, R. J.; Ferrer, M. L.; Gutiérrez, M. C.; del Monte, F. Reline aqueous solutions behaving as liquid mixtures of H-bonded co-solvents: microphase segregation and formation of co-continuous structures as indicated by Brillouin and H-1 NMR spectroscopies. *Phys. Chem. Chem. Phys.* **2017**, *19*, 17103−17110.
(45) Kalhor, P.; Zheng, Y. Z.; Ashraf, H.; Cao, B.; Yu, Z. W. Influence of Hydration on the Structure and Interactions of Ethaline Deep-Eutectic Solvent: A Spectroscopic and Computational Study. *ChemPhysChem* **2020**, *21*, 995−1005.
(46) Mhanna, R.; Lefort, R.; Noirez, L.; Morineau, D. Microstructure and concentration fluctuations in alcohol-Toluene and alcohol-Cyclohexane binary liquids: A small angle neutron scattering study. *J. Mol. Liq.* **2016**, *218*, 198−207.
(47) García, G.; Aparicio, S.; Ullah, R.; Atilhan, M. Deep Eutectic Solvents: Physicochemical Properties and Gas Separation Applications. *Energy Fuels* **2015**, *29*, 2616−2644.
(48) Hou, X.-D.; Li, A.-L.; Lin, K.-P.; Wang, Y.-Y.; Kuang, Z.-Y.; Cao, S.-L. Insight into the structure-function relationships of deep eutectic solvents during rice straw pretreatment. *Bioresour. Technol.* **2018**, *249*, 261−267.
(49) Verma, R.; Mohan, M.; Goud, V. V.; Banerjee, T. Operational Strategies and Comprehensive Evaluation of Menthol Based Deep Eutectic Solvent for the Extraction of Lower Alcohols from Aqueous Media. *ACS Sustainable Chem. Eng.* **2018**, *6*, 16920−16932.
(50) Kaul, M. J.; Qadah, D.; Mandella, V.; Dietz, M. L. Systematic evaluation of hydrophobic deep-melting eutectics as alternative solvents for the extraction of organic solutes from aqueous solution. *RSC Adv.* **2019**, *9*, 15798−15804.
(51) Shahbaz, K.; Mjalli, F. S.; Hashim, M. A.; ALNashef, I. M. Using Deep Eutectic Solvents for the Removal of Glycerol from Palm Oil-Based Biodiesel. *J. Appl. Sci.* **2010**, *10*, 3349−3354.
(52) López-Porfiri, P.; Brennecke, J. F.; Gonzalez-Miquel, M. Excess Molar Enthalpies of Deep Eutectic Solvents (DESs) Composed of Quaternary Ammonium Salts and Glycerol or Ethylene Glycol. *J. Chem. Eng. Data* **2016**, *61*, 4245−4251.
(53) Almásy, L.; Jancsó, G. Small-angle neutron scattering and Kirkwood-Buff integral study of aqueous solutions of pyridine. *J. Mol. Liq.* **2004**, *113*, 61−66.
(54) Almásy, L.; Turmine, M.; Perera, A. Structure of aqueous solutions of ionic liquid 1-butyl-3-methylimidazolium tetrafluoroborate by small-angle neutron scattering. *J. Phys. Chem. B* **2008**, *112*, 2382−2387.
(55) D'Arrigo, G.; Teixeira, J. Small-angle neutron-scattering study of D2O alcohol-solutions. *J. Chem. Soc., Faraday Trans.* **1990**, *86*, 1503−1509.
(56) D'Arrigo, G.; Giordano, R.; Teixeira, J. Small-angle neutron scattering studies of aqueous solutions of short-chain amphiphiles. *Eur. Phys. J. E: Soft Matter Biol. Phys.* **2003**, *10*, 135−142.
(57) Marczak, W.; Czech, B.; Almásy, L.; Lairez, D. Molecular clusters in aqueous solutions of pyridine and its methyl derivatives. *Phys. Chem. Chem. Phys.* **2011**, *13*, 6260−6269.
(58) Schroer, W.; Triolo, A.; Russina, O. Nature of Mesoscopic Organization in Protic Ionic Liquid-Alcohol Mixtures. *J. Phys. Chem. B* **2016**, *120*, 2638−2643.

https://dx.doi.org/10.1021/acs.jpcb.0c06317
J. Phys. Chem. B 2020, 124, 9126−9135

ANNEX-IV

On the coupling between ionic conduction and dipolar relaxation in deep eutectic solvents: Influence of hydration and glassy dynamics

Authors

Aicha Jani, Benjamin Malfait and Denis Morineau

On the coupling between ionic conduction and dipolar relaxation in deep eutectic solvents: Influence of hydration and glassy dynamics

Cite as: J. Chem. Phys. **154**, 164508 (2021); https://doi.org/10.1063/5.0050766
Submitted: 18 March 2021 . Accepted: 13 April 2021 . Published Online: 27 April 2021

Aicha Jani, Benjamin Malfait, and Denis Morineau

The Journal of Chemical Physics ARTICLE scitation.org/journal/jcp

On the coupling between ionic conduction and dipolar relaxation in deep eutectic solvents: Influence of hydration and glassy dynamics

Cite as: J. Chem. Phys. 154, 164508 (2021); doi: 10.1063/5.0050766
Submitted: 18 March 2021 • Accepted: 13 April 2021 •
Published Online: 27 April 2021

Aicha Jani, Benjamin Malfait, and Denis Morineau[a)]

AFFILIATIONS

Institute of Physics of Rennes, CNRS-University of Rennes 1, UMR 6251, F-35042 Rennes, France

Note: This paper is part of the JCP Special Topic on Chemical Physics of Deep Eutectic Solvents.
[a)]**Author to whom correspondence should be addressed:** denis.morineau@univ-rennes1.fr

ABSTRACT

We have studied the ionic conductivity and the dipolar reorientational dynamics of aqueous solutions of a prototypical deep eutectic solvent (DES), ethaline, by dielectric spectroscopy in a broad range of frequencies (MHz–Hz) and for temperatures ranging from 128 to 283 K. The fraction of water in the DES was varied systematically to cover different regimes, starting from the pure DES and its water-in-DES mixtures to the diluted electrolyte solutions. Depending on these parameters, different physical states were examined, including low viscosity liquid, supercooled viscous liquid, amorphous solid, and freeze-concentrated solution. Both the ionic conductivity and the reorientational relaxation exhibited characteristic features of glassy dynamics that could be quantified from the deviation from the Arrhenius temperature dependence and non-exponential decay of the relaxation function. A transition occurred between the water-in-DES regime (<40 wt. %), where the dipolar relaxation and ionic conductivity remained inversely proportional to each other, and the DES-in-water regime (>40 wt. %), where a clear rotation–translation decoupling was observed. This suggests that for a low water content, on the timescale covered by this study (~10^{-6} to 1 s), the rotational and transport properties of ethaline aqueous solutions obey classical hydrodynamic scaling despite these systems being presumably spatially microheterogeneous. A fractional scaling is observed in the DES-in-water regime due to the formation of a maximally freeze-concentrated DES aqueous solution coexisting with frozen water domains at sub-ambient temperature.

I. INTRODUCTION

Recently, deep eutectic solvents (DESs) have received increasing attention as an emerging class of solvents.[1–6] The majority of DESs are obtained by mixing of an H-bond donor (HBD) (typically an organic molecular component such as an amide, carboxylic acid, or polyol) with an H-bond acceptor (HBA) or with a molecular ionic species.[6] In the most frequently studied systems, i.e., type III DESs, the latter consists of a quaternary ammonium salt. For compositions approaching the eutectic point, a large decrease in the melting point is obtained so that DESs form a liquid phase at room temperature.[7,8] This phenomenon can be amplified by non-ideal mixing effects, which are favored by ionic and H-bonding interactions and specific spatial correlations between the DES constituents.[9,10] Nowadays, DESs are contemplated as cost-effective and sustainable alternatives to classical organic solvents.[3–6] They exhibit many performant properties, such as low volatility and high solvating and extracting properties. DESs have been considered for practical applications in a growing number of industrial processes, including extraction, (bio)synthesis, catalysis, electrochemistry, and carbon dioxide capture.[6]

The ionic conductivity of DESs makes them good candidates as alternative electrolytes for applications related to energy harvesting and storage.[6,11–15] Recently, choline chloride-based DESs (i.e., ethaline, reline, and aqueous solution of glyceline) have been studied as electrolytes for electrochemical applications,[11,12] redox flow batteries,[13] lithium-ion batteries,[14] and dye-sensitized solar cells.[15]

From a fundamental point of view, it is striking that the ionic and molecular mobilities of DESs question classical theories. The rotational and translational dynamics of fluorescent dyes have been studied in reline,[16] ethaline,[17] and acetamide–urea DESs.[18] They exhibit a fractional viscosity dependence and deviations from the

hydrodynamic predictions based on Stokes–Einstein and Stokes–Einstein–Debye theories. These results suggest that the molecular motions of the fluorescent dyes are sensitive to the existence of dynamic heterogeneity in DESs. High frequency (GHz) dielectric relaxation (DR) studies have also demonstrated the deviation from the hydrodynamic predictions for molecular rotation, indicating the critical role of collective reorientation relaxation and H-bond fluctuations in regulating the DR dynamics.[19,20] From the combination of molecular dynamics (MD) simulation and neutron scattering (NS), a microscopic relation was made between the transport properties and liquid structure of ethaline.[21] Different translational diffusion and rotational relaxation depending on the DES constituent were observed, and evidence for long-lasting dynamic heterogeneity (>10 ns at 298 K) was inferred from the non-Gaussian character of the van Hove function related to self-diffusion of chloride anions. Interestingly, dynamic heterogeneities were found to result from the complex interplay of the solvation structure and H-bond dynamics.[21]

Aiming at a better understanding of the dynamics of DESs, it is worth noting that only a few studies have addressed longer time relaxation processes (i.e., longer than a few ns) so far.[22–24] Dielectric spectroscopy (DS) is a perfectly well-suited method because it allows independent measurements of the ionic conductivity and the orientation dipolar dynamics in an extended frequency range.[25] This provides a complementary view on the translation and rotational motions of DES species.[24] Moreover, it bridges the gap from short ($\sim 10^{-9}$ to 10^{-6} s) to ultra-long ($\sim 10^{2}$ s) timescales, which are typical for the dynamical range going from a low-viscosity liquid to an amorphous solid. Due to the large depression of the eutectic melting point, DESs are usually liquid in a wide range of temperatures, and in frequent cases, eutectic crystallization can be avoided. This further extends the slowing down of the DES dynamics in the supercooled and glassy states, implying that their dynamics should be studied over many decades.[24,26] For ethaline, a comprehensive DS study has shown that the ionic transport and the reorientation dipolar motions were strongly influenced by the glassy dynamics.[24] In addition, it was demonstrated that both dynamics obeyed the same temperature dependence. This unique scaling might arise from a direct translational–rotational coupling, such as revolving-door mechanism, or might be due to the coupling of both dynamics to viscosity. While the distinction between the two hypotheses could not be made in that study,[24] a complementary study including rheological measurements recently concluded the non-relevance of the revolving-door mechanism.[27] The second hypothesis would imply that hydrodynamic predictions from Stoke–Einstein and Stoke–Einstein–Debye models are fulfilled, thus minimizing the influence of dynamic heterogeneity.

In order to better understand the role of dynamic heterogeneity, an attractive approach would consist in varying gradually the solvation properties and H-bond interactions. Although conceivable in molecular models, this goal is more challenging in experiments. In the present study, we propose to use different hydration levels of DESs as control parameters. In fact, water addition is recognized as a way to formulate DES-based solvents with tailored properties.[10,26,28–38] More specifically, the structure of DESs is greatly influenced by water in several ways.[10,28,29,37,39,40] Although supramolecular ionic clusters formed by the association of the initial DES components seem resistant to moderate hydration levels in the so-called "water-in-DES" regime, water molecules often participate in the H-bond complexes of the original DESs as an additional HBD.[39,41–43] The preferential solvation of chloride by water was also reported in choline chloride-based DESs.[28,34,44,45] The dielectric relaxation study of aqueous solution of glyceline and reline performed at room temperature and high (microwave) frequencies (0.05–89 GHz) indicates that a structural transition occurs for a water mole fraction about 0.8, from the homogeneous electrolyte solution to a micro-heterogeneous structure with water-rich and DES-rich pools.[46] The micro-segregation of species into regions of different compositions can result in co-continuous structures and mesoscopic length scale heterogeneities.[10,36,37,40,47]

In the present study, we have addressed the relative impact of these structural reorganizations on transport properties, dipolar relaxation, and glassy behavior. We have performed a dielectric spectroscopy study of the prototypical ethaline DES (choline chloride/ethylene glycol, 1:2) and nine different aqueous mixtures thereof, which were recently studied by differential scanning calorimetry (DSC) and neutron scattering.[26,40] The ionic conductivity and reorientation dynamics were shown to vary by more than six decades in the entire studied temperature range of 128–283 K. In the "DES-in-water" region (>40 wt. %), according to the designation introduced by Roldán-Ruiz *et al.*,[37] an abrupt decoupling between transport properties and dipolar relaxation was observed. This was attributed to phase separation and the formation of a maximally freeze concentrated DES solution during cooling. In the "water-in-DES" regime (<40 wt. %), the solution obviously formed a macroscopically homogeneous liquid phase and presented characteristic features of glassy dynamics, i.e., non-Arrhenius temperature dependence and non-exponential relaxation functions. In this range of compositions, temperatures, and timescales, this study indicates that only a marginal decoupling between ionic transport and dipolar dynamics is observed.

II. METHODS

A. Samples

Choline chloride (>99%) and ethylene glycol (anhydrous, 99.8%) were purchased from Sigma–Aldrich. DESs were prepared by weighting and adding ethylene glycol and choline chloride in a molar ratio of 2:1, which is the accepted composition of the eutectic mixture.[48,49] The DESs were mixed by mechanical agitation at about 60 °C for 30 min until a clear homogeneous liquid phase was obtained and served as stock solutions. A series of ten working solutions were prepared by pipetting and addition of deionized water, corresponding to regularly spaced values of the mass fraction of water W from 0 to 90 (wt. %).

B. Dielectric spectroscopy experiments

The sample was prepared in parallel plate geometry between two gold-plated electrodes with a diameter of 20 mm and a spacing of 260 μm maintained by Teflon spacers. It was placed in the cryostat and maintained under a dry nitrogen atmosphere. The complex impedance of the as-prepared capacitor was measured from 1 to 10^{6} Hz with a Novocontrol high resolution dielectric Alpha analyzer with an active sample cell. The measurements were performed

at thermal equilibrium with a temperature step of 5 K, covering the temperature range from 283 to 128 K (10 to −145 °C). The temperature of the sample was controlled using a Quatro temperature controller (Novocontrol) with nitrogen as a heating/cooling agent, providing temperature stability within 0.1 K.

III. RESULTS AND DISCUSSION

A. Dielectric permittivity spectra

The complex dielectric function of the sample $\varepsilon^*(f) = \varepsilon'(f) - i\varepsilon''(f)$ was evaluated for the ten DES samples with different hydration levels, where f denotes the frequency of the electric field, ε' and ε'' are the real and loss parts of the complex dielectric function, and i symbolizes the imaginary unit. The two components are presented in Figs. 1(a) and 1(b) for a mixture of ethaline with W = 10 wt. % of water. Qualitatively comparable spectra were obtained for all the samples, as illustrated in Figs. S1–S10 in the supplementary material. Depending on the temperature and frequency ranges, different contributions were observed in the instrumental frequency window. At high temperature, the complex dielectric function was dominated by ionic conductivity. The dc conductivity only contributes to the dielectric loss. This was revealed by a power law term $(-1/f)$ in the intensity of the dielectric loss [cf. blue dashed line with slope −1 on a log–log scale in Fig. 1(b)]. Additionally, polarization effects due to the blocking electrodes were detected, as usually observed for conducting liquids. These phenomena led to a huge increase in ε' and a deviation of ε'' from the $(-1/f)$ scaling at lower frequency. These effects are illustrated in the supplementary material in Figs. S11(a) and S11(b) for a water–ethaline mixture (W = 10 wt. %), which are full scale representations of the data shown in Figs. 1(a) and 1(b). They do not hold any useful physical information on the samples and have been excluded from the discussion. In the low temperature range, typically below 210 K, a main peak appeared in the dielectric loss. It was also associated with a sigmoidal step in the real permittivity ε', as indicated by solid lines and red filled areas in Figs. 1(a) and 1(b). This was attributed to the dipolar α-relaxation process, in agreement with the interpretation made for anhydrous ethaline.[24]

The dielectric measurements were analyzed quantitatively by fitting the complex dielectric function by a model including a Havriliak–Negami function (HN-model)[50] and a dc-conductivity term according to the following equation:

$$\varepsilon^*(\omega) = \varepsilon_\infty + \frac{\Delta\varepsilon}{(1 + (i\omega\tau_{HN})^\alpha)^\beta} - i\frac{\sigma}{\omega\varepsilon_0}, \quad (1)$$

where ε_∞ is the sample permittivity in the limit of high frequency and $\Delta\varepsilon$ and τ_{HN} are the dielectric strength and the HN-relaxation time of the mode. According to the formalism of the HN-model, the exponent parameters α and β account for the symmetric and the asymmetric broadening of the complex dielectric function with respect to the Debye one. σ stands for the DC conductivity of the sample and ε_0 the permittivity of vacuum. The application of this model provided fits of the real and loss parts of the complex dielectric function with good quality in the temperature and frequency regions where electrode polarization was not significant, as illustrated in Fig. 1. Differences between the real part of the complex dielectric function measured at T = 178 K and the fitted model (red-filled area) are obvious in Fig. 1(a) for frequency smaller than 10^2 Hz since electrode polarization was not included. Concerning the loss part, the agreement between the experimental result (symbol) and the fitted model (line) was better than the symbol size for the entire range presented in Fig. 1(b). The electrode contribution was estimated in the supplementary material (cf. Fig. S12), and it was shown to be insignificant in the frequency range determined by the relaxation process.

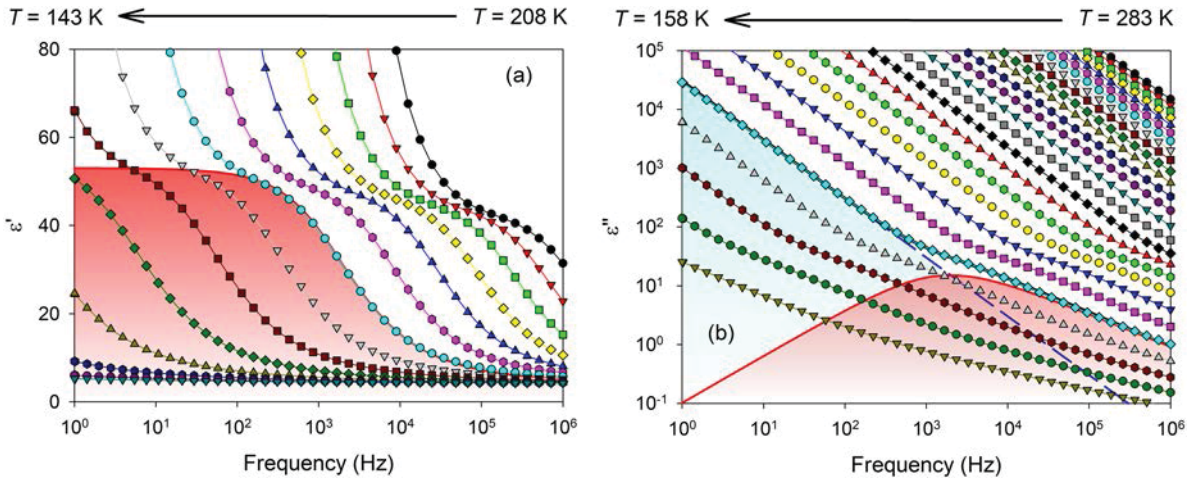

FIG. 1. (a) Real and (b) loss parts of the complex dielectric function of a mixture of ethaline with W = 10 wt. % of water as a function of the frequency and the temperature. The different experimental curves (line connected data points) correspond to temperatures varying (a) from 208 to 143 K and (b) from 283 to 158 K, with decreasing steps of 5 K from right to left. The components of the fitted model are illustrated for the selected temperature T = 178 K. The solid line with a red-filled area in both panels denotes the dipolar relaxation modeled by a Havriliak–Negami function, and the dashed line with a blue-filled area in (b) denotes the ionic dc-conductivity. For the loss part (b), the total fitted model is undistinguishable from the experimental data. The deviation due to electrode polarization that was not included in the model is seen at low frequency for the real part. This is illustrated for T = 178 K, by a difference between line connected symbols and the solid line with a red-filled area in (a).

As a whole, the fitted model corresponds to the description that is frequently used for prototypical dipolar liquids.[25] For the present DES components having dipolar moments, it was reasonably found that, along with dc-conductivity, the spectra are dominated by reorientational dynamics. If present, ac-conductivity contributions must be hidden by the dipolar relaxation, and they were not included in the description. The relaxation time associated with the maximum in the lost part of the complex dielectric function frequency was computed according to the following equation:[51]

$$\tau = \tau_{HN} \sin\left(\frac{\pi a}{2+2\beta}\right)^{-1/\alpha} \sin\left(\frac{\pi a\beta}{2+2\beta}\right)^{1/\alpha}. \quad (2)$$

B. Ionic conductivity around room temperature

The ionic conductivities measured by fitting the complex dielectric function were found to be in good agreement with recent measurements reported in the complementary region above room temperature by Lapena *et al.*[35] These measurements were, however, limited to pure ethaline and one ethaline–water mixture (8 wt. %) as illustrated in Fig. 2(a). On increasing the amount of water at a constant temperature (T = 283 K), the conductivity gradually increased until it reached a maximum value for W > 40% as illustrated in Fig. 2(b). This non-monotonous behavior has also been observed by molecular dynamics simulations of aqueous reline and ethaline solutions by Celebi *et al.*[52] The initial increase in conductivities with addition of water was attributed to the destabilization of the H-bond associations between DES species, which resulted in a smaller viscosity and faster transport properties. For W > 40%, DES constituents were found to be fully dissolved into a DES-in-water aqueous solution, which implied that the ionic conductivity eventually decreased due to dilution effects.

C. Translational dynamics at variable temperatures

The ionic conductivities measured in the temperature range from 158 to 283 K are illustrated in Fig. 3 in the Arrhenius representation. Two qualitatively different behaviors were observed depending on the hydration level. For low hydration levels (0%–30%), a continuous temperature variation of the conductivity was obtained, while a discontinuity was observed for larger dilution (40%–90%). The discontinuity occurred at a temperature that depended on W, as illustrated by an arrow in Fig. 3(b) for W = 90%. These two ranges of compositions correspond to the usually denoted DES-in-water and water-in-DES regimes.[37]

A clear explanation of this dependence on the water dilution can be found in the phase diagram of the ethaline–water system, which was recently determined by calorimetry (cf. Fig. 4).[26] It has been shown that below a threshold value, W_g' ~ 30%, water hydration molecules strongly interact with DES molecular units. In this range of compositions, the hydrated DES forms a single phase system, even at low temperature, where it presents a single glass transition. On the contrary, for $W > W_g'$, the aqueous solution phase separates on cooling into a pure ice phase and a maximally freeze-concentrated aqueous solution of the DES having the composition W_g'.

For $W < W_g'$, the conductivity monotonously increases with the fraction of water. This behavior follows the observations made previously around room temperature and confirms the plasticizing effect of water. For $W > W_g'$, the opposite dependence of the conductivity with the fraction of water is observed below T_c. This is due to the formation of a spatially heterogeneous phase separated system, where the ionic diffusion process that persists in the freeze-concentrated electrolyte is restricted by the coexisting ice matrix. Although the composition of the conducting freeze-concentrated electrolyte (W_g') does not depend on the initial composition W, the overall conductivity of the

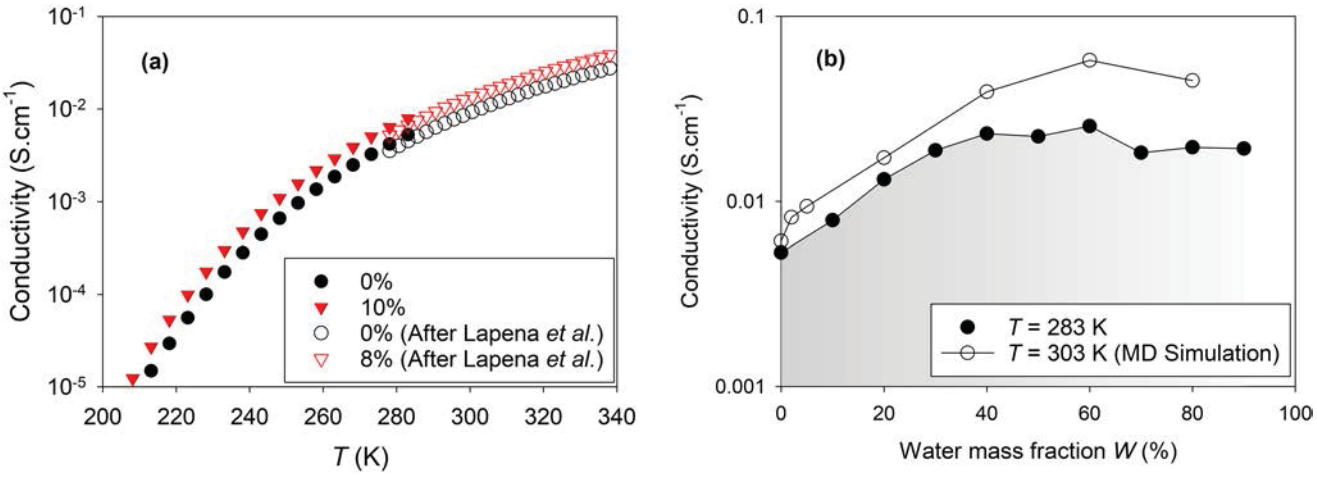

FIG. 2. (a) Comparison of the conductivity measured in the present study from the fit of the complex dielectric function of ethaline (filled circles) and an ethaline–water mixture with W = 10 wt. % (filled triangles) with the measurements performed above room temperature by Lapena *et al.*[35] for similar compositions (open symbols). (b) Effect of water on the conductivity measured in the present study at 283 K (filled circles with the shaded area) and by molecular dynamics simulation at 303 K (open circles) by Celebi *et al.*[52]

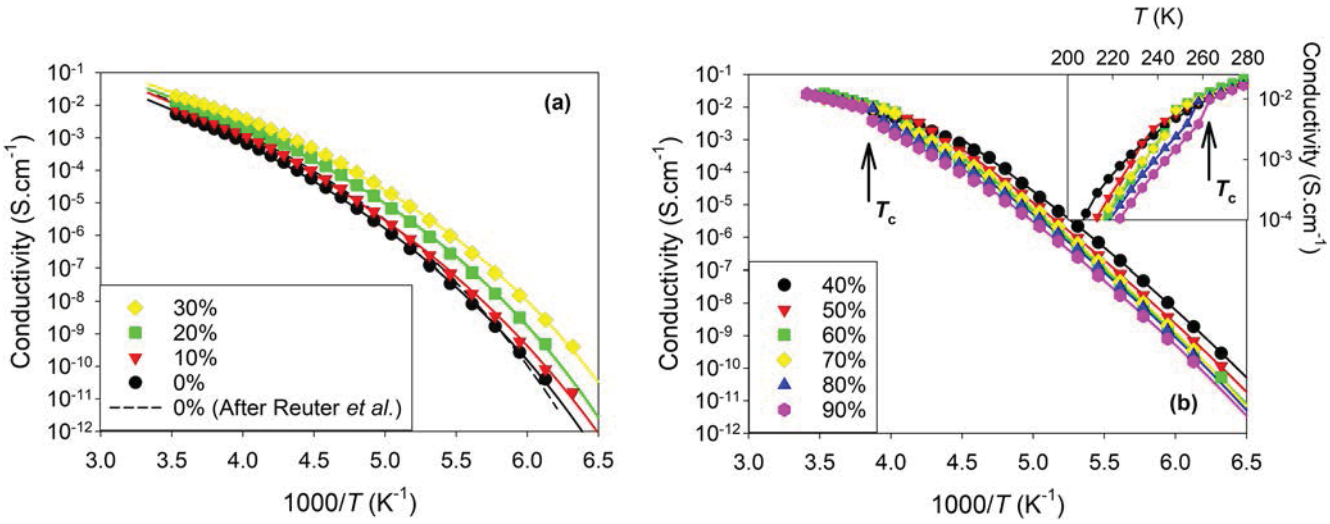

FIG. 3. Temperature dependence of the conductivity of aqueous mixtures of ethaline in the Arrhenius representation for different values of the water mass fraction W. The solid line denotes fits with a VTF law. (a) Water-in-DES regime, with W = 0%–30%. (b) DES-in-water regime, with W = 40%–90%. The crystallization temperature T_c is indicated by an arrow for W = 90%. Inset: magnified view of the crystallization region with temperature on a linear scale.

heterogeneous system decreases as a function of the relative fraction of ice formed.

D. Reorientational dynamics

The dielectric relaxation times are illustrated in the Arrhenius representation in Fig. 5. As for the transport properties, two different behaviors were observed depending on the regime of hydration. For low hydration levels ($W < W_g'$), the dipolar relaxation became faster with the addition of water [cf. Fig. 5(a)]. It was accelerated by up to a factor of 100 for the hydration level W = 30%, with respect to the neat DES. The acceleration of the reorientational dynamics at a low hydration level resembles the observation made for the conductivity. As general trends, these observations confirm that the addition of water to the DES reduces viscosity and enhances molecular mobility.

For high hydration levels ($W > W_g'$), the dipolar dynamics depended only marginally on the amount of water. Indeed, the relaxation times measured for six different compositions essentially seen on a single curve, which extended over seven decades in time [cf. Fig. 5(b)]. This behavior differs from the ionic conductivity that decreases with W. This apparently contradictory observation finds a clear explanation. The dipolar relaxation probes the reorientational dynamics of the DES solution on a local scale. For $W > W_g'$, the co-existence of ice with the phase forming the maximally freeze-concentrated solution of the DES does not affect the rotational dynamics of the DES molecules. This implies that the size of the DES domains is large enough to limit the influence of interfacial and confinement effects. On the contrary, these conditions may not be fulfilled for ionic conduction, which proceeds through translational diffusion of the ionic species.

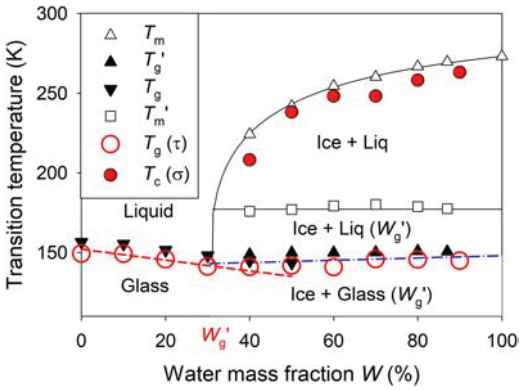

FIG. 4. Phase diagram of the DES aqueous mixtures as a function of the water mass fraction. Filled circles denote the crystallization temperature determined from conductivity, and open circles denote the isochronic glass transition temperature determined from dielectric relaxation time. Calorimetric determinations of the liquidus (T_m), the onset of melting (T_m'), the glass transition temperature of the whole aqueous solution (T_g), or only the unfrozen part coexisting with ice (T_g') are extracted from the study by Jani *et al.*[26]

E. Glassy dynamics

We now analyze in more detail the functional temperature dependence of both dynamics. In all cases, a strong deviation from an Arrhenius behavior was observed. This is demonstrated by the curvature in the Arrhenius plots of the conductivity and the relaxation time shown in Figs. 3 and 5. This increase in the apparent activation energy during cooling is typical for glass-forming liquids, and it has been already discussed for neat ethaline.[24] For all the water–ethaline mixtures studied, the existence of a glass transition has been actually demonstrated by DSC.[26] A complementary estimation of the glass transition temperature has also been evaluated from the present dielectric measurements by

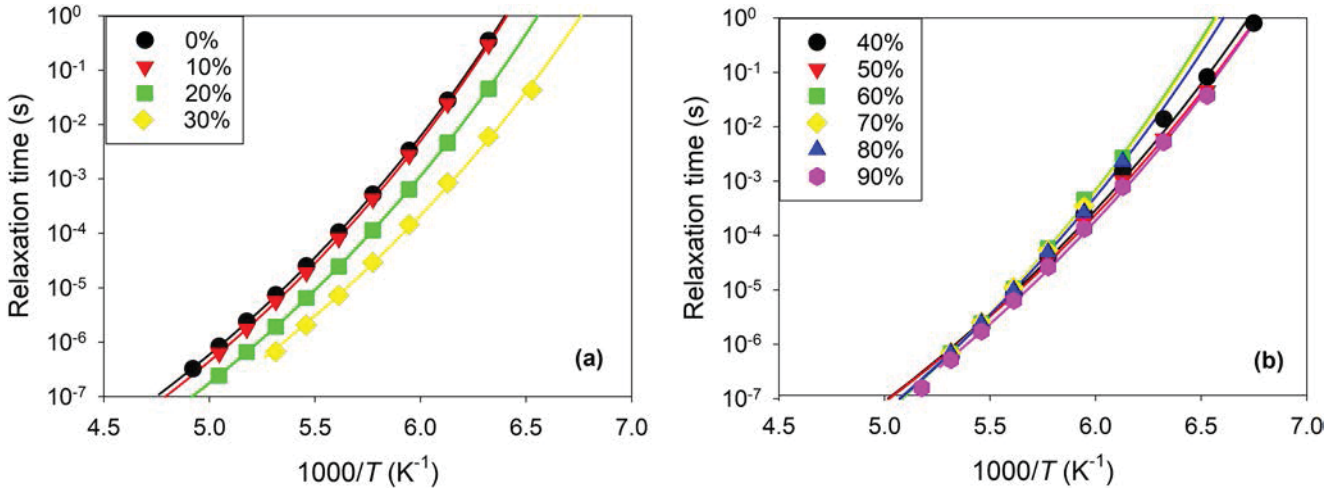

FIG. 5. Temperature dependence of the relaxation time of aqueous mixtures of ethaline in the Arrhenius representation for different values of the water mass fraction *W*. The solid line denotes fits with a VTF law. (a) Water-in-DES regime, with *W* = 0%–30%. (b) DES-in-water regime, with *W* = 40%–90%.

extrapolation of the relaxation time to 10^2 s as illustrated by $T_g(\tau)$ in Fig. 4.

The deviations of the dipolar relaxation and conductivity from the Arrhenius behavior were described by the empirical Vogel–Fulcher–Tammann (VFT) law. For the relaxation time, the classical VFT equation is given by Eq. (3), while the modified version corresponding to Eq. (4) is classically adopted for the ionic transport,[24]

$$\tau = \tau_0 \exp\left(\frac{D_\tau T_{0\tau}}{T - T_{0\tau}}\right), \tag{3}$$

$$\sigma = \sigma_0 \exp\left(\frac{-D_\sigma T_{0\sigma}}{T - T_{0\sigma}}\right). \tag{4}$$

In these two equations, τ_0 and σ_0 are the pre-exponential factors and D_x and T_{0x} ($x = \tau$ and σ) are the strength parameters and the Vogel–Fulcher temperatures associated with the dipolar relaxation and conductivity, respectively. A large deviation from an Arrhenius behavior is characterized by small values of D_x, while an Arrhenius behavior is recovered for large D_x and $T_{0x} \approx 0$. Satisfactory fits of the experimental relaxation times and conductivities were obtained for the studied range of temperatures and water mass fractions as illustrated by solid lines in Figs. 3 and 5. The deviation of the relaxation time from an Arrhenius behavior has been considered for many decades as a salient feature of most of the glass-forming systems in their liquid and supercooled states. It has been recognized as an evidence for the cooperative nature of the structural relaxation.[53] The non-Arrhenius character has been used to define a parameter, named the fragility index *m*, which categorizes a series of glass-forming liquids according to the nature of their dynamics in terms of fragile or strong systems.[54] For ethaline, we found the value of the fragility index to be around *m* = 48, which corresponds to the type of intermediate system according to this classification. For pure ethaline, Reuter *et al.* found a slightly larger value of the fragility index (*m* = 60), which might be attributed to the larger frequency range adopted in that study (10^9 to 10^{-1} Hz). Interestingly, we observed that the fragility of ethaline decreased with the addition of water, as illustrated in Fig. 6, and then reached a plateau value (*m* = 40) for a water mass fraction larger than *W* = 40%. The invariance of *m* in the DES-in-water regime, i.e., for *W* > 40%, agrees well with the formation on cooling of a maximally freeze-concentrated solution with fixed composition W_g' and dipolar dynamics. In the water-in-DES regime, the possible reduction of fragility of a DES with addition of water has never been reported so far, though it can be seen as moderate, if one considers that the entire fragility scale extends from *m* = 16 for strong liquids to *m* = 170 for extremely fragile systems.

Another salient observation concerns the deviation of the relaxation function from a simple Debye process. In the time domain, the non-exponential character of the relaxation function of liquids is often expressed by a stretched exponential function, also denoted as the Kohlrausch–Williams–Watts function. To conform with this representation, we applied the numerical ansatz that connects the

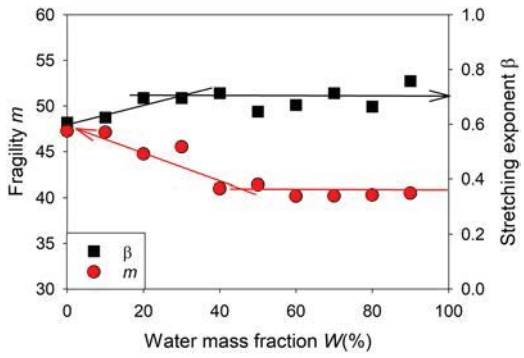

FIG. 6. Dependence on the water amount of the fragility index (circle) and the stretching exponent of the dipolar relaxation (square).

stretching exponent β_{KWW} with the HN parameters obtained in the frequency domain, i.e., $\beta_{KWW} = (\alpha\beta)^{\frac{1}{1.23}}$.[55] We found that the values of β_{KWW} increased from 0.6 to 0.7 with the addition of water and saturated for a mass fraction larger than $W = 40\%$, as illustrated in Fig. 6. In glass-forming liquids, the non-exponential character of the structural relaxation is classically attributed to the presence of a distribution of relaxation times. There are a growing number of evidences that this distribution actually reflects the presence of spatially heterogeneous dynamics.[53] Accordingly, it seems counter-intuitive that the addition of water to the DES resulted in apparently more homogeneous reorientational dynamics. From a structural point of view, the addition of water as a competing HBD and as a solvating agent with respect to the initial DES constituents rather results in to the formation of a broader distribution of local environments.[10,28,36,40,47] Therefore, one would expect a decrease in β_{KWW} with increasing W. A possible rationalization is suggested by the concomitant reduction of fragility of the DES with the addition of water. As shown in Fig. 6, the increase in β_{KWW} seems correlated with the decrease in the fragility index m. A relationship between fragility and non-exponentiality has been established for numerous very different glass-forming systems.[54] It appears that ethaline and water–ethaline mixtures also obey this relationship between β_{KWW} and m. Their dynamics compare well with those of other H-bonded liquids, such as polyalcohols, which fall in the category of intermediate and moderately non-Debye liquids (cf. Fig. 3 in Ref. 54). Moreover, on addition of water, the increase in β_{KWW} with decreasing m is in qualitative agreement with the linearly decreasing dependence, which was proposed for molecular glass formers in that study.[54] Supporting pioneering ideas about the concept of cooperativity dynamics,[53] many studies indicate that the glassy slowdown is accompanied by the growing length scale of transient domains.[56,57] In this context, one may speculate that the nanosegregation of DES components with the addition of water, while favoring structural heterogeneity with the formation of domains having a distinct composition, would restrict the growth of dynamic cooperativity to values bounded by the domain typical size.[36,40] A microscopic description of the cooperative character of the molecular dynamics in DESs would be desirable to test this idea, which shares similarity with the concept cut-off on the cooperativity length introduced for nanoconfined liquids.[58–60]

F. Rotation–translation decoupling

In order to address the (de)coupling of the ionic transport and the reorientation dipolar motions, we have compared in Fig. 7 the strength parameter evaluated from VTF fits of both dynamical processes. The same values are obtained for neat ethaline, which is in agreement with the recent study concluded that both dynamics obeyed the same temperature dependence.[24] A difference between both strength parameters is observed on addition of water. It remains very small up to $W = 40$, indicating the opposite effect of water on the fragility when refereeing to the reorientation or translation.

It should be pointed out that the frequency and temperature ranges covered by both processes are different in DS experiments, which might influence the determination of the strength parameters. To overcome the question, we have also represented the conductivity as a function of the relaxation time for a limited selection of

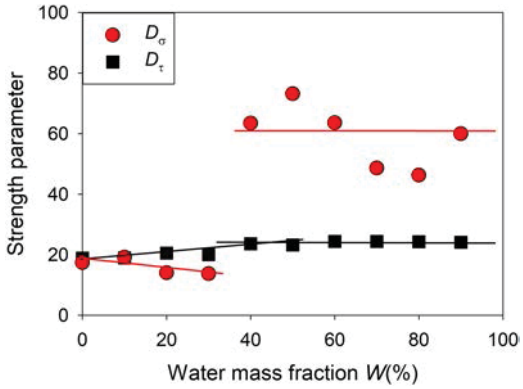

FIG. 7. Dependence on the water mass fraction of the strength parameter of the dipolar relaxation (circle) and the ionic conductivity (square) of ethaline aqueous mixtures.

temperatures where both processes are measurable simultaneously in the DS spectra, as illustrated in Fig. 8(a). It confirms that for $W < 40\%$, and in this temperature range, both quantities are essentially inversely proportional. This relationship is indicated by a solid line in Fig. 8(a). For neat ethaline, this inverse proportionality has been already demonstrated.[24] In this study, the authors concluded that the question remained opened, however, whether the two processes were actually coupled to viscosity, implying that the Stokes–Einstein and Stokes–Einstein–Debye relationships were fulfilled or that both processes were directly coupled to each other. The latter case was illustrated by the revolving-door or paddle-wheel mechanism, which was also considered for ionic liquids where paths for ion diffusion are opened by the rotation of other dipolar ions.[61] The addition of water to the choline based DES is known to modify significantly the hydration shell of chloride anions, which are preferentially solvated by water.[28,34,44,45] The H-bond interactions within the original DES supramolecular complexes are also affected by water acting as an additional HBD.[39,41–43] For these reasons, it seems unlikely that a persistent revolving-door mechanism can tolerate the effects of adding up to 40% of water to ethaline. It rather indicates a more classical scenario in which both dynamics are coupled to viscosity, in accordance with the predictions from hydrodynamics. This is also in accord with the conclusions from a recent study.[27]

For a large water mass fraction ($W > 40\%$), a completely different situation is observed, with a large decoupling between both dynamics. This is illustrated by a sudden increase in the strength parameter of the ionic conductivity from about $D_\sigma = 15$–60 at $W = 40\%$, which is in close agreement with the Arrhenius behavior of the conductivity shown in Fig. 3(b). Likewise, a breakdown of the inverse proportionality is observed, indicating a fractional translational–rotational coupling with $\sigma \propto \tau^{-0.9}$, as illustrated in Fig. 8(b). This phenomenon provides a clear illustration of the possible effects of strong spatial heterogeneities, with the latter being due to the coexistence of domains formed by maximally freeze-concentrated DES aqueous solutions and by solid water. The composition $W = 40\%$ is at the frontier between the two different regimes.

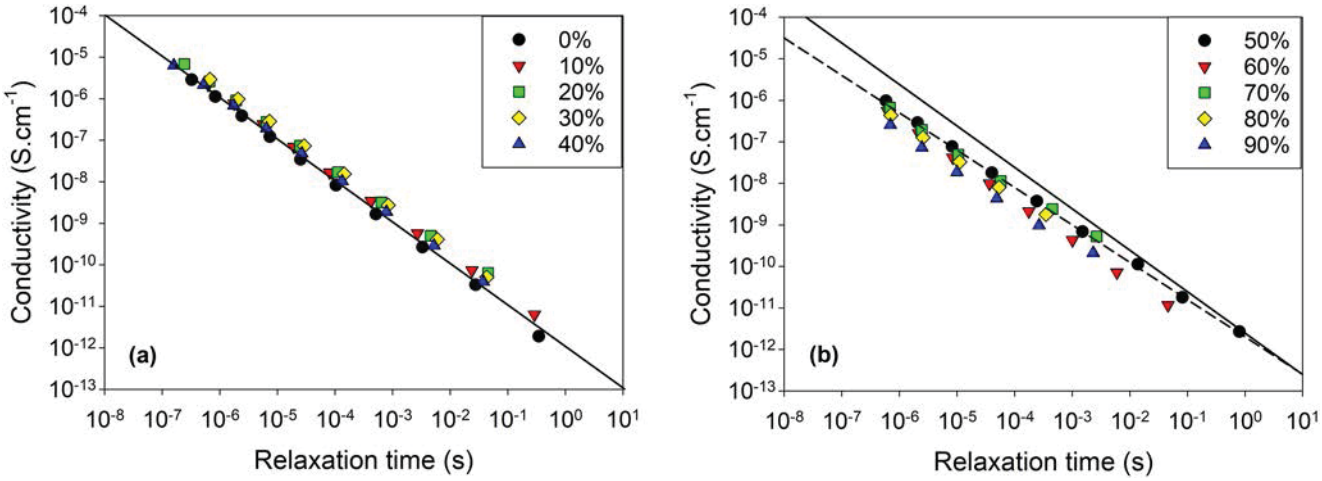

FIG. 8. Dependence of the ionic conductivities on their reorientational relaxation times of aqueous mixtures of ethaline as a function of the water mass fraction. (a) Water-in-DES regime, with W = 0%–40%. (b) DES-in-water regime, with W = 50%–90%. The solid line with a slope of −1 in (a) and (b) indicates the inverse proportionality, $\sigma \propto \tau^{-1}$, while the dashed line in (b) has a slope of −0.9, indicating $\sigma \propto \tau^{-0.9}$.

According to the phase diagram, a fraction of water already crystallizes at W = 40%; however, as illustrated in Fig. 8(a), the ionic conductivity of the solution still scales with the relaxation time, which is probably due to the low volume fraction of ice.

IV. CONCLUSIONS

The existence of dynamic heterogeneity in DESs has been indicated by clear deviations of the rotational–translational dynamics of dye molecules from the Stokes–Einstein–Debye hydrodynamic predictions. Dielectric spectroscopy is a unique method to determine simultaneously the reorientational dynamics of dipolar molecules and the transport properties of ionic species on an extended range of frequencies. So far, this method has been barely used for DESs, although a recent study has pointed to the existence of a coupling between both processes for ethaline.

In the present study, we have used the fraction of water in ethaline DES aqueous mixtures as a varying control parameter of the solvation and H-bond interactions. The reorientational dynamics and the ionic conductivity of ten ethaline solutions were studied in the temperature range of 128–283 K and the MHz–Hz frequency range. Two different regimes were observed depending on the water mass fraction W, which agrees with the published phase diagram of ethaline aqueous solutions.

In the water-in-DES regime (<40 wt. %), the DES aqueous mixtures did not form classically phase separated systems. The relaxation time and the conductivity presented characteristic features of glass-forming systems, including a deviation from the Arrhenius temperature dependence and a non-exponential decay of the relaxation function. The addition of water resulted in an acceleration of both dynamics, by up to a factor of 100, indicating a plasticizing effect of water on the DES. Moreover, according to the dipolar relaxation, the addition of water concomitantly reduced the fragility index m and increased the stretching exponent β_{KWW}. According to the values of both parameters, ethaline and ethaline–water mixtures fall in the category of intermediate glass-forming liquids. The values of β_{KWW} and m fulfill the relationship made for intermediate molecular glass-forming liquids such as polyalcohols.

Interestingly, it can be concluded that in this range of compositions, temperatures, and timescales, the dipolar relaxation and ionic conductivity remained inversely proportional to each other. The persistence of a direct coupling mechanism, where paths for ion diffusion are opened by the rotation of other dipolar ions, is improbable. Although such a paddle-wheel mechanism was indicated for ionic liquids, and also invoked as a possible process for neat ethaline, it seems unlikely that it remains unaffected despite the important modifications in ion solvation and H-bond interaction induced by the water addition to the DES components. The applicability of the Stokes–Einstein–Debye relation rather indicates that both dynamics are equally coupled to viscosity, which is also supported by very recent findings.[27] This conclusion also implies that the dynamic heterogeneity plays a secondary role in the present experimental situation.

In the DES-in-water regime (>40 wt. %), a clear rotation–translation decoupling is observed, including a transition toward a nearly Arrhenius dependence of the ionic transport and a fractional relation between conductivity and dipolar relaxation with $\sigma \propto \tau^{-0.9}$. This behavior is attributed to the spatially heterogeneous nature of the phase-separated sample, where domains formed by maximally freeze-concentrated DES aqueous solutions coexist with frozen water.

SUPPLEMENTARY MATERIAL

See the supplementary material for the real and loss parts of the complex dielectric function of all the samples studied in the present work and evaluation of the contribution due to electrode polarization.

ACKNOWLEDGMENTS

Support from Rennes Metropole and Europe (FEDER Fund—CPER PRINT2TAN) and the ANR (Project NanoLiquids No. ANR-18-CE92-0011-01) is expressly acknowledged. This work was part of the Ph.D. thesis of A.J., who benefits from a grant from the French Ministry of Higher Education, Research, and Innovation. The authors are grateful to the CNRS—network SolVATE (No. GDR 2035) for financial support and fruitful discussions. We thank one of the referees for bringing to our attention the e-print of a recent study. This work later appeared as a manuscript cited as Ref. 27.

DATA AVAILABILITY

The data that support the findings of this study are available from the corresponding author upon reasonable request.

REFERENCES

[1] A. P. Abbott *et al.*, Chem. Commun. **9**, 70 (2003).
[2] A. P. Abbott *et al.*, J. Am. Chem. Soc. **126**, 9142 (2004).
[3] Q. Zhang *et al.*, Chem. Soc. Rev. **41**, 7108 (2012).
[4] E. L. Smith, A. P. Abbott, and K. S. Ryder, Chem. Rev. **114**, 11060 (2014).
[5] X. Ge *et al.*, J. Mater. Chem. A **5**, 8209 (2017).
[6] B. B. Hansen *et al.*, Chem. Rev. **121**, 1232 (2021).
[7] L. J. B. M. Kollau *et al.*, Chem. Commun. **54**, 13351 (2018).
[8] M. A. R. Martins, S. P. Pinho, and J. A. P. Coutinho, J. Solution Chem. **48**, 962 (2019).
[9] S. Kaur, A. Malik, and H. K. Kashyap, J. Phys. Chem. B **123**, 8291 (2019).
[10] S. Kaur, A. Gupta, and H. K. Kashyap, J. Phys. Chem. B **124**, 2230 (2020).
[11] S. Fryars *et al.*, J. Electroanal. Chem. **819**, 214 (2018).
[12] F. C. Zhen *et al.*, J. Phys. Chem. B **124**, 1025 (2020).
[13] Q. Xu *et al.*, Chem. Phys. Lett. **708**, 48 (2018).
[14] L. Millia *et al.*, Solid State Ionics **323**, 44 (2018).
[15] C. L. Boldrini *et al.*, Energy Technol. **5**, 345 (2017).
[16] R. K. Gautam, A. Chatterjee, and D. Seth, J. Mol. Liq. **280**, 399 (2019).
[17] S. S. Hossain and A. Samanta, J. Phys. Chem. B **121**, 10556 (2017).
[18] N. Subba *et al.*, J. Phys. Chem. B **123**, 9212 (2019).
[19] K. Mukherjee *et al.*, J. Chem. Phys. **149**, 124501 (2018).
[20] E. Tarif *et al.*, J. Chem. Sci. **131**, 43 (2019).
[21] Y. Zhang *et al.*, J. Phys. Chem. B **124**, 5251 (2020).
[22] S. N. Tripathy *et al.*, J. Chem. Phys. **142**, 184504 (2015).
[23] A. Faraone *et al.*, J. Phys. Chem. B **122**, 1261 (2018).
[24] D. Reuter *et al.*, Phys. Chem. Chem. Phys. **21**, 6801 (2019).
[25] F. Kremer and A. Schönhals, *Broadband Dielectric Spectroscopy* (Springer, Berlin, 2002).
[26] A. Jani, T. Sohier, and D. Morineau, J. Mol. Liq. **304**, 112701 (2020).
[27] D. Reuter *et al.*, J. Chem. Phys. **154**, 154501 (2021).
[28] O. S. Hammond, D. T. Bowron, and K. J. Edler, Angew. Chem., Int. Ed. **56**, 9782 (2017).
[29] H. Passos *et al.*, ACS Sustainable Chem. Eng. **4**, 2881 (2016).
[30] Y. Dai *et al.*, Food Chem. **187**, 14 (2015).
[31] A. Yadav *et al.*, Fluid Phase Equilib. **367**, 135 (2014).
[32] X. Meng *et al.*, New J. Chem. **40**, 4492 (2016).
[33] C. Ma *et al.*, Chem. Soc. Rev. **47**, 8685 (2018).
[34] P. Kumari *et al.*, Acs Omega **3**, 15246 (2018).
[35] D. Lapena *et al.*, Fluid Phase Equilib. **492**, 1 (2019).
[36] E. Posada *et al.*, J. Mol. Liq. **276**, 196 (2019).
[37] M. J. Roldán-Ruiz *et al.*, J. Mol. Liq. **284**, 175 (2019).
[38] R. Ahmadi *et al.*, Phys. Chem. Chem. Phys. **20**, 18463 (2018).
[39] O. S. Hammond *et al.*, J. Phys. Chem. B **121**, 7473 (2017).
[40] L. Percevault *et al.*, J. Phys. Chem. B **124**, 9126 (2020).
[41] I. Delso *et al.*, J. Mol. Liq. **290**, 111236 (2019).
[42] N. López-Salas *et al.*, ACS Sustainable Chem. Eng. **8**, 12120 (2020).
[43] N. López-Salas *et al.*, ACS Sustainable Chem. Eng. **7**, 17565 (2019).
[44] L. D. Weng and M. Toner, Phys. Chem. Chem. Phys. **20**, 22455 (2018).
[45] L. Gontrani *et al.*, Phys. Chem. Chem. Phys. **20**, 30120 (2018).
[46] V. Agieienko and R. Buchner, Phys. Chem. Chem. Phys. **22**, 20466 (2020).
[47] E. Posada *et al.*, Phys. Chem. Chem. Phys. **19**, 17103 (2017).
[48] K. Shahbaz *et al.*, J. Appl. Sci. **10**, 3349 (2010).
[49] P. López-Porfiri, J. F. Brennecke, and M. Gonzalez-Miquel, J. Chem. Eng. Data **61**, 4245 (2016).
[50] S. Havriliak and S. Negami, J. Polym. Sci., Part C: Polym. Symp. **14**, 99 (1966).
[51] R. Díaz-Calleja, Macromolecules **33**, 8924 (2000).
[52] A. T. Celebi, T. J. H. Vlugt, and O. A. Moultos, J. Phys. Chem. B **123**, 11014 (2019).
[53] G. Adam and J. H. Gibbs, J. Chem. Phys. **43**, 139 (1965).
[54] R. Bohmer *et al.*, J. Chem. Phys. **99**, 4201 (1993).
[55] F. Alvarez, A. Alegra, and J. Colmenero, Phys. Rev. B **44**, 7306 (1991).
[56] M. D. Ediger, Annu. Rev. Phys. Chem. **51**, 99 (2000).
[57] L. Berthier *et al.*, Science **310**, 1797 (2005).
[58] M. Arndt *et al.*, Phys. Rev. Lett. **79**, 2077 (1997).
[59] R. Richert, Annu. Rev. Phys. Chem. **62**, 65 (2011).
[60] D. Morineau, Y. D. Xia, and C. Alba-Simionesco, J. Chem. Phys. **117**, 8966 (2002).
[61] P. Sippel *et al.*, Phys. Rev. E **98**, 052605 (2018).

ANNEX-V

Phase behavior of aqueous solutions of ethaline deep eutectic solvent

Authors

Aicha Jani, Thibaut Sohier and Denis Morineau

Journal of Molecular Liquids 304 (2020) 112701

Contents lists available at ScienceDirect

Journal of Molecular Liquids

journal homepage: www.elsevier.com/locate/molliq

Phase behavior of aqueous solutions of ethaline deep eutectic solvent

Aicha Jani, Thibaut Sohier, Denis Morineau *

Institute of Physics of Rennes, CNRS-University of Rennes 1, UMR 6251, F-35042 Rennes, France

ARTICLE INFO

Article history:
Received 3 December 2019
Received in revised form 31 January 2020
Accepted 12 February 2020
Available online 13 February 2020

Keywords:
Deep eutectic solvents
Ethaline
Maximally freeze-concentrated solution
Differential scanning calorimetry

ABSTRACT

We have established a detailed phase diagram of a prototypical DES as a function of the hydration level. Two distinct thermal phase behaviors are observed depending on the water content with respect to a cross-over composition W_g' = 30%. For $W < W_g$', the formation of ice is not observed under the experimental conditions used in this study, and the solution falls in the category of glassforming systems. Fully vitreous states could also be obtained between 30% and 50%, but they are metastable with respect to water crystallization. For $W > W_g$', ice crystallization occurs but the residual DES solution remains amorphous (liquid or glassy). In the latter case, whatever the initial water fraction, this transformation finally ends at the fixed composition W_g' corresponding to 6 to 10 water molecules per choline ion for the two studied DESs. We infer that the residual liquid water molecules forming this maximally freeze-concentrated solution are strongly interacting with DES molecular units. This situation is also known as the "water-in-DES" case. Conversely, ice crystallization concerns free water molecules, provided that $W > W_g$', also known as the "DES-in-water" case. This entire phase behavior is explained in the context of maximally freeze-concentrated solutions and attributed to the concomitant effects of ice freezing depression, glassforming ability of weakly hydrated DES ($W < W_g$') and water structure distortion. This study also highlights the potential of DESs for their uses in freeze-drying processes and biopreservative applications.

1. Introduction

For the last decade, deep eutectic solvents (DESs) have been the matter of tremendous interest. They are presented as promising alternative to classical solvents, combining many benefits of ionic liquids, while being more affordable and usually less toxic. There include high solvating and extracting properties and low volatility. Prototypical DESs can also exhibit specific nanostructures, which are maintained during freezing or the addition of water, making them resilient to dissociation into clusters of the H-bonded molecules [1,2]. As such, the introduction of DESs in more sustainable industrial processes has been considered in many different fields such as extraction, (bio)synthesis, catalysis, electrochemistry, carbon dioxide capture [3–5].

The notion of DESs has been introduced in the pioneering work of Abbott et al. [6,7]. Originally, they were obtained by mixing a hydrogen bond acceptor or an organic salt (generally a quaternary ammonium) with a hydrogen bond donor (e.g. acid, alcohol). The mixing of the two or more solids forming the DES, exhibits a large melting point depression associated to the existence of an eutectic point [8,9]. For practical application, it is expected that the eutectic point lies below room temperature, insuring that the binary mixture is liquid in normal condition. Non-ideal mixing effects, which could arise from the specific H-bonded association of the DES compounds is generally accepted to explain the exceptional lowering of the melting point of certain DESs well below room temperature, as well as their remarkable solvent properties.

Recently the notion of DES has been considered in a more loose way in the literature, including liquid mixtures formed by H-bonded systems that do not necessarily present non-ideality. Even more, the experimental determination of the eutectic point remains unsolved for many of them. As underlined in ref. [9], it demonstrates the need for a stricter definition and consequently a deeper thermodynamic characterization of DESs.

An even more complex situation can be encountered when DES is used as ingredient in the preparation of multicomponent systems. A first step in this direction concerns the addition of water to DES, which is proposed to circumvent some limitations, such as viscosity, while keeping its functional properties [10]. The integrity of DES could be destroyed in biphasic aqueous systems, while its local arrangement could be preserved in single-phase aqueous DES mixtures up to a moderate degree of hydration [1,11]. The physical properties of water-ionic liquids and water-DES mixtures, including excess properties, viscosity, acoustic, structural and optical properties have been studied around ambient temperature and above [1,12–19].

In the present work, we investigated the phase behavior of aqueous mixtures of a prototypical DES (Ethylene Glycol/Choline Chloride) system from mild hydration levels to complete dilution and temperatures ranging from −150 to 50 °C. We have established a detailed phase diagram resolving the transitions between equilibrium phases as well as

* Corresponding author.
E-mail address: denis.morineau@univ-rennes1.fr (D. Morineau).

https://doi.org/10.1016/j.molliq.2020.112701
0167-7322/

metastable glassy states. Interestingly, the phase behavior highlights a cross-over in the thermodynamic behavior at a hydration level W_g'~30% where the structure of DES is usually disrupted. The nature of this specific composition, which is recovered on cooling in the fluid phase whatever the initial DES composition, is discussed in the frame of maximally freeze-concentrated solutions. While this concept has been commonly used in relation to freeze-drying processes, its application to DES aqueous solutions is original.

2. Methods

2.1. Samples

Choline chloride (>99%) and ethylene glycol (anhydrous, 99.8%) were purchased from Sigma-Aldrich. Two DES were prepared by weighting and adding ethylene glycol and choline chloride in a molar ratio of 2:1 and 3:1, which is in the region of maximum freezing depression [20,21].The DES were mixed by mechanical agitation at about 60 °C for 30 min until a clear homogeneous liquid phase was obtained and served as stock solutions. Two series of 10 working solutions were prepared by pipetting and addition of deionized water.

2.2. DSC experiments

The differential scanning calorimetry (DSC) measurements were performed with a Q-20 TA Instrument equipped with a liquid nitrogen cooling system. The melting transition of an indium sample was used for calibration of temperature and heat flux. The samples were loaded in sealed aluminum hermetic pans and their masses, typically 6 mg were measured with a microbalance. In general, the temperature was ramped linearly on cooling and heating in the temperature range from −150 °C to 50 °C (scanning rate of 10 °C.min^{-1}). Quenched samples were obtained by cooling the sample from 50 °C down to −150 °C at the fastest speed achieved with this DSC furnace, which was varying from −60 °C.min^{-1} around room temperature to −20 °C.min^{-1} on approaching the lowest temperature limit −150 °C.

3. Results and discussion

For the smallest values of the water mass fractions W = 0–30%, no obvious crystallization was observed when cycling the solution in the temperature range from −150 °C to 50 °C at 10 °C.min^{-1} except for a small exothermic peak at −25 °C on heating the pure DES. For all samples, the occurrence of a glass transition was indicated by a jump of the heat capacity, as shown in Fig. 1. The value of T_g decreases gradually from −116 to −125 °C when the water fraction increases. This indicates an acceleration of the structural relaxation associated to the glassy dynamics. Obviously, the addition of water reduces the viscosity of the DES solution, as observed for other aqueous solutions [22]. This plasticizing effect may arise from the enhancement of the mobility of the solute molecules, when they are surrendered by the more dynamic and smaller sized water molecules. Additional effects could also be invoked, such as the reduction of the electrostatic interactions between ionic species as well as a disruption of the H-bond interactions within the DES supramolecular structures.

For intermediate values of the water mass fractions W = 40% and 50%, different behaviors were observed depending on the cooling rate. The phenomenon is illustrated for W = 50% in Fig. 2 and is discussed hereafter. For a moderate rate of 10 °C.min^{-1}, the solution crystallized during cooling, as indicated by the exothermic signal around T_c = −56 °C. However, crystallization could be avoided if a faster cooling rate of about 60 °C.min^{-1} was applied. In the latter case, the entire solution was obviously quenched in a vitreous state. Both vitreous and crystallized solutions were subsequently heated up from −150 °C to 30 °C following the same heating ramp of 10 °C.min^{-1}. The quenched solution presented a glass transition at T_g, followed by a crystallization as indicated by an exothermic peak at about −120 °C in Fig. 2. On further heating, the thermogram presented a very broad endothermic peak, which extended from T_m' = −96 °C to T_m = −31 °C. Differently, the solution, which was allowed to crystallize during a slower cooling ramp only presented a glass transition and a broad melting peak, without any additional crystallization on heating. Moreover, the glass transition temperature T_g' was significantly higher than T_g, which implies that after crystallization occurred, the remaining unfrozen solution had a different composition from the whole initial solution. In both cases however, the broad melting peak was comparable in shape and intensity, which suggests that the crystallization occurring on slow cooling or the cold crystallization on heating after a thermal quench eventually led to a comparable fraction of ice and composition of the remaining liquid solution.

A similar behavior was also observed for W = 40% (not shown), which also allowed studying the glass transition of a fully vitrified solution T_g and a mixture of glassy solution coexisting with ice T_g' as well. Apart from the slightly different values of the temperatures of transitions, some differences in the thermal behavior were also observed with respect to W = 50%. Indeed, on slow cooling at 10 °C.min^{-1} crystallization did not occur, but rather during the subsequent heating above T_g (at T_c = −77 °C). Once crystallization was observed, the sample was cycled back to −150 °C in order to later study T_g' during a second heating branch at 10 °C.min^{-1}.

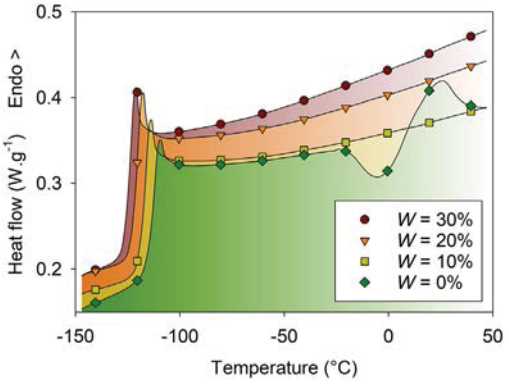

Fig. 1. Thermograms measured during heating from −150 °C to 50 °C at 10 °C.min^{-1} after a preceding cooling ramp at the same rate, for the smallest values of the water mass fraction in aqueous solutions of Ethaline (2:1) DES mixtures, W = 0, 10, 20, 30%. The signature of the glass transition of the whole solution is indicated by a jump of the heat capacity at T_g.

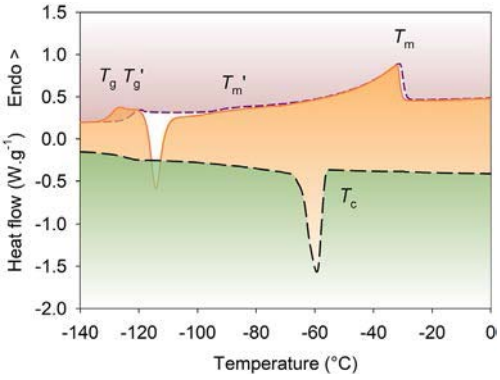

Fig. 2. Thermograms measured for aqueous solution of Ethaline (2:1) DES mixture W = 50%. Heat flux measured on cooling from 30 °C to −150 °C at 10 °C.min^{-1} (medium dash). Heat flux measured on heating from 30 °C to −150 °C at 10 °C.min^{-1} after a thermal quench (solid line) and after a slow cooling at the same rate (short dash). The glass transition of the whole quenched solution is indicated by a jump at T_g, while the glass transition of the freeze-concentrated solution stands at T_g'.

Finally, a third behavior was observed for the largest values of the water mass fraction $W = 60, 70, 80, 87\%$, as shown in Fig. 3. In this case, crystallization could not be avoided even when applying thermal quench. The thermograms measured during heating present a glass transition at about the same temperature $T_g' = -123$ °C and a broad endothermic peak, which intensity increased with the amount of water. The ice melting process associated to this broad peak was always initiated at about the same temperature $T_m' = -95 \pm 2$ °C for all the water compositions where crystallization occurred (i.e. $W = 40$–87%), while the final melting occurred at temperatures increasing from $T_m = -49$ °C to -3 °C when W increased.

In order to better characterize the nature of the unfrozen phase that co-exist with ice, we applied two methods. First, we calculated the melting enthalpy $\Delta H(W)$ by integration of the melting peak on a temperature range encompassing the region from T_m' to T_m, as a function of the composition W. A linear variation was observed, as presented in Fig. 4(a) where the melting enthalpy was normalized with respect to its value for $W = 100\%$, i.e. $\Delta H_r(W) = \frac{\Delta H(W)}{\Delta H(100)}$. Assuming that the melting enthalpy of ice is not affected by the coexistence with the unfreezable DES solution and neglecting the melting point depression effects, $\Delta H_r(W)$ can be considered as a measure of the mass fraction of frozen water. By extrapolation of $\Delta H_r(W)$ to vanishing values, we could concluded that the formation of ice was incomplete and that the unfreezable water content in the DES solution was $W_g' = 30\%$.

The second approach is presented in Fig. 4(b), where the glass transition temperature of the whole aqueous solution (T_g) or only the unfrozen part coexisting with ice (T_g') is plotted as a function of the water content W. We observed that the glass transition temperature of the solution readily decreased from $T_g = -116.6$ °C to -129.7 °C for increasing values of water ($W = 0$–50%). This systematic acceleration of the relaxation dynamics of the DES with the addition of water was already discussed in the previous part. At variance, once ice had crystallized, the glass transition temperature of the unfrozen solution (T_g') presented a much weaker dependence, slightly increasing from $T_g' = -124.4$ °C to -122.5 °C for increasing values of water ($W = 40$–90%). This indicates that after the crystallization of ice, it remains an unfrozen glassforming aqueous solution of DES with an almost fixed composition. The latter could be estimated by using the measured characteristic dependence of T_g with W as a calibration curve, and determining the unfrozen water content as the composition where T_g is equal to T_g'. In order to account for the minor variation of T_g', we applied a linear extrapolated, as presented in Fig. 4(b). This second independent method gave a same determination of the water composition of the unfrozen solution $W_g' = 30\%$.

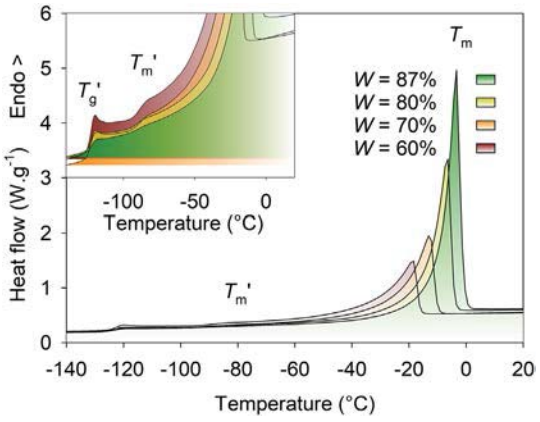

Fig. 3. Thermograms measured during heating from −150 °C to 30 °C at 10 °C.min^{-1} after a preceding cooling ramp at the same rate, for the largest values of the water mass fraction in aqueous solutions of Ethaline (2:1) DES mixtures, $W = 60, 70, 80, 87\%$. The glass transition of the freeze-concentrated solution is indicated by a jump at T_g' (cf. magnified view in inset), while the melting of the frozen ice appears as a broad endothermic peak that extends from T_m' to T_m.

The resulting phase behaviors were determined as presented in Fig. 5(a) and (b). It should be stressed that the studied systems are actually a ternary mixture (Ethylene Glycol/Choline Chloride/Water), considering that the DES compound, which is classically named Ethaline in the literature, is already a binary liquid. With this important caution in mind, a pseudo-binary phase diagram could be determined along the line of constant Ethylene Glycol/Choline Chloride relative mole ratio. This representation is of most interest for practical use, when the water content is the main varying parameter in order to optimize the solvent properties or during industrial processing. It can be also argued that the absence of any phase separation or liquid-liquid transition, apart from ice crystallization, makes this representation particularly sensible and scientifically sound.

The phase diagrams corresponding to the two studied Ethaline compositions, comprising Ethylene Glycol/Choline Chloride in a 2:1 and 3:1 mol ratio, are presented in Fig. 5(a) and (b), respectively. It should be stressed however that they do not differ significantly. Hence, the same discussion and conclusions hold for both systems. To understand the stoichiometric proportions that may be driving the molecular level interactions, the phase diagrams as a function of the water mole fraction x are also represented in Fig. 6(a) and (b). The variation of the melting transition with the composition W (40–90%), could be compared to the behavior usually observed for binary systems that exhibit an eutectic point, where the later determines the fixed temperature T_E at which melting starts. Obviously, this scenario does not apply in the present situation, since no crystallization was observed in the DES-rich region ($W = 0$–30%). Moreover, the observation of a glass transition at T_g' for $W = 40$–90% indicates that, apart from ice, the remaining solution did not crystallize.

Interestingly, the observed phenomenon is in perfect qualitative agreement with the thermal behavior of solute/water binary solutions comprising amorphous cryoprotectants (including polyols, carbohydrates, polymers and proteins). [22–26]. However, it has been hardly addressed for DES in the literature [27]. According to the numerous studies on their phase diagrams, the crystallization of water to ice induces a residual liquid phase, which composition is enriched in solutes. As such, it is denoted the maximally freeze-concentrated solution. Interestingly, its water composition is barely dependent on the initial composition of the solution and for the present system it corresponds to a water mass fraction $W_g' = 30\%$. It is therefore straightforward that for $W > W_g'$, provided that ice crystallization occurred, this composition determined the value of its glass transition T_g' and fixed the chemical potential of the solution, and so the temperature T_m' corresponding to the onset of ice melting [28].

The water molar fraction of the maximally freeze-concentrated solution can be calculated from the mass fraction $W_g' = 30\%$. The ternary composition of the maximally freeze concentrated solution are Water/Ethylene Glycol/Choline Chloride (6:2:1) and (10:3:1) for the two studied ethaline aqueous solutions, and later referred as ethaline(2:1)-6w and ethaline(3:1)-10w.

This study raises questions about the mechanisms that control the composition of the maximally freeze concentrated DES solution. From a thermodynamic or structural point of view, it may be considered that the unfrozen water molecules retained in the DES system during ice formation are involved in the formation of stable structures. Recent Brillouin studies have indicated the existence of a crossover in the sound propagation velocity in different DES for an aqueous dilution around $W = 30\%$ [17,18]. Along with NMR data, this result has been interpreted as the transitioning of the liquid structure from a H_2O-based to a DES-based H-bonded network. FTIR and NMR studies of choline chloride/glycol water solutions have also indicated that the interactions between DES components were initially maintained during water addition, and weaken gradually up to $W = 50\%$ [29]. For water-reline (reline being the DES

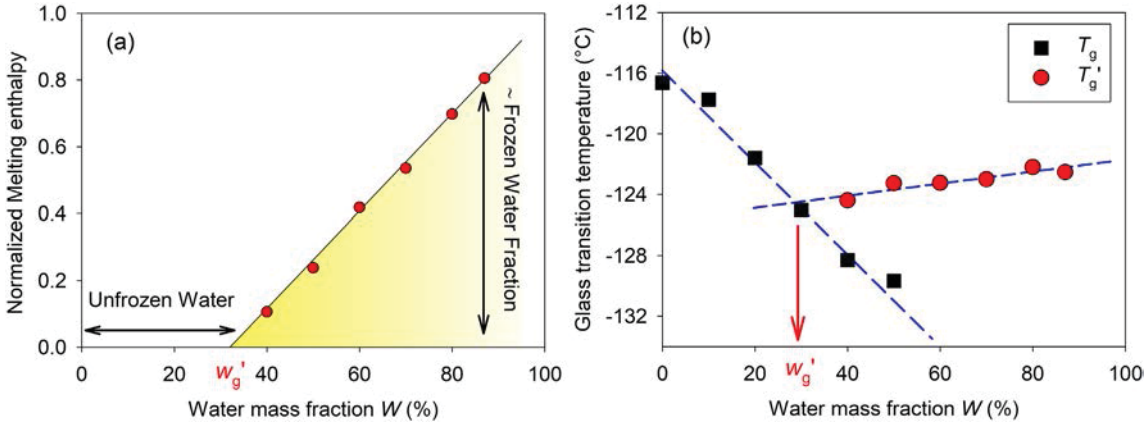

Fig. 4. Water mass fraction in aqueous solutions of Ethaline (2:1) DES mixtures as a function of (a) the normalized melting enthalpy of the freezable water and (b) the glass transition of the unfrozen solution T_g in the absence of ice (squares) and T_g' when coexisting with ice (circle). For $W = 40$ and 50%, T_g corresponds to the fully vitrified solution, which is metastable with respect to the case when ice coexists with a more concentrated glassy solution (T_g').

mixture formed with choline chloride and urea) both neutron scattering experiments and simulated X-ray scattering structure functions demonstrated that the DES structure was qualitatively retained up to the hydration value of $W = 41\%$ (i.e. reline-10w) [1,15]. Up to this composition, it appeared that water molecules are systematically involved in the solvation of choline ions, and higher level of water are needed to induce the transition from water-in-DES to aqueous solution of DES components. The formation of strong water-DES interaction was further supported by a FTIR and Raman vibrational spectroscopy study of water-glyceline (glyceline being the DES mixture formed with choline chloride and glycerol), which indicated that a maximum association is reached for 0.9 mol fraction of water/DES (i.e. glyceline-9w) [19].

In the frame of the present study, it is of special interest to notice that the ongoing crystallization of ice that occurs during cooling of a DES aqueous solution gradually increases the solute concentration of the co-existing liquid phase. Starting from an initially dilute range (eg. $W > 50\%$), the aqueous DES solution evolves from the "DES-in-water" to "water-in-DES" situation, according to the designation introduced by ref. [18]. This transformation is eventually arrested when $W_g' = 30\%$ (i.e. 6w to 10w), which is precisely in the range where the structural transitions have been observed in water-DES mixtures. It is therefore likely that the water molecules remaining in the maximally freeze-concentrated DES solution are actually sequestrated in a structure, which is dominated by the DES interactions and stops further water crystallization.

However, it does not imply that the phenomenon is fully driven by thermodynamics. If so, it would mean that the chemical potential of the entrapped water molecules at W_g', which participate in the hydration of DES compounds and most likely to the solvation of choline cations, is equal to that of ice even at the lowest studied temperature [1]. Studies of maximally freeze-concentrated solution of alcohols, carbohydrates and biological materials of interest for cryobiological, pharmaceutical or food applications have emphasized the importance of dynamical effects and metastability [23–26,28]. In fact, the formation of ice increases the solute concentration of the unfrozen phase. According to the liquidus line, it implies that the temperature of the system should be further decreased in order to enlarge the fraction of ice formed. However the lowering of the temperature and the increase in the solute concentration concomitantly raises the viscosity of the unfrozen part. Therefore, ice formation becomes extremely slow on approaching T_m' as the viscosity reaches the typical value of 10^7 Pa.s, and it is completely stopped in the glassy state at temperature below T_g'. For water-ethaline aqueous solution, we determined that the region of maximally freeze-concentrated solution extends on a temperature range of 27 °C between T_m' and T_g'. This is larger than reported for most commonly studied polyols and carbohydrates for freeze-drying application, which are rather in the range 5 to 15 °C [23]. Although standing beyond the scope of the present article, a possible interpretation of the broader range between T_m' and T_g' is related to the specific nature of DES, which is a multicomponent system comprising strong interactions (ionic, H-bonds) and favored structures, such as solvated

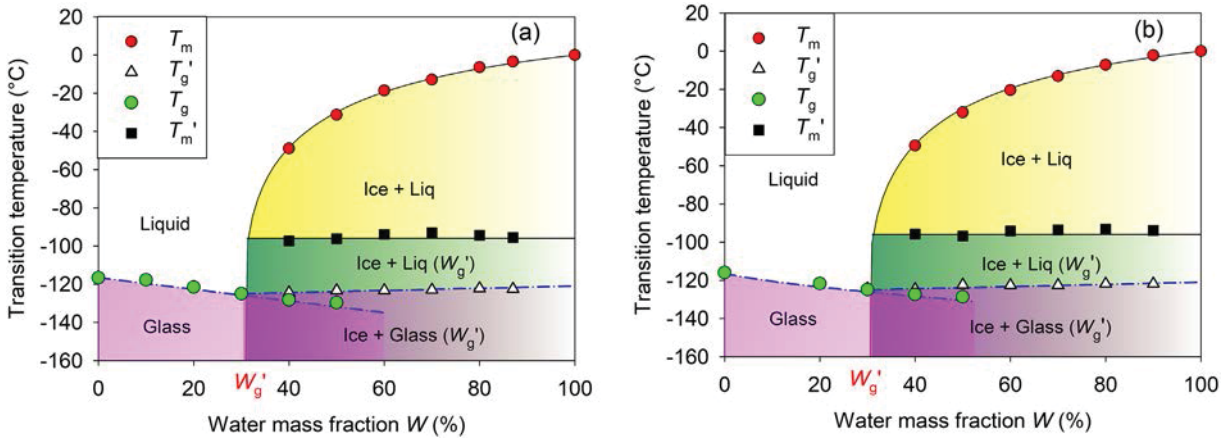

Fig. 5. Phase diagram of aqueous solutions of Ethaline DES mixtures as a function of the water mass fraction W for two molar compositions of Ethaline (a) Ethylene Glycol/Choline Chloride in a 2:1 mol ratio and (b) Ethylene Glycol/Choline Chloride in a 3:1 mol ratio.

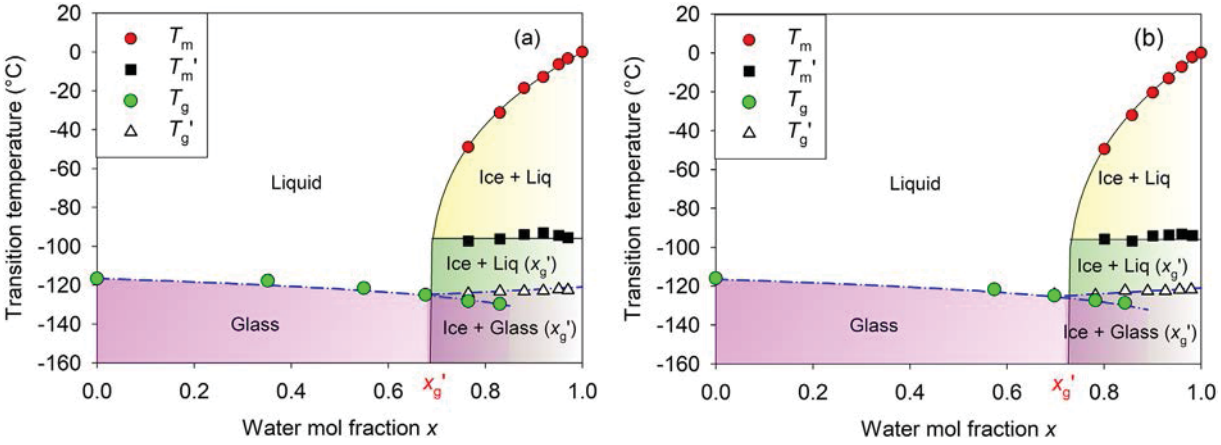

Fig. 6. Phase diagram of aqueous solutions of Ethaline DES mixtures as a function of the water mole fraction x for two molar compositions of Ethaline (a) Ethylene Glycol/Choline Chloride in a 2:1 mol ratio and (b) Ethylene Glycol/Choline Chloride in a 3:1 mol ratio.

units discussed before that further reduces the crystallization dynamics. Whenever the water mobility is fast enough, it is also likely that the remaining water involved in the solvated units is sufficiently much distorted from bulk water, due to interactions with the DES molecules that it will be unable to crystallize.

Because of this tendency to form strong H-bonds, it would be of great interest to further study how they distort the water network and participate to the solvation shell of active pharmaceutical agents and biomolecules, which commonly are considered as interesting features of bioprotectant agents [30,31]. Furthermore, one might speculate that controlling the stability of the maximally freeze concentrated solution on an extended temperature could reduce the risks of devitrification and cold crystallization in a temperature range near and above T_g', the occurrence of which is usually deleterious to the stability of solvated proteins and is considered as a critical parameter for the design of optimal freeze-drying processes for cryopreservation [32,33]. Finally, it is worth mentioning the proximity of $T_g' = -124$ °C is significantly lower than for usual freeze-concentrated and freeze-dried materials, which can be associated to the low value of T_g of the pure DES itself [23,34]. As a result, it also lies close to the temperature ($T_g^{water} = -137$ °C), which has been considered as the glass transition temperature of pure water, although the exact location of the liquid-to-glass transition of bulk water has be questioned recently and it is still the matter of exciting discussion [35].

4. Conclusions

The phase behavior of aqueous solutions of the deep eutectic solvent ethaline was studied by calorimetry from −150 to 50 °C. The fraction of water was varied extensively $W = 0$–90% from composition where the DES structure dominates to the diluted regime of aqueous dispersion of the DES components. The former case is characterized by the absence of crystallization and the formation of a glassy DES solution on cooling. In this case, water acts as a plasticizer but the phase behavior of the pure DES is retained. The latter case is characterized by the crystallization of ice, which phase separates from a maximally freeze-concentrated DES solution. In this situation, whatever the initial composition is, the composition of the unfrozen liquid is constant $W_g' = 30\%$, which corresponds to the ternary compositions Water/Ethylene Glycol/Choline Chloride (6:2:1) and (10:3:1) for the two studied systems, also referred as ethaline(2:1)-6*w* and ethaline(3:1)-10*w*. Interestingly, this phenomenon drives the transition of the DES aqueous mixture from the "DES-in-water" to "water-in-DES" regime. We infer that the value of the maximally freeze-concentration, which lies in the region where a cross-over in the structure of DES was reported for many systems, is determined by the extreme slowdown of ice formation as the viscosity of the unfrozen solution increases on approaching the glass transition of the maximally freeze-concentrated DES solution $T_g' = -124$ °C as well as strong interactions between the remaining water molecules and the solvated DES units.

The formation of maximally freeze-concentrated solution has been extensively studied for polyols, proteins and carbohydrates, which are relevant to cryobiology and freeze-drying processes but similar studies on DES are scarce in the literature. Beyond the fundamental interest of a better understanding of the low-temperature behavior of hydrated DES, we hope that this study could also be helpful for developing innovative processes based on the freeze-drying of DES solutions for materials design, cryoprotectant and pharmaceutic applications.

Author statement

Thibaut Sohier: Investigation, Writing - Review & Editing.
Aicha Jani: Investigation, Writing - Review & Editing.
Denis Morineau: Conceptualization, Investigation, Writing - Original Draft, Supervision, Funding acquisition.

Declaration of competing interest

The authors declare that they have no known competing financial interests or personal relationships that could have appeared to influence the work reported in this paper.

Acknowledgments

Support from Rennes Metropole and Europe (FEDER Fund – CPER PRINT$_2$TAN), and the ANR (Project NanoLiquids N° ANR-18-CE92-0011-01) is expressly acknowledged. This work is part of the PhD thesis of A.J. who benefits from a grant from the French Ministry of Higher Education, Research, and Innovation. The authors are grateful to the CNRS – network SolVATE (GDR 2035) for financial support and fruitful discussions.

References

[1] O. Hammond, D. Bowron, K. Edler, The effect of water upon deep eutectic solvent nanostructure: an unusual transition from ionic mixture to aqueous solution, Angewandte Chemie-International Edition 56 (33) (2017) 9782–9785.
[2] O. Hammond, D. Bowron, A. Jackson, T. Arnold, A. Sanchez-Fernandez, N. Tsapatsaris, V. Sakai, K. Edler, Resilience of malic acid natural deep eutectic solvent nanostructure to solidification and hydration, J. Phys. Chem. B 121 (31) (2017) 7473–7483.
[3] Q. Zhang, K. Vigier, S. Royer, F. Jerome, Deep eutectic solvents: syntheses, properties and applications, Chem. Soc. Rev. 41 (21) (2012) 7108–7146.

[4] E. Smith, A. Abbott, K. Ryder, Deep Eutectic Solvents (DESs) and their applications, Chem. Rev. 114 (21) (2014) 11060–11082.
[5] X. Ge, C. Gu, X. Wang, J. Tu, Deep eutectic solvents (DESs)-derived advanced functional materials for energy and environmental applications: challenges, opportunities, and future vision, J. Mater. Chem. A 5 (18) (2017) 8209–8229.
[6] A. Abbott, G. Capper, D. Davies, R. Rasheed, V. Tambyrajah, Novel solvent properties of choline chloride/urea mixtures, Chem. Commun. (1) (2003) 70–71.
[7] A. Abbott, D. Boothby, G. Capper, D. Davies, R. Rasheed, Deep eutectic solvents formed between choline chloride and carboxylic acids: versatile alternatives to ionic liquids, J. Am. Chem. Soc. 126 (29) (2004) 9142–9147.
[8] L. Kollau, M. Vis, A. van den Bruinhorst, A. Esteves, R. Tuinier, Quantification of the liquid window of deep eutectic solvents, Chem. Commun. 54 (95) (2018) 13351–13354.
[9] M. Martins, S. Pinho, J. Coutinho, Insights into the nature of eutectic and deep eutectic mixtures, J. Solut. Chem. 48 (7) (2019) 962–982.
[10] Y. Dai, G. Witkamp, R. Verpoorte, Y. Choi, Tailoring properties of natural deep eutectic solvents with water to facilitate their applications, Food Chem. 187 (2015) 14–19.
[11] H. Passos, D. Tavares, A. Ferreira, M. Freire, J. Coutinho, Are aqueous biphasic systems composed of deep eutectic solvents ternary or quaternary systems? ACS Sustain. Chem. Eng. 4 (5) (2016) 2881–2886.
[12] A. Yadav, S. Trivedi, R. Rai, S. Pandey, Densities and dynamic viscosities of (choline chloride plus glycerol) deep eutectic solvent and its aqueous mixtures in the temperature range (283.15-363.15) K, Fluid Phase Equilib. 367 (2014) 135–142.
[13] X. Meng, K. Ballerat-Busserolles, P. Husson, J. Andanson, Impact of water on the melting temperature of urea plus choline chloride deep eutectic solvent, New J. Chem. 40 (5) (2016) 4492–4499.
[14] C. Ma, A. Laaksonen, C. Liu, X. Lu, X. Ji, The peculiar effect of water on ionic liquids and deep eutectic solvents, Chem. Soc. Rev. 47 (23) (2018) 8685–8720.
[15] P. Kumari, S. Shobhna; Kaur, H. Kashyap, Influence of hydration on the structure of reline deep eutectic solvent: a molecular dynamics study, Acs Omega 3 (11) (2018) 15246–15255.
[16] D. Lapena, L. Lomba, M. Artal, C. Lafuente, B. Giner, Thermophysical characterization of the deep eutectic solvent choline chloride:ethylene glycol and one of its mixtures with water, Fluid Phase Equilib. 492 (2019) 1–9.
[17] E. Posada, M. Roldan-Ruiz, R. Rioboo, M. Gutierrez, M. Ferrer, F. del Monte, Nanophase separation in aqueous dilutions of a ternary DES as revealed by Brillouin and NMR spectroscopy, J. Mol. Liq. 276 (2019) 196–203.
[18] M. Roldan-Ruiz, R. Jimenez-Rioboo, M. Gutierrez, M. Ferrer, F. del Monte, Brillouin and NMR spectroscopic studies of aqueous dilutions of malicine: determining the dilution range for transition from a “water-in-DES” system to a “DES-in-water” one, J. Mol. Liq. 284 (2019) 175–181.
[19] R. Ahmadi, B. Hemmateenejad, A. Safavi, Z. Shojaeifard, A. Shahsavar, A. Mohajeri, M.H. Dokoohaki, A.R. Zolghadr, Deep eutectic-water binary solvent associations investigated by vibrational spectroscopy and chemometrics, Phys. Chem. Chem. Phys. 20 (27) (2018) 18463–18473.
[20] K. Shahbaz, S. Mjalli Farouq, M. Hashim, I.M. ALNashef, Using deep eutectic solvents for the removal of glycerol from palm oil-based biodiesel, J. Appl. Sci. 10 (2010) 3349–3354.
[21] P. Lopez-Porfiri, J. Brennecke, M. Gonzalez-Miquel, Excess molar enthalpies of deep Eutectic Solvents (DESs) composed of quaternary ammonium salts and glycerol or ethylene glycol, Journal of Chemical and Engineering Data 61 (12) (2016) 4245–4251.
[22] K. Elamin, J. Sjostrom, H. Jansson, J. Swenson, Calorimetric and relaxation properties of xylitol-water mixtures, J. Chem. Phys. 136 (10) (2012).
[23] Y.H. Roos, Frozen state transitions in relation to freeze drying, J. Therm. Anal. 48 (3) (1997) 535–544.
[24] D.A. Jahn, J. Wong, J. Bachler, T. Loerting, N. Giovambattista, Glass polymorphism in glycerol-water mixtures: I. a computer simulation study, Phys. Chem. Chem. Phys. 18 (16) (2016) 11042–11057.
[25] J. Bachler, V. Fuentes-Landete, D.A. Jahn, J. Wong, N. Giovambattista, T. Loerting, Glass polymorphism in glycerol-water mixtures: II. Experimental studies, Phys. Chem. Chem. Phys. 18 (16) (2016) 11058–11068.
[26] L.D. Weng, W.Z. Li, J.G. Zuo, Two applications of the thermogram of the alcohol/water binary system with compositions of cryobiological interests, Cryobiology 62 (3) (2011) 210–217.
[27] M.C. Gutierrez, M.L. Ferrer, C.R. Mateo, F. del Monte, Freeze-drying of aqueous solutions of deep eutectic solvents: a suitable approach to deep eutectic suspensions of self-assembled structures, Langmuir 25 (10) (2009) 5509–5515.
[28] J. Schawe, A quantitative DSC analysis of the metastable phase behavior of the sucrose-water system, Thermochim. Acta 451 (1–2) (2006) 115–125.
[29] F. Gabriele, M. Chiarini, R. Germani, M. Tiecco, N. Spreti, Effect of water addition on choline chloride/glycol deep eutectic solvents: characterization of their structural and physicochemical properties, J. Mol. Liq. 291 (2019).
[30] T. Arakawa, S. Timasheff, Stabilization of protein-structure by sugars, Biochemistry 21 (25) (1982) 6536–6544.
[31] A. Hedoux, J. Willart, R. Ionov, F. Affouard, Y. Guinet, L. Paccou, A. Lerbret, M. Descamps, Analysis of sugar bioprotective mechanisms on the thermal denaturation of lysozyme from Raman scattering and differential scanning calorimetry investigations, J. Phys. Chem. B 110 (45) (2006) 22886–22893.
[32] G. Fahy, D. Macfarlane, C. Angell, H. Meryman, Vitrification as an approach to cryopreservation, Cryobiology 21 (4) (1984) 407–426.
[33] X. Tang, M. Pikal, Design of freeze-drying processes for pharmaceuticals: practical advice, Pharm. Res. 21 (2) (2004) 191–200.
[34] P. Debenedetti, Supercooled and glassy water, Journal of Physics-Condensed Matter 15 (45) (2003) R1669–R1726.
[35] J. Swenson, Possible relations between supercooled and glassy confined water and amorphous bulk ice, Phys. Chem. Chem. Phys. 20 (48) (2018) 30095–30103.

TABLE OF FIGURES

CHAP-I

CHAP-III

Synthèse de thèse : Nanostructuration de liquides binaires et d'eau par confinement dans des organosilicates périodiques mésoporeux

Auteur : Aîcha Jani

Directeur : Denis Morineau

Jury : Diane Rebiscoul, Sophie Le Caer, Jean Le Bideau, Marie-Vanessa Coulet, Anthony Szymczyk, Denis Morineau

Date de soutenance (prévue) : 06/12/2021

Mention : Physique

Ce projet de thèse a été motivé par le nombre croissant d'observations d'un phénomène de démixtion induit par le nano-confinement des mélanges binaires totalement miscibles en bulk dans les conditions normales. Une description complète d'une nanostructuration cœur-coquille a été réalisée pour un mélange binaire prototype de tert-butanol et de toluène confiné dans des silices mésoporeux du point de vue structural et dynamique. Parmi de nombreux effets de confinement fascinants, la formation de cette nouvelle structure est assez remarquable et soulève plusieurs questions sur son origine physique. Dans des études récentes, cette nanoségrégation (structure cœur-coquille) était liée à l'interaction liquide-surface précisément l'interaction préférentielle de l'alcool avec le silicate.

Inspirés par ces études, nous avons cherché à mieux comprendre comment nous pourrions modifier/contrôler les propriétés physiques (en particulier la dynamique et la structure) par un contrôle nanométrique de la chimie de surface. Nous avons pu atteindre cet objectif en utilisant un système d'organosilicates mésoporeux périodiques (PMOs) avec une surface hybride avec une modulation du caractère hydrophobe/hydrophile le long du pore assurant ainsi une modulation des interactions molecule/surface.

Dans la première partie du projet de thèse, nous avons étudié la dynamique de l'eau liquide confinée dans des silices mésoporeux de type MCM-41 et des organosilicates mésoporeux périodiques de type PMO par des expériences de diffusion incohérente quasiélastique de neutrons (QENS). L'effet de l'ajustement de l'interaction eau/surface sur la mobilité de l'eau, tout en maintenant la taille des pores dans l'intervalle de 3,5 à 4,1 nm, a été évalué à partir de l'étude comparative de trois PMOs comprenant différentes unités

organiques et le MCM-41. Un intervalle de temps étendue a été obtenue en combinant deux spectromètres de l'Insitut Laue Langevin (IN5B et IN16B) offrant des résolutions d'énergie complémentaires. En raison des effets de confinement, l'eau a été efficacement maintenue en phase liquide sur une plage de température étendue (de 300 K à 243 K). Nous avons pu mettre en évidence l'existence de deux mouvements indépendants: un mouvement local rapide et un deuxième transrationnel de diffusion confinée. Toutes les molécules effectuent les mouvements locaux, alors que le mouvement de translation d'une fraction des molécules est figé sur l'échelle de temps expérimentale. Nous avons également fourni plusieurs paramètres tels que la fraction non mobile/mobile, le coefficient de diffusion, le temps de résidence, le rayon de confinement, le temps de relaxation local ainsi que leurs dépendances en température et à la nature de surface de pore. Nous avons pu démontrer que la force de l'interaction interfaciale contrôle la dynamique lente, que nous avons attribuée à la diffusion translationnelle des molécules interfaciales, tandis que la dynamique de l'eau au centre des pores est peu affectée par ces interactions.

Dans une deuxième partie du projet de thèse, l'effet de la modulation des interactions liquide-liquide et liquide-surface sur la dynamique des liquides binaires a été abordé. En étendant les études précédentes dans des mésoporeux de silice, nous avons sélectionné le même mélange prototype de tert-butanol et de toluène. Étant donné que ce mélange ne cristallise plus sous confinement, les expériences QENS ont été réalisées avec succès à l'état liquide sur une large plage de températures de 315 à 220 K. Nous avons appliqué des effets de variation de contraste isotopique pour mettre en évidence la dynamique du composant hydrogéné dans le mélange et minimiser la contribution de son complémentaire deutéré. Par conséquent, nous avons fait varier la concentration de tert-butanol hydrogéné (TBAH) et de toluène hydrogéné (TOLH), ainsi que leurs homologues deutérés (respectivement de TOLD et TBAD). Nous avons étudié les effets de mélange sur la dynamique de chaque composant et nous avons comparé les deux états confiné et bulk. Pour les mélanges confinés, nous avons défini deux modes locaux indépendants réalisés par les molécules hydrogénées (mode lent (S) et mode rapide (F)) et trois modes indépendants pour les molécules hydrogénées dans les mélanges en bulk (mode translationnel (T), mode lent (S) et mode rapide (F)). Le mode rapide (F) est caractérisé par un temps de relaxation τ_F qui présente une faible dépendance à la température, à la concentration et à la nature de la molécule (TBAH ou TOLH) et reste essentiellement comprise entre 0,2 ps et 0,5 ps. Cependant, le

mode lent (S) caractérisé par un temps de relaxation τ_S présente une dépendance en température notable, allant de 4 ps à 15 ps dans le cas de TBAH et de 3,5 ps à 9 ps dans le cas de TOLH pour une baisse en température de 315 K à 220 K. Nous avons également réussi à décrire la géométrie de trajectoire des deux modes locaux avec un bon accord avec les données expérimentales pour les liquides confinés. Un même modèle a fonctionné plus approximativement pour l'état bulk en raison de degrés de liberté supplémentaires, fournis par la diffusion translationnelle sur l'échelle de temps expérimentale étudiée. La géométrie de la trajectoire du mode rapide a été décrite avec un modèle de saut entre 3 sites (pour la rotation des hydrogènes méthyliques) et une rotation dans une sphère gaussienne (pour le reste des hydrogènes). Les rayons caractéristiques obtenus étaient de l'ordre de 1 Å ± 0,1, ce qui est en accord avec la géométrie de la molécule. Et la géométrie de la trajectoire du mode local lent, a été décrite par une rotation isotrope à la surface d'une sphère de rayon 2,6 Å ± 0,5 et 3,5 Å ± 0,5 respectivement pour les molécules TBAH et TOLH. Ce mode est donc attribué à la rotation isotrope globale de la molécule autour de son centre de masse. Également, nous avons évalué les coefficients de diffusion du TBAH et du TOLH dans des mélanges en bulk qui ont montré un comportement très différent, avec un ralentissement de la diffusion du TOLH en y ajoutant le liquide TBA plus visqueux et une accélération de la diffusion du TBA en y ajoutant le liquide TOL. De manière très intéressante, ceci est contraire à l'état confiné, qui présentait une augmentation contre-intuitive de la fraction de molécules de TBA non mobiles lors de sa dilution avec du TOL. Cet « effet anti-plastifiant » était lié à l'adsorption spécifique des molécules de TBA à l'interface poreuse. Pour approfondir cette hypothèse structurelle, nous avons effectué une étude structurelle et quantifié l'interaction molécules-surface par des expériences de diffraction de neutrons aux petits angles et de sorption dynamique de vapeur.

Les expériences de sorption dynamique de vapeur nous ont permis de quantifier les interactions de la matrice DVB-PMO avec les molécules TBA et TOL. Nous avons démontré l'affinité thermodynamique beaucoup plus élevée de la surface DVB-PMO pour les molécules TBA (10 fois plus grande) par rapport à celle du TOL. De plus, nous avons montré l'effet de la chimie de surface sur l'affinité thermodynamique aux molécules adsorbées en comparant les résultats de DVB-PMO avec ceux de MCM-41. Nous avons constaté que l'affinité du MCM-41 pour les molécules TBA est 10 fois plus importante que celle du DVB-PMO. En pouvant exclure les deux structures extrêmes possibles

(c'est-à-dire le mélange homogène et le modèle core-shell entièrement démixé), nos résultats ont mis en évidence un autre modèle inhomogène pour les systèmes confinés dans le PMO qui suppose uniquement une interaction spécifique entre les unités tert-butanol et silice.

Les expériences de diffraction de neutrons aux petits angles (SANS), nous ont permis de mieux comprendre la structuration des molécules TBA et TOL dans le DVB-PMO. En effectuant des calculs prédictifs de l'intensité de diffusion de différents modèles de nanostructuration à l'intérieur du pore, nous avons trouvé une meilleure cohérence avec le même modèle inhomogène précédemment proposé suite aux expériences DVS, fournissant une image microscopique, bien que probablement simplifiée, du mélange liquide nanoconfiné dans le PMO.

A notre connaissance, cette étude qui a examiné de manière approfondie l'effet de la modulation de l'interaction surface/molécule sur les propriétés physiques de l'eau et des mélanges miscibles binaires confinés est totalement originale par rapport à ce qu’il existe en littérature.

Abstract:

Inspired by recent studies that related the surface-induced nanosegregation (core−shell structure) to liquid-surface interaction, we aimed to modify/control physical properties (in particular dynamics and structure) through nanoscale control of surface interactions by using PMOs system with a hybrid surface with controlled hydrophobic/hydrophilic modulated units. Hence, we have investigated the dynamics of liquid water confined in periodic mesoporous organosilicas (PMOs) and mesostructured porous silica (MCM-41) by incoherent quasielastic neutron scattering experiments (QENS). Importantly, we demonstrated that the strength of the water/surface interaction determines the long-time tail of the dynamics, which we attributed to the translational diffusion of interfacial molecules, while the water dynamics in the pore center is barely affected by the interface hydrophilicity. The vapor sorption method allowed us to quantify the interactions of the DVB-PMO matrix with TBA and TOL molecules and to show the effect of surface chemistry on the thermodynamic affinity to adsorbed molecules by comparing DVB-PMO results with those obtained with MCM-41. Importantly, we showed that mixture nanostructuring in DVB-PMO is different of the core-shell model. Small angle neutron scattering experiments allowed us to better understand the structuring of TBA and TOL molecules into the DVB-PMO pore cavity and to propose an alternative model which showed a high consistence with experimental result. We have, also, investigated the dynamics of tert-butanol and toluene mixture confined in divinylbenzene (DVB)-PMO by QENS experiments. We succeeded in describing the spatial trajectory of the different motions performed by both molecules (tert-butanol and toluene) with a fairly good agreement with experimental data in various mixtures concentration and temperature range under confinement and in bulk state.

Résumé :

Inspirés par des études récentes qui reliaient la structure cœur-coquille induite par confinement à l'interaction liquide-surface, nous avons cherché à modifier/contrôler les propriétés physiques (en particulier la dynamique et la structure) par modulation de ces interactions en utilisant des nanopores hybrides dont la chimie de surface est modulée d'une manière contrôlée. Nous avons étudié, alors, la dynamique de l'eau liquide confinée dans des organosilices mésoporeux périodiques (PMO) et de la silice mésoporeuse (MCM-41) par des expériences de diffusion quasi-élastiques incohérentes de neutrons (QENS). Nous avons démontré que la force de l'interaction interfaciale contrôle la dynamique lente, que nous avons attribuée à la diffusion translationnelle des molécules interfaciales, tandis que la dynamique de l'eau au centre des pores n'est pas trop affectée par ces interactions. La méthode de sorption de vapeur nous a permis de quantifier les interactions surface/molécule et investiguer l'effet de la nature de la surface sur l'affinité thermodynamique des molécules adsorbées. Également, on a pu montrer que la nanostructuration du mélange dans le DVB-PMO est différente de la structure cœur-coquille. Des expériences de diffusion de neutrons aux petits angles SANS nous ont permis de mieux identifier sa nature et de proposer un modèle alternatif cohérent avec l'expérience. Nous avons également étudié la dynamique du mélange tert-butanol et toluène confiné dans du divinylbenzene (DVB)-PMO par QENS. Par cette technique nous avons réussi à décrire la géométrie de trajectoire des différents mouvements effectués par les deux molécules (tert-butanol et toluène) à différentes conditions (variation de concentration et/ou de température, sous confinement ou en bulk).